tecnalia
MEMBER OF BASQUE RESEARCH & TECHNOLOGY ALLIANCE

eman ta zabal zazu
Universidad del País Vasco
Euskal Herriko Unibertsitatea

Departamento de Ingeniería Mecánica / Ingeniaritza Mekanikoa Saila

BIO-INSPIRED DESIGN AND MANUFACTURING METHODOLOGIES FOR LIGHTWEIGHT, FUNCTIONALITY CUSTOMIZED AND SUSTAINABLE METALLIC COMPONENTS

Ignacio Laraudogoitia Blanc

BIO-INSPIRED DESIGN AND MANUFACTURING METHODOLOGIES FOR LIGHTWEIGHT, FUNCTIONALITY CUSTOMIZED AND SUSTAINABLE METALLIC COMPONENTS

Ph.D. THESIS
presented to obtain the degree of
Doctor

Ignacio Laraudogoitia Blanc

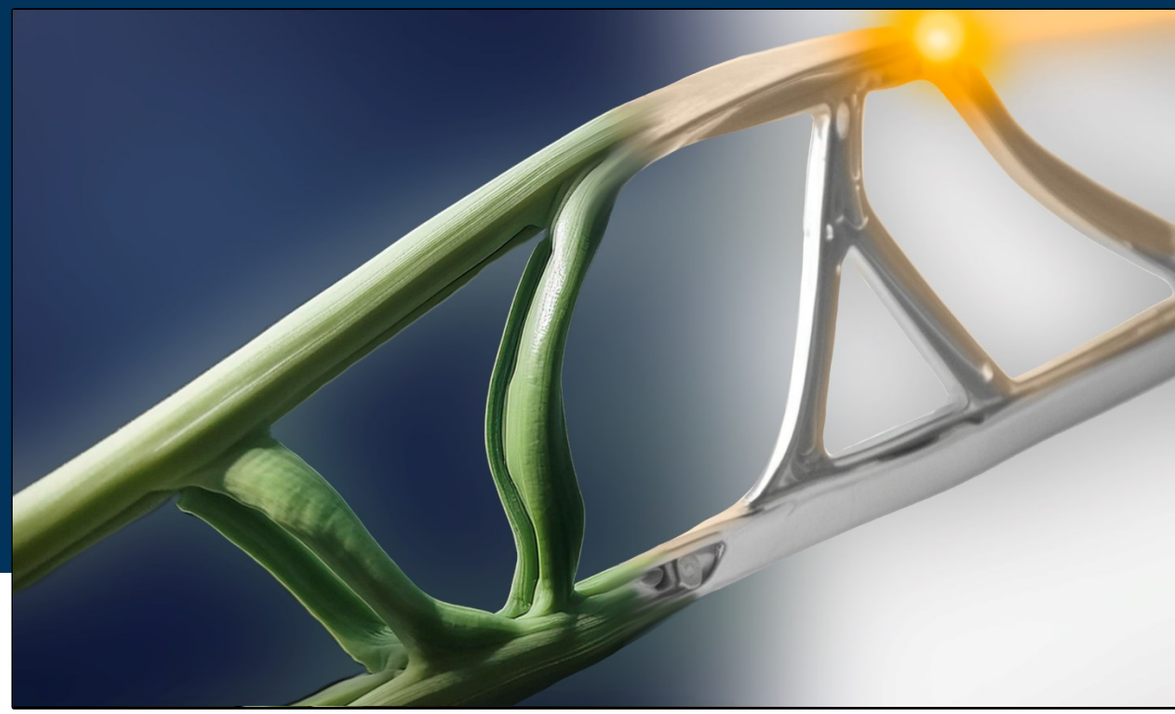

THESIS ADVISOR
Prof. Franck Andrés Girot Mata
Dr. Maider Garcia de Cortazar Aguirrezabal

Jul 2024, Bilbao

eman ta zabal zazu
Universidad del País Vasco
Euskal Herriko Unibertsitatea

INGENIARITZA MEKANIKOA SAILA
DEPARTAMENTO DE INGENIERÍA MECÁNICA

eman ta zabal zazu

Universidad del País Vasco
Euskal Herriko Unibertsitatea

BIO-INSPIRED DESIGN AND MANUFACTURING METHODOLOGIES FOR LIGHTWEIGHT, FUNCTIONALITY CUSTOMIZED AND SUSTAINABLE METALLIC COMPONENTS

Ignacio Laraudogoitia Blanc

Thesis presented to the University of the Basque Country for the degree of Doctor

Department of Mechanical Engineering

Thesis advisors

Pr. Franck Andrés Girot Mata

Dr. Maider García de Cortázar Aguirrezabal

July 2024

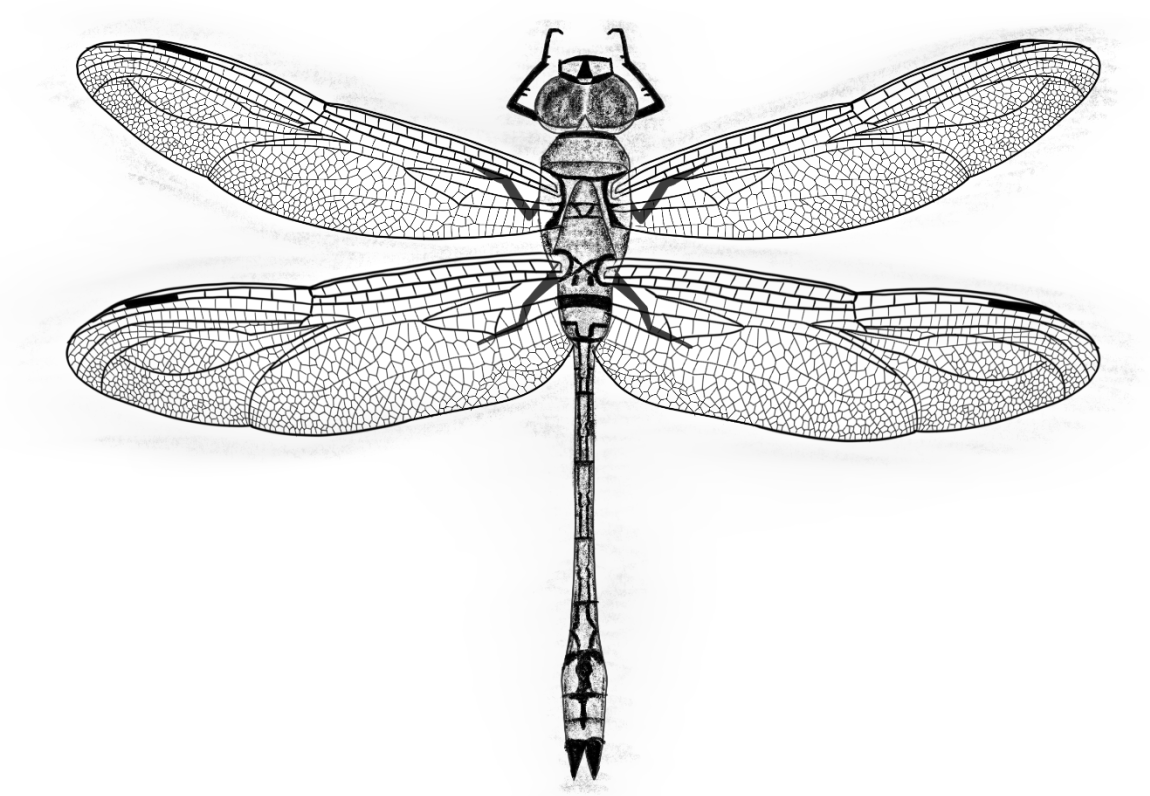

"The answers to our questions are everywhere; we just need to change the lens with which we see the world."

Janine M. Benyus

Universidad del País Vasco | Euskal Herriko Unibertsitatea

NAZIOARTEKO BIKAINTASUN CAMPUSA
CAMPUS DE EXCELENCIA INTERNACIONAL

TESI ZUZENDARIAREN BAIMENA TESIA AURKEZTEKO	AUTORIZACIÓN DEL/LA DIRECTORA/A DE TESIS PARA SU PRESENTACIÓN

Zuzendariaren izen-abizenak /Nombre y apellidos del/la director/a:

Franck Andrés Girot Mata

IFZ /NIF: 78958405A

Tesiaren izenburua / Título de la tesis:

Bio-inspired design and manufacturing methodologies for lightweight, functionality customized and sustainable metallic components

Doktorego programa / Programa de doctorado: **Ingeniería mecánica**

Doktoregaiaren izen-abizenak / Nombre y apellidos del/la doctorando/a:

Ignacio Laraudogoitia Blanc

Unibertsitateak horretarako jartzen duen tresnak emandako ANTZEKOTASUN TXOSTENA ikusita, baimena ematen dut goian aipatzen den tesia aurkez dadin, horretarako baldintza guztiak betetzen baititu.	Visto el INFORME DE SIMILITUD obtenido de la herramienta que a tal efecto pone a disposición la universidad, autorizo la presentación de la tesis doctoral arriba indicada, dado que reúne las condiciones necesarias para su defensa.

Tokia eta data / Lugar y fecha:

Bilbao, 8 de julio de 2024

Sin. / Fdo.: Tesiaren zuzendaria / El/La director/a de la tesis

Universidad del País Vasco | Euskal Herriko Unibertsitatea

NAZIOARTEKO BIKAINTASUN CAMPUSA
CAMPUS DE EXCELENCIA INTERNACIONAL

TESI ZUZENDARIAREN BAIMENA TESIA AURKEZTEKO	AUTORIZACIÓN DEL/LA DIRECTORA/A DE TESIS PARA SU PRESENTACIÓN

Zuzendariaren izen-abizenak /Nombre y apellidos del/la director/a:
Maider García de Cortázar Aguirrezabal
IFZ /NIF: 44152593-E

Tesiaren izenburua / Título de la tesis:

Bio-inspired design and manufacturing methodologies for lightweight, functionality customized and sustainable metallic components

Doktorego programa / Programa de doctorado: **Ingeniería mecánica**

Doktoregaiaren izen-abizenak / Nombre y apellidos del/la doctorando/a:

Ignacio Laraudogoitia Blanc

Unibertsitateak horretarako jartzen duen tresnak emandako ANTZEKOTASUN TXOSTENA ikusita, baimena ematen dut goian aipatzen den tesia aurkez dadin, horretarako baldintza guztiak betetzen baititu.	Visto el INFORME DE SIMILITUD obtenido de la herramienta que a tal efecto pone a disposición la universidad, autorizo la presentación de la tesis doctoral arriba indicada, dado que reúne las condiciones necesarias para su defensa.

Tokia eta data / Lugar y fecha:
Donostia, 2024ko Uztailak 8.



Sin. / Fdo.: Tesiaren zuzendaria / El/La director/a de la tesis

AUTORIZACIÓN DEL DEPARTAMENTO

El Consejo del Departamento de Ingeniería Mecánica en reunión celebrada el día 16 de julio de 2024 ha acordado dar la conformidad a la

admisión a trámite de presentación de la Tesis Doctoral titulada:

Bio-inspired design and manufacturing methodologies for lightweight, functionality customized and sustainable metallic com

dirigida por el Dr. Franck Andrés Girot Mata y la Dra. Maider García de Cortázar Aguirrezabala

---

y presentada por Don Ignacio Laraudogoitia Blanc

ante este Departamento.

En Bilbao a 16 de julio de 2024

VºBº DIRECTOR/A DEL DEPARTAMENTO

SECRETARIO/A DEL DEPARTAMENTO

Fdo.: _____

Fdo.: _____

Universidad del País Vasco | Euskal Herriko Unibertsitatea

NAZIOARTEKO BIKAINTASUN CAMPUSA
CAMPUS DE EXCELENCIA INTERNACIONAL

ACTA DE GRADO DE DOCTOR O DOCTORA
ACTA DE DEFENSA DE TESIS DOCTORAL

DOCTORANDO/A DON/DÑA. Ignacio Laraudogoitia Blanc

TITULO DE LA TESIS: *Bio-inspired design and manufacturing methodologies for lightweight, functionality customized and sustainable metallic components*

El Tribunal designado por la Comisión de Postgrado de la UPV/EHU para calificar la Tesis Doctoral arriba indicada y reunido en el día de la fecha, una vez efectuada la defensa por el/la doctorando/a y contestadas las objeciones y/o sugerencias que se le han formulado, ha otorgado por_____la calificación de:
unanimidad ó mayoría

SOBRESALIENTE / NOTABLE / APROBADO / NO APTO

Idioma/s de defensa (en caso de más de un idioma, especificar porcentaje defendido en cada idioma):

Castellano _____

Euskera _____

Otros Idiomas (especificar cuál/cuales y porcentaje) Inglés 100%

En _____a _____de _____de 2024

EL/LA PRESIDENTE/A, EL/LA SECRETARIO/A,

Fdo.: Fdo.:

Dr/a: Rubén Ansola Loyola __ Dr/a: Edurne Iriondo Plaza

VOCAL 1º, VOCAL 2º, VOCAL 3º,

Fdo.: Fdo.: Fdo.:

Dr/a: Nicolas Perry_____Dr/a: Ibai Ulacia Garmendia__Dr/a: Ana Pilar Valerga Puerta

EL/LA DOCTORANDO/A,

Fdo.: Ignacio Laraudogoitia Blanc

Author: Ignacio Laraudogoitia Blanc

ACKNOWLEDGEMENTS

To start, I would like to thank all those who have been directly involved in all the work presented throughout this manuscript. To Christian Hamm, Nils Kaiser and Nils Niebuhr (as well as the rest of the team) at the Alfred Wegener Institut for welcoming me so warmly at a time when human relations were strictly distant and for the unequalled value of the knowledge I took away from there. To Joseba Albizuri from UPV-EHU, Nicolas Perry from ENSAM, Eva Anglada from Tecnalia, Borja Pelayo from UPV-EHU and Nils Goosens from Zarm Technik without whom much of the work presented here would not have been possible, a thousand thanks.

Of course, I would like to greatly thank the work of my two thesis supervisors Dr. Maider García de Cortázar Aguirrezabal and Pr. Franck Andrés Girot Mata who have guided me on this arduous path. Thank you for having trusted me in every step I have decided to take in all the projects we have done and thank you for having put all your efforts in making this work a bit easier.

Me gustaría mencionar también a todos los miembros del “Palomar” en la Escuela de Ingenieros de Bilbao por los innumerables cafés, comidas y demás eventos en los que hemos estado y disfrutado juntos. Me llevo amistades para toda la vida. Con especial agradecimiento a Mario Renderos por su inagotable fuente de sabiduría y su disponibilidad perpetua a ayudar a todo el que se lo pida.

Mila esker Tecnaliako adiskideei, Donostian dagozanak baita Irunen dagozanei be, zeuen prestutasunagatik eta lehen momentutik neuri emondako ongietorriagatik. Oraindino gauza politak daukaguz egiteko. Aipatu beharra dago, tesi honek iraun dauen denporan, bai Errealak ta bai Athleticek kopak irabazi dabezela Bizkaia-Gipuzkoa konexio hau indartuz.

Eskerrak emon nahiko neuskiez be bai kuadrillako lagunei, lan gogor guztien atzean beti egon behar dagoelako deskonektatu egiten zaituen jendea, handiak zarete! Eskerrik asko Donostirako kotxean nigaz joan dan jende guztiari, zuek ezagutu duzuelako nire siestarik sakonenak.

Para seguir, me gustaría agradecer a toda mi familia, tanto a los Laraudogoitia como a los Blanc. Sí, a toda. Somos muchos, y cada uno con sus particularidades, pero todos me hacéis aprender algo cada día, mil gracias. Esto hay que celebrarlo como nosotros sabemos. Escribiendo esto me acuerdo de los que no están aquí, que sé que estarían tan orgullosos como el resto o más. Os echo de menos.

Me gustaría agradecer a mi hermana Carlota y a mis padres Tayde e Iñaki por el apoyo incondicional que me demuestran en cada reto que me propongo, por todo el amor que recibo a diario y por saber vivir la vida como nadie, esto también va por vosotros.

Finalmente, me gustaría agradecer a la persona que me ha aguantado en los últimos años (los más duros) de este trabajo. Sin tu apoyo, cariño y comprensión esto no habría sido posible. Porque eres mi compañera en los ratos más bonitos, pero también en los más difíciles. Benetan eta betirako maite zaitut Ainhotxu.

Author: Ignacio Laraudogoitia Blanc

ABSTRACT

In this contribution, the problem of traditional engineering component design is addressed, which employs an outdated methodology that leads to time-consuming iterative tasks, component overdimensioning, and material waste. This negatively impacts technological advancement and diminishes machine efficiency. The overdimensioning at the component level extrapolates to the assembly level and, ultimately, to the machine level, creating a domino effect and negatively affecting overall machine efficiency. Achieving greater machine efficiency requires highly customized components tailored to their specific functionality. Additionally, the subtractive manufacturing system is also deemed obsolete due to material waste and consumed energy resources. This issue particularly affects industries such as aerospace, automotive, and energy production, where accumulating heavier and less function-oriented parts results in high costs.

Nature serves as a clear example of how things should be designed and manufactured. In nature, everything is "crafted" with the exact amount of material adapted to specific boundary conditions. In fact, the process of creation is additive, not subtractive, optimizing the necessary resources to "build" material. Taking advantage of what nature has proven to work engineers can enhance their way of designing.

The objective of this thesis is to create a methodology that integrates different advanced design methods, such as topology optimization, generative design, parametric design/optimization, and eco-design, among other bio-inspired design approaches. This strategy aims to optimize the parts and custom them on their functionality in the most effective way possible. Always considering the operational boundary conditions, the manufacturing method, and the intended material. Possible manufacturing methods, loads, and stresses the component must endure, as well as potential materials suitable for each use case, will be discussed in the design phase to achieve the final goal.

The methodology employed will initially involve an in-depth review of the state of the art regarding the functioning of nature in terms of design and, on the other hand, advanced design and manufacturing methods in general. This will be followed by a thorough selection of the best tools and methods for both design and validation. Subsequently, a variety of use cases with different specifications will be selected to validate the proposed methodology across a broad spectrum. Each of these cases will undergo a tailored design methodology. Finally, the developed methodology will be validated in the earlier phases through simulation and, in some cases, experimental validation.

The results of this thesis demonstrate that technological advances, both in computing and manufacturing methods, allow for the design and fabrication of more function-oriented, efficient, and sustainable components, bringing humanity closer to achieving a level of perfection similar to that found in nature. Furthermore, it highlights the obsolescence of traditional design and manufacturing methods based on the designer/operator's experience, paving the way for new methods that reduce project execution times and enhance machine performance and efficiency.

Author: Ignacio Laraudogoitia Blanc

The work conducted throughout this thesis serves as a foundation for future research opportunities that may arise from applying these methods to components subjected to other physical-chemical phenomena, such as thermal management. Emphasis is placed on the need to harness the rise of artificial intelligence to reduce simulation times and further improve design methodologies, reinforcing the concepts presented here.

Author: Ignacio Laraudogoitia Blanc

RESUMEN

En esta contribución, se aborda el problema del diseño tradicional de componentes de ingeniería, que emplea una metodología obsoleta que conduce a tareas iterativas que consumen mucho tiempo, sobredimensionamiento de componentes y desperdicio de material. Esto impacta negativamente en el avance tecnológico y disminuye la eficiencia de las máquinas. El sobredimensionamiento a nivel de componentes se extrapola al nivel de ensamblaje y, finalmente, al nivel de la máquina, creando un efecto dominó que afecta negativamente la eficiencia general de la máquina. Lograr una mayor eficiencia de la máquina requiere componentes altamente personalizados adaptados a su funcionalidad específica. Además, el sistema de fabricación sustractiva también se considera obsoleto debido al desperdicio de material y al consumo de recursos energéticos. Este problema afecta particularmente a industrias como la aeroespacial, la automotriz y la producción de energía, donde la acumulación de piezas más pesadas y menos orientadas a la función resulta en altos costos.

La naturaleza sirve como un claro ejemplo de cómo deberían diseñarse y fabricarse las cosas. En la naturaleza, todo está "creado" con la cantidad exacta de material adaptado a condiciones de contorno específicas. De hecho, el proceso de creación es aditivo, no sustractivo, optimizando los recursos necesarios para "construir" material. Aprovechando lo que la naturaleza ha demostrado que funciona, los ingenieros pueden mejorar su forma de diseñar.

El objetivo de esta tesis es crear una metodología que integre diferentes métodos de diseño avanzado, como la optimización topológica, el diseño generativo, el diseño/optimización paramétrica y el ecodiseño, entre otros enfoques de diseño bioinspirado. Esta estrategia tiene como objetivo optimizar las piezas y personalizarlas en función de su funcionalidad de la manera más efectiva posible. Siempre considerando las condiciones de contorno operativas, el método de fabricación y el material previsto. Los posibles métodos de fabricación, cargas y tensiones que el componente debe soportar, así como los materiales potenciales adecuados para cada caso de uso, se discutirán en la fase de diseño para lograr el objetivo final.

La metodología empleada implicará inicialmente una revisión exhaustiva del estado del arte en cuanto al funcionamiento de la naturaleza en términos de diseño y, por otro lado, de los métodos avanzados de diseño y fabricación en general. Esto será seguido por una selección minuciosa de las mejores herramientas y métodos tanto para el diseño como para la validación. Posteriormente, se seleccionará una variedad de casos de uso con diferentes especificaciones para validar la metodología propuesta en un amplio espectro. Cada uno de estos casos pasará por una metodología de diseño personalizada. Finalmente, la metodología desarrollada se validará en las fases iniciales a través de simulaciones y, en algunos casos, validación experimental.

Los resultados de esta tesis demuestran que los avances tecnológicos, tanto en informática como en métodos de fabricación, permiten el diseño y la fabricación de componentes más orientados a la función, eficientes y sostenibles, acercando a la humanidad a lograr un nivel de perfección similar al encontrado en la naturaleza. Además, se destaca la obsolescencia de los métodos

tradicionales de diseño y fabricación basados en la experiencia del diseñador/operador, allanando el camino para nuevos métodos que reducen los tiempos de ejecución de proyectos y mejoran el rendimiento y la eficiencia de las máquinas. El trabajo realizado a lo largo de esta tesis sirve como base para futuras oportunidades de investigación que puedan surgir de la aplicación de estos métodos a componentes sometidos a otros fenómenos físico-químicos, como la gestión térmica. Se enfatiza la necesidad de aprovechar el auge de la inteligencia artificial para reducir los tiempos de simulación y mejorar aún más las metodologías de diseño, reforzando los conceptos presentados aquí.

Author: Ignacio Laraudogoitia Blanc

LABURPENA

Ikerketa honetan, ingeniaritza-osagai tradizionalen diseinuaren arazoa aztertzen da, zeinak metodologia zaharkitua erabiltzen baitu, zeregin iteratibo luzeak, osagaien gehiegizko dimentsionamendua eta material-xahutzea eraginez. Honek aurrerapen teknologikoan eragin negatiboa du eta makinen eraginkortasuna murrizten du. Osagai-mailan ematen den gehiegizko dimentsionamenduak muntaketa-mailara eta, azkenean, makina-mailara estrapolatzen da, domino-efektua sortuz eta makinen eraginkortasun orokorrean eragin negatiboa izanez. Makinen eraginkortasun handiagoa lortzeko, funtzionalitate espezifikoetara egokitutako osagai oso espezializatuak behar dira. Gainera, fabrikazio-sistema subtraktiboa ere zaharkitutzat jotzen da, material-xahutzea eta energia-baliabideen kontsumoa direla eta. Arazo honek bereziki eragiten die aeroespazialaren, automobilgintzaren eta energia-ekoizpenaren industriei, non pieza astunagoak eta funtzio-orientazio txikiagokoak pilatzeak kostu handiak eragiten baititu.

Natura adibide argia da gauzak nola diseinatu eta fabrikatu behar diren erakusten duena. Naturan, dena "eraikitzen" da baldintza espezifikoetara egokitutako material kantitate zehatzarekin. Izan ere, sorkuntza-prozesua gehigarria da, ez subtraktiboa, materiala "eraikitzeko" beharrezko baliabideak optimizatuz. Naturak funtzionatzen duela frogatu duenaz baliatuz, ingeniariek beren diseinu-modua hobe dezakete.

Tesi honen helburua da diseinu-metodo aurreratu desberdinak integratzen dituen metodologia bat sortzea, hala nola optimizazio topologikoa, diseinu generatiboa, diseinu/optimizazio parametrikoa eta eko-diseinua, besteak beste, naturan inspiratutako diseinu-ikuspegietan oinarrituta. Estrategia honen helburua piezak optimizatzea eta haien funtzionalitatera ahalik eta modu eraginkorrenean egokitzea da. Beti ere, funtzionamendu-baldintza mugatzaileak, fabrikazio-metodoa eta erabili nahi den materiala kontuan hartuz. Fabrikazio-metodo posibleak, osagaiak jasan behar dituen kargak eta tentsioak, eta kasu bakoitzerako egokiak diren material potentzialak diseinu-fasean eztabaidatuko dira azken helburua lortzeko.

Erabilitako metodologiak hasiera batean naturaren funtzionamenduari buruzko artearen egoeraren azterketa sakona egingo du diseinuari dagokionez, eta, bestetik, diseinu eta fabrikazio metodo aurreratuei buruzkoa orokorrean. Ondoren, diseinu eta balidaziorako tresna eta metodo onenak hautatuko dira zorroztasunez. Jarraian, espezifikazio desberdinak dituzten erabilera-kasu ugari aukeratuko dira proposatutako metodologia espektro zabal batean balidatzeko. Kasu hauetako bakoitzak diseinu-metodologia pertsonalizatua jasoko du. Azkenik, garatutako metodologia hasierako faseetan balioztatuko da simulazioaren bidez eta, kasu batzuetan, balidazio esperimental baten bidez.

Tesi honen emaitzek erakusten dute aurrerapen teknologikoek, bai konputazioan bai fabrikazio-metodoetan, aukera ematen dutela funtzioetara bideratuagoak, eraginkorragoak eta jasangarriagoak diren osagaiak diseinatu eta fabrikatzeko, gizateria naturan aurkitzen den perfekzio-mailara hurbilduz. Gainera, diseinu eta fabrikazio metodo tradizionalen zaharkitzea nabarmentzen du, diseinatzaile/operadorearen esperientzian oinarrituta, proiektuen exekuzio-

Author: Ignacio Laraudogoitia Blanc

denborak murriztu eta makinen errendimendua eta eraginkortasuna hobetzen dituzten metodo berriei bidea irekiz. Tesi honetan zehar egindako lanak etorkizuneko ikerketa-aukerak sortzen ditu, metodo hauek beste fenomeno fisiko-kimiko batzuen menpe dauden osagaietan aplikatzetik etor daitezkeenak, hala nola kudeaketa termikoan. Adimen artifizialaren gorakada aprobetxatzeko beharra azpimarratzen da simulazio-denborak murrizteko eta diseinu-metodologiak are gehiago hobetzeko, hemen aurkeztutako kontzeptuak sendotuz.

Author: Ignacio Laraudogoitia Blanc

GENERAL CONTENTS

Chapter 1 : Introduction 1
1.1 General context 1
1.2 Problem description 3
1.3 Scope of the thesis 5
1.4 Manuscript structure 6
1.5 References 8
Chapter 2 : Literature review 9
2.1 Natural design foundations and terminology on inspiration from nature 9
2.1.1 Natural patterns 11
2.1.2 Nature mimicking 31
2.2 Bioinspiration in engineering design 32
2.2.1 Engineering design, manufacturing and validation process 32
2.2.2 Bioinspired design approaches 36
2.3 Design for manufacturing 50
2.3.1 Design for Casting 51
2.3.2 Design for Additive Manufacturing 57
2.4 Conclusions 59
2.5 References 61
Chapter 3 : Bioinspired design methodologies and tools applied to an aeronautical assembly column 71
3.1 Introduction 71
3.2 Theoretical framework 73
3.2.1 Experimental Modal Analysis (EMA) 78
3.3 Methodology 78
3.3.1 Design methodology and selection 79
3.3.2 Eco-design analysis 81
3.3.3 Problem definition 84
3.3.4 Design and optimization 88
3.3.5 Outcome selection and validation 92
3.3.6 Design for manufacturing 98
3.4 Manufacturing process 105

3.4.1 Simulation ... 105
3.4.2 Mold manufacturing ... 106
3.4.3 Casting process ... 107
3.5 Physical Validation ... 108
3.6 Conclusions ... 111
3.7 References ... 113
Chapter 4 : Reaction wheel for small- and medium-sized satellites ... 117
4.1 Introduction ... 117
4.2 Theoretical framework ... 120
4.2.1 Theory of reaction wheels ... 120
4.2.2 Theory of balance in rotational motion ... 125
4.3 Methodology ... 127
4.3.1 Problem definition ... 127
4.3.2 Design and optimization ... 131
4.3.3 Outcome selection and validation ... 137
4.3.4 Design for manufacturing ... 138
4.3.5 Eco-design analysis ... 144
4.4 Manufacturing process ... 146
4.5 Physical validation ... 148
4.6 Discussion ... 149
4.6.1 Bioinspired design process ... 150
4.6.2 Material selection ... 150
4.6.3 Casting process ... 151
4.6.4 Physical validation ... 152
4.7 Conclusions ... 152
4.8 References ... 154
Chapter 5 : Scaled gear for wind turbines ... 157
5.1 Introduction ... 157
5.2 Theoretical framework: gear theory, failure mechanisms ... 161
5.2.1 Fundamental gear theory ... 161
5.2.2 Movement and load transmission fundamentals ... 163
5.2.3 Failure analysis and wear mechanisms ... 165

5.3 Methodology 167
5.3.1 Problem definition 167
5.3.2 Design and optimization 169
5.3.3 Validation 172
5.3.4 Manufacturing 175
5.4 Conclusions 176
5.5 References 178
Chapter 6 : Supplemental airfoil for low-speed aircraft 180
6.1 Introduction 180
6.2 Types of flight 181
6.2.1 Aircraft types 182
6.2.2 Natural flight types 184
6.3 Theoretical Framework: Fluid Mechanics, Aerodynamics, and CFD Fundamentals 186
6.3.1 Fluid mechanics fundamentals 186
6.3.2 Fundamentals of Aerodynamics 187
6.3.3 Fundamentals of CFD 200
6.4 Use case description 202
6.5 Methodology 204
6.5.1 Bioinspired airfoil selection 204
6.5.2 Two-dimensional analysis 208
6.5.3 Bio-inspired 3D features selection and construction 220
6.5.4 Three-dimensional analysis 223
6.6 Discussion 232
6.7 Conclusions 234
6.8 References 236
Chapter 7 : Computer aided system for casting design (eCAST) 240
7.1 Introduction 240
7.2 Theoretical framework 241
7.3 Methodology 248
7.3.1 Introduction to Synera usage and Add-In development 249
7.3.2 eCAST Add-In development workflow 252
7.3.3 Results 259

7.4 Discussion 264
7.5 Conclusions 266
7.6 References 267
Chapter 8 : Conclusions and future developments 268
8.1 Conclusions 268
8.2 Future developments 271
8.3 References 272

Author: Ignacio Laraudogoitia Blanc

LIST OF FIGURES

Figure 1.1. Traditional design and manufacturing iterative process (top). New design and manufacturing paradigm (bottom). 3
Figure 1.2. Life cycle of a tree, depicting the natural circular process. 5
Figure 2.1. Evolution's design examples: a) Diatoms and their many different shapes. b) Leopard shark denticles with a topographic image. c) A type of Morpho butterflies' wing in different scales. (Sources: a) [9]; b) [6]; c) [8]) 10
Figure 2.2. Graphic expression of cumulative selection. 1. Random mutation 2. Due to environmental conditions, a part of the population disappear. 3-The fittest specimens thrive. (Source: [12]) 11
Figure 2.3. Geometric details for a regular n-gon inscribed in a circle (**a**) size of the n-gon cells (**b**) [15] 13
Figure 2.4. The stochastic structure shown by the collision of different sized bubbles (**left**). The composite structure defined by Weaire and Phelan for the best 3D space distribution (**right**) [17]. 15
Figure 2.5. Voronoi tesselation with disordered origin points (**left**). Voronoi tesselation with ordered origin points (**right**). 16
Figure 2.6. Microscopic image of Aulonia Hexagona diatom [18] 17
Figure 2.7. Periodic membrane structures are common in living cells. Many of these appear to be related to periodic minimal surfaces: (a) the D-surface in leaf membranes; (b) the P-surface in algae; (c) the G-surface in lamprey epithelial cells [19] 18
Figure 2.8. Zoomed image of a Romanesco broccoli [20] 19
Figure 2.9. Crack propagation velocity and morphology diagram [14] 20
Figure 2.10. Multiple-point crack propagation example in dried mud [21]. 20
Figure 2.11. Basaltic columns from Reynisfjara beach in Iceland. 21
Figure 2.12. Rivers and meanders as seen from space (source: Google earth) 22
Figure 2.13. Waves seen from a Belousov-Zhabotinsky reaction [22] 23
Figure 2.14. Waves as seen in sand dunes with periodic wind forces in Corralejo Fuerteventura 24
Figure 2.15. Turing patterns formation process (**left**). Turing pattern example (**right**) [24] 25
Figure 2.16. Form generation in animal tails based on length [25] (**left**), giraffe spot pattern [26] (**center**), leopard spot pattern [26] (**right**) 26
Figure 2.17. Examples of different phyllotaxis distributions: spiral (a), distichous (b), and whorled (c) [14]. 27
Figure 2.18. Different vortex patterns in nature in different scales: a hurricane viewed from space [29] (**a**), a Kármán vortex street behind an island [30] (**b**), and a smoke vortex ring [31] (**c**) 28
Figure 2.19. Diagram of a phyllotactic pattern demonstrating the arrangement of leaves or florets in a spiral configuration. The numbers indicate the sequential order of leaf placement, showing the typical 137.5° divergence angle [14] 29

Figure 2.20. Examples of the Fibonacci sequence in nature: a Fibonacci spiral diagram [32] (**a**), a spiral arrangement of leaves in an aloe plant [33] (**b**), and the spiral pattern of a nautilus shell [34] (**c**)..... 30
Figure 2.21. Iterative process of traditional engineering design and manufacturing, illustrating the stages from problem definition (1) to implementation/commercialization (6). 32
Figure 2.22. The engineering component design and production method based on the DNA-encoded construction processes of living beings..... 34
Figure 2.23. Types of structural optimization: (**a**) size optimization in a truss structure, (**b**) shape optimization, and (**c**) topology optimization [62]. 39
Figure 2.24. Discretization of a two-dimensional beam: a beam fixed at one end with a force applied at the other end (**left**). The beam is divided into 10x20 square elements of equal size for analysis (**right**). 40
Figure 2.25. Optimal material distribution in a discretized beam with a fixed end and an applied force, using the design variable of element density and a volume constraint of 60 blocks. 41
Figure 2.26. Optimal design results for material and void using various powers p in the SIMP interpolation scheme, and using the Hashin-Shtrikman upper bound. The graph above shows the penalized value as a function of the starting value for different p values [69]. 42
Figure 2.27. Level set representations: (a) 2D topology, (b) corresponding level set function, and more complex representations of benchmark structures (c) and (d) [76]. 43
Figure 2.28. Schematic representation of casting elements. 53
Figure 3.1. Single degree of freedom dynamic system of a mass and a spring subjected to gravitational force [15]..... 73
Figure 3.2. Damped single degree of freedom dynamic system subjected to a displacement. [15] 74
Figure 3.3.Graphic expression of the three types of damped systems based on the damping critical value. 1) Underdamped 2) Overdamped 3) Critically damped [15]..... 76
Figure 3.4. Schematic view of a single degree of freedom dynamic system subjected to a harmonic external force [15]..... 77
Figure 3.5. A plot of the normalized amplitude by the Frequency ratio that illustrate the resonance phenomenon [15]..... 78
Figure 3.6. The bioinspired outcome with the hexapods attached. 82
Figure 3.7. The graphic of the results of the ecodesign analysis for two solutions. 84
Figure 3.8.. The wing skin panels for Boeing's first 737 MAX airplane are loaded on fixtures into an automated assembly machine in the company's plant in Renton, Wash., on 2 June 2015 (source: [25]) [**left**]. The simplified reference design of the assembly column based on the fixtures used in assembly lines [**right**]..... 85
Figure 3.9. Operational load case graphic expression. 86
Figure 3.10. Outside boundary of the obstacle geometry (**left**) and preserve geometry and tool clearance obstacle geometry (**right**) of the Fusion 360 simulation. 88
Figure 3.11. Evolution of designs in Fusion 360. Reference design and F360 design..... 89

Figure 3.12. Design space (**left**) and non-design geometry (**right**) for Altair Optistruct Topology Optimization. 89
Figure 3.13. (**A**) Optistruct topology optimization result in element density plot. (**B**) Outcome of the simulation translated into a solid. 90
Figure 3.14. Skeleton diameter distribution after parameter optimization. 91
Figure 3.15. The Voronoi distribution according to the load lines from Topology Optimization (**left**). Skeleton lines extracted from the Topology Optimization (**right**). 92
Figure 3.16. Evolution of designs in Synera. Reference design, Skeleton design, and Voronoi design. 92
Figure 3.17. Representation of the results in a percentage scale so it is possible to compare each of the designs with the others. Furthermore, a limit has been set to accept the outcomes. This limit is represented as a black dashed line and the yellow shaded areas are the ones that serve as graphic representations of acceptable values for each of the factors. Artwork made with MS Excel. 94
Figure 3.18. (**Top**) Von Mises equivalent stress diagram in MPa for the 5 solutions with the initial load cases. (**Middle**) Deformation in mm of the 5 solutions for the initial load cases (**Bottom**). 95
Figure 3.19. Maximum equivalent Von Mises stress for the worst load case scenario in the Voronoi outcome. 96
Figure 3.20. Bending of an infinite and of a finite width plate with a single elliptical hole stress concentration factor case as defined by [41] (**top**). The case analyzed in this study with the real dimensions (**bottom**). 97
Figure 3.21. S-N curve for AlSi10Mg alloy and the modified curve to meet the axial tension samples (**left**). Goodman line and the situation of the outcome for the studied load case (**right**). 98
Figure 3.22. Changes in the structure according to the manufacturing constraints. Wall thickness correction bigger than 7 mm (**left**) and rounding of sharp edges (**right**). 99
Figure 3.23. All the possibilities of filling orientations for the part. 100
Figure 3.24. Metal pouring point at the bottom of the area with bigger mass in blue color. 100
Figure 3.25. Gating system layout in yellow. 101
Figure 3.26. Sleeve of the sprue KALPUR model from FOSECO. [42] 101
Figure 3.27. Foseco catalogue for the riser's sleeves, model KALMIN. [42] 103
Figure 3.28. The geometry that define the mold cavity or the casting design and the part. 104
Figure 3.29. Different volumes as defined in ProCAST. 105
Figure 3.30. Solid fraction of the partially filled part at the further end of the filling (**left**). Temperatures of the melt when the part is fully filled (**right**). 106
Figure 3.31. Result of shrinkage porosity in the part after full solidification. 106
Figure 3.32. Mold design for Binder Jetting (**top**). Mold parts as manufactured (**Bottom**) 107
Figure 3.33. Outcome of the casting process. Inner surfaces (**left**) whole part (**right**) 108
Figure 3.34. Modal test configuration for free vibration conditions with the data-acquisition device, the accelerometer in the top right area of the part, and the hammer at UPV/EHU's facilities. 109

Figure 3.35. The FRF of the signal from one of the acquisition nodes in two directions X and Y (**Up**). The results comparison of the generic material properties selected for the FEA (**left**) and the results of the modal test (**right**) (**Down**). 110
Figure 3.36. Samples taken from the casting process of the part (**left**). Archimedes test for determining the density of the material (**right**). 111
Figure 4.1. Overview of the space sector by McKinsey & Company. Information from Center for strategic international studies; Curnchbase; Euroconsult; Northern Sky Research; organization websites; PitchBook; public press; Space Foundation; Union of Concerned Scientists; McKinsey Analysis [4]. 118
Figure 4.2. An scheme of a disk with its O-O axis of rotation and relevant dimensions (**right**). An scheme of a ring with its O-O axis of rotation and relevant dimensions (**left**). Adapted from [18]. 122
Figure 4.3. Visual scheme of the motion of a reaction wheel and the satellite to which is attached. 124
Figure 4.4. Top view and cross-section of the design space (**grey**) and non-design space (**blue**) used for topology optimization [22]. 131
Figure 4.5. Topology optimization result using 6 (**top**) or 3 (**bottom**) rotational symmetric sectors [22] 132
Figure 4.6. Final design of the rotor in a rendered (left) and schematic (right) representation, including an overview about the marine microorganisms used to abstract bio-inspired design principles and structures (modified according to [[22], [26], [27],)..... 134
Figure 4.7. Visual representation of the parameters taken into account for the parameter optimization [22]. 136
Figure 4.8. Different views of the bioinspired rotor [22]. 137
Figure 4.9. Section of the outcome with the manufacturing constraints applied. 139
Figure 4.10. Three orientations possible for filling the part. **A)** Part filled horizontally placed and upwards. **B)** Part horizontally placed and filled downwards. **C)** Filling in vertical [22]..... 140
Figure 4.11. Geometric parameters for commercial sprue selection. In the present case D2 is 70 mm, D1 is 152 mm, h1 is 126 mm and h2 is 181 mm (**top**). Sleeve dimensions for the sprue (**bottom**) [31]. 141
Figure 4.12. Solid fraction of the casting design without feeders. 142
Figure 4.13. Solid fraction of the casting design with feeders in the launch lock cavities. 143
Figure 4.14. Mold parting line in red and geometry in grey [22]..... 144
Figure 4.15. Eco-design analysis comparing energy consumption (in MJ) for different manufacturing methods: gravity casting, additive manufacturing via SLM, and machining. 145
Figure 4.16. Eco-design analysis comparing the carbon footprint (in kg CO2) for different manufacturing methods: gravity casting, additive manufacturing via SLM, and machining. 145
Figure 4.17. Molten metal pouring into the mold (**top**). The area where the riser has been removed (**bottom-left**). The overall view of the manufactured part (**bottom-right**). 147
Figure 4.18. Physical validation setup [22]. 148
Figure 4.19. Rotor vibrational measurements for 1000 RPM rotation down to 0 RPM [22]..... 149

Figure 5.1. Overall share of energy from renewable resources in 2022 by Eurostat. Source: [1] 158
Figure 5.2. Drawings of a wind turbines from outside (left) and from inside (right)..... 160
Figure 5.3. Spur gear nomenclature [2]. 162
Figure 5.4. Spur gear's load transmission drawing. 164
Figure 5.5. Design space and boundary conditions of the defined problem. 168
Figure 5.6. Topology optimization result for one tooth (left). The most restrictive side of the topology optimization result mirrored and multiplied for 15 teeth (right) 170
Figure 5.7. Pictures of different diatom species: Thalassosira [14], Arachnodiscus [15] and Rocella [16] from left to right respectively. 170
Figure 5.8. Design of the radial Voronoi pattern of one solution of the gear wheel in the center. In the outer images the examples of the diatoms for which several features have been applied [16] 171
Figure 5.9. Several designs extracted of the parameter study performed to the gear wheel (4 out of 150). 172
Figure 5.10. Von Mises stress result from the structural analysis simulation (Top) Signed Von Mises stress result from the structural analysis simulation (Bottom) 173
Figure 5.11. Bending of a gear tooth of 20º pressure angle for stress concentration factor as defined by [23] 174
Figure 5.12. S-N curve for both materials studied and their modified curves to meet with the fatigue criteria. 175
Figure 5.13. Goodman diagram for both materials and the gear situation for the studied load case. 175
Figure 5.14. Final part manufactured by SLM AlSi10Mg additive manufacturing. 176
Figure 6.1. Hot air balloons [1] (**left**) and a Zeppelin airship [2] (**right**)..... 182
Figure 6.2. Aircraft types: Commercial airplane [3] (**top**), glider [4] (**middle left**), hang glider [5] (**middle right**), paraglider [6] (**bottom left**), paramotor [7] (**bottom right**). 183
Figure 6.3. Rotorcraft types: Helicopter [8] (**top left**), autogyro [9] (**top right**), compound helicopter [10] (**bottom left**), tiltrotor [11] (**bottom right**). 184
Figure 6.4. Gliding animals: Flying squirrel (**left**), flying fish (**right**)..... 185
Figure 6.5. Albatross in flight [15]. 185
Figure 6.6. Descriptive diagram of the Venturi effect. 187
Figure 6.7. Aerodynamic study of airfoil shapes: airflow streamlines around an airfoil (**top**) and drag force acting on an airfoil (**bottom**). 187
Figure 6.8. Characteristic curves of RAF 32 airfoil: lift curve, drag curve and lift-to-drag ratio (L/D) as a function of angle of attack [18]..... 189
Figure 6.9. Comparison of laminar flow (top) and turbulent flow (bottom) illustrating the differences in fluid motion and behavior [19]. 191
Figure 6.10. Diagram of boundary layer behavior over an airfoil, showing regions of laminar and turbulent flow, boundary layer transition, separation point, and wake formation [20]. 192

Figure 6.11. Diagram of the boundary layer structure near a wall, illustrating the freestream flow, edge of the boundary layer, outer layer, fully-turbulent region or log-layer, inner layer, sublayer, and buffer layer [22]. 195
Figure 6.12. Velocity profile in a turbulent boundary layer near a wall, showing the relationship between velocity U+ and wall distance y+. The plot includes the linear region U+=y+ and the logarithmic region described by the log law [23]..... 196
Figure 6.13. Diagram of an airfoil showing key geometric parameters [24]. 197
Figure 6.14. Comparison of airfoil shapes with varying thicknesses (6% to 20%) and their corresponding lift coefficient (**top**) and drag coefficient (**bottom**) as functions of angle of attack. 199
Figure 6.15. Comparison of airfoil shapes with varying camber percentages (0% to 3.5%) and their corresponding lift coefficient as a function of angle of attack (**top**), and lift coefficient versus drag coefficient (**Bottom**)..... 200
Figure 6.16. Comparison of two different mesh types used in CFD simulations: (a) structured mesh and (b) unstructured mesh [25]. 201
Figure 6.17. Airspace categorization for urban air mobility [27]. 203
Figure 6.18. Geometry of the reference airfoil DAE-11 showing the camber line and thickness distribution [31]..... 204
Figure 6.19. Geometry of the GOE 174 (Albatros 5020) airfoil, showing the camber line and thickness distribution [31]..... 205
Figure 6.20. Geometry of the bio-inspired owl airfoil, showing the normalized thickness distribution along the chord [32]. 206
Figure 6.21. Geometry of the dolphin-inspired airfoil, based on the pectoral fin..... 207
Figure 6.22. Domain definition for the 2D fluid dynamics study of the airfoils..... 209
Figure 6.23. Surface definition for the fluid dynamics analysis, identifying the airfoil profile geometry as the "wing" to specify the interaction surfaces and the direction of fluid flow..... 210
Figure 6.24. Definition of inlet surfaces, where the air will enter the domain, are indicated on the upper, lower, and initial surfaces of the rectangular prism..... 210
Figure 6.25. Definition of the outlet surface indicating the area through which air exits the domain. 211
Figure 6.26. Definition of the two independent wall surfaces delimiting the domain in the Z direction. 211
Figure 6.27. Mesh definition using polyhedral elements for the main volume and prism elements for the boundary layer. 212
Figure 6.28. 2D CFD simulation results for the airfoil. Velocity magnitude distribution around the airfoil (**top**). Pressure distribution around the airfoil (**bottom**)..... 214
Figure 6.29. Velocity magnitude distribution in the flow field around the airfoil. 215
Figure 6.30. Fluid velocity distribution around the airfoil at a 10° angle of attack, illustrating boundary layer separation and turbulence in the wake..... 215
Figure 6.31. Aerodynamic efficiency (Cl/Cd) as a function of angle of attack for different airfoil profiles in the study..... 220

Figure 6.32. 3D wing configuration with a variable chord, decreasing by 15% from root to tip along the 1.5m wingspan. 221
Figure 6.33. 3D wing configuration with a 15% chord reduction from root to tip and a 10° sweep. The sweep effect on subsonic or low-speed aircraft performance is analyzed, inspired by natural examples such as the Java cucumber seeds and the wings of gliding birds like albatrosses [36][37]. 222
Figure 6.34. 3D wing configuration with variable chord and leading-edge tubercles inspired by the humpback whale's flipper. The graph indicates the tubercle distance proportion applied onto the design [38]. 223
Figure 6.35. Domain used for 3D analysis of wing configuration with tubercles. 224
Figure 6.36. Definition of control volumes for meshing. 225
Figure 6.37. Meshed 3D block defining the whole domain (**left**). Detailed view of element distribution of the wing model (**right**). 226
Figure 6.38. Velocity magnitude distribution around the 3D wing model with tubercles (side and top views). 227
Figure 6.39. Pressure distribution around the 3D wing model with tubercles (side and top views). 228
Figure 6.40. Aerodynamic efficiency (CL/CD) of various wing configurations of the 3D analysis at different angles of attack 231
Figure 6.41. Lift force (N) for various wing configurations at different angles of attack (0° to 5°). 232
Figure 6.42. Comparison of lift coefficients [39]..... 233
Figure 6.43. Pressure distribution around a 3D wing model with tubercles. 234
Figure 7.1. Phase diagram for aluminum-silicon alloys [4] 242
Figure 7.2. Schematic of mode of freezing in pure metals. Crystallization begins at the mold wall and advances into the casting interior on a plane solidification front (**left**). Schematic of intermediate mode of freezing having a moderate freezing range (**right**) [3]. 243
Figure 7.3. Effect of increasing riser solidification time on the soundness of a Al-14Si alloy plate [5]. 246
Figure 7.4. Riser and casting part volume ratio to part aspect ratio. Curve A is the minimum ratio to satisfy the thermal requirement and Curve B is the minimum to satisfy the volume requirement of risers [5]. 247
Figure 7.5. Volume of metal usage for different riser geometries and configurations. (a) Cylindrical, (b) hemispherical, (c) reverse tapered riser and (d) exothermic sleeve [5]. 248
Figure 7.6. Geometry creation and Boolean operation workflow inside Synera. 250
Figure 7.7. Finite element model construction inside Synera. 250
Figure 7.8. Data structure and data transformation workflow inside Synera. 251
Figure 7.9. For loop workflow inside Synera..... 251
Figure 7.10. Different private nodes inside Synera marketplace. The nodes shown are from HyperMesh, Mocha and Dendrise respectively. 252
Figure 7.11. Overview of the node for the riser theoretical dimensioning. 254

Figure 7.12. Overview of the Geometry Builder node. 255
Figure 7.13. Overview of the ProCast Launcher node. 257
Figure 7.14. Diagram depicting the whole set up and workflow for the eCAST Add-In. 258
Figure 7.15. Geometry to be used to illustrate the application of the Add-In. 259
Figure 7.16. Geometrical output of the theoretical dimensioning for different part designs. A thick plate example of a single module (**left**), an example resembling a single-module narrow plate (**center**), and an example of a stepped part with three modules (**right**). 260
Figure 7.17. The actual result of the riser-to-part volume ratio based on the aspect ratio of the plate. 261
Figure 7.18. Result of the shell mesh after the meshing process in Synera (**left**). Result of the volume differentiation in ProCast (**right**). 262
Figure 7.19. The ProCast Launcher node with the input parameters and the results using the theoretical dimensions of the riser. 262
Figure 7.20. Result of the solid fraction of the part and riser with the theoretical dimensions of the riser (**left**). The same showing shrinkage porosity results instead (**right**). 263
Figure 7.21. Optimization response definition for minimizing average shrinkage porosity in Synera. 264
Figure 7.22. Optimization loop results with 150 iterations in Synera 264
Figure 7.23. Average shrinkage porosity values for each optimization iteration to the ratio of riser and part thermal modules. 265

LIST OF TABLES

Table 2-1. List of values of n for the n-gon. 14
Table 2-2. Comparison of various topology optimization methods, including their approaches, strengths, and weaknesses. 45
Table 2-3. Classification of additive manufacturing technologies: Direct Energy Deposition (DED), Powder Bed Fusion (PBF), and other methods [110]. 57
Table 3-1. Evaluation criteria of the 8 commercial software. 80
Table 3-2. Rudder dimensions for different Airbus and Boeing airplanes [46]. 83
Table 3-3. Summary of the results of all designs where mass, first eigenfrequency, maximum Von Mises stress, maximum displacements and safety factor are shown. Note that SI stands for Skeleton Improved design. 93
Table 3-4. Table showing the values of the feeding factor for different metal alloys [45]. 104
Table 3-5. Experimental and corrected Young's modulus FEA first three modes in free vibration configuration. 111
Table 4-1. Parameter definition for discretizing geometry and perform a parameter optimization 135
Table 4-2. CAD-model based reaction wheel rotor performance of the bio-inspired design, a simplified commercial design [6] and a conceptual design [14]. Improved values of the new design are written in bold and less-performable values are underlined. 138
Table 6-1. Turbulence models with their particularities, pros and cons [21]. 194
Table 6-2. Dimensional parameters of the owl-based profile [32] 206
Table 6-3.Dolphin fin offsets for different chord distance values [33]. 207
Table 6-4. Results of 2D analysis for DAE-11 airfoil. 216
Table 6-5. Results of 2D analysis for Albatross airfoil. 217
Table 6-6. Results of 2D analysis for Owl airfoil. 218
Table 6-7. Results of 2D analysis for Dolphin airfoil. 219
Table 6-8. Results of 3D analysis for Albatross airfoil wing with chord diminution. 228
Table 6-9. Results of 3D analysis for Albatross airfoil wing with chord diminution and humpback whale tubercles. 229
Table 6-10. Results of 3D analysis for DAE-11 airfoil wing with chord diminution. 229
Table 6-11. Results of 3D analysis for DAE-11 airfoil wing with chord diminution and humpback whale tubercles. 230
Table 6-12. Results of 3D analysis for DAE-11 airfoil wing with chord diminution and swept wings. 230
Table 6-13. Results of 3D analysis for DAE-11 airfoil wing with chord diminution, humpback whale tubercles and swept wings. 231

Author: Ignacio Laraudogoitia Blanc

ACRONYMS

AI:	Artificial Intelligence
AM:	Additive Manufacturing
AND:	A logical operator or conjunction
ANSYS:	Analysis System (a software suite for engineering simulation)
AOCS:	Attitude and Orbit Control System
ASSESS:	Analysis and Simulation Software for Engineering Systems Strategy
BESO:	Bi-directional Evolutionary Structural Optimization
BIO:	Biological or Bio-inspired
BZ:	Belousov-Zhabotinsky (a type of chemical reaction)
CAD:	Computer-Aided Design
CAE:	Computer-Aided Engineering
CAGR:	Compound Annual Growth Rate
CAM:	Computer-Aided Manufacturing
CCM:	Computational Continuum Mechanics or Composite Curve Member
C_D:	Coefficient of Drag
CFD:	Computational Fluid Dynamics
CFRP:	Carbon Fiber Reinforced Polymer
C_L:	Lift Coefficient
COVID:	Coronavirus Disease (COVID-19)
CSV:	Comma-Separated Values (a file format)
DED:	Directed Energy Deposition (a type of additive manufacturing)
DLA:	Differential Lock Actuator
DMLS:	Direct Metal Laser Sintering
DNA:	Deoxyribonucleic Acid
DNS:	Direct Numerical Simulation

Author: Ignacio Laraudogoitia Blanc

DSC: Deformable Simplicial Complex

EBM: Electron Beam Melting

EBW: Electron Beam Welding

EHU: Euskal Herriko Unibertsitatea (University of the Basque Country)

EMA: Experimental Modal Analysis

ENSAM: École Nationale Supérieure d'Arts et Métiers (French engineering school)

EO: Earth Observation

ESA: European Space Agency

ESI: Engineering System International

ESO: Evolutionary Structural Optimization

EU: European Union

F_D: Drag force

FE: Finite Element

FEA: Finite Element Analysis

FEM: Finite Element Method

F_L: Lift force

FOSECO: Foundry Services Company (specializing in metal casting)

FRF: Frequency Response Function

GOE: General Operating Expenses or German Airfoil (a specific airfoil design)

ICP: Inductively Coupled Plasma

II: Two (Roman numeral)

JARVIS: Just A Rather Very Intelligent System (fictional AI system)

KALMIN: Brand name for a series of insulating materials

KALPUR: Brand name for a series of exothermic feeders

LENS: Laser Engineered Net Shaping

LEO: Low Earth Orbit

Author: Ignacio Laraudogoitia Blanc

LLC: Limited Liability Company

LMD: Laser Metal Deposition

LOBSTER: Likely an acronym for a project

MAX: Maximum

MIDACO: Mixed Integer Distributed Ant Colony Optimization

MJ: MegaJoule

MMC: Metal Matrix Composite

MS: Manuscript or Microsoft

NAFEMS: National Agency for Finite Element Methods and Standards

NFL: National Football League

NXG: Next Generation

OASIS: Open Access Single entry point for scale-up of Innovative Smart lightweight composite materials and components

PBF: Powder Bed Fusion

PCB: Printed Circuit Board

PEEK: Polyether Ether Ketone

PSD: Power Spectral Density

RAF: Royal Air Force

RAMP: Reliability Availability Maintainability and Predictability

RANS: Reynolds-Averaged Navier-Stokes

RMS: Root Mean Square

RPM: Revolutions Per Minute

SI: International System of Units

SIMP: Solid Isotropic Material with Penalization

SLM: Selective Laser Melting

SPD: Solid Phase Distribution

Author: Ignacio Laraudogoitia Blanc

TO:	Topology Optimization
UAM:	Urban Air Mobility
UAV:	Unmanned Aerial Vehicle
UPV:	Universidad del País Vasco (University of the Basque Country)
USA:	United States of America
USD:	United States Dollar
UTS:	Ultimate Tensile Strength
VTOL:	Vertical Take-Off and Landing
XII:	Twelve (Roman numeral)
XTAE:	Likely a specific acronym not widely known, needs context for precise definition
XZ:	Refers to the plane defined by the X and Z axes

Chapter 1: Introduction

1.1 General context

The world today is facing significant and interconnected challenges that impact engineering and manufacturing. One of the most urgent issues is climate change. Global temperatures have risen by approximately 1.45°C above pre-industrial levels, with 2023 setting new records for average temperatures and extreme weather events. This increase is largely due to higher greenhouse gas emissions, which are causing severe environmental and socio-economic effects, including more frequent heatwaves, rising sea levels, and disruptions to natural and human systems [1].

In addition to climate change, the scarcity of raw materials is becoming increasingly critical. The COVID-19 pandemic and geopolitical tensions have exacerbated supply chain disruptions, making raw materials harder to obtain. The demand for raw materials is expected to nearly double by 2050 due to population growth, rising living standards, and the transition to low-carbon technologies. Given these pressures, industries are exploring various strategies to mitigate the impact of raw material shortages. These include developing new mining projects and seeking alternative materials. However, these solutions often face significant delays due to long lead times, regulatory hurdles, and the need for substantial capital investment [2].

Simultaneously, there is a need to rethink the way we design and manufacture. Instead of focusing solely on sourcing raw materials to address these challenges, components should be designed to be more recyclable. Efforts should also be made to design and manufacture components with less material and to extend the lifespan of products to avoid obsolescence. Furthermore, addressing climate change requires making all industrial processes more efficient. The key to both of these challenges is optimization. Optimization from upstream to downstream—from production processes to the optimization of all machinery and the components that comprise them. This approach can lead to a reduction in energy costs and the amount of material required by the industrial and service sectors [3].

The sectors that could benefit most from this new paradigm of design and manufacturing include aerospace, automotive, urban mobility, energy production, construction, and machine tools, among others.

The aerospace sector, for example, is projected to grow significantly in the coming years. According to industry reports, the global aerospace market is expected to reach USD 430.9 billion by 2025, driven by the demand for more fuel-efficient aircraft and the expansion of air travel [4]. Technological advancements are crucial to meet these demands, emphasizing the need for improved materials, more efficient components, and advanced manufacturing processes.

Developing more efficient components can significantly impact the aerospace industry as well as other transport-related industries. Enhanced efficiency can lead to lighter and stronger materials,

which reduce the overall weight of aircraft. This reduction in weight directly translates to lower fuel or power consumption, thereby decreasing operational costs and carbon emissions. Efficient components can also increase the reliability and longevity of machine systems. By incorporating advanced sensors and smart materials, maintenance can become more predictive and less reactive, reducing downtime and increasing the operational availability of aircraft. This shift towards more efficient components not only supports the environmental goals of reducing emissions but also aligns with the economic objectives of reducing costs and improving performance.

Similarly, the energy sector is undergoing a transformative phase. The global renewable energy market is anticipated to grow at a compound annual growth rate (CAGR) of 7.9% from 2020 to 2027 [5]. This growth is driven by the increasing adoption of renewable energy sources and the need for modernizing the grid infrastructure. To support this transition, there is a significant need for technological advancements that can enhance efficiency and reduce costs.

Advanced manufacturing processes, such as additive manufacturing, have revolutionized the field of mechanical design and manufacturing. This technology enables the production of components with intricate geometries that are not feasible with conventional subtractive manufacturing methods. For instance, lattice structures can be designed to provide high strength-to-weight ratios, which are particularly beneficial in the aerospace and automotive industries where weight reduction is critical. Additionally, additive manufacturing allows for the customization of components to meet specific requirements, facilitating rapid prototyping and reducing time-to-market for new products [6].

Moreover, additive manufacturing supports the principle of design for sustainability. By optimizing material usage and reducing waste, this technology contributes to more sustainable manufacturing processes. It also enables the use of advanced materials, such as high-performance polymers and metal alloys, which can enhance the durability and functionality of components. The ability to print parts on demand also reduces the need for large inventories, thus lowering storage costs and minimizing the environmental impact associated with overproduction and waste.

The integration of new AI models further enhances the potential of additive manufacturing by enabling more sophisticated design and optimization processes. AI-driven design tools can analyze vast amounts of data to identify optimal design parameters, predict the performance of components, and suggest improvements while reducing computing time. This leads to more efficient and innovative designs that maximize performance while minimizing material usage, production costs, and time-to-market [7]. AI-powered simulation tools can predict the behavior of materials and components under various conditions, allowing engineers to test and validate designs virtually before physical production. This reduces the need for costly and time-consuming physical prototypes and accelerates the development cycle.

To achieve this paradigm shift, mechanical design plays a crucial role. A change in mindset in this area involves embracing advanced design techniques to achieve a holistic approach to design. This can be driven by the emergence and development of additive manufacturing, which allows for the creation of complex and lightweight structures that were previously impossible with traditional manufacturing methods. Additionally, the integration of new AI models can further enhance the optimization and innovation of design processes.

By focusing on these strategies, industries can not only address the immediate challenges of material scarcity and climate change but also pave the way for a more sustainable and efficient future in engineering and manufacturing.

1.2 Problem description

The traditional engineering process, long established as a reliable framework for design and manufacturing, is increasingly recognized as inadequate for addressing modern global issues. This methodology is characterized by an iterative process that often lacks efficiency and precision, resulting in several critical issues as seen in **Figure 1.1** (top).

The reliance on outdated, experience-based methods leads to a design cycle that is excessively repetitive and time-consuming. Engineers traditionally follow a cycle of designing, testing, and modifying components based on empirical data and past experiences. While this approach can ensure reliability, it often results in inefficiency. Consequently, the process is slow, resource-intensive, and prone to producing suboptimal designs. Furthermore, traditional Computer-Aided Design (CAD) tools are becoming obsolete because they cannot manage the complex geometries and Boolean operations needed for the demanded designs.

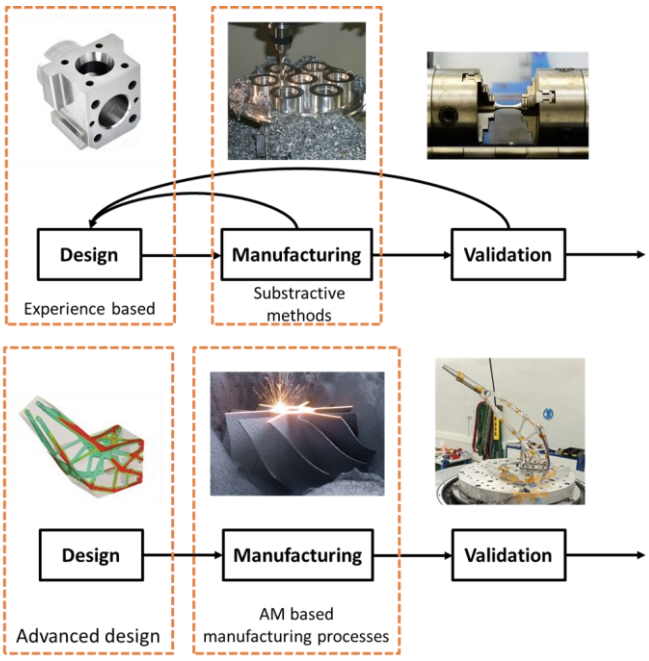

Figure 1.1. *Traditional design and manufacturing iterative process (top). New design and manufacturing paradigm (bottom).*

A significant consequence of these outdated methods is the overdimensioning of components. To ensure safety and functionality under uncertain conditions, engineers frequently design parts with excessive material. This practice, while minimizing the risk of failure, leads to components that are unnecessarily heavy and bulky. The overdimensioning issue extends to entire assemblies and ultimately impacts the efficiency of machines. The extra material not only increases manufacturing costs but also contributes to higher operational costs due to the increased weight.

The traditional subtractive manufacturing processes exacerbate these inefficiencies. Subtractive methods involve extracting the desired shape from larger blocks of material, inherently generating significant waste. This approach is not only wasteful but also environmentally detrimental due to the excessive consumption of raw materials and energy. Furthermore, traditional manufacturing techniques are often incapable of producing the complex geometries required for modern designs, thereby limiting the potential for innovation and optimization.

In sectors such as aerospace, automotive, and energy production, where performance and efficiency are paramount, the inefficiencies inherent in traditional engineering design and manufacturing can be particularly detrimental. The cumulative effect of these outdated practices highlights the pressing need for a shift towards more advanced and efficient engineering methodologies.

The reliance on traditional design and manufacturing processes is increasingly unsustainable in the face of modern technological challenges and environmental considerations. There is a need to adopt methodologies that integrate advanced design techniques, mainly based on algorithmic methods that can achieve designs not conceivable by human designers through experience alone. The product would be tailored to the exact purpose of the component’s entire life cycle, with the least material possible and designed to be recycled. This approach resembles the way nature performs its design and production processes through evolution. Over millions of years, natural selection has developed self-equilibrated ecosystems by generating "products" designed to withstand boundary conditions with the least material possible, and that material can feed the next generations of the same products, as encoded in DNA see **Figure 1.2**.

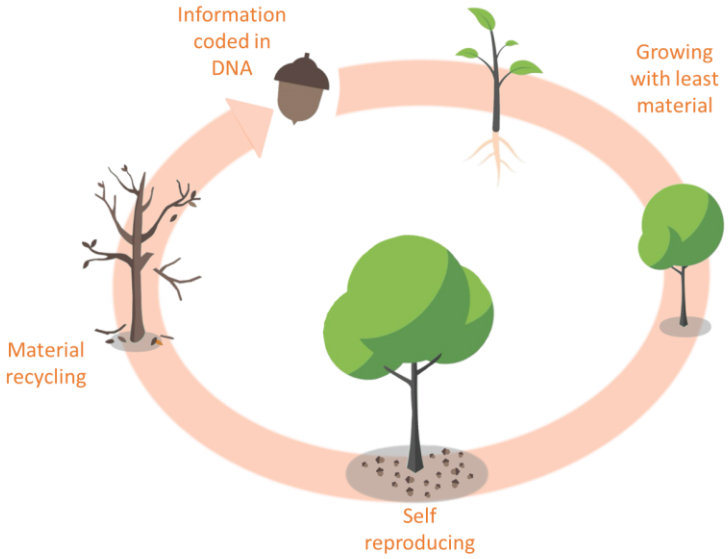

Figure 1.2. *Life cycle of a tree, depicting the natural circular process.*

One way to address these challenges is to explore different bio-inspired design techniques. These methods include, among others, topology optimization, generative design, parametric optimization, true biomimicry and eco-design. These approaches can help create components that are precisely tailored to their functional requirements, minimizing material use and enhancing overall efficiency.

Topology optimization, for instance, allows for the creation of designs that use material only where it is structurally necessary, leading to lighter and stronger components. Generative design uses algorithms to explore all possible permutations of a solution, quickly generating design alternatives that meet specified criteria. Parametric optimization involves adjusting the parameters of a design to achieve the best performance. True biomimicry tries to replicate what can be seen in nature to be applied in optimized human made products, and eco-design focuses on minimizing environmental impact throughout the product's lifecycle.

By integrating these advanced techniques, the engineering process can become more efficient, sustainable, and capable of meeting the demands of modern technology and environmental standards by mimicking nature. This shift not only addresses the limitations of traditional methods but also opens up new opportunities for innovation and optimization in engineering design and manufacturing.

1.3 Scope of the thesis

The objective of this thesis is to explore different techniques and define one to be used throughout the study that address the limitations of traditional engineering by leveraging advanced computational tools and bio-inspired principles to create more efficient and sustainable components. Explore different advanced manufacturing techniques and use holistic design

philosophy to obtain the best solutions without defects. This way all the iterative processes could be avoided as seen in **Figure 1.1** (Bottom).

Adopting a holistic perspective from the design phase of the manufacturing and life of the metallic component can significantly enhance its efficiency, sustainability, and functionality.

1.4 Manuscript structure

The structure of the manuscript is divided into eight chapters, each addressing a specific aspect of the research and its applications. The first chapter is the introductory section, where the context is presented, detailing the global challenges of climate change, material scarcity, and technological advancements. It also identifies the specific problem this thesis aims to solve: the inefficiencies and limitations of traditional engineering design and manufacturing processes. This chapter concludes by outlining the objectives and the proposed methodology of the thesis.

Following this, Chapter 2 provides a comprehensive review of the existing literature and the state-of-the-art in advanced design methods mainly focused on bio-inspired design strategies and design for manufacturing. This includes an in-depth examination of techniques such as topology optimization, generative design, parametric design/optimization, and eco-design, alongside other bio-inspired design approaches. This review sets the foundation for understanding the current landscape and identifying the gaps that this thesis aims to address.

In Chapter 3, there is a review and selection of different design methodologies. This chapter involves applying three selected methodologies to a specific case study to determine the most suitable one for the research objectives. While the selection may not be universally optimal, it serves as a practical basis for the rest of the thesis. The example is the redesign of an aeronautic tooling present in many assembly lines.

Chapters 4, 5, and 6 showcase examples of the applied methodology in various sectors. Chapter 4 focuses on the space sector, demonstrating how the methodology can optimize reaction wheels for weight and structural integrity for harsh space conditions. Chapter 5 extends this application to the energy harvesting sector, highlighting the design of components that withstand cyclic loading conditions. Chapter 6 applies the methodology to the aeronautic, with one example emphasizing aerodynamic optimization rather than structural, to illustrate the versatility of the approach.

Chapter 7 details the development of an automated design process for casting components. This chapter aims to reduce manufacturing defects and eliminate the reliance on the experience of workshop personnel, thereby improving efficiency and consistency in production.

Finally, Chapter 8 presents the conclusions drawn from the research. It summarizes the key findings, discusses the implications for the field of engineering, and suggests directions for future research. This concluding chapter ties together the insights gained from the various applications

of the methodology, reinforcing the overall contributions of the thesis to advancing sustainable and efficient engineering practices.

1.5 References

[1] "State of the Global Climate 2023." Accessed: Jun. 13, 2024. [Online]. Available: https://wmo.int/publication-series/state-of-global-climate-2023

[2] "The Growing Role of Minerals and Metals for a Low Carbon Future," *The Growing Role of Minerals and Metals for a Low Carbon Future*, Jun. 2017, doi: 10.1596/28312.

[3] M. Geissdoerfer, P. Savaget, N. M. P. Bocken, and E. J. Hultink, "The Circular Economy – A new sustainability paradigm?," *J Clean Prod*, vol. 143, pp. 757–768, Feb. 2017, doi: 10.1016/J.JCLEPRO.2016.12.048.

[4] "Aerospace Materials Market, Latest Global Industry Size Forecast Report." Accessed: Jun. 13, 2024. [Online]. Available: https://www.marketsandmarkets.com/Market-Reports/aerospace-materials-market-266342713.html?gad_source=1&gclid=Cj0KCQjwsaqzBhDdARIsAK2gqndjh6zm_LFHrPf1kAdym_IHnBRYsPyGB9Q_92Gqa3_glo2Ghr-YwYQaAhaoEALw_wcB

[5] "Renewable Power Generation Market Size Report, 2020-2027." Accessed: Jun. 13, 2024. [Online]. Available: https://www.grandviewresearch.com/industry-analysis/renewable-power-generation-market

[6] T. D. Ngo, A. Kashani, G. Imbalzano, K. T. Q. Nguyen, and D. Hui, "Additive manufacturing (3D printing): A review of materials, methods, applications and challenges," *Compos B Eng*, vol. 143, pp. 172–196, Jun. 2018, doi: 10.1016/J.COMPOSITESB.2018.02.012.

[7] T. Wuest, D. Weimer, C. Irgens, and K. D. Thoben, "Machine learning in manufacturing: advantages, challenges, and applications," *Prod Manuf Res*, vol. 4, no. 1, pp. 23–45, Jun. 2016, doi: 10.1080/21693277.2016.1192517.

Chapter 2: Literature review

2.1 Natural design foundations and terminology on inspiration from nature

For context, it is known after analyzing the rocks on earth's crust and those on its surroundings (the moon rocks and meteorites found on the earth's surface); that the planet is around 4.54 billion (+-50M) years old [1]. One billion years after, the first living organisms appeared in the sea in the form of cyanobacteria [2].

During millions of years, life thrived and evolved in the oceans from unicellular algae to vast coral reefs, from primitive fish in the shallow waters 490 million years ago [3] to massive sharks in the deep sea. The changes in the design of species have been powered by the need of succeeding in a certain environment. In order to thrive, a living organism must make sure to feed with its specific resources and mate before passing away. If there would be just one species, it would have been quite easy to succeed. Nevertheless, as many different species appeared, the predator-prey relation started. This forced the cumulative selection to work to survive as species. The diatoms and the radiolarians, for instance, are a great example of this. They are the most abundant living organisms in the oceans; they serve as the basis of the food chain in the seas and make a crucial role in the atmosphere's CO2 absorption. Therefore, this kind of phytoplankton has many predators such as the copepods that suppose a group between 55-95% of the total zooplankton in the ocean. Therefore, for succeeding they have to be strongly defended and at the same time, as they are autotroph they need to absorb the CO2 in the atmosphere by floating on the ocean's surface and at once, have direct contact with sunlight for doing the photosynthesis. This means that they need to have a strong defense for avoiding being eaten in great amounts, but they have to be light enough to float in the euphotic zone, the upper layer of the ocean. Millions of years of evolution have entailed an impressive diversity of silica exoskeletons (up to 100.000) developed by this type of unicellular algae that, in order to thrive, have engineered one of the most optimized and beautiful structures in nature [4]. Still, this competition does not refer to the defensive part of the predator-prey relation only. In fact, in order to improve their attacking weapons, the predators, have developed during the ages diverse methods to balance the defensive methods evolved in their preys. The shark scales serve as an example of this attack and defense in the genetic mutation race. Actually, when looking into a microscope, the shark scales or denticles appear to have a specific design for a concrete goal. Denticles form, size and aligning varies for each shark type, and as seen in [5] and in [6] each of those work differently to different water flow velocities. Although all of them do a hydrodynamic job, some of them are useful for moving at great velocities because the denticles reduce the drag force in those conditions like the Mako's scales (200µm), the fastest shark on earth. However, others help to reduce the drag and increase thrust doing less effort while moving like in the case of the Leopard Shark (0.5mm).

The impressive designs do not stick to water creatures only, 430 million years ago, plants started colonizing the mainland creating another source of nutrients for ocean living organisms. 30

million years after, the first primitive fish started to crawl out of the water and was the beginning of a nowadays seen generation of vertebrate land creatures. From there, mammals, reptiles, etc. descended [7]. Insects, however, are thought to be descendants from crustaceans and myriapods . One of the most astonishing designs in nature can be found in the insect family, more specifically in the *morpho* butterfly subgenre. These species have developed a very special way for camouflaging, thermoregulation and signaling. They are known for their iridescent and colorful blue wings that reflect light as very few things in the natural world. When looking into a microscope the butterflies' wings, some quasi-periodic ridges whose cross-sections resemble pine trees can be seen. These nanostructures, regulate the wavelength reflected creating a metallic-like color not possible to achieve with common pigments or dyes. Furthermore, depending on the angle that light hits those nanostructures they bright in a different way, helping these beings to change the reflectiveness and thus, giving them the ability to communicate with other congeners [8].

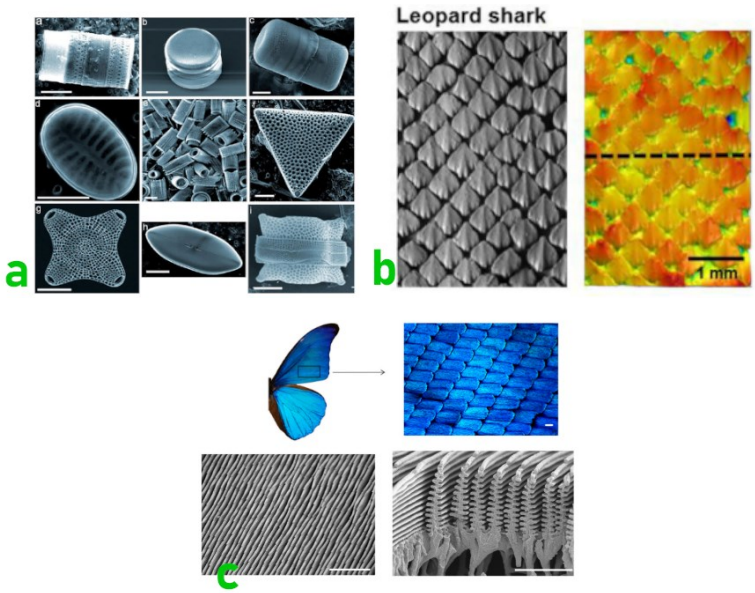

***Figure 2.1**. Evolution's design examples: a) Diatoms and their many different shapes. b) Leopard shark denticles with a topographic image. c) A type of Morpho butterflies' wing in different scales. (Sources: a)* [9]*; b)* [6]*; c)* [8]*)*

As far as it is known, nature is capable of the most impressive designs ever imagined by the human brain. Thanks to Darwin and his theory of evolution, it is known that these designs are not spontaneous, but have been developing step-by-step over millions of years. He presented a disruptive theory that claimed that every species that have succeeded until nowadays have had to develop gradually and create generation-by-generation different methods to thrive in extreme changing environmental conditions [10]. Richard Dawkins subsequently enhanced this theory; he defined for the first time the term *cumulative selection*. This concept refers to a cumulative non-random process with which the random genetic changes in some individuals become global for the whole species. This process works as a natural sieve where one small change happens into one specimen's gene chain and then it reproduces in the next generation. This deviation

accumulates to generate a mutation. If the change in these mutated individuals suits better with the environmental conditions where they coexist with non-mutated congeners, those specimens may thrive and surpass the “older” version of the species becoming a globalized mutation. If the mutation translates into a weakening of the species, those individuals would not succeed and the mutation would not accumulate. Therefore, the genetic changes would not perpetuate [11]. This process is illustrated and simplified in **Figure 2.2** were a population of mice that some are black and others white due to natural genetic variation have moved to a land with dark soil. The mice that are white are easier to catch for predators and most of the mice that reach reproductive age are black. The offspring of these mice will be “blacker” becoming a global mutation.

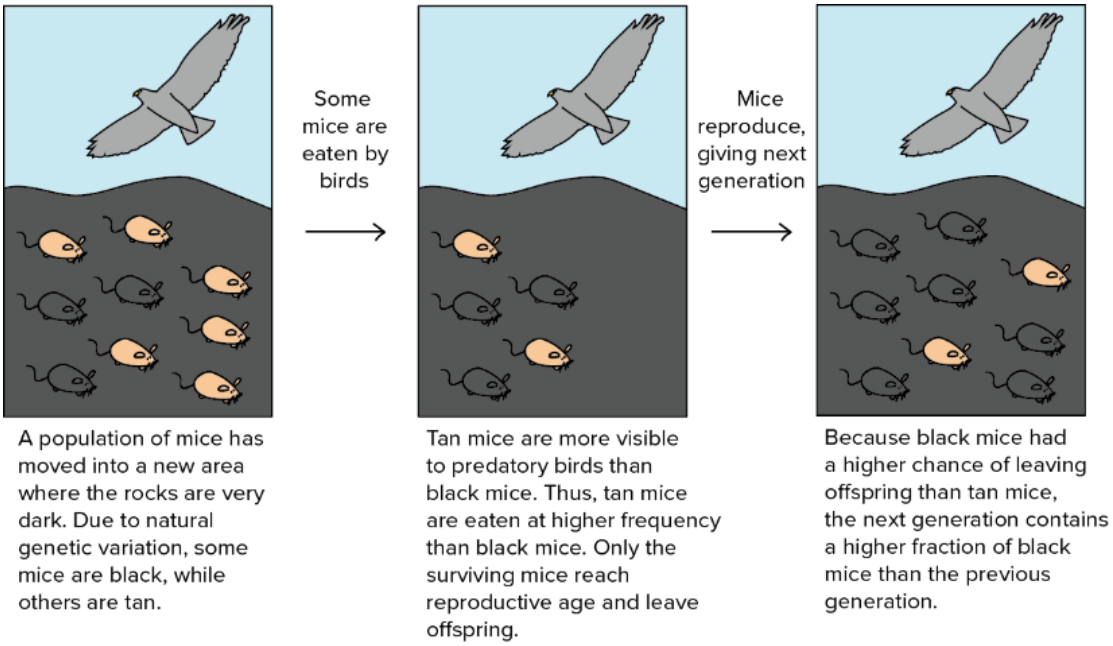

***Figure 2.2**. Graphic expression of cumulative selection. 1. Random mutation 2. Due to environmental conditions, a part of the population disappear. 3-The fittest specimens thrive. (Source:* [12]*)*

2.1.1 Natural patterns

To deeply understand the forms found in nature and thereby emulate these natural designs to create specialized structures with minimal material use and environmental consideration, it's essential to recognize and explain the patterns present in nature and how they form.

Initially, it's crucial to differentiate between a pattern and a form. A pattern is an arrangement of similar shape units that repeat periodically, extending through space. In contrast, a form is the finite, characteristic outline of a class of objects.

Patterns are observed both in living beings and in physical-chemical processes in inanimate objects. Interestingly, there are significant similarities between patterns in living organisms and those in inanimate processes. But why is this so? Natural selection is often referred to as a 'black box' that generates optimal forms for species' survival. However, this only partly explains the range of mutations that occur. It's unclear whether what we observe is solely due to random

species changes or whether the phenomena generating these patterns have a limited range of options. For instance, the hexagonal pattern of a honeycomb is not a result of bees experimenting with various geometric shapes until finding the most material-efficient one. Rather, bees use hexagonal shapes due to the way they construct their honeycombs, a process that will be further explored in subsequent sections.

The natural language of patterns is mathematics, which has the capability to define them precisely. For instance, the curvature in the shell of the Nautilus mollusk is a logarithmic spiral. This form was first described by René Descartes in 1638. It is defined as the curve traced by a point rotating around an origin at a constant angular velocity, while the linear velocity increases in direct proportion to its distance from the origin. The equation defining this curve in polar coordinates is as follows:

$$r = ae^{k\varphi}, \varphi \in \mathbb{R} \quad (1)$$

Or

$$\varphi = \frac{1}{k} ln \frac{r}{a} \quad (2)$$

With $a > 0, k \neq 0$ being real constants.

The mathematical expression in question allows for an exact definition of the curve, illustrating that its shape remains "similar" throughout its trajectory, though its size varies. This leads to the inquiry: why does the shell of this mollusk adopt such a form? Clearly, the mere definition of the curve is insufficient, indicating that mathematics alone is not the only necessary field of knowledge. A comprehensive understanding of the origins of these shapes necessitates an exploration into the physical and chemical processes occurring in natural phenomena. This interdisciplinary approach is exemplified in [13] and [14], which both underscore the significance of integrating multiple disciplines to comprehend natural patterns.

Furthermore, the classification of these natural patterns can vary depending on the perspective from which they are examined. This manuscript presents a classification believed to be most suitable for the forthcoming analysis.

Bubbles

Water, as the fundamental element of life, exhibits a phenomenon known as surface tension, akin to other fluids. Surface tension is a cohesive force among molecules, enabling liquids to resist external forces. This phenomenon arises due to the molecules at the liquid's surface not being surrounded by identical molecules on all sides, creating a sort of "skin". It is this surface tension that facilitates the formation of water droplets and bubbles.

Commonly, it is perceived that fluids lack a characteristic shape, assuming the form of their containers. However, they do possess an intrinsic shape, which is highly susceptible to external

forces such as gravity or air friction. Unlike crystalline structures, where molecules are orderly arranged, liquid molecules are randomly distributed, rendering them isotropic. In other words, the natural shape of liquids, due to surface tension, is spherical. As all physical systems tend to their most stable state, for fluids, the spherical form represents the state of lowest energy. This phenomenon also influences the morphology of crystals and the microstructure of metals, affecting the solidification process of different phases.

Returning to the example of honeycomb structures, one might ponder the optimal way to divide space using polygons. It is evident that space can be completely filled without gaps only using triangles, squares, or hexagons. However, hexagonal patterns have the smallest total perimeter when summing the lengths of each cell's walls. The hexagonal geometry, therefore, represents an efficient and structurally sound solution in natural and engineered systems, reflecting a harmonious balance between material use and spatial division. This can be demonstrated by considering a generic polygon with 'n' sides inscribed in a circle as seen in **Figure 2.3**.

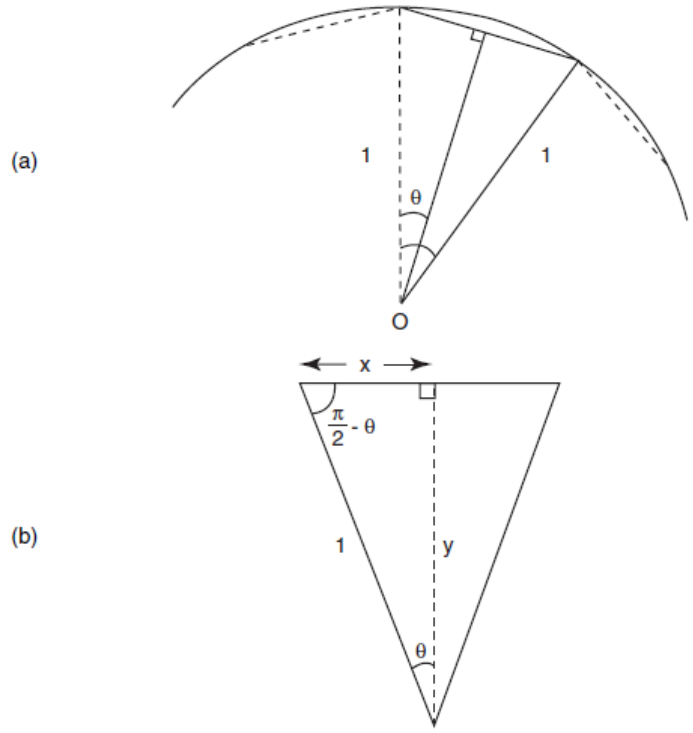

***Figure 2.3**. Geometric details for a regular n-gon inscribed in a circle (**a**) size of the n-gon cells (**b**)* [15]

The area of this n-side polygon should be given by:

$$A = n \times \frac{1}{2} \times 2x \times y = nr^2 sin\frac{\pi}{n}\cos\frac{\pi}{n} \quad (3)$$

And the perimeter is given by:

$$P = 2nr\sin\frac{\pi}{n}$$

The area-to-perimeter ratio is crucial in determining the efficiency of space utilization by the polygon and is expressed as: (4)

$$R = \frac{A}{P} = \frac{r}{2}\cos\frac{\pi}{n} \quad (5)$$

In comparing polygons with 3 (triangles), 4 (squares), and 6 (hexagons) sides, this ratio helps in determining which shape offers the most efficient use of space relative to its perimeter. Notably, the maximum possible ratio is defined by a circle, where $R = 0.5r$. This represents an asymptote in the graph depicting the growth of this ratio, implying that the circle is the most space-efficient shape in terms of the area-to-perimeter ratio. In other words, as the number of sides 'n' increases, the regular polygon increasingly approximates a circle, thereby maximizing the area enclosed for a given perimeter as illustrated in **Table 2-1**. List of values of n for the n-gon..

***Table 2-1**. List of values of n for the n-gon.*

n	$\cos\frac{\pi}{n}$	R(n)
3	0.5	0.25r
4	0.707	0.354r
6	0.866	0.433r

As demonstrated mathematically, the construction of a honeycomb utilizes less material than other geometric spatial partitions. This observation raises questions about the spatial and material management strategies of bees. The process, however, does not imply a conscious understanding of these efficiencies by the bees. The honeycomb structure emerges as a result of individual cells initially forming as spherical bubbles. During their development, these bubbles collide and reshape, eventually adopting a hexagonal configuration that minimizes energy and material use. The uniformity of this structure is attributed to the bees' communication capabilities, which ensure equidistant spacing of the bubbles.

The honeycomb represents an example of efficient structural formation in nature, a phenomenon that extends beyond the realm of apian architecture. Structures formed by the surface tension of water or mixtures of water and surfactants, such as soap, are prevalent. These formations often appear in three-dimensional foam structures. The challenge in these cases is to determine the optimal shape for space-filling efficiency.

Addressing this challenge, Dennis Weaire and Robert Phelan proposed a model that contradicts Lord Kelvin's conjecture on minimal surfaces. Their model posits that optimal space division is not achieved through a uniform shape. Instead, they propose a composite structure of eight cells, six with 14 faces and two with 12 faces, combining pentagons and hexagons as seen in **Figure 2.4**.

This model represents a more efficient method for space division than previously understood, providing new insights into the spatial organization in natural and synthetic structures [16].

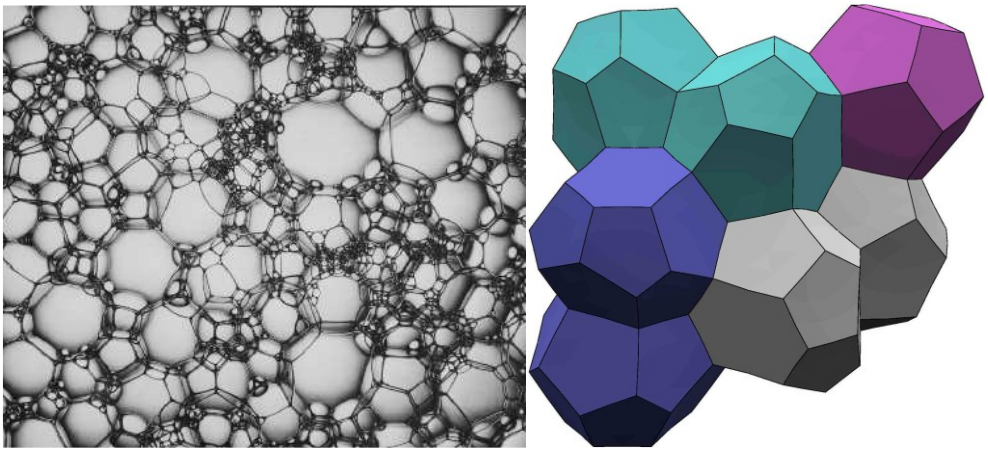

***Figure 2.4**. The stochastic structure shown by the collision of different sized bubbles (**left**). The composite structure defined by Weaire and Phelan for the best 3D space distribution (**right**)* [17].

Many natural phenomena can be accurately modeled using the Voronoi diagram. This mathematical concept, the Voronoi diagram, can be defined as a method of partitioning a space into distinct regions. Each region is determined by its proximity to a set of predefined points, known as seed points or sites, distributed within the space. Essentially, for each seed point, there is a corresponding region consisting of all points closer to that seed point than to any other. This results in a mosaic-like pattern, where each tile represents the influence zone of each seed point.

When these points are arranged in an orderly manner as seen in **Figure 2.5**, the pattern produced is akin to that observed in bee honeycombs. In the case of honeycombs, the centers of the hexagonal cells can be seen as 'seed points'. The walls of the cells then approximate the boundaries created in a Voronoi diagram, where each cell boundary represents the point equidistant from neighboring centers. This resemblance not only demonstrates the practical applications of Voronoi diagrams in understanding natural patterns but also highlights the inherent mathematical properties found in nature.

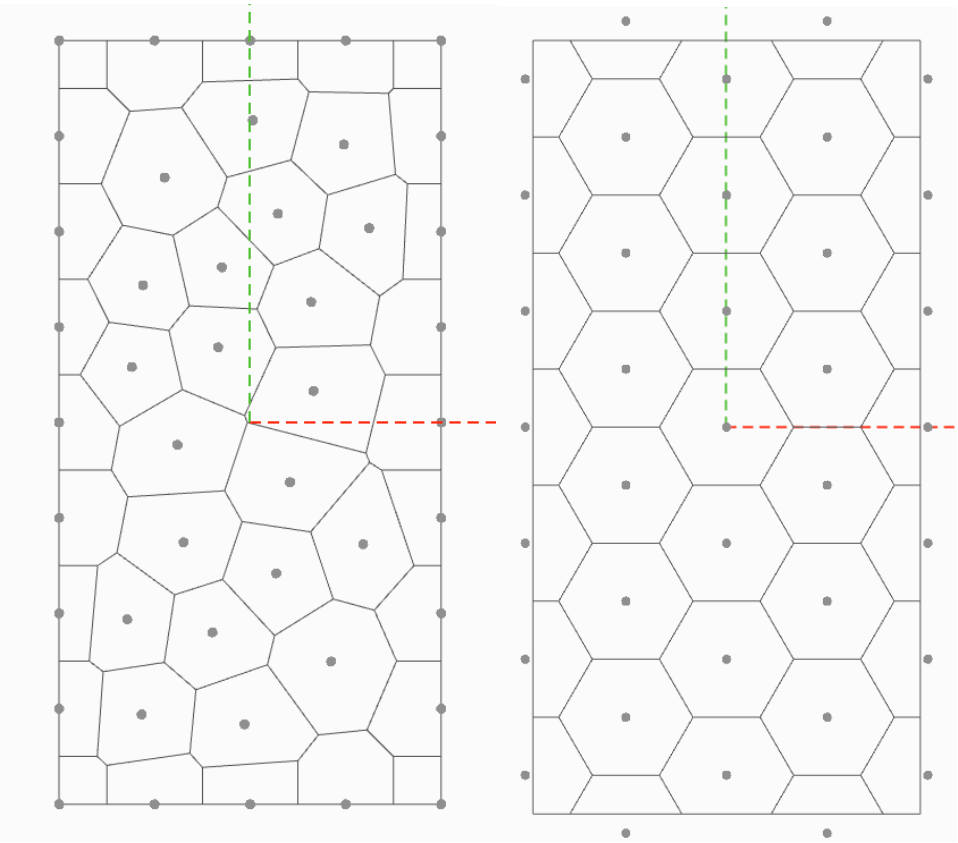

***Figure 2.5**. Voronoi tesselation with disordered origin points (**left**). Voronoi tesselation with ordered origin points (**right**).*

Among the examples found in nature, certain organisms stand out for their complex and sophisticated structures, created through bubble-based phenomena. These include diatoms and radiolarians, marine organisms that construct shells with patterns formed by membranes and vesicles packed in foams. These organisms generate a foam of bubbles around themselves, where the bubbles collide and merge. The material is deposited at the boundaries between these bubbles.

One of the most notable examples is Aulonia hexagona, a diatom characterized by its spherical shell divided into hexagonal and pentagonal cells. This structure is a direct consequence of Euler's rule, which states that it is impossible to form a spherical polyhedron using only hexagons. To achieve a spherical form, pentagons must be incorporated, breaking the hexagonal pattern where necessary. This rule underlies the intricate geometric complexity of many natural forms.

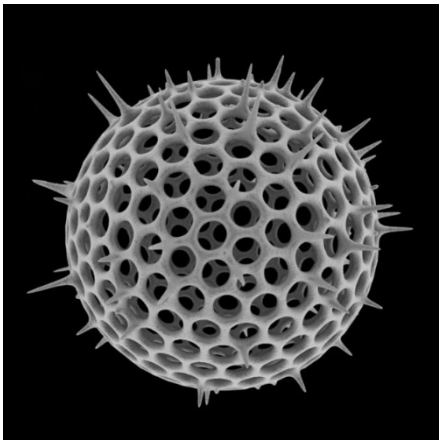

***Figure 2.6**. Microscopic image of Aulonia Hexagona diatom* [18]

Structures of significant interest in science, also naturally occurring through bubble-related processes, include periodic minimal surfaces. These surfaces arise when the concentration of a surfactant in a liquid exceeds a critical threshold, leading to the formation of cubic phases known as periodic minimal surfaces. Periodic minimal surfaces are characterized by their ability to separate two volumes of space with the least possible surface area. A key feature of these surfaces is that their mean curvature is zero at every point, indicating that the surface is locally area-minimizing.

Periodic minimal surfaces are mathematically intriguing and physically relevant. The concept of mean curvature is central to understanding these surfaces. Mean curvature is defined as the average of the curvatures in two orthogonal directions at any point on a surface. For periodic minimal surfaces, this value is uniformly zero, which means these surfaces are not bending towards or away from the enclosed volume on average at any point. This property makes them optimal for minimizing surface area between two volumes.

Several types of periodic minimal surfaces are known, each with unique geometric configurations. For instance, the Schwartz P, Schwartz D, and Schwartz G surfaces are notable examples. The Schwartz P surface, characterized by its triply periodic labyrinth of interconnected straight tunnels, the Schwartz D surface with its intricate diamond-like structure, and the Schwartz G surface, noted for its gyroid pattern, demonstrate the diverse and complex nature of these minimal surfaces.

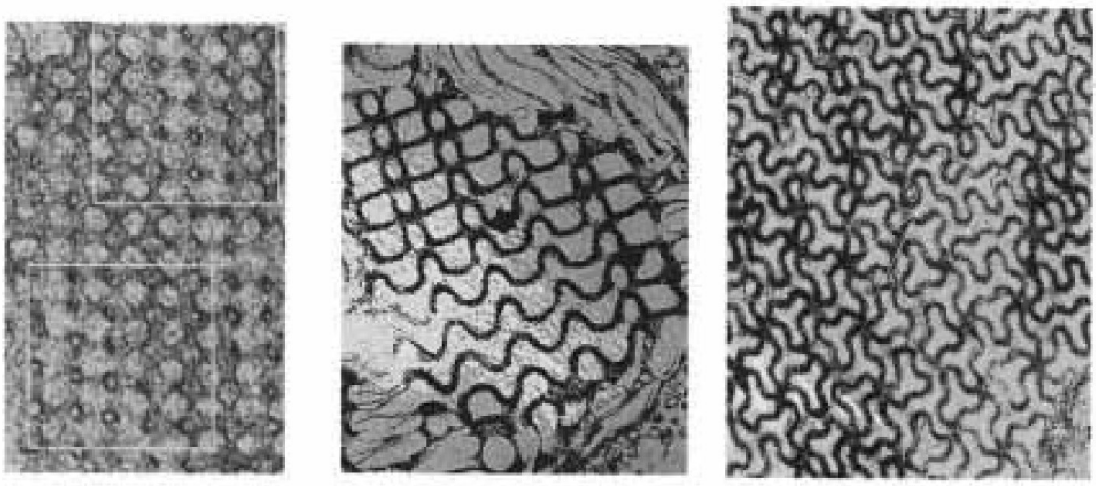

***Figure 2.7**. Periodic membrane structures are common in living cells. Many of these appear to be related to periodic minimal surfaces: (a) the D-surface in leaf membranes; (b) the P-surface in algae; (c) the G-surface in lamprey epithelial cells* [19]

Fractals, Breakdowns & meanders

Fractals are prevalent structures in nature, characterized by their undefined shape and repetitive patterns across different scales. These structures were brought into the spotlight by mathematician Benoit B. Mandelbrot, who is often credited with their discovery. In his seminal paper “How long is the coastline of Britain?”, Mandelbrot discussed the intriguing observation that the measured perimeter of the coast of Great Britain varied depending on the map scale used. The finer the map's detail, the longer the coastline appeared. This led to the realization that discussing a fixed perimeter for such irregular shapes was nonsensical, as it changed with the scale of measurement.

Mandelbrot proposed a paradigm shift in the definition of dimension and introduced the concept of fractal dimension. The measurement of a continuous curve using a "measuring stick" of length a illustrates this concept. Suppose this stick fits N times along the curve, then the measured length $L = N \cdot a$. Naturally, $N = \frac{L}{a}$ which is a function of a, $N = N(a)$. Therefore, if $a = 1$, $N(1) = L$. Similarly, if $a = 1/2$, $N(\frac{1}{2}) = 2L$, and so on. For fractal curves, the relationship is defined as:

$$N = L\, a^{-D} \tag{6}$$

where 'D' is the fractal dimension and 'D > 1'.

Fractals are not limited to mathematical theory but are mirrored in numerous natural phenomena that exhibit patterns of repetition and scaling. Patterns in leaves and flowers often manifest fractal forms, as do coastlines, rivers, and mountain ranges. Interestingly, some phenomena, such as crystal formation, defy the expected geometric ordering at the atomic level and instead grow

into branching structures. These forms are influenced by factors like temperature, pressure, concentration, or flow.

Other examples include snowflakes and tree branches. Models such as the Diffusion-limited Aggregation model (DLA) have been developed to simulate the creation of these structures. The DLA model enables the simulation of branching structures with a fractal dimension similar to the dendrites found in minerals. One of the most common examples of fractals in natures is the Romanesco broccoli as seen in **Figure 2.8**.



***Figure 2.8**. Zoomed image of a Romanesco broccoli* [20]

Cracks and fractures are common occurrences in brittle materials. The pattern formed by these cracks results from various factors, including the material's microstructure, the distribution of stress, and the rate of propagation. Initially, cracks tend to start with high acceleration, which gradually becomes more moderate as they reach maturity as illustrated in **Figure 2.9**. At this stage, they begin to branch out at a more constant velocity. Similar to previously mentioned natural phenomena, the dimensioning of these patterns cannot be confined to an integer but requires a fractal dimension due to their intricate nature.

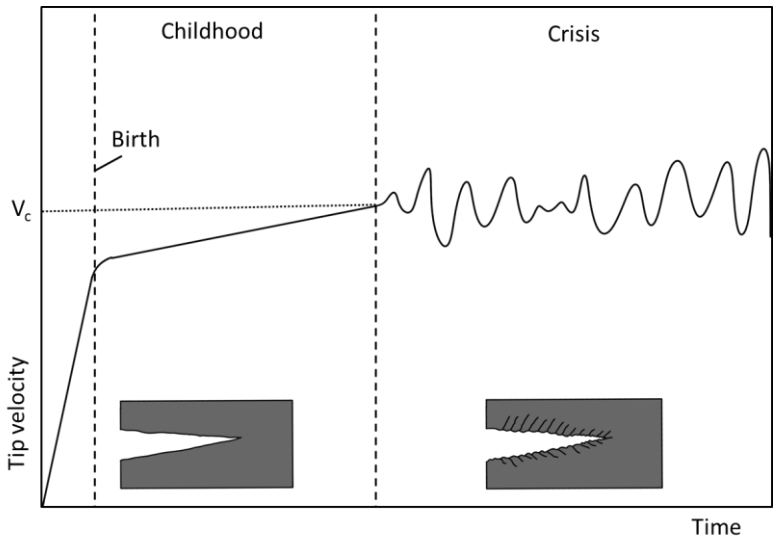

***Figure 2.9**. Crack propagation velocity and morphology diagram* [14]

Cracks can originate from a single point, as explained, or they can emerge simultaneously from multiple points. This latter form of cracking is often due to the uniform contraction or expansion of a thin material layer, such as the drying of soil in a dry season.



***Figure 2.10**. Multiple-point crack propagation example in dried mud* [21].

In the early stages of this phenomenon, cracks tend to form at 120° angles as seen in **Figure 2.10**, creating patterns reminiscent of regular hexagons or similar to those shown by Voronoi diagram. However, as the propagation continues, the cracks begin to spread in different directions, disrupting this initial pattern and leading to more complex formations, as typically observed in various materials.

An interesting geological example of this process is the formation of basalt columns. The rapid solidification in these structures inhibits further propagation of cracks, resulting in a pattern that

closely resembles regular hexagons as seen in the **Figure 2.11**. This phenomenon demonstrates the interplay between the speed of a material's phase transition and the resulting crack patterns.



***Figure 2.11**. Basaltic columns from Reynisfjara beach in Iceland.*

The way water flows in rivers and meanders can be analogously described as a crack that grows slowly or quasi-statically. The study of these patterns has been of great scientific importance. Robert Horton, for instance, made significant contributions to the understanding of meandering rivers by classifying their tributaries according to a specific order. This classification enabled a mathematical approach to understanding how water flows behave in terms of length and number of tributaries. Consequently, it was observed that water flows form fractal patterns similar to those seen in cracks or Diffusion-limited Aggregation (DLA) clusters.

Just like cracks or electrical discharges, water, through the process of erosion, seeks the shortest path to its final destination. This phenomenon reflects a natural optimization process, where the flow of water incrementally carves out a path through the landscape, constantly adjusting and reshaping its course to find the most efficient route to a lower elevation.

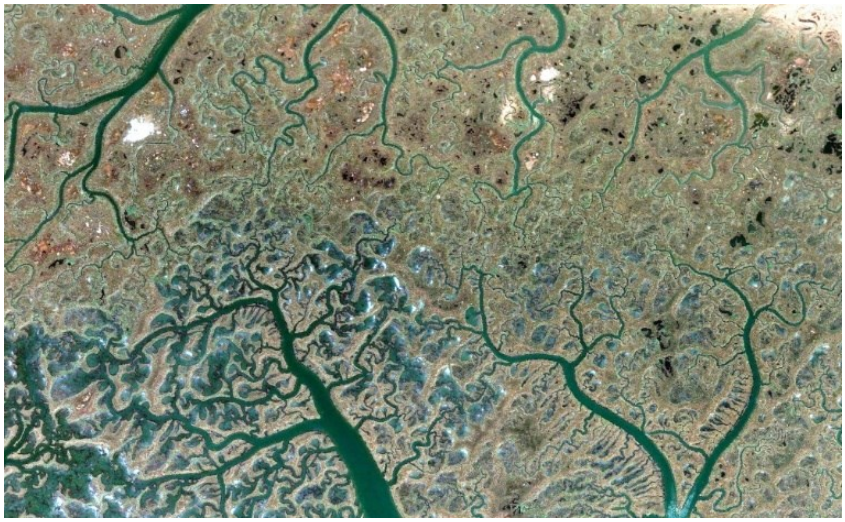

***Figure 2.12**. Rivers and meanders as seen from space (source: Google earth)*

Waves

The creation of patterns in nature is often linked to the disruption of equilibrium. Various phenomena, including chemical reactions, can significantly influence this process. Waves, for instance, are typically generated by dynamic, non-equilibrium phenomena. A prominent example of this is the Belousov-Zhabotinsky (BZ) reaction, which stands as a classic model of non-equilibrium thermodynamics. These reactions, characterized by their sequential and repetitive nature, generate oscillatory patterns and wave propagation.

To understand the BZ reaction, one can envision a flat environment with cells interacting among themselves. These cells can exist in three different states: receptive, excited, and refractory. When in the excited state, cells emit stimuli. If neighboring cells are receptive, they too become excited. However, post-excitation, these cells enter a refractory period where they become unresponsive to any surrounding activity. This refractory state is crucial for the observation of fluctuations and the creation of distinct patterns in these reactions as seen in **Figure 2.13**.



***Figure 2.13**. Waves seen from a Belousov-Zhabotinsky reaction* [22]

This process exemplifies a reaction-diffusion system, a concept recognized for its significant role in generating natural patterns. Alan Turing, in his landmark paper "The Chemical Basis of Morphogenesis," predicted the capability of such systems to produce a variety of patterns. This concept, elaborated further in this chapter, underlines the mathematical and chemical foundations of pattern formation in nature [23].

Beyond chemical reactions, other examples of wave patterns, such as sand dunes and ocean waves, are predominantly shaped by wind. Dunes vary in type and characteristics, influenced by wind patterns and sand accumulation. In the case of ocean waves, the oscillatory nature of wind imparts a quasi-periodic motion to the sea surface, resulting in undulatory patterns.

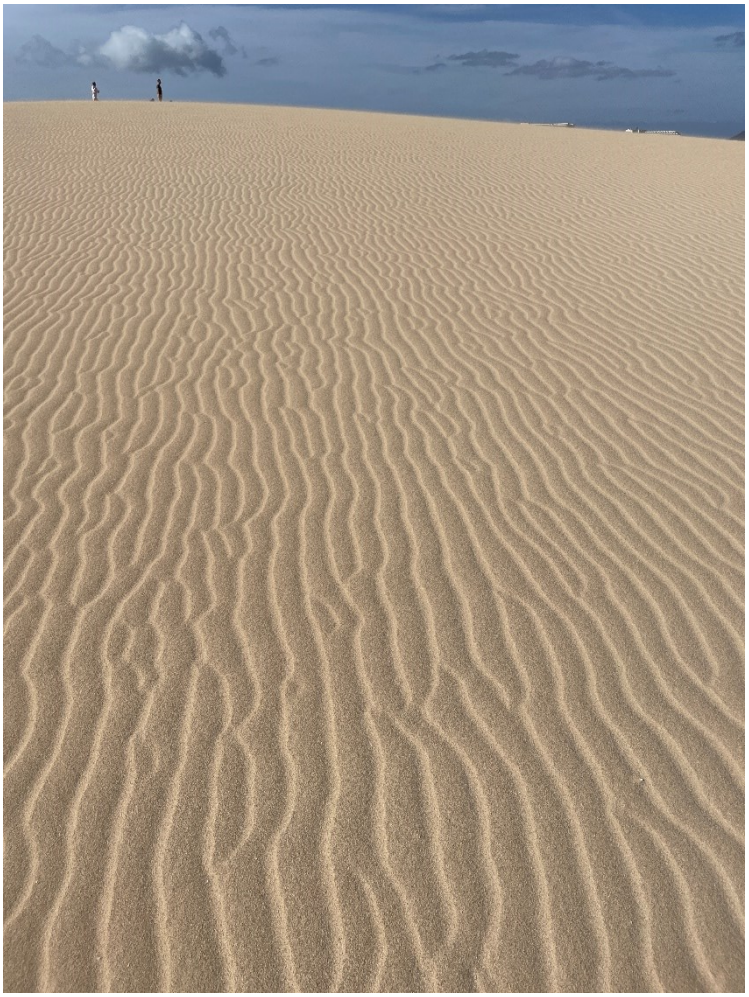

***Figure 2.14**. Waves as seen in sand dunes with periodic wind forces in Corralejo Fuerteventura*

Bodies

Living organisms possess certain characteristics that enable them to survive and thrive over other species that lack these attributes. While Darwin's theory of natural selection addresses survival and adaptation, it doesn't fully explain the complexities of morphogenesis. This term refers to the development of patterns and structures in organisms, evident in the skin and fur patterns of zebras, giraffes, and leopards, among others. Alan Turing laid the groundwork for understanding morphogenesis and the loss of equilibrium in a spherical embryo, leading to the development of various forms or limbs in a single organism. Turing described a reaction-diffusion system driven

primarily by morphogens. Unlike the Belousov-Zhabotinsky reaction, Turing's reaction is "stationary" and can create lines and spots of different chemical compositions.

The process of these reactions is illustrated in **Figure 2.15** with a scenario where a compound A produces an autocatalytic reaction, generating more of compound A. Simultaneously, compound A gives rise to an inhibitory compound B, which prevents further formation of A. The formation of patterns with different compositions depends on the diffusion rates/capacities of these compounds.

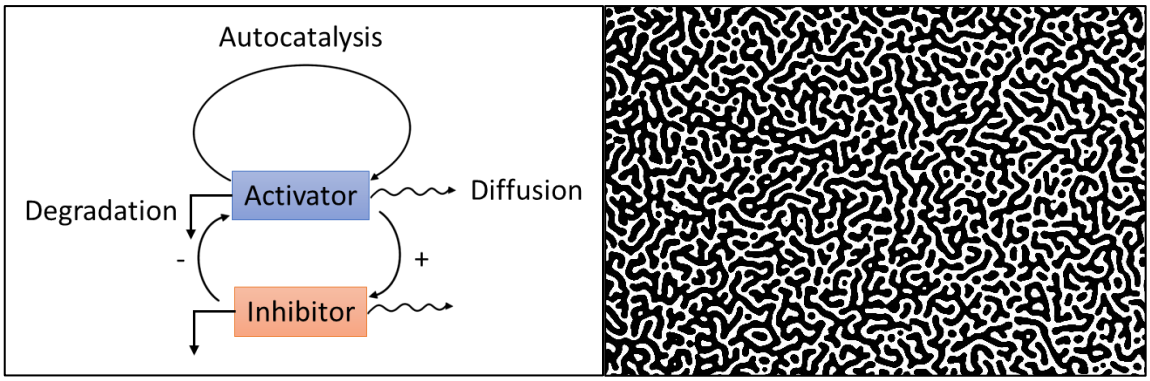

***Figure 2.15**. Turing patterns formation process (**left**). Turing pattern example (**right**)* [24]

Applying this concept to animal skin and fur patterns, focusing on melanocytes, the pigment-producing cells. Melanocytes contain a protein called melanin, which determines the color they produce. The distribution of activators and inhibitors of these proteins is determined during embryogenesis (when the embryos are originated). This information is processed by melanocytes to create the observed mature patterns. [25] model, simulating spots on a geometry similar to a tail, showed that if the length is below a critical value, the tail is filled with stripes; as length increases, spots begin to appear. Modifying this model can also predict patterns in giraffes and leopards as seen in **Figure 2.16**.



***Figure 2.16**. Form generation in animal tails based on length* [25] *(**left**), giraffe spot pattern* [26] *(**center**), leopard spot pattern* [26] *(**right**)*

A similar phenomenon occurs with the patterns seen in butterflies and moths. Here, patterns are confined to areas bounded by veins, and each section is independent of the others, resulting in lines and spots varying by region.

The development of limbs, such as arms and legs, is also determined by these reaction-diffusion systems, as demonstrated by [27]. Similarly, the orderly distribution of leaves and branches on a plant stem can be preceded by a Turing-type system. Phyllotaxis, the arrangement of leaves on a plant stem, typically maximizes sunlight exposure. This configuration isn't due to plants' knowledge or random selection by nature but results from a physicochemical process.

The three main configurations of phyllotaxis are spiral, distichous, and whorled which can be seen in **Figure 2.17**. The spiral pattern is where leaves are arranged 137.5° apart from each other in a spiral form. In the distichous configuration, leaves are arranged in a spiral with 180° between them. The whorled pattern forms small clusters of two or more leaves at regular intervals along the stem. [26] work demonstrated that these arrangements could be explained by reaction-diffusion processes.

Understanding these natural patterns provides insights into the complexity of biological development and the underlying principles that guide the formation of structures in living organisms.

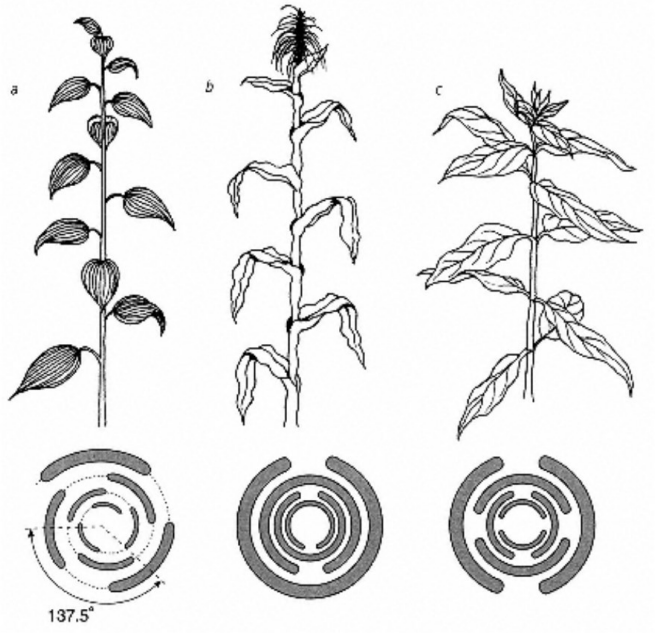

***Figure 2.17**. Examples of different phyllotaxis distributions: spiral (a), distichous (b), and whorled (c)* [14].

Spirals

Spirals are a geometric shape observed in numerous natural phenomena, ranging from macro to nanoscale. These include galaxies with spiral pitches of 10^{20} meters, hurricanes and auroras with diameters up to 10^{5} meters, vortices created at the wingtips of airplanes at around 10^{2} meters, the microstructure of some crystals at 5×10^{-6} meters, and even the atomic organization of matter like nanotubes with pitches of 10^{-8} meters. Generally, in these inanimate events, the formation of spirals is driven by nonlinear processes.

The formation of spirals in aerodynamic phenomena is particularly intriguing. Hurricanes, for instance, form in warm regions where large amounts of water evaporate and rise due to convection. The condensation of this water vapor leads to the formation of massive clouds. The condensation of such large volumes of water releases tremendous energy, which heats the clouds. High atmospheric pressure above these clouds then causes a vortex in the opposite direction. This results in the formation of spiral rainbands, with air currents being directed downwards due to the Coriolis effect, creating spiral shapes that rotate counterclockwise in the Northern Hemisphere and clockwise in the Southern Hemisphere.

In the case of turbulence caused by obstacles, phenomena such as the Karman vortex street emerge. Initially observed by Von Karman in 1911 in his laboratory, this vortex pattern has also been seen in cloud formations around isolated islands or mountains through satellite imagery. A Karman vortex street is a fluid dynamics phenomenon where a repetitive pattern of swirling vortices forms behind an obstacle in a flow. This pattern is caused by a process known as vortex shedding, responsible for the unstable separation of fluid flow around blunt bodies.

Another turbulent spiral phenomenon occurs primarily in airplanes, most evidently at the wingtips. This phenomenon is known as wake turbulence, characterized by the disturbance it creates in the atmosphere behind aircraft. Wake turbulence can be particularly hazardous, especially during takeoff and landing phases, due to the intense vortices generated by the aircraft's wings. All the examples based on fluid dynamics are illustrated in**Figure 2.18**.

These spiral phenomena, ranging from the vast scales of galaxies to the intricate patterns of nanotubes, demonstrate the pervasive and universal nature of spiral patterns in both natural and man-made environments. Understanding these phenomena not only provides insights into the fundamental principles of physics and fluid dynamics but also has practical implications in fields such as meteorology, aviation, and material science [22, 28].

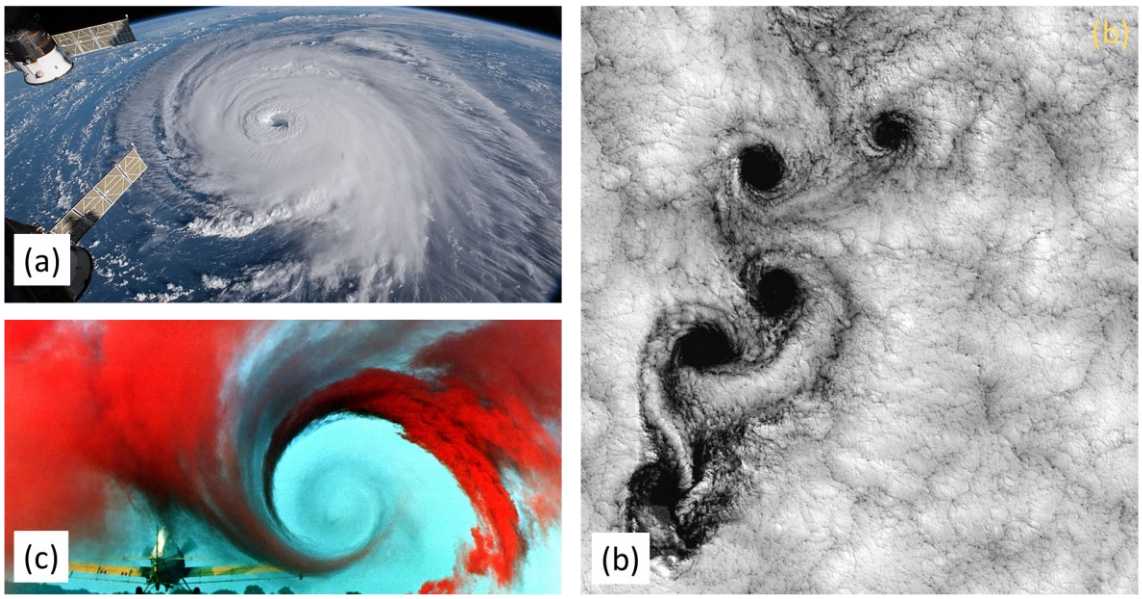

***Figure 2.18**. Different vortex patterns in nature in different scales: a hurricane viewed from space* [29] *(**a**), a Kármán vortex street behind an island* [30] *(**b**), and a smoke vortex ring* [31] *(**c**).*

The phenomena previously discussed relate to inanimate events, yet spirals are also a prevalent geometric pattern in nature. A classic example of this is the arrangement of florets in flowers or the scales on a pine cone. When observed closely, as indicated in **Figure 2.19**, one can notice that the numbers of spirals in different directions differ by Fibonacci numbers. Following one set of spiral lines, the difference might be 8, while in another line, it could be 13.

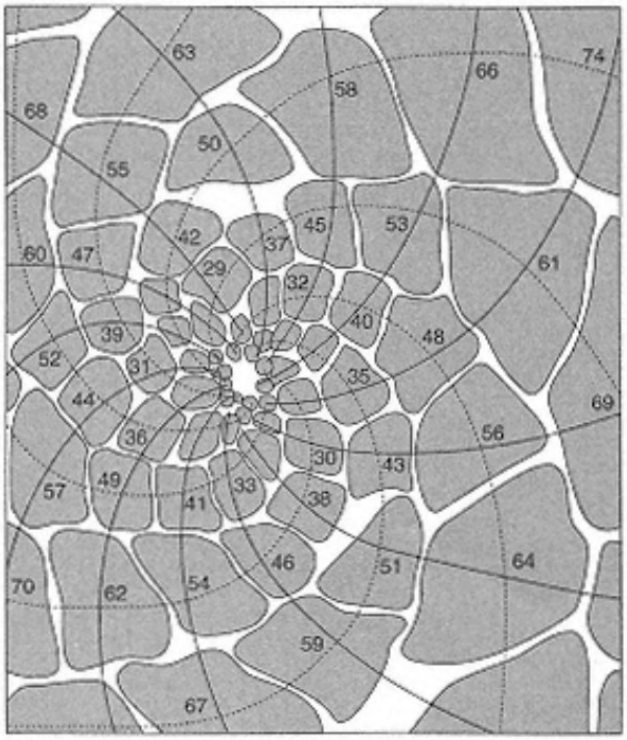

***Figure 2.19**. Diagram of a phyllotactic pattern demonstrating the arrangement of leaves or florets in a spiral configuration. The numbers indicate the sequential order of leaf placement, showing the typical 137.5° divergence angle* [14].

These pairs of numbers are not fixed and can vary, with common examples being 5 and 8 or 3 and 5. These pairs are reminiscent of the Fibonacci sequence, an infinite series of natural numbers defined as follows:

$$f_0 = 0 \tag{7}$$

$$f_1 = 1 \tag{8}$$

$$f_n = f_{n-1} + f_{n-2} \tag{9}$$

This sequence generates numbers such as 0, 1, 1, 2, 3, 5, 8, 13, 21, 34, etc., encompassing the pairs mentioned earlier, like (3, 5), (5, 8), and (8, 13). Plant phyllotaxis typically adheres to this sequence. Furthermore, the ratio of successive Fibonacci numbers converges to a constant value, the Golden Ratio (approximately 0.618034). For instance, 8/13 ≈ 0.615 and 21/13 ≈ 0.619, gradually approaching the Golden Ratio. Known since ancient Greece, this ratio was believed to create aesthetically pleasing proportions and was widely used in architecture and art.

The Golden Ratio is prevalent in many natural spirals, such as the logarithmic spiral introduced at the start of this chapter. Now, with the Fibonacci sequence and Golden Ratio in mind, one can see their application in various natural forms, from the spirals of animal horns and tails to the shells of mollusks and, of course, in plant phyllotaxis.

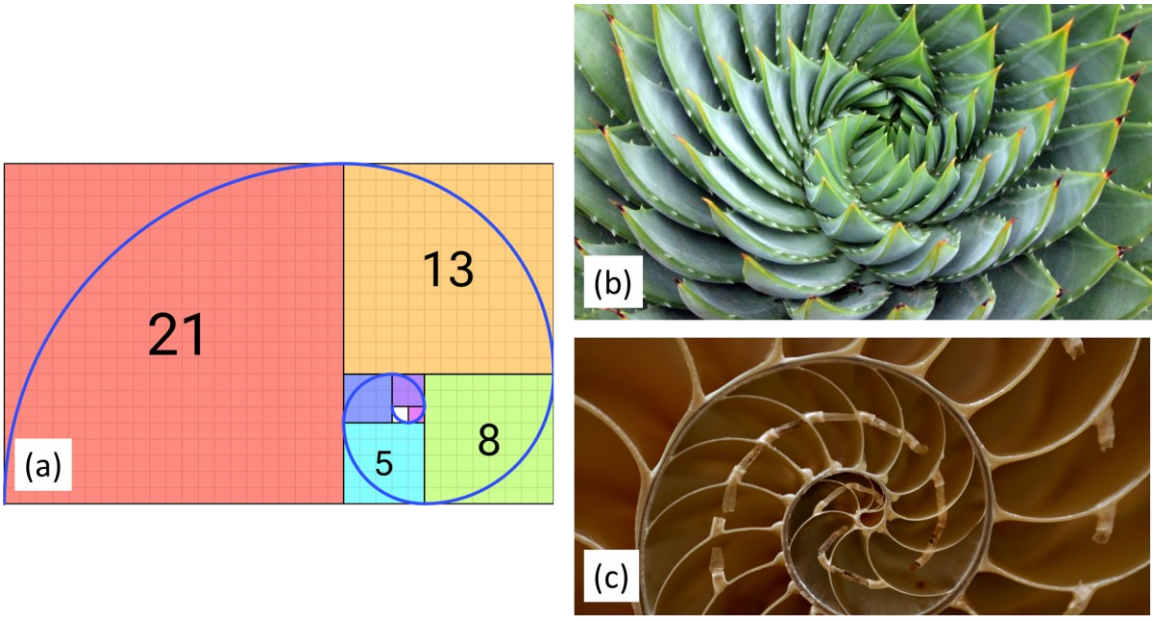

***Figure 2.20**. Examples of the Fibonacci sequence in nature: a Fibonacci spiral diagram* [32] *(**a**), a spiral arrangement of leaves in an aloe plant* [33] *(**b**), and the spiral pattern of a nautilus shell* [34] *(**c**).*

The previous section discussed phyllotaxis in terms of angles and leaf arrangement. To link this with the Fibonacci sequence and Golden Ratio, consider dividing a circle such that the ratio of the larger arc's perimeter to the smaller arc's perimeter equals the ratio of the circle's total perimeter to the larger arc. This ratio is the Golden Ratio, resulting in an angle close to 137.5°. This angle is commonly observed in the arrangement of leaves, petals, and seeds in many plants, demonstrating a remarkable consistency with the Fibonacci sequence and the Golden Ratio. This interplay of mathematics and biology not only illustrates the harmony of natural patterns but also underscores the universal presence of these mathematical principles in the natural world.

This review of patterns found in nature reveals that many natural forms share underlying mechanisms and common parameters. Such a discovery suggests the existence of a 'unified theory' that could explain the emergence of patterns in the natural world. Understanding these forms and their creation processes is crucial, and this summary illustrates that natural selection operates within a more limited spectrum of possibilities than one might initially think. It's not so much a black box of infinite possibilities, but rather a set of well-defined patterns and processes.

Exploration of these patterns demonstrates that numerous natural phenomena, from the formation of spirals in galaxies to growth patterns in plants, adhere to universal mathematical and physical principles. For instance, the Fibonacci sequence and the Golden Ratio are found across a wide range of natural contexts, providing a foundation for pattern formation. Similarly, reaction-diffusion systems described by Alan Turing show how simple chemical interactions can lead to complex morphological formations in living organisms.

This understanding not only deepens appreciation for nature but also has practical applications. Inspirating from nature, for example, using patterns and strategies found in nature, can lead to

the development of new technologies and materials. Principles of natural pattern formation can also inform sustainable design and architecture, offering innovative solutions to modern challenges.

Subsequent sections will explore how this knowledge can be applied in various fields, ranging from engineering and design to environmental science. By understanding patterns in nature, the secrets of the natural world are deciphered, and new ways of thinking and problem-solving in the human realm are opened up.

2.1.2 Nature mimicking

There are several concepts that capture the essence of drawing inspiration from nature for human design, each with its nuanced interpretation. The term "Biomimetics," introduced by [35], focuses on replicating principles observed in nature for technical solutions, primarily aimed at enhancing existing designs. "Biomimicry," coined by [36], shares a similar philosophy with biomimetics but places greater emphasis on environmental sustainability.

"Bio-inspired designs" refer to the practice of developing products inspired by nature without directly copying natural elements. This approach seeks to integrate natural inspiration with technical enhancements, aiming to improve product performance by incorporating nature-influenced features [37]. "Bionics," as defined by Steele in 1960, originally aligned closely with bio-inspired design, drawing inspiration from biological systems for technical applications without direct mimicry. However, in modern usage, particularly in the English-speaking world, "bionics" is often associated with advanced prosthetics and robotics.

All these concepts revolve around the central theme of using nature as a blueprint for technical solutions. The goal of this work is to harness the power of imitating nature to enhance technical solutions, whether through direct replication or inspired adaptation

Drawing inspiration from nature for the design and improvement of human-used products is not a novel concept. Throughout history, there have been numerous instances where human designers have turned to natural examples for innovative solutions. A prominent figure in this regard was the Italian engineer Leonardo da Vinci, who, fascinated by the flight of birds, envisioned a machine capable of flying by flapping its wings, an early example of bionics. Additionally, there have been various historical examples like Baker's 16th-century ship hull design inspired by fish bodies, or the winglets on airplane wings proposed by Rechtenberg in 1973, based on bird flight [38]. Everyday examples include the invention of Velcro and the application of ant colony behaviors to traffic management and computing.

Incorporating nature's designs into human engineering has proven beneficial for several reasons. Nature, through millions of years of evolution, has optimized various systems and structures for efficiency, resilience, and sustainability. By observing and mimicking these systems, human engineering can leapfrog in innovation, bypassing extensive trial-and-error processes. This approach is particularly advantageous in solving complex engineering problems where traditional

methods fall short. For instance, the streamlined shape of a fish has inspired more efficient aquatic and aerial vehicle designs, and the study of bird flight has led to significant advancements in aerodynamics.

Moreover, bio-inspired engineering often leads to more sustainable and environmentally friendly solutions. Nature's designs are inherently resource-efficient and well-adapted to their environments, offering a blueprint for sustainable innovation. By emulating these designs, engineers can create products that are both effective and ecologically sound.

2.2 Bioinspiration in engineering design

2.2.1 Engineering design, manufacturing and validation process

The traditional methods of engineering design and manufacturing, along with the products derived from these methods, are increasingly becoming obsolete. Traditional design approaches often fall short due to their reliance on the designer's experience rather than the intended function of the product. This leads to products being overengineered, containing more material than necessary, and consequently being heavier than required. Additionally, basing designs on a designer's experience may introduce operational deficiencies. These may not be critical initially but can contribute to the product's long-term obsolescence.

One fundamental issue with traditional design methodologies is their iterative nature, as illustrated in **Figure 2.21**. This process often fails to fully consider subsequent stages, leading to frequent revisits to the starting point, increased production time, and unnecessary waste generation. Although there are several ways to illustrate the conventional design process [39], the most accurate for this case is the one shown in [40], although the version in [41] is not too far from the latter.

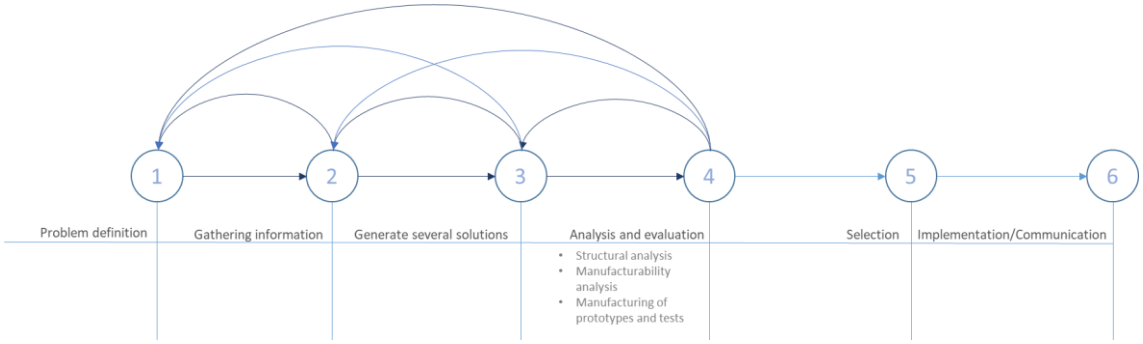

***Figure 2.21**. Iterative process of traditional engineering design and manufacturing, illustrating the stages from problem definition (1) to implementation/commercialization (6).*

1) **Problem definition**: This stage involves clearly identifying the problem that needs to be solved. It includes understanding the needs of the client or market, technical and economic constraints, and the objectives of the project. Accurately defining the problem is essential to guide the entire design process.

2) **Gathering information**: Here, the engineer collects all relevant information pertaining to the problem. This might include existing data, studies of previous cases, industry standards and regulations, and any other resources that can provide context and background for the design.
3) **Generate several solutions**: In this phase, multiple potential solutions are explored and developed. Creativity and innovation are encouraged, often using brainstorming techniques or design thinking. The goal is to generate a wide range of ideas, without critically evaluating them at this stage.
4) **Analysis and evaluation**: this stage can be divided into several sub-stages;
    a. Structural analysis: The strength, stability, and durability of the designed components or structures are evaluated. This may involve using simulation and modeling software to predict how the designs will behave under various conditions.
    b. Manufacturability study: This analysis determines how feasible it is to manufacture the proposed design in terms of costs, available resources, and manufacturing techniques. This might require consulting with manufacturing experts or conducting a cost analysis.
    c. Manufacturing of prototypes and tests: Developing physical or virtual prototypes to test the proposed solutions. This includes defining the validation procedure, conducting tests to validate the functionality, safety, and performance of the design.
5) **Selection**: Based on the results of the analysis and evaluation stage, the most appropriate solution is chosen. This decision is made by considering various factors such as costs, efficiency, feasibility, and compliance with client requirements.
6) **Implementation/Communication**: The selected solution is implemented. This may involve preparing detailed documentation, engineering drawings, and communicating with production or construction teams. Additionally, it is crucial to effectively communicate the design details to all stakeholders, including clients, marketing teams, and manufacturing or construction personnel.

This process, as illustrated in the image, is iterative and thus lengthy and costly. Indeed, relying on their experience, designers create an initial design, which sometimes progresses to digital validation. This may require returning to the geometry construction stage, and the same applies to subsequent stages of manufacturing process simulation, actual manufacturing, and final validation.

Traditional engineering manufacturing methods often employ subtractive processes, meaning they start with a larger amount of material and then remove material to achieve the desired shape. This is the case with machining processes, for example. The problems with these methods include material waste and the need for coolants and lubricants, which hinder material reuse and contribute to pollution. Additionally, the shapes that can be obtained are limited.

As a result, products derived from this production process have several deficiencies. They are often not specifically designed for their function, leading to being oversized. In some cases, products are conceived in such a way that the potential to combine several elements of a set into a single product is overlooked. Material selection is based on experience, so it is not fully

optimized for the product's lifecycle. Often, the design does not consider the reuse or recycling of the product, leading to more limited end-of-life options and complex disposal. Not to mention, the time and cost of producing these elements can often be prohibitive due to the iterative nature of the process.

A possible solution to these issues is a paradigm shift in the production process of engineering components. Observing nature, the production process is encoded in the DNA of living beings, where evolution has dictated how to construct various structures based on environmental conditions (limited by the physical-chemical phenomena that direct them), the survival mechanisms needed by the species, and all with the necessary amount of material and just enough to perpetuate the species.

As has been demonstrated, there are sufficient examples to believe that nature can be a great model to emulate. This leads to proposing a paradigm shift in the productive process of engineering components. An ideal design and manufacturing process for engineering components would be holistic, where each piece is specifically conceived and executed to meet the operational requirements, designed to be manufactured in a specific way and with the appropriate material. Similarly, the products of this process should be as minimally oversized as possible, use the necessary amount of material only in strictly necessary areas, have the ability to adapt throughout their useful life to new conditions, and at the end of their life, integrate into the environment so that the material can be used to build new products. This approach resembles the design and production method encoded in the DNA of living beings, essentially mimicking the natural process for generating components at another level.

Therefore, the method of design and production of engineering components based on the construction process encoded in the DNA of living beings can be as illustrated in **Figure 2.22**. It is defined with the following points:

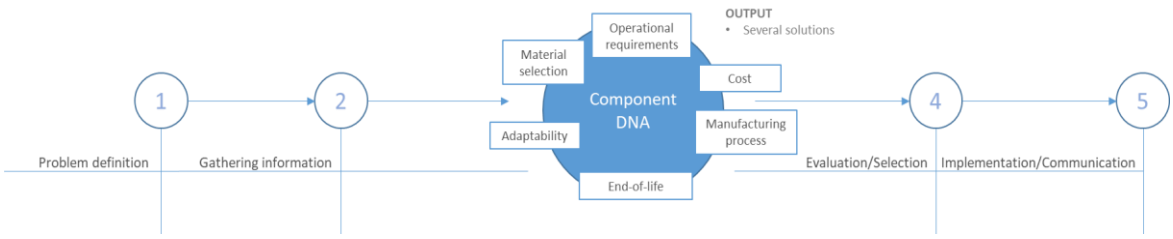

***Figure 2.22**. The engineering component design and production method based on the DNA-encoded construction processes of living beings*

1) **Problem definition**: This stage involves clearly identifying the problem that needs to be solved. It includes understanding the needs of the client or market, technical and economic constraints, and the objectives of the project. Accurately defining the problem is essential to guide the entire design process.
2) **Gathering information**: Here, the engineer collects all relevant information pertaining to the problem. This might include existing data, studies of previous cases, industry

standards and regulations, and any other resources that can provide context and background for the design.

3) **Component DNA**: is a core segment of the design and production process, where the essence of the component is conceptualized and defined. This stage is crucial as it sets the foundation for the component's entire lifecycle, from creation to eventual disposal or repurposing. Here, the various critical aspects:
    a. Material Selection: Choose or design materials based on their properties, sustainability, cost, and compatibility with the product's intended use.
    b. Operational Requirements: Define the operational environment and conditions under which the component will function, including loads, environmental conditions, design envelope and maintenance.
    c. Cost Analysis: Evaluate the cost implications of the design, including material costs, manufacturing expenses, and long-term maintenance.
    d. Manufacturing Process: Determine the most efficient and effective manufacturing process, considering factors like production volume, technology availability, and quality control.
    e. End of Life Considerations: Plan for the component's end of life, focusing on environmental responsibility. This includes strategies for recycling, repurposing, or safe disposal, ensuring the component's lifecycle is as sustainable as possible.
    f. Adaptability Over Lifecycle: Ensure the design can adapt to changing conditions, potential upgrades, or varied uses throughout its lifecycle.
4) **Evaluation/Selection**: Analyze and validate the potential solutions with all the information accumulated in the previous stages, and select the best one based on efficiency, effectiveness, and feasibility.
5) **Implementation/Communication:** The selected solution is implemented. This may involve preparing detailed documentation, engineering drawings, and communicating with production or construction teams. Additionally, it is crucial to effectively communicate the design details to all stakeholders, including clients, marketing teams, and manufacturing or construction personnel.

This ideal process, until now unachievable, is now within reach in the short term, thanks to concepts like generative design and the use of artificial intelligence (AI). Generative design already encompasses the automatic generation of solutions, albeit in a nascent form, covering areas such as cost analysis, manufacturing methods, and operational requirements [42]. The aspect of material selection has been explored in [43], highlighting its importance for both component performance and sustainability. A key step towards achieving a holistic process may involve revisiting the design of materials tailored for specific applications [44]. The study of a component's end-of-life is increasingly relevant due to the scarcity of raw materials and the climate crisis, as seen in [45]. The adaptability of a component throughout its lifecycle requires mechanisms currently in the process of implementation, such as programmed damage and repair [46], reactive element approaches [47], shape-memory alloys [Coupling Shape-Memory Alloy and Embedded Informatics toward a Metallic Self-Healing Material], and Metal Matrix Composites (MMC) [48].

The key would be to find a holistic design capable of encompassing all the mentioned aspects. This way, it would radically change the way engineering components are currently produced, leading to reduced costs, material waste, environmental impact, and iterative processes.

2.2.2 Bioinspired design approaches

It is commonly believed that shapes consisting of curves and rounded vertices are considered organic or bioinspired forms. While this is not entirely incorrect, it's important to note that generally, these forms do not have direct biological or natural input. Similarly, designs intended for biological use, such as prosthetics, might be considered bioinspired due to their role. This concept applies to countless examples of various origins. To classify these, the following will explain each form of imitation of nature in product design.

For bioinspired products, there are two approaches to design: those that go from biology to design, also known as solution-driven, and those that go from design to biology, or problem-driven. In the first approach, the designer is inspired by a biological element and applies it to their design idea. In the second approach, there is a specific problem, and a solution is sought in nature [36, 49, 50].

However, when executing bioinspired design in these components, there is another classification based on how nature is to be imitated. According to [51], there are four types of imitation, but for the purposes of this discussion and in light of the aforementioned, they will be referred to differently, yet essentially, they remain the same. These are: True Bioinspiration of Natural Form, Customized and Freeform Design, Simulation-Driven Design, and Cellular and Lattice Design. Additionally, it is suggested here to include Eco-Design as a fifth approach. These approaches are not mutually exclusive; more than one can be used in a single design logically. However, it is thought useful to develop each one in more detail due to their diverse nature.

True bioinspiration of natural form

True bioinspiration of natural forms is based on the direct and intentional imitation of structures that serve specific functionalities in nature for the design of engineering components. As seen in previous sections, natural structures have been optimized over generations to fulfill specific functions, minimizing the amount of energy and material needed for construction, while simultaneously adapting to their environment. Although the materials commonly used in nature are generally not metals, the structural functions of these forms can be extrapolated to components made of other materials, such as metals. For instance, in [52], examples of studies on biological forms and their potential for solutions with specific physical characteristics, including mechanical, thermal, electrical, and acoustic requirements, are presented.

It's also important to note that many natural structures are multifunctional. For example, osteoderms – thin bone plates in the skin that serve as natural armor for some living beings – have a defensive role and may be optimized for thermoregulation at the same time [53]. Therefore, it's crucial to consider the various functions that a biological feature may have before applying it to engineering products.

This approach can be applied across different scales. Biological materials are not characterized by exceptional mechanical properties per se. However, due to certain microarchitectures

categorized as fibrous, helical, gradient, layered, tubular, cellular, suture, and overlapping [54], these materials can achieve mechanical properties that are unattainable for traditional industrial materials. These microarchitectures can be replicated in industrially used materials to study their benefits, as discussed in [55].

Customized and freeform design

Advanced manufacturing methods, such as additive manufacturing, advanced casting techniques, and multi-axis machining, have rendered traditional CAD tools, originally designed for creating forms with vertices and straight lines, more flexible. This has led to the emergence of computational design tools that enable more organic shapes using T-splines and B-splines (polyNURBS). These tools have also propelled methods of topology optimization and the direct imitations discussed in the previous section, thanks to their design flexibility.

This bioinspiration approach can be utilized in various cases. One of the most obvious applications is the customization of implants for specific patients using images or 3D scans of the implant in question [56]. This technique has been applied in fields ranging from medical devices to personalized healthcare solutions, where individual anatomical differences are critical in implant design and fabrication.

Additionally, this approach has been employed in areas such as art, fashion, and jewelry [57], where the ability to create intricate and organic designs is highly valued. In the sports industry, examples include Adidas Futurecraft [58], where footwear is designed for optimal performance and comfort, and in the design of NFL helmets [59], where safety and aerodynamics are key considerations.

Simulation-driven bioinspired design

This bioinspired design approach primarily focuses on optimizing components based on certain constraints and objectives. In other words, for a given load case, the optimal material distribution is determined through an iterative process to minimize material use and enhance specific functionalities of the component. This method is also known as topology optimization, which is a part of structural optimization. This stage-wise optimization process is akin to most evolutionary processes in nature, and the removal of material in low-stress areas mirrors strategies used in natural systems, hence the motivation to categorize this process as bioinspired [51]. However, beyond structural optimization, a classic method in engineering, other more modern design methods have emerged, such as generative design, parametric design, and field-driven design. While these concepts are similar, they have their own unique characteristics.

Structural optimization

The structural optimization problem is centered on selecting optimal values for design variables to minimize a specified objective function while satisfying a set of predetermined constraints, as outlined in [60]. Consistent with the principles detailed in [61], structural optimization aims to

determine the optimal material distribution within a given volume or domain. This distribution must safely transmit or support applied load conditions. To achieve this, various objective functions are considered, including increasing stiffness, reducing stress, minimizing deformation, altering natural frequencies, and enhancing buckling strength.

In general terms, structural optimization is a method used to determine the optimal material distribution in a linear elastic structure to meet specific boundary conditions. As previously discussed in this chapter, a significant issue with current engineering components is that they are often overdesigned and inefficient. Structural optimization of these components can achieve key objectives such as:

- **Reducing Weight**: Crucial for industries like aerospace and automotive, weight reduction can lead to decreased consumption of propulsion resources, whether electricity or fuel/oxidizers.
- **Minimizing Material Use**: By reducing the amount of material required for construction, the demand for raw material extraction is lowered, thereby facilitating the use of these materials for other components.
- **Improving Performance**: When optimized for one or more objective functions, a component can enhance various performance aspects, such as strength-to-weight ratio, durability, stiffness, or vibration resistance.

Structural optimization methods can be classified into three distinct types:

1- **Size Optimization:** In this approach, the design domain of the structure is known and fixed, but optimization is sought through dimensioning. For example, selecting the optimal thickness for a beam or the ideal members for a truss structure.
2- **Shape Optimization:** This method aims to determine the optimal shape of the design domain, like the external shape of a beam or the design of holes to lighten it.
3- **Topology Optimization:** This type of optimization directly determines the material distribution within a defined design domain. It involves defining the number, shape, and location of holes or material-free areas, as well as the connectivity within the design space to effectively transfer applied loads.

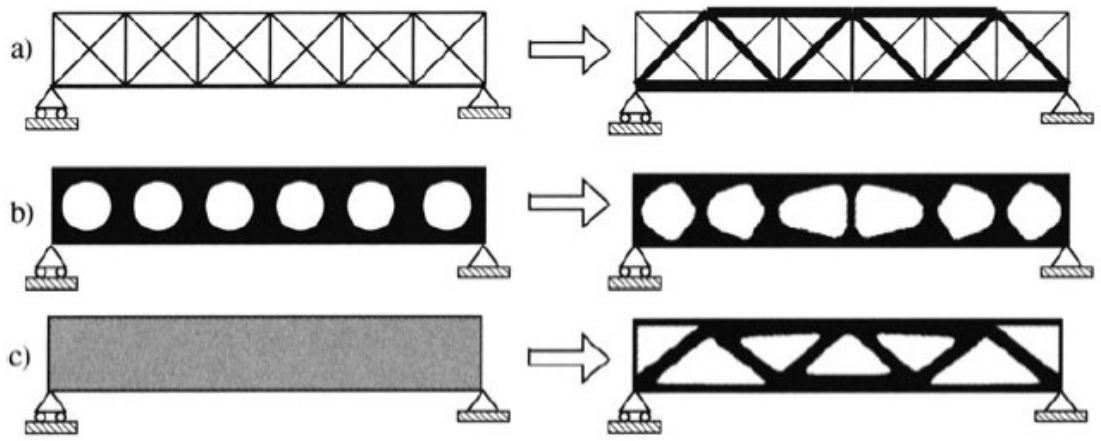

***Figure 2.23**. Types of structural optimization: (**a**) size optimization in a truss structure, (**b**) shape optimization, and (**c**) topology optimization* [62]*.*

Both size and shape optimization are highly valuable, particularly for redesigning existing structures. However, these methods are often limited by the pre-existing elements of the structure, such as beams, truss elements, or external shapes and holes. In contrast, topology optimization is only constrained by the defined design domain, allowing for the creation of material arrangement and connectivity (topology) that best suits objectives and constraints without the need for a pre-existing design.

Topology optimization is an iterative process best solved using numerical methods. The most efficient current approach is through Computer Aided Design (CAD) tools and the Finite Element Method (FEM). Therefore, defining the problem and its boundary conditions accurately is crucial, as is correctly defining the design space or domain and the discretization (meshing) applied to it.

The concept of topology optimization was first introduced in an article published in 1904 by Australian mechanical engineer Michell. Michell's work focused on the least-volume topology of trusses with a single condition and a stress constraint [63]. His significant contributions to topology optimization included the introduction of elements now known as layout optimization, continuum-type optimal criteria, adjoint strain field, and ground structure [64]. Approximately 70 years later, [65] extended Michell's theory from trusses to beam systems and introduced the first general theoretical background of topology optimization, termed 'optimal layout theory'. Since then, there has been a scientific revolution in this field, particularly over the last 30 years, with many groundbreaking articles. There are three main approaches to tackle the topology optimization problem: element-based solution approaches (density, topological derivatives, level set, phase field, etc.), discrete approaches (evolutionary-based algorithms), and combined approaches [66].

To better understand the method governing topology optimization, the design problem can be generally defined. The goal is to find a material distribution that minimizes an objective function F subject to a volume constraint $G_0 \leq 0$ and possibly other M constraints $G_i \leq 0, i = 1 \dots M$. The material distribution is described by the density variable $\rho(x)$ which can take the value 0 (void)

or 1 (solid material) at any point in the design space Ω. Hence, the mathematical problem can be formulated as:

$$\begin{cases} Min: F = F(u(\rho),\rho) = \int_{\Omega} f(u(\rho),\rho)dV \\ s.t.: G_0(\rho) = \int_{\Omega} f(u(\rho),\rho)dV - V_0 \leq 0 \\ \quad : G_i(u(\rho),\rho) \leq 0, j = 1,\dots,M \\ \quad : \rho(x) = 0 \; or \; 1, \forall x \in \Omega \end{cases} \tag{10}$$

Where the state field u satisfies the linear and nonlinear state equation [66]. This concept becomes clearer through a basic example. Suppose there is a two-dimensional beam fixed at one end with a force f applied at the other end. To conduct the study, it is necessary to discretize the space into elements. For illustration, as seen in **Figure 2.24** the beam is divided into square elements of equal size, dividing the space into 10x20 elements.

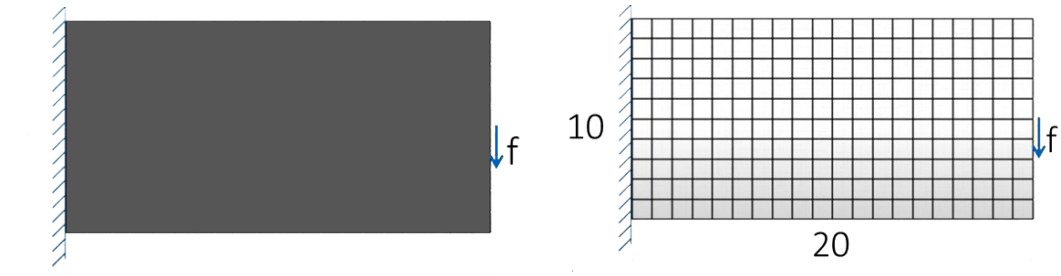

***Figure 2.24**. Discretization of a two-dimensional beam: a beam fixed at one end with a force applied at the other end (**left**). The beam is divided into 10x20 square elements of equal size for analysis (**right**).*

As previously mentioned, the goal of topology optimization is to obtain the optimal material distribution to fulfill the objective function. So, how does one choose this distribution if constrained to only 60 elements? Considering the possible combinations:

$$C(200,60) = \frac{200!}{60!\,(200-60)} = 7.04x10^{51} \tag{11}$$

It becomes apparent that finding the optimal distribution for this load case is not as straightforward as it might seem. If the interest, for example, is to maximize the beam's stiffness, the objective function can be defined as the elastic energy:

$$c = \frac{1}{2}U^T KU \tag{12}$$

Where c is the elastic energy, U is the displacement, and K is the stiffness matrix of the structure. When applying both the design variable of the element's density and the volume constraint of 60 blocks, it results, after several iterations, that the optimal result is as shown in the **Figure 2.25**.

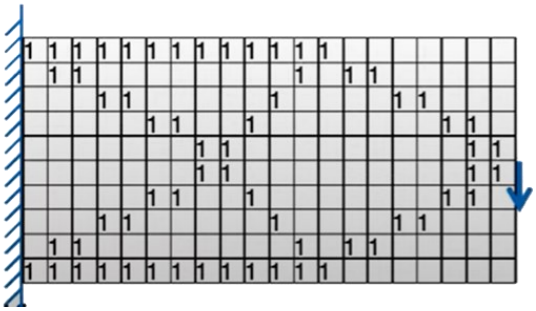

***Figure 2.25**. Optimal material distribution in a discretized beam with a fixed end and an applied force, using the design variable of element density and a volume constraint of 60 blocks.*

This example illustrates the purpose of topology optimization and also explains the general formulation of the problem. However, one of the challenges with this discretized optimization is that the density values only take 0 or 1, making it difficult to solve. Indeed, methods exist to resolve this, but the complexity increases exponentially as the number of elements grows to thousands or millions [66]. Nevertheless, as will be seen throughout this section, there are efficient ways to solve discrete methods in topology optimization.

The following will detail discretized topology optimization methods based on continuous design variables.

Density Approach Methods The density approach in topology optimization emerged after the introduction of the Homogenization approach by [67]. Bendsøe first introduced this approach in 1989, suggesting the Simplified Isotropic Material with Penalization (SIMP) method[68]. In SIMP, to facilitate the convergence of the homogenization method, a penalization exponent is applied to the density value [69]:

$$E(\rho i) = g(\rho i)E_0 = \rho i^p E_0, \quad g(\rho i) = \rho i^p \tag{13}$$

where p is the penalization parameter, and E_0 is the Young's modulus of the solid material. The penalization parameter controls the relationship between material density and Young's modulus. When $p = 1$ corresponding to the variable-thickness-sheet case, this value can lead to diffuse or "gray" zones, complicating clear results. With $p > 1$ discretized or "black and white" zones are favored, yielding clearer solutions, typically with $p = 3$ and an acceptable number of iterations. However, as p increases, the problem may converge too quickly, potentially causing issues [69].

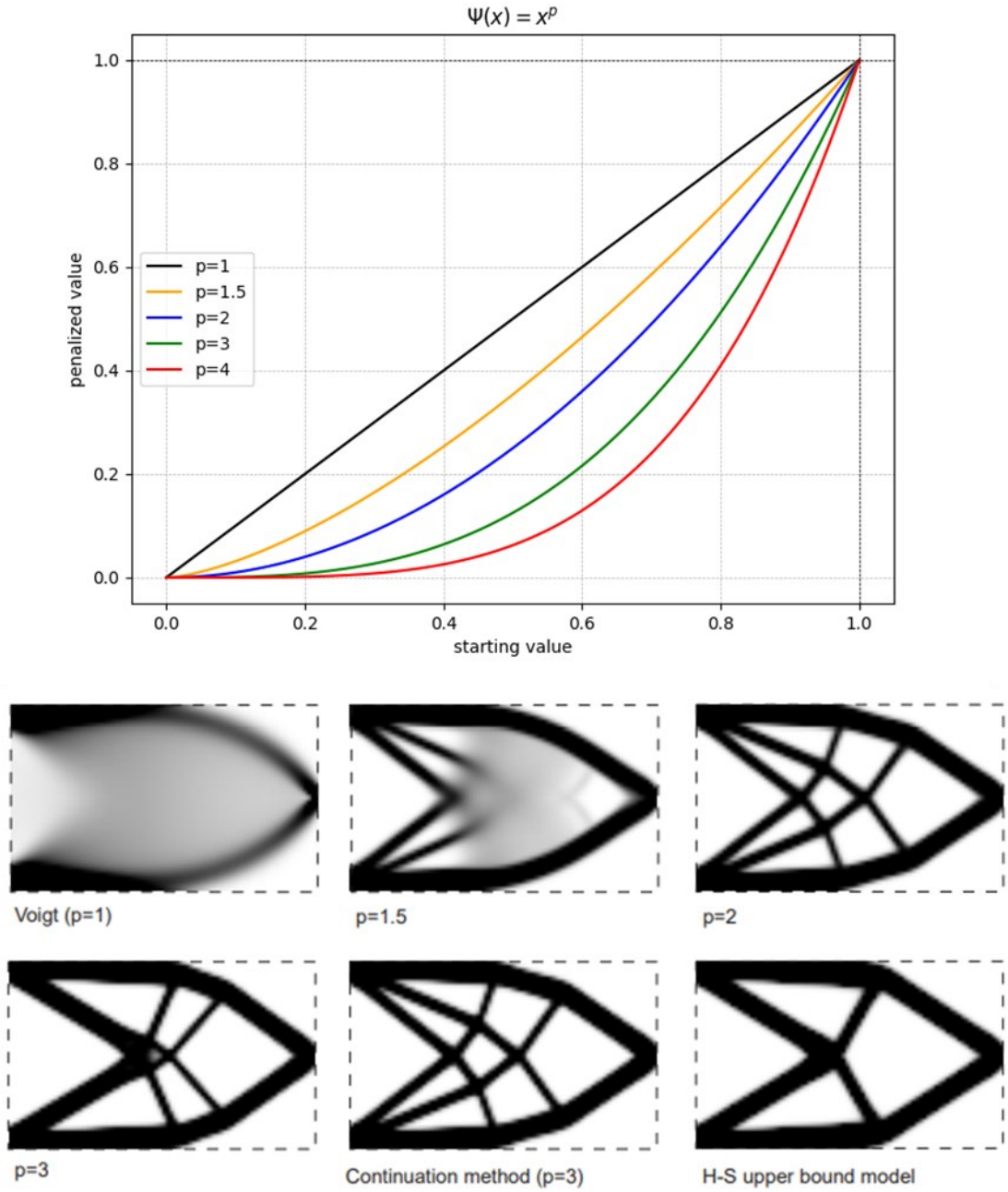

***Figure 2.26**. Optimal design results for material and void using various powers p in the SIMP interpolation scheme, and using the Hashin-Shtrikman upper bound. The graph above shows the penalized value as a function of the starting value for different p values* [69].

The SIMP method is one of the most implemented and mathematically studied methods (State of the Art of Generative Design and Topology Optimization and Potential Research Needs). The SIMP approach was further complemented by the RAMP (Rational Approximation of Material Properties) approach, introduced to address some limitations of SIMP. Unlike SIMP, RAMP maintains a nonzero gradient when the density $\rho i = 0$, potentially influencing convergence properties and addressing issues in dynamic problems [70].

Topological Derivatives concept was first introduced by [71] and focuses on predicting the impact of introducing infinitesimal holes at any point in the design domain, acting as a driver for generating new holes. This approach requires the use of complex mathematics and can be effective in determining the optimal placement of necessary holes in a structure. As demonstrated in [72], this method validates the optimal parameters of p presented by [69].

In the **level set approach**, the boundary of the design is defined by the zero-level contour of the level set function $\Phi(\mathrm{x})$ Therefore, the structure is defined within the domain where the level set function takes positive values [73–75]. This is represented as:

$$\rho = \begin{cases} 0 : \forall x \in \Omega : \Phi < 0 \\ 1 : \forall x \in \Omega : \Phi \geq 0 \end{cases} \tag{14}$$

This approach dictates that anything falling below the level set function will be removed from the material of the structure.

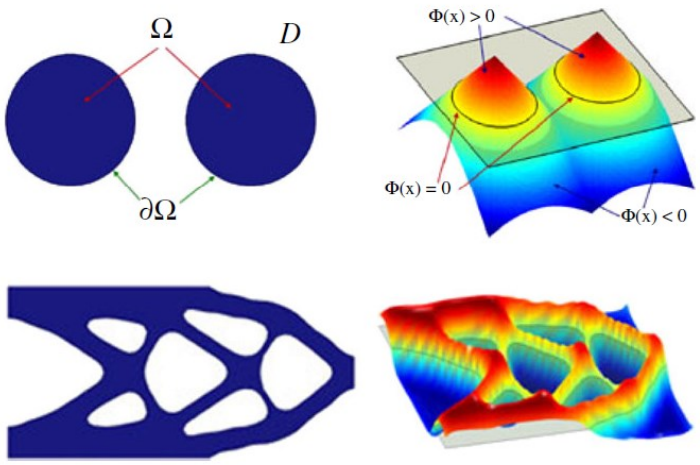

***Figure 2.27**. Level set representations: (a) 2D topology, (b) corresponding level set function, and more complex representations of benchmark structures (c) and (d)* [76].

The level set function is most often updated via the Hamilton-Jacobi equation. This equation uses a speed function or velocity field, V , to evolve the level set function. The speed function represents the sensitivity of moving the interface in the normal direction with respect to a merit function, scaled by the spatial gradient of the level set function.

In the **Discrete Approach in Topology Optimization**, the design variables that typically define the presence or absence of material are considered discretely. This means the design variables are binary – the material density is either 0 or 1, eliminating "gray" areas that are characteristic of the density approach.

Directly formulating the problem with discrete design variables makes it challenging to solve. In fact, only a few small problems have been solved to global optimality [77]. The suitability of using methods based on sensitivity analysis as well as nature-inspired methods such as genetic

algorithms, insect colony algorithms, or differential evolutionary techniques has been discussed. However, it has been shown that these are not useful for a majority of topology optimization problems [78, 79].

An important branch of discrete approaches in topology optimization is the evolutionary optimization methods. Evolutionary Structural Optimization (ESO) and Bi-directional Evolutionary Structural Optimization (BESO) represent significant strands within discrete approaches in topology optimization. These methods have evolved from simple hard-kill strategies to more sophisticated schemes employing gradient analysis and filtering techniques [80–82].

A challenge with ESO and BESO approaches is the lack of algorithmic convergence and the appropriate selection of stopping criteria. In fact, the review [66] suggests reconsidering BESO methods as "discrete density approaches" or "discrete SIMP approaches." This reclassification aligns with the understanding that these methods, while discrete, still operate on principles similar to those of density-based optimization, albeit with binary rather than continuous variables. This rethinking highlights the ongoing development and refinement in the field of topology optimization, where approaches are continuously evolving to address complex design challenges more effectively.

Lagrangian approaches y combined shape and topology optimization. As discussed in the previous sections, there are structural optimization methods that combine topology optimization with size and shape optimization. However, few methods address the problem holistically. Notable approaches in combined topology optimization include the extended Finite Element Method (xFEM) [83] and the Deformable Simplicial Complex (DSC) [84]. The xFEM aims to introduce a generalized and adaptive finite element scheme capable of working with meshes that accurately represent smooth boundaries. Meanwhile, the DSC scheme combines non-parametric shape optimization approaches with the flexibility to introduce and eliminate holes.

The resurgence of Lagrangian approaches in topology optimization requires more research to understand their pros and cons compared to non-parametric shape optimization methods and level set methods. These methods confront challenges due to the discontinuous nature of topological changes in mechanical models. While topological changes are non-differentiable in Lagrangian methods, they are continuous and differentiable in Eulerian methods like SIMP and level set methods using surrogate material concepts. Identifying specific contexts where Lagrangian methods surpass Eulerian approaches is a crucial area for future research.

There are numerous approaches to topology optimization, but the ones discussed here are among the most significant to date. The following table provides a concise summary of these methods, highlighting their strengths, weaknesses, and key reference articles:

***Table 2-2**. Comparison of various topology optimization methods, including their approaches, strengths, and weaknesses.*

Approach				Strengths	Weaknesses	References
CATEGORY	**DISCRETE MESH & CONTINOUS VARIABLES**	**DENSITY-BASED**	Solid Isotropic Microstructures with penalization (SIMP)	Simple implementation, effective for a wide range of problems.	Can lead to intermediate density solutions, "Grey" areas.	[69]
			Rational Approximation of Material Properties (RAMP)	Alleviates non-concavity of SIMP interpolation, ensuring convergence to 0-1 solutions	Non-zero gradient for zero density can affect convergence properties	[70]
		Topological derivatives		Predicts the influence of introducing infinitesimal holes, useful for generating new holes	Complex mathematics, less effective for finite-sized holes	[71]
		Level set		Clear definition of solid-void interface, suited for stochastic shape variations	Challenged by discontinuous topology changes, complex implementation	[73]
	DISCRETE VARIA	Evolutionary structural Optimization (ESO)		Intuitive, simple hard-kill strategies for material removal	Limited by only making discrete updates, may fail in certain scenarios	[80, 81]

		Bidirectional Evolutionary Structural Optimization (BESO)	Extension of ESO, allows material reintroduction, employs gradient analysis	Algorithmic convergence issues, lack of generality for multiple constraints	[82]
	COMBINED SHAPE & TOPOLOGY	Extended Finite Element Method (xFEM)	Overcomes need for extensive re-meshing, represents smooth boundaries	Can be computationally expensive, complex implementation	[83]
		Deformable Simplicial Complex (DSC)	Combines non-parametric shape optimization with hole introduction/removal	full potential and limitations yet to be explored	[84]

Generative Design

Topology optimization has been a focus of research for some time. Recently, however, a new concept known as generative design has emerged. This concept is somewhat ambiguous and varies depending on the definition. In the context of engineering component optimization, generative design can be described as the process of using algorithms to explore design variations beyond what is currently possible with traditional design methods [85]. This can be achieved through various computational methods, such as topology optimization [86], cellular automata [87], genetic algorithms [88], or artificial intelligence systems [89].

Today, generative design is often understood as an advanced form of topology optimization that incorporates manufacturing constraints, production costs, and structural safety factors [42]. This understanding is largely driven by commercial design tools that promote this type of design. For instance, the ASSESS Initiative, a multi-industry organization whose objective is to bring together key players to guide and influence software tool strategies for performing model-based analysis, simulation, and systems engineering, defined generative design as "a tool that uses algorithmic methods to generate feasible designs or outcomes from a set of performance objectives, performance constraints, and design space for specified use cases" [90]. In fact, This organization, backed by NAFEMS (International Association for the Engineering Modelling, Analysis and Simulation Community) defined 15 key points to rate generative design tools with the specific requirements each software item must accomplish to reach a rating of from 1 to 5, avoiding the subjectivity of this qualification.

Parametric design and field driven design

Parametric design in engineering refers to a design approach where the design is defined using parameters and rules. These parameters can be adjusted to manipulate the outcome of the design. This approach is often used in conjunction with computer-aided design (CAD) tools, allowing engineers to quickly explore a wide range of design alternatives and optimize the design based on specific criteria.

In the context of engineering part design, parametric design can be applied to various fields, including mechanical, civil, and electrical engineering. For instance, it can be used to design complex gear systems, where the gear parameters are defined and manipulated to achieve optimal performance[91]. In the field of civil engineering, parametric design can be used to optimize the design of structures like bridges, where the geometry and material selection can be adjusted to achieve a balance between aesthetic appeal, structural integrity, and buildability[92]. It is also widely used for prosthetic design [93].

https://www.ncbi.nlm.nih.gov/pmc/articles/PMC6342901/This could also be linked with the Freeform and customized design approach.

Field driven design is a design approach in engineering that focuses on optimizing the performance of a part or system by considering the distribution of physical fields, such as stress,

temperature, or magnetic fields, during the design process. This approach can be applied to various engineering disciplines, including mechanical, electrical, and thermal engineering.

Applications of field driven design can be found in a wide range of industries, such as automotive, aerospace, electronics, and energy. Some examples include:

1. Designing lightweight structures for automotive and aerospace applications, where minimizing weight while maintaining structural integrity is crucial. Field driven design can help optimize the distribution of material to reduce weight and improve performance.

2. Designing heat sinks and cooling systems for electronic devices, where efficient heat dissipation is essential for reliable operation. Field driven design can help optimize the geometry and material selection to maximize heat transfer and minimize thermal resistance.

3. Designing magnetic components, such as transformers and inductors, where the magnetic field distribution is critical for efficient energy conversion. Field driven design can help optimize the core shape, winding arrangement, and material selection to minimize losses and improve efficiency.

Artificial intelligence for engineering design

Artificial Intelligence (AI) is revolutionizing the field of engineering structure design, particularly in structural optimization. The examined article offers a detailed insight into the current advancements and future expectations in this exciting domain [94].

Presently, Deep Generative Models (DGMs), encompassing neural networks, Generative Adversarial Networks (GANs), Variational Autoencoders (VAEs), and reinforcement learning, are playing a pivotal role. These models have found promising applications in topology optimization, where they are used to predict optimized topologies, enhance computational efficiency, and explore new designs [95, 96]. This approach has been successfully applied in areas such as solid mechanics, fluid dynamics, additive manufacturing, and heat transfer.

Additionally, DGMs are being used for the design of microstructures, nanostructures, and metamaterials. These models are assisting in the reconstruction of microstructural images and the inverse design of materials, crucial for applications in fields like photonics and phononics [97, 98].

However, the use of AI in structural design is not without challenges. Performance evaluation of designs, data scarcity, and the creativity gap are significant obstacles. Particularly, the tendency of models to mimic training data rather than generating novel designs is a concern that needs to be addressed.

Looking forward, there are high expectations for improvement in several aspects. DGMs are expected to advance in assessing and optimizing the actual functional performance of designs. Overcoming data scarcity through improved machine learning techniques will allow for more

accurate and diverse design generation. Significant progress is also anticipated in the models' ability to generate innovative and creative designs, overcoming the current tendency to replicate existing designs.

Another area of future development is the integration of physical and manufacturing constraints into AI models, resulting in more practical and feasible designs. Additionally, increased collaboration between human designers and AI models is expected, where both can learn and benefit from each other. This collaboration promises to enhance the design process, blending human creativity and intuition with AI's computational power and data processing capabilities.

Cellular and lattice design

Humans have been utilizing cellular materials like wood, cork, and bamboo for several millennia before we understood the structural reasons for their intriguing behavior. This is detailed in [99]. Today, the design and origin of lattices are greatly influenced by mathematics and crystallography, as indicated in reference [100], and they also adhere to Maxwell's criterion of stability, primarily developed for large engineering structures, as indicated in reference [101]. The main advantage of cellular or lattice structures is their ability to achieve performance objectives while significantly reducing mass, a principle often observed in nature, as mentioned in reference [102]. Although cellular materials usually have lower effective stiffness and strength, this reduction is often acceptable and can be customized for specific applications or varied locally. Beyond mere weight reduction, lattices are valuable for other properties, such as thermal and acoustic characteristics, and their ability to absorb energy under compression loads, playing a vital protective role in nature. This is discussed in references [103] and [86]. Cellular materials are also crucial for the optimization of large-scale multifunctional designs, such as in aircraft wings, as mentioned in [104].

Eco-design

Eco-design is the field of design primarily dedicated to creating products with consideration for their environmental impact throughout their lifecycle. It's a key aspect to consider in future designs to reduce the environmental footprint. Eco-design can be considered a method of bioinspired design insofar as it is a way to recycle materials used in components and, like the cycle of life, tends to create products derived from other products. However, its origin is not inherently bioinspired.

The previously mentioned bioinspired design approaches can partly contribute to eco-design. Indeed, optimizing components for functionality helps reduce weight and the amount of material used. Manufacturing methods like additive manufacturing and casting aid in reducing the necessary material quantity.

In the field of engineering, eco-design has evolved significantly, ranging from academic research to large-scale commercial applications. An article published in "Design Science" by the University of Cambridge describes a methodological approach to eco-design that includes identifying case

studies and exploring key themes in eco-design, such as optimal resource use, life cycle management, and the integration of data and analysis. This approach is based on representative case studies from various industries and addresses concurrent environmental and economic issues [105].

Furthermore, a special edition of "Sustainability" on "Product Eco-Design in the Era of Circular Economy" explores eco-design methodologies geared towards the circular economy and life cycle engineering. The articles in this special edition undergo rigorous peer review and focus on innovative eco-design methodologies and practical applications in engineering. These include extended lifecycle strategies and effective management of closed-loop strategies, such as product reuse, remanufacturing, and recycling of materials [106].

2.3 Design for manufacturing

Design for Manufacturing (DfM) is a product design approach specifically aimed at making products easier and more cost-effective to manufacture. It involves designing products with the manufacturing process in mind to minimize complexity and costs while maximizing efficiency and quality. The goal of DfM is to simplify the manufacturing process by reducing material use, minimizing the number of parts, optimizing the use of standard components, and facilitating the assembly process. This can be achieved by taking into account design guidelines but also with CAM tools and based in simulation.

DfM is part of a broader set of design philosophy known as Design for X (DfX), where "X" can stand for any number of specific focuses such as assembly, testing, cost, environment, etc. In the context of DfM, the focus is on reducing overall production costs and ensuring that the product can be manufactured using standard industrial practices without requiring custom machinery or processes that would increase the cost and complexity of production.

The principles of DfM are applied during the early stages of product design to ensure that the product is optimized for the manufacturing process. This includes considerations such as selecting materials that are readily available and suitable for mass production, designing parts that can be easily fabricated using common manufacturing processes, and creating designs that are easy to assemble with minimal labor [107].

The methodology of Design for Manufacturing (DfM), when applied to advanced manufacturing methods, is pivotal in achieving the complex and intricate geometries characteristic of bioinspired components. In this context, two primary methods are considered advanced: various forms of casting, each with differing levels of flexibility and modernization, and additive manufacturing, which currently stands as the bastion of design freedom. In the following subsections a breakdown of these methodologies will be described.

2.3.1 Design for Casting

Metal casting is an ancient technique that has seen significant evolution over the course of history, adapting to the changing needs of industry and technology. Initially, casting was performed using simple methods, involving sand molds and molten metal. Over time, this technique was refined and diversified, allowing for the creation of metal parts with increasingly complex geometries.

In modern times, the manufacture of castings for metals with complex geometries faces certain design constraints. These limitations are primarily dictated by the mold's ability to capture fine details, the fluidity of the molten metal, and the feasibility of extracting the cast piece from the mold without causing damage. These factors compel designers to carefully consider tolerances, draft angles, and corner radii in their designs.

The most commonly used techniques today for casting complex geometries include die casting, sand casting, and investment casting or "lost wax" casting. Each of these techniques offers specific advantages. For instance, die casting is ideal for mass production of parts with tight tolerances and high-quality surface finishes. Sand casting, on the other hand, is more flexible in terms of part size and complexity but typically requires more post-processing. Investment casting is renowned for its ability to produce parts with extremely fine details and design complexity.

Furthermore, the introduction of digital technologies and additive manufacturing has revolutionized the field of casting, enabling the creation of molds and models with complexities previously unachievable. These technologies have not only expanded design capabilities but also reduced production times and increased the efficiency of the casting process.

As discussed above, DfM is an important process to obtain a good quality product, minimizing cost and process iterations. In this case, Design for Casting (DfC) is equally important. Design for Casting can involve various considerations, such as the shape and size of the part, the material being used, the type of casting process (e.g., die casting, sand casting, investment casting), and the characteristics of the casting equipment [108].

Achieving optimal quality in metal casting involves multiple critical aspects. The **melt** must be at the correct temperature, have minimal gas content, and be free from surface films. The **material** selection must be tailored for both functionality and fluidity within the mold. **Mold design** is crucial in facilitating and controlling the flow turbulence of the molten metal during filling. It must also ensure appropriate heat flow for the material and be airtight. The design of both the casting part and the **feeding and ventilation system** is vital to ensure proper flow of the molten metal, prevent isolated metal pools and defects due to shrinkage, reduce residual stress, and facilitate gas escape, thus avoiding voids and bubbles. Finally, **solidification** must be carefully managed, sometimes requiring uniform temperature throughout the system or controlled or forced cooling for specific results.

The design significantly impacts the quality, efficiency, and viability of the produced parts. A well-conceived design ensures not only the geometrical and functional precision of the final piece but also optimizes the casting process itself. Key aspects of a well-designed casting process include:

1. **Quality of the part:** A good design ensures that the cast part meets required specifications, minimizing defects like porosity, sand inclusions, distortions, and uneven contractions.
2. **Production efficiency:** An optimized design allows for efficient manufacturing, reducing material and energy wastage, and maximizing process yield.
3. **Cost-effectiveness:** By reducing defects and improving efficiency, an effective design decreases operational costs and enhances profitability.

Essential elements in a casting process include:

- **Mold:** Contains and shapes the molten metal and must be designed to withstand extreme temperatures and allow for appropriate contraction.
- **Feeding System**, including:
    - **Sprues:** Channels that lead the liquid metal from outside the mold to the cavity.
    - **Runners:** Connect sprues to the mold cavity.
    - **Risers:** Reservoirs of liquid metal that compensate for metal contraction during cooling and solidification.
- **Ventilation System:** Allows gas escape, preventing voids or bubbles.
- **Cores:** Used to form internal cavities or complex details that cannot be directly molded.

The design of these elements, traditionally based on the experience and practical knowledge of foundry workers, has evolved towards a more scientific and technological approach. The main things to have in mind are described below as explained in [109].

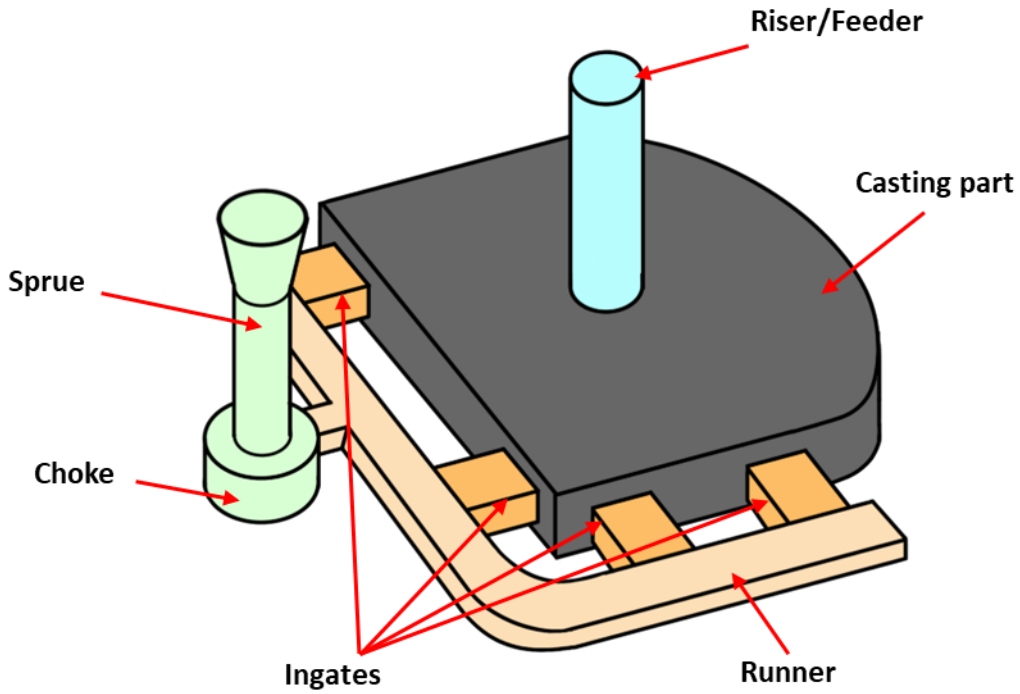

***Figure 2.28**. Schematic representation of casting elements.*

Sprue design

When designing the gating system in the casting process, several key aspects must be considered to ensure efficient and high-quality mold filling. These aspects include:

1. **Design of the pouring Basin**: A weir basin (pouring basin with a vertical step) is recommended. This design halts the horizontal flow of metal over the top of the sprue and prevents turbulence. Gating basins without a step are not advised as they can allow the metal to flow too quickly, leading to issues.

2. **Avoidance of Counterproductive Designs**: It is crucial to avoid sprue designs that could introduce turbulence or allow the entry of unwanted components such as air, dross, and slag into the mold. Simpler designs that prevent turbulence are generally recommended.

3. **Control of the sprue End**: The design of the choke should be such that it halts the downward vertical velocity of the metal. Older designs using a cup-shaped blind end were not useful as they allowed the metal to be expelled upwards and out of the basin.

4. **Surge Control Systems**: For advanced control, the runner can be extended at the base of a vertical circular cylinder, where the runner enters tangentially. This setup helps to regulate the pressure in the gating system and ensures proper filling of the lower part of the cast piece.

5. **Integrated Design with the Feeding System**: The gating design should be effectively integrated with the entire feeding system, including runners, feeders, and vents, to ensure consistent and complete filling of the mold.

Runners and ingates design

When designing runners (feeding channels) in the casting process, several key aspects must be considered to ensure efficient and high-quality mold filling:

1. **Balanced Design**: It is crucial to have a runner design that ensures an even delivery of molten metal to the mold. An unbalanced design can lead to uneven metal distribution, affecting the quality of the casting.

2. **Reduction of Cross-Sectional Area in the Runner**: When more than one gate is connected to the runner, it's necessary to reduce the cross-sectional area of the runner as it passes each gate. Traditionally, this has been done in a series of steps, known as a stepped runner design. For instance, for three gate entries, the cross-sectional area of the runner is reduced by one-third of the runner's height as it passes each gate.

3. **Use of Filters in Runners**: Filters with extruded or pressed straight holes can be effective when used tangentially in the runners. These filters can achieve comparable reliability in mechanical properties to well-placed ceramic foam filters. This highlights the importance of downward-directed flow through the filters.

4. **Design for Runner Division**: In situations where the runner needs to split in opposite directions, it's important to consider the depth and geometry of the runner to ensure adequate flow through the filters and into the gates.

Gate design

Gates are the final component of the filling system in casting and have a profound effect on the flow of molten metal into the mold cavity. Every part of the filling system, including the gates, serves a special purpose and is critical for the success of the casting process.

1. **Design of Gates**: The limitations on the length of the gates' slots must often be considered to control lateral velocities within the mold. This may require the use of more than one gate. Designing gates in the form of slots can be challenging, as sometimes the mold doesn't provide sufficient length for the required slot length. In such cases, the casting engineer must seek the best possible compromise. For aluminum alloy castings, it has been found that if the area of the gate is within a factor of 2 of the area required to achieve a velocity of 0.5 m/s, then the casting is usually satisfactory. Gray iron and carbon steel are somewhat more tolerant of higher velocities at the gate.

Venting channel design

When designing venting channels in a casting process, several key factors must be taken into account to ensure the effectiveness of the process and the quality of the final cast part. Venting channels are essential for allowing the escape of gases and trapped air in the mold during the filling and solidification of the metal, thereby preventing casting defects such as porosity or internal cavities.

1. **Strategic Location**: Venting channels should be placed in areas of the mold where gas accumulation is likely, particularly at high points and confined areas of the design.
2. **Appropriate Size**: The channels should be large enough to effectively allow the escape of gases, but not so large that they permit the leakage of molten metal.
3. **Minimization of Oxidation**: Venting channels help reduce the oxidation of the molten metal by limiting its prolonged exposure to air.
4. **Control of Internal Mold Pressure**: Proper ventilation helps balance the pressure inside the mold during the casting process.
5. **Prevention of Metal Contamination**: By allowing the escape of gases, venting channels help prevent the inclusion of gases and other contaminants in the metal.

Risers/Feeders

When designing risers (also known as feeders) in the casting process, several important factors must be considered to ensure effective feeding of molten metal and to avoid defects in the final piece. Here are some key points drawn from the provided documents:

1. **Function of Risers**: Risers serve as reservoirs of metal whose function is to feed the upper parts of the mold during the solidification and contraction of the metal. This is crucial to compensate for the shrinkage that occurs during the cooling and solidification of the metal, thereby preventing defects such as porosity and the formation of internal cavities.
2. **Location and Design**: Proper placement of risers relative to the parts of the mold that will require feeding is essential. In some cases, risers can be positioned on top of the vertical feeding channel (riser) as an extension, which leverages the hotter metal in the riser to feed the casting. This design helps ensure that areas requiring more metal during solidification receive adequate feeding. The dimensions of the risers depend of several factors but the most important that a riser must ensure is that it will not solidify before the casting part does so it can provide molten metal to avoid shrinkage.
3. **Disadvantages of Riser and Slot Gate System**: One disadvantage of combining risers and slot gates is the finishing and cutting issue, as gates often need to be located on the external surfaces of the casting. This requires significant post-processing work to achieve an acceptable cosmetic finish.

Mold cavity/Casting part

When designing the mold cavity in a casting process, several key factors are crucial to ensure the quality and viability of the final piece. Here's a detailed description of each:

1. **Orientation of the part**: The orientation of the piece within the mold directly affects how the molten metal flows and how solidification occurs. Proper orientation can help minimize defects such as porosity and ensure uniform filling. Furthermore, the orientation influences the ease of extracting the piece from the mold without damage.

2. **Minimum thicknesses**: The minimum thicknesses in the design of the piece are critical to ensure that the molten metal can completely fill the mold cavity before beginning to solidify. Too thin a section may not fill adequately, while overly thick sections can cause issues with shrinkage and uneven cooling.

3. **Rounding radii**: Rounding radii at corners and transitions of the piece are important to avoid stress concentrations and fractures during casting and cooling. Generous radii facilitate a smoother flow of metal and reduce the risk of crack formation due to shrinkage.

4. **Shrinkage coefficient**: Each metal has a specific shrinkage coefficient that must be taken into account in the design of the mold cavity. This coefficient determines how much the metal will shrink upon solidifying and cooling. The mold design must be adjusted to compensate for this shrinkage, ensuring that the cast piece has the desired final dimensions.

The manufacturing method known as casting, a process where a material, typically metal, is melted and poured into a mold to achieve a desired shape, raises an interesting debate regarding its classification as bioinspired. Bioinspiration involves learning from nature and emulating its strategies, designs, or processes to solve human problems. At first glance, casting may not seem to directly follow patterns or strategies from nature, yet there are arguments that could support its consideration as bioinspired.

On one hand, nature itself provides precedents for processes akin to casting. Some insects and animals create structures through the secretion and solidification of materials, somewhat resembling the casting process. Furthermore, the potential to improve and evolve casting processes by applying bioinspired principles presents an intriguing field of research. This could encompass aspects such as the process's energy efficiency, waste minimization, or the creation of structures with enhanced properties, mimicking natural formations.

While casting as a process is not directly derived from nature, exploring how bioinspiration can influence and enhance this method reveals a promising area. The application of lessons learned from nature to current technological and manufacturing needs opens new avenues for innovation in the field of casting. This perspective not only fosters a deeper understanding of natural

processes but also encourages the development of more sustainable, efficient, and innovative casting techniques.

2.3.2 Design for Additive Manufacturing

Additive manufacturing in metals encompasses a variety of technologies, each with its unique characteristics and applications. Based on a chapter from a book on additive manufacturing technologies, we can describe the main methodologies in this field:

1. **Directed Energy Deposition (DED)**: This technology involves melting material that is locally fed into a build layer, typically within an inert gas atmosphere. It's mainly used with metals and metal alloys, and the feed material can be in the form of powder or wire. DED technologies include Laser Metal Deposition (LMD), Laser Engineered Net Shaping (LENS), Electron Beam Welding (EBW), and Electron Beam Freeform Fabrication (EBF3). DED is ideal for repairing components like turbine blades, engine combustion chambers, compressors, airfoils, and rotor disks (blisks) [110].

2. **Powder Bed Fusion (PBF)**: PBF technologies work by melting metal powder locally on a substrate to form layers. After forming a layer, a leveling roller distributes a new layer of powder. The unfused powder is reused and supports subsequent layers. PBF technologies include Direct Metal Laser Sintering (DMLS), Selective Laser Melting (SLM), and Electron Beam Melting (EBM). PBF can create internal passages and generally produces higher fidelity build features compared to DED processes [110].

3. **Other Relevant Metal Additive Technologies**: These include binder jetting printing and Supersonic Particle Deposition (SPD), also known as Cold Spray, or sheet lamination. Binder jetting printing is used for rapid prototyping and the manufacturing of sand cores and molds for producing large metal parts. SPD operates by consolidating micro-sized metal particles onto a suitable substrate via ballistic impact. This technology is suitable for ceramic and polymeric powders and has been used for repairing and enhancing the airworthiness and integrity of aging aeronautical structures [110].

***Table 2-3**. Classification of additive manufacturing technologies: Direct Energy Deposition (DED), Powder Bed Fusion (PBF), and other methods* [110].

Additive Manufacturing Technologies		
Direct energy deposition (DED)	**Powder Bed Fusion (PBF)**	**Other**
Laser Metal Deposition (LMD)/ Laser Engineered Net Shaping (LENS)	Direct Metal Laser Sintering (DMLS) Selective Laser Melting (SLM) Electron Beam Melting (EBM)	Binder Jetting Supersonic Particle Deposition (SPD)/Cold spray

Electron Beam Welding (EBW)/Electron Beam Freeform Fabrication (EBF^3) Wire Arc Additive Manufacturing (WAAM)		

Design for Additive Manufacturing (DfAM) is a specialized approach to design that optimizes for the unique capabilities of Additive Manufacturing (AM) technologies. Unlike traditional manufacturing methods, DfAM leverages the ability of AM to create complex geometries, intricate details, and custom designs that would be difficult or impossible to achieve with conventional manufacturing processes. This design paradigm is crucial because it allows for the full exploitation of the potential of AM, such as significant reductions in material waste, enhanced product performance, and the ability to create customized solutions for specific applications. The importance of DfAM lies in its ability to merge creativity with the technological advances of AM, paving the way for innovative products that are both cost-effective and environmentally sustainable, while also catering to the growing demand for personalization in product design [107].

The importance of DfAM lies in its ability to merge creativity with the technological advances of AM, paving the way for innovative products that are both cost-effective and environmentally sustainable, while also catering to the growing demand for personalization in product design.

To achieve optimal quality in metal additive manufacturing, several critical aspects of the process must be considered. First, the selection of powder material is fundamental, needing to be suitable for the desired mechanical and thermal properties, as well as ensuring good powder flowability and density. The quality of the powder, including its particle size distribution and morphology, directly impacts the accuracy and characteristics of the final product. Secondly, precise control of process conditions, such as laser or electron beam energy, scanning speed, and working atmosphere, is essential to ensure proper melting of the powder and to avoid defects such as porosity or residual stresses. Additionally, the design of the object and support structures should be optimized to facilitate the correct melting and solidification of the material, minimize deformations, and facilitate heat removal during the process. The build strategy, including the orientation of the piece and the layer sequence, plays a crucial role in reducing stresses and improving mechanical properties. Finally, post-processing, which may include heat treatments, machining, or polishing depending on the method, is vital for removing any additional structures and enhancing the surface and structural properties of the printed object, ensuring it meets the specific requirements of its application. [111].

In terms of bioinspiration, additive manufacturing, though not an exact replica of natural processes, is emerging as the method most closely aligned with construction forms observed in

nature. In most cases, natural organisms develop structures additively and in layers, akin to additive manufacturing, which involves progressively depositing material [Layered Patterns in Nature, Medicine, and Materials: Quantifying Anisotropic Structures and Cyclicity]. However, to fully mirror natural processes, additive manufacturing would need to incorporate mechanisms for environmental adaptation. Examples of this adaptability are seen in termites adjusting their nests, the structure of trees, and bones that reinforce their structures in an adaptive manner. While additive manufacturing processes are approaching how nature builds, they still lack the capability to fully adapt to the environment once the component is operational.

This gap, however, presents a tremendous opportunity for the future of engineering and manufacturing. Bioinspiration could play a crucial role in the evolution of additive manufacturing. By leveraging principles and strategies observed in nature, it's possible not only to enhance current processes but also to achieve operational adaptability, one of the outstanding challenges in engineering. The potential for additive manufacturing to evolve into more dynamic and environmentally responsive systems is significant, and its exploration could lead to substantial innovations in how we design and manufacture in the future. Bioinspiration, therefore, is not just a model to emulate but also an inexhaustible source of ideas for enhancing and expanding the capabilities of additive manufacturing.

2.4 Conclusions

The analysis of nature's cumulative selection processes and the formation of efficient, scalable structures demonstrates that natural design is methodical and interconnected, rather than chaotic. Both living organisms and inanimate elements, influenced by similar natural forces, often result in analogous forms, revealing common patterns across various domains. These observations suggest that nature's design principles are highly effective and should be incorporated into human engineering practices.

This review examined bioinspiration concepts and various techniques applicable to engineering design. These techniques are progressively being integrated into contemporary engineering, largely due to advancements in manufacturing processes such as additive manufacturing. This integration together with the exploration of components' life cycle is crucial for developing holistic engineering designs that mimic the lifecycle patterns observed in nature, thereby promoting sustainability and efficiency.

Future engineering design should adopt these bioinspired techniques to ensure that products are not only efficient and functional but also environmentally responsible throughout their lifecycle. This manuscript explores these principles comprehensively, providing a framework for implementing nature-inspired designs in engineering.

Understanding and emulating natural patterns in engineering design highlight the potential for significant advancements in creating more efficient, sustainable, and resilient structures. The

principles of evolution and natural selection emphasize the importance of iterative improvement and adaptation, which can significantly influence modern engineering practices.

2.5 References

[1] R. M. Hazen, "How Old is Earth, and How Do We Know?," *Evolution: Education and Outreach*, vol. 3, no. 2, pp. 198–205, May 2010, doi: 10.1007/S12052-010-0226-0/FIGURES/11.

[2] T. Tashiro *et al.*, "Early trace of life from 3.95 Ga sedimentary rocks in Labrador, Canada," *Nature 2017 549:7673*, vol. 549, no. 7673, pp. 516–518, Sep. 2017, doi: 10.1038/nature24019.

[3] C. Pimiento, "Our shallow-water origins," vol. 362, no. 6413, 2018, doi: 10.1126/science.aav3494.

[4] C. Hamm, *Evolution of Lightweight Structures*, vol. 6. in Biologically-Inspired Systems, vol. 6. Dordrecht: Springer Netherlands, 2015. doi: 10.1007/978-94-017-9398-8.

[5] L. Wen, J. C. Weaver, P. J. M. Thornycroft, and G. V. Lauder, "Hydrodynamic function of biomimetic shark skin: Effect of denticle pattern and spacing," *Bioinspir Biomim*, vol. 10, no. 6, 2015, doi: 10.1088/1748-3190/10/6/066010.

[6] A. G. Domel, G. Domel, J. C. Weaver, M. Saadat, K. Bertoldi, and G. V. Lauder, "Hydrodynamic properties of biomimetic shark skin: Effect of denticle size and swimming speed," *Bioinspir Biomim*, vol. 13, no. 5, p. aad418, 2018, doi: 10.1088/1748-3190/aad418.

[7] K. Jun Tong, S. Duchêne, S. Y. W. Ho, and N. Lo, "Comment on 'phylogenomics resolves the timing and pattern of insect evolution,'" *Science (1979)*, vol. 349, no. 6247, p. 487, 2015, doi: 10.1126/science.aaa5460.

[8] C. A. Tippets, Y. Fu, A. M. Jackson, E. U. Donev, and R. Lopez, "Reproduction and optical analysis of Morpho-inspired polymeric nanostructures," *Journal of Optics (United Kingdom)*, vol. 18, no. 6, 2016, doi: 10.1088/2040-8978/18/6/065105.

[9] E. De Tommasi, J. Gielis, and A. Rogato, "Diatom Frustule Morphogenesis and Function: a Multidisciplinary Survey," *Mar Genomics*, vol. 35, no. July, pp. 1–18, 2017, doi: 10.1016/j.margen.2017.07.001.

[10] C. Darwin, *On the origin of species by means of natural selection, or preservation of favoured races in the struggle for life*. London, 1859.

[11] R. Dawkins, *The Blind Watchmaker*. London, 1986.

[12] "Becker Science." Accessed: Jan. 09, 2024. [Online]. Available: https://sites.google.com/site/beckerscience/science-homework/homework1023-1027

[13] D. W. Thompson, *On Growth and Form*. Cambridge University Press, 1992. doi: 10.1017/CBO9781107325852.

[14] P. Ball, *The self-made tapestry : pattern formation in nature*. Oxford University Press, 1999.

[15] J. A. Adam, “Mathematics in nature: Modeling patterns in the natural world,” *Mathematics in Nature: Modeling Patterns in the Natural World*, Oct. 2011, doi: 10.5860/choice.41-6486.

[16] D. Weaire and R. Phelan, “A counter-example to Kelvin’s conjecture on minimal surfaces,” *Philos Mag Lett*, vol. 69, no. 2, pp. 107–110, 1994, doi: 10.1080/09500839408241577.

[17] D. Weaire and S. Hutzler, “Foams and analogous cellular systems,” 2010. [Online]. Available: https://www.researchgate.net/publication/265117106

[18] “RADIOLARIAN | fickleandfreckled | Flickr.” Accessed: Jan. 09, 2024. [Online]. Available: https://www.flickr.com/photos/51770637@N06/6939385351/

[19] Z. A. Almsherqi, T. Landh, S. D. Kohlwein, and Y. Deng, “Chapter 6 Cubic Membranes: The Missing Dimension of Cell Membrane Organization,” *Int Rev Cell Mol Biol*, vol. 274, no. C, pp. 275–342, Jan. 2009, doi: 10.1016/S1937-6448(08)02006-6.

[20] “Romanesco broccolli light experiments II | The fractal beaut… | Flickr.” Accessed: Jan. 09, 2024. [Online]. Available: https://www.flickr.com/photos/146132872@N05/42184014112/in/photolist-2cMd15W-QLnTv2-CAt4mv-rkTu4W-251zNrh-7B1poF-pPjVSN-pxFA4C-hyRpQT-FUiSUR-QmkQCJ-bbzfnM-AcL8SH-rqnDSy-r4XsJL-7EZYaV-27gE6J9-7QiDtr-pvtGrM-dmxbfa-DM3Mt9-DvVGcG-3Pq84h-dL5Xdq-nyC3RJ-bJWRQ4-2d3YZ5G-b76Mxz-bXqyqL-FzMSkx-q7LDuB-NbDq6d-8uLrVy-MSaEuT-rSzwhS-5KNrn-6q2eT-244a1Eg-8ZEL8H-fh5MPN-boxCEk-DbNR3v-mibofy-gADPnd-cj2ENw-G1tivT-ak7exC-Fx1PcA-7Mk698-5ZLX4x/

[21] “Dried Earth | Taken at our first stop on the tour of the nor… | Flickr.” Accessed: Jan. 09, 2024. [Online]. Available: https://www.flickr.com/photos/scottthegreat/331639145/in/photolist-viJLi-2nxBBe3-2oZFWbM-2m2urgF-JYoxK9-9tUm3H-xtWznE-9QEdZW-2onK257-2nyfaFa-HvGBX-92yyCa-ifmJ9-CrDi4t-CwCKij-MHVimx-2m68GYc-hMonW9-9yDYk2-4sYzmX-Hk1p2U-ENfmZJ-25nY8cr-2iTNYYt-8pJDbE-28WvhVq-7toT6X-2aBM6nt-25xtp5x-28EYPQK-2237A4F-wLXJJ-eMfJhg-3UeNgG-8zJEoJ-GTRVXL-9GiTCT-RzLk6T-2kYEKGN-KJtYtD-2hKgKHi-2iDKc1c-2kEdet6-2j4pvzc-2juVMX6-NrDaPK-2oJJsM3-pcrCmh-2gfEaSp-py7ZhE

[22] K. Tsuji and S. C. Müller, Eds., *Spirals and Vortices*. in The Frontiers Collection. Cham: Springer International Publishing, 2019. doi: 10.1007/978-3-030-05798-5.

[23] A. M. Turing, “The Chemical Basis of Morphogenesis,” *Philos Trans R Soc Lond B Biol Sci*, vol. 237, no. 641, pp. 37–72, 1952, Accessed: Jan. 09, 2024. [Online]. Available: http://www.jstor.org/about/terms.html.

[24] kjpargeter, “Fondo abstracto con un diseño de patrón turing orgánico | Vector Gratis.” Accessed: Jan. 09, 2024. [Online]. Available: https://www.freepik.es/vector-gratis/fondo-abstracto-diseno-patron-turing-organico_37167887.htm#query=patron%20turing&position=1&from_view=keyword&track=ais&uuid=14c234b0-fc70-425e-8175-139b4da081d5

[25] J. D. Murray, “Discussion: Turing’s theory of morphogenesis-Its influence on modelling biological pattern and form,” *Bull Math Biol*, vol. 52, no. 1–2, pp. 119–152, 1990, doi: 10.1007/BF02459571/METRICS.

[26] A. J. Koch and H. Meinhardt, “Biological pattern formation: from basic mechanisms to complex structures,” *Rev Mod Phys*, vol. 66, no. 4, p. 1481, Oct. 1994, doi: 10.1103/RevModPhys.66.1481.

[27] J. D. Murray and G. F. Oster, “Generation of biological pattern and form,” *IMA J Math Appl Med Biol*, vol. 1, no. 1, pp. 51–75, 1984, doi: 10.1093/IMAMMB/1.1.51.

[28] “Wake Turbulence.” Accessed: Jan. 09, 2024. [Online]. Available: https://www.faa.gov/air_traffic/publications/atpubs/aim_html/chap7_section_4.html

[29] “Dramatic Views of Hurricane Florence from the Internationa… | Flickr.” Accessed: Jan. 09, 2024. [Online]. Available: https://www.flickr.com/photos/gsfc/42828603210/

[30] “von Karman Vortices.” Accessed: Jan. 09, 2024. [Online]. Available: https://earthobservatory.nasa.gov/images/2613/von-karman-vortices

[31] “Results for ‘EL-1996-00130’ | NASA Image and Video Library.” Accessed: Jan. 09, 2024. [Online]. Available: https://images.nasa.gov/search?q=EL-1996-00130&page=1&media=image,video,audio&yearStart=1920&yearEnd=2023

[32] “File:Fibonacci Spiral.svg - Wikimedia Commons.” Accessed: Jan. 09, 2024. [Online]. Available: https://commons.wikimedia.org/wiki/File:Fibonacci_Spiral.svg

[33] “Aloe Plant | Jean Ogden Just Chaos Photography | Flickr.” Accessed: Jan. 09, 2024. [Online]. Available: https://www.flickr.com/photos/7326810@N08/1636684209/

[34] “Nautilus | rainy city | Flickr.” Accessed: Jan. 09, 2024. [Online]. Available: https://www.flickr.com/photos/furphotos/49872038707/in/photolist-2iZ2eAk-bAgCtn-bnmKFj-bAgCuM-2jZ7M9t-2o8zTsg-218C3j7-ybG5G-2oTojx5-8cK6F-9DD41-poF65L-66bdaX-76Z85Z-5zabUM-2o8AmUP-4gLaTS-EQttEk-CX4awT-2k1We5g-2oTpUCr-2oTpsLi-GFVW2A-43SQwS-7MHNXa-SD35RF-2hqyB9z-29gVZDZ-4F5vC1-2iWahCf-4iQY7z-2oTpTDN-Ff7m8u-oypGFH-4749L4-7Kc7Mh-dUM7DS-2oFQyvB-4dXFJp-53YtUb-2aUA3CU-2fp34-e4vvaC-2oTjtw3-23dSG8N-9aZ5XG-2mRES1y-a6xPCF-a7oFDC-61RyuY

[35] O. Schmitt, “Some interesting and useful biomimetic transforms,” in *Third Int. Biophysics Congress*, Boston, 1969.

[36] J. M. Benyus, *Biomimicry: innovation inspired by nature*, 1st ed. New York, 1997.

[37] H. Hashemi Farzaneh and U. Lindemann, *A Practical Guide to Bio-inspired Design*. 2019. doi: 10.1007/978-3-662-57684-7.

[38] W. Nachtigall and A. Wisser, *Bionics by examples : 250 Scenarios from Classical to Modern Times*. 2014. [Online]. Available: https://books.google.co.uk/books?id=ZamgBAAAQBAJ&pg=PA7&lpg=PA7&dq=c.lie+pilot+fish+1905&source=bl&ots=uKWqbFLvgA&sig=AICvxZQbc6XzthPpbsG5cLf4v4U&hl=en&sa=X&ved=0ahUKEwiCsJ3Xy7zQAhWrDMAKHc90BTIQ6AEIHzAB#v=onepage&q=c.lie pilot fish 1905&f=false%5Cnhttps:/

[39] B. Gagnon, R. Leduc, and L. Savard, "From a conventional to a sustainable engineering design process: Different shades of sustainability," *Journal of Engineering Design*, vol. 23, no. 1, pp. 49–74, 2012, doi: 10.1080/09544828.2010.516246.

[40] S. Mosborg, R. Adams, R. Kim, C. J. Atman, J. Turns, and M. Cardella, "Conceptions of the engineering design process: An expert study of advanced practicing professionals," *ASEE Annual Conference and Exposition, Conference Proceedings*, pp. 2143–2169, 2005, doi: 10.18260/1-2--14999.

[41] K. Mulder, *Sustainable development for engineers*, Greenleaf. Sheffield, 2006.

[42] M. Leary, "Generative design," *Design for Additive Manufacturing*, no. Chapter 2, pp. 203–222, 2020, doi: 10.1016/b978-0-12-816721-2.00007-5.

[43] M. Sivaram, S. A. Karuppusamy, V. Porkodi, and V. Manikandan, "Selection of Material using IWDNN Algorithm for Multiphase Material Component Design," *2019 Global Conference for Advancement in Technology, GCAT 2019*, Oct. 2019, doi: 10.1109/GCAT47503.2019.8978314.

[44] S. S. Babu, "Tools for Alloy Design," *Encyclopedia of Materials: Metals and Alloys*, pp. 245–262, Jan. 2022, doi: 10.1016/B978-0-12-819726-4.00142-3.

[45] L. F. Dumée, "Circular Materials and Circular Design—Review on Challenges Towards Sustainable Manufacturing and Recycling," *Circular Economy and Sustainability*, vol. 2, no. 1, pp. 9–23, Mar. 2022, doi: 10.1007/S43615-021-00085-2/METRICS.

[46] M. Arseenko *et al.*, "A new healing strategy for metals: Programmed damage and repair," *Acta Mater*, vol. 238, p. 118241, Oct. 2022, doi: 10.1016/J.ACTAMAT.2022.118241.

[47] C. R. Fisher, J. J. M. Jr, H. B. Henderson, M. S. Kesler, and M. V. Manuel, "A Reactive Element Approach to Improve Fracture Healing in Metallic Systems," *Front Mater*, vol. 6, p. 436175, Aug. 2019, doi: 10.3389/FMATS.2019.00210/BIBTEX.

[48] N. van Dijk and S. van der Zwaag, "Self-Healing Phenomena in Metals," *Adv Mater Interfaces*, vol. 5, no. 17, p. 1800226, Sep. 2018, doi: 10.1002/ADMI.201800226.

[49] M. K. Thompson *et al.*, "Design for Additive Manufacturing: Trends, opportunities, considerations, and constraints," *CIRP Annals*, vol. 65, no. 2, pp. 737–760, Jan. 2016, doi: 10.1016/J.CIRP.2016.05.004.

[50] J. Pandremenos, E. Vasiliadis, and G. Chryssolouris, “Design Architectures in Biology,” *Procedia CIRP*, vol. 3, no. 1, pp. 448–452, Jan. 2012, doi: 10.1016/J.PROCIR.2012.07.077.

[51] A. du Plessis *et al.*, “Beautiful and Functional: A Review of Biomimetic Design in Additive Manufacturing,” *Addit Manuf*, vol. 27, no. March, pp. 408–427, 2019, doi: 10.1016/j.addma.2019.03.033.

[52] Y. Yang *et al.*, “Recent Progress in Biomimetic Additive Manufacturing Technology: From Materials to Functional Structures,” *Advanced Materials*, vol. 30, no. 36, p. 1706539, Sep. 2018, doi: 10.1002/ADMA.201706539.

[53] C. Broeckhoven, A. du Plessis, and C. Hui, “Functional trade-off between strength and thermal capacity of dermal armor: Insights from girdled lizards,” *J Mech Behav Biomed Mater*, vol. 74, pp. 189–194, Oct. 2017, doi: 10.1016/J.JMBBM.2017.06.007.

[54] S. E. Naleway, M. M. Porter, J. McKittrick, and M. A. Meyers, “Structural Design Elements in Biological Materials: Application to Bioinspiration,” *Advanced Materials*, vol. 27, no. 37, pp. 5455–5476, Oct. 2015, doi: 10.1002/ADMA.201502403.

[55] A. Velasco-Hogan, J. Xu, and M. A. Meyers, “Additive Manufacturing as a Method to Design and Optimize Bioinspired Structures,” *Advanced Materials*, vol. 30, no. 52, p. 1800940, Dec. 2018, doi: 10.1002/ADMA.201800940.

[56] I. Gibson *et al.*, “The use of rapid prototyping to assist medical applications,” *Rapid Prototyp J*, vol. 12, no. 1, pp. 53–58, 2006, doi: 10.1108/13552540610637273/FULL/XML.

[57] Y. L. Yap and W. Y. Yeong, “Additive manufacture of fashion and jewellery products: a mini review,” *Virtual Phys Prototyp*, vol. 9, no. 3, pp. 195–201, 2014, doi: 10.1080/17452759.2014.938993.

[58] “adidas Futurecraft: 3D-Printed Personalized Shoe | Materialise.” Accessed: Jan. 09, 2024. [Online]. Available: https://www.materialise.com/en/inspiration/cases/adidas-futurecraft-3d-printed-personalized-shoe

[59] “Riddell and Carbon® Produce First-Ever 3D Printed Football Helmet Liner.” Accessed: Jan. 09, 2024. [Online]. Available: https://www.carbon3d.com/news/press-releases/riddell-carbon-produce-football-helmet

[60] U. Kirsch, *Structural Optimization*. Berlin, Heidelberg: Springer Berlin Heidelberg, 1993. doi: 10.1007/978-3-642-84845-2.

[61] Querin Osvaldo M., Victoria Mariano, Alonse Cristina, Ansola Rubén, and Martí Pascual, *Topology Design Methods for Structural Optimization*. 2017. Accessed: Jan. 09, 2024. [Online]. Available: https://books.google.be/books?id=lsacBAAAQBAJ&pg=PA54&lpg=PA54&dq=fg+fem+garcia+ruiz&source=bl&ots=hmo5iPSNHe&sig=ACfU3U20fS1yhbi6BbL2j1OTqyXV-

BEeIg&hl=nl&sa=X&ved=2ahUKEwiqzeSMq9voAhUtsaQKHYN5BwoQ6AEwAHoECAgQLw#v=onepage&q&f=false

[62] M. P. Bendsøe and O. Sigmund, "Topology Optimization," *Topology Optimization*, 2004, doi: 10.1007/978-3-662-05086-6.

[63] A. G. M. Michell, " LVIII. The limits of economy of material in frame-structures ," *The London, Edinburgh, and Dublin Philosophical Magazine and Journal of Science*, vol. 8, no. 47, pp. 589–597, Nov. 1904, doi: 10.1080/14786440409463229.

[64] G. I. N. Rozvany, "A critical review of established methods of structural topology optimization," *Structural and Multidisciplinary Optimization*, vol. 37, no. 3, pp. 217–237, Jan. 2009, doi: 10.1007/S00158-007-0217-0/METRICS.

[65] G. I. N. Rozvany, "Grillages of maximum strength and maximum stiffness," *Int J Mech Sci*, vol. 14, no. 10, pp. 651–666, Oct. 1972, doi: 10.1016/0020-7403(72)90023-9.

[66] O. Sigmund and K. Maute, "Topology optimization approaches: A comparative review," *Structural and Multidisciplinary Optimization*, vol. 48, no. 6, pp. 1031–1055, Dec. 2013, doi: 10.1007/S00158-013-0978-6/FIGURES/2.

[67] M. P. Bendsøe and N. Kikuchi, "Generating optimal topologies in structural design using a homogenization method," *Comput Methods Appl Mech Eng*, vol. 71, no. 2, pp. 197–224, Nov. 1988, doi: 10.1016/0045-7825(88)90086-2.

[68] M. P. Bendsøe, "Optimal shape design as a material distribution problem," *Structural Optimization*, vol. 1, no. 4, pp. 193–202, Dec. 1989, doi: 10.1007/BF01650949/METRICS.

[69] M. P. Bendsøe and O. Sigmund, "Material interpolation schemes in topology optimization," *Archive of Applied Mechanics*, vol. 69, no. 9–10, pp. 635–654, 1999, doi: 10.1007/S004190050248/METRICS.

[70] M. Stolpe and K. Svanberg, "An alternative interpolation scheme for minimum compliance topology optimization," *Structural and Multidisciplinary Optimization*, vol. 22, no. 2, pp. 116–124, Feb. 2001, doi: 10.1007/S001580100129/METRICS.

[71] H. A. Eschenauer, V. V. Kobelev, and A. Schumacher, "Bubble method for topology and shape optimization of structures," *Structural Optimization*, vol. 8, no. 1, pp. 42–51, Aug. 1994, doi: 10.1007/BF01742933/METRICS.

[72] S. Amstutz, "Connections between topological sensitivity analysis and material interpolation schemes in topology optimization," *Structural and Multidisciplinary Optimization*, vol. 43, no. 6, pp. 755–765, Jun. 2011, doi: 10.1007/S00158-010-0607-6/FIGURES/6.

[73] S. Osher and J. A. Sethian, “Fronts propagating with curvature-dependent speed: Algorithms based on Hamilton-Jacobi formulations,” *J Comput Phys*, vol. 79, no. 1, pp. 12–49, Nov. 1988, doi: 10.1016/0021-9991(88)90002-2.

[74] J. A. Sethain, *Level set methods and fast marching*. 1999. Accessed: Jan. 09, 2024. [Online]. Available: http://books.google.fr/books?id=ErpOoynE4dIC&printsec=frontcover&dq=Level+set+methods+and+fast+marching+methods&hl=&cd=1&source=gbs_api%0Apapers3://publication/uuid/9C109E10-ADC2-4137-90A7-434FE8362031

[75] G. Allaire, F. Jouve, and A. M. Toader, “A level-set method for shape optimization,” *C R Math*, vol. 334, no. 12, pp. 1125–1130, Jan. 2002, doi: 10.1016/S1631-073X(02)02412-3.

[76] J. D. Deaton and R. V. Grandhi, “A survey of structural and multidisciplinary continuum topology optimization: Post 2000,” *Structural and Multidisciplinary Optimization*, vol. 49, no. 1, pp. 1–38, Jan. 2014, doi: 10.1007/S00158-013-0956-Z/FIGURES/14.

[77] M. Stolpe and M. P. Bendsøe, “Global optima for the Zhou-Rozvany problem,” *Structural and Multidisciplinary Optimization*, vol. 43, no. 2, pp. 151–164, Feb. 2011, doi: 10.1007/S00158-010-0574-Y/TABLES/4.

[78] K. Svanberg and M. Werme, “Topology optimization by a neighbourhood search method based on efficient sensitivity calculations,” *Int J Numer Methods Eng*, vol. 67, no. 12, pp. 1670–1699, Sep. 2006, doi: 10.1002/NME.1677.

[79] O. Sigmund, “On the usefulness of non-gradient approaches in topology optimization,” *Structural and Multidisciplinary Optimization*, vol. 43, no. 5, pp. 589–596, May 2011, doi: 10.1007/S00158-011-0638-7/FIGURES/2.

[80] R. Ansola, E. Veguería, J. Canales, and J. A. Tárrago, “A simple evolutionary topology optimization procedure for compliant mechanism design,” *Finite Elements in Analysis and Design*, vol. 44, no. 1–2, pp. 53–62, Dec. 2007, doi: 10.1016/J.FINEL.2007.09.002.

[81] R. Ansola, E. Veguería, A. Maturana, and J. Canales, “3D compliant mechanisms synthesis by a finite element addition procedure,” *Finite Elements in Analysis and Design*, vol. 46, no. 9, pp. 760–769, Sep. 2010, doi: 10.1016/J.FINEL.2010.04.006.

[82] X. Huang and Y. M. Xie, “A further review of ESO type methods for topology optimization,” *Structural and Multidisciplinary Optimization*, vol. 41, no. 5, pp. 671–683, May 2010, doi: 10.1007/S00158-010-0487-9/FIGURES/6.

[83] L. Van Miegroet and P. Duysinx, “Stress concentration minimization of 2D filets using X-FEM and level set description,” *Structural and Multidisciplinary Optimization*, vol. 33, no. 4–5, pp. 425–438, Apr. 2007, doi: 10.1007/S00158-006-0091-1/METRICS.

[84] M. K. Misztal and J. A. Bærentzen, “Topology-adaptive interface tracking using the deformable simplicial complex,” *ACM Transactions on Graphics (TOG)*, vol. 31, no. 3, Jun. 2012, doi: 10.1145/2167076.2167082.

[85] V. M. Pomazan and S. R. Sintea, “Solving structural design challenges with generative solutions,” *Scientific Bulletin of Naval Academy*, vol. 2020, pp. 41–46, 2020, doi: 10.21279/1454-864X-20-I1-006.

[86] B. Li, H. Liu, Z. Yang, and J. Zhang, “Thin-Walled Structures Sti ff ness design of plate / shell structures by evolutionary topology optimization,” *Thin Walled Structures*, vol. 141, no. April, pp. 232–250, 2019, doi: 10.1016/j.tws.2019.04.012.

[87] S. Wolfram, “Cellular automata as models of complexity,” no. I, 1984.

[88] M. Gen and L. Lin, “Genetic algorithms,” *Wiley Encyclopedia of Computer Science and Engineering*, pp. 1–15, 2007.

[89] SJ. Russell and P. Norvig, *Artifcial intelligence: a modern approach*.

[90] J. Walsh and K. Meintjes, “Understanding a Generative Design Enabled Design Process Paradigm Shift Acknowledgements,” 2019.

[91] Y. Liu, Y. Li, L. Ma, B. Chen, and R. Li, “Parametric design approach on high-order and multi-segment modified elliptical helical gears based on virtual gear shaping,” *Proc Inst Mech Eng C J Mech Eng Sci*, vol. 236, no. 9, pp. 4599–4609, May 2022, doi: 10.1177/09544062211058396.

[92] S. James, K. Karius, and T. Gapinski, “Varvsbron, Innovation in Bridge Design, Engineering & Advanced Surface Modelling,” *Footbridge 2022, Madrid: Creating Experience*, May 2022, doi: 10.24904/FOOTBRIDGE2022.248.

[93] A. Jabran, C. Peach, Z. Zou, and L. Ren, “Parametric Design Optimisation of Proximal Humerus Plates Based on Finite Element Method,” *Ann Biomed Eng*, vol. 47, no. 2, p. 601, Feb. 2019, doi: 10.1007/S10439-018-02160-6.

[94] L. Regenwetter, A. H. Nobari, and F. Ahmed, “Deep Generative Models in Engineering Design: A Review,” *Journal of Mechanical Design*, vol. 144, no. 7, Jul. 2022, doi: 10.1115/1.4053859/1136676.

[95] B. Li, C. Huang, X. Li, S. Zheng, and J. Hong, “Non-iterative structural topology optimization using deep learning,” *Computer-Aided Design*, vol. 115, pp. 172–180, Oct. 2019, doi: 10.1016/J.CAD.2019.05.038.

[96] M. M. Behzadi and H. T. Ilieş, “Real-Time Topology Optimization in 3D via Deep Transfer Learning,” *Computer-Aided Design*, vol. 135, p. 103014, Jun. 2021, doi: 10.1016/J.CAD.2021.103014.

[97] Z. Yang, X. Li, L. C. Brinson, A. N. Choudhary, W. Chen, and A. Agrawal, "Microstructural materials design via deep adversarial learning methodology," *Journal of Mechanical Design*, vol. 140, no. 11, Nov. 2018, doi: 10.1115/1.4041371/477902.

[98] R. Cang, H. Li, H. Yao, Y. Jiao, and Y. Ren, "Improving direct physical properties prediction of heterogeneous materials from imaging data via convolutional neural network and a morphology-aware generative model," *Comput Mater Sci*, vol. 150, pp. 212–221, Jul. 2018, doi: 10.1016/J.COMMATSCI.2018.03.074.

[99] L. J. Gibson and M. F. Ashby, "Cellular materials in nature and medicine," *Integr Comp Biol*, vol. 51, pp. E47--E47, 2010, Accessed: Jan. 10, 2024. [Online]. Available: https://books.google.com/books/about/Cellular_Materials_in_Nature_and_Medicin.html?hl=es&id=AKxiS4AKpyEC

[100] D. Bhate, C. A. Penick, L. A. Ferry, and C. Lee, "Classification and Selection of Cellular Materials in Mechanical Design: Engineering and Biomimetic Approaches," *Designs 2019, Vol. 3, Page 19*, vol. 3, no. 1, p. 19, Mar. 2019, doi: 10.3390/DESIGNS3010019.

[101] J. C. Maxwell, "I.—On Reciprocal Figures, Frames, and Diagrams of Forces," *Earth Environ Sci Trans R Soc Edinb*, vol. 26, no. 1, pp. 1–40, 1870, doi: 10.1017/S0080456800026351.

[102] D. Baumeister, R. Tocke, J. Dwyer, S. Ritter, and J. Benyus, *Biomimicry.net | AskNature.org*. 2012.

[103] T. McNulty *et al.*, "A framework for the design of biomimetic cellular materials for additive manufacturing," 2020. Accessed: Jan. 09, 2024. [Online]. Available: https://asu.elsevierpure.com/en/publications/a-framework-for-the-design-of-biomimetic-cellular-materials-for-a

[104] T. A. Schaedler and W. B. Carter, "Architected Cellular Materials," *https://doi.org/10.1146/annurev-matsci-070115-031624*, vol. 46, pp. 187–210, Jul. 2016, doi: 10.1146/ANNUREV-MATSCI-070115-031624.

[105] H. Kim, F. Cluzel, Y. Leroy, B. Yannou, and G. Y. Le Bris, "Research perspectives in ecodesign," *Design Science*, vol. 6, p. e7, Nov. 2020, doi: 10.1017/DSJ.2020.5.

[106] N. Boorsma, E. Polat, C. Bakker, D. Peck, and R. Balkenende, "Development of the Circular Product Readiness Method in Circular Design," *Sustainability (Switzerland)*, vol. 14, no. 15, Aug. 2022, doi: 10.3390/SU14159288.

[107] M. K. Thompson *et al.*, "Design for Additive Manufacturing: Trends, opportunities, considerations, and constraints," *CIRP Annals*, vol. 65, no. 2, pp. 737–760, Jan. 2016, doi: 10.1016/J.CIRP.2016.05.004.

[108] B. Ravi, R. C. Creese, and D. Ramesh, "Design for Casting-A New Paradigm for Preventing Potential Problems," *Transactions of the American Foundry Society*, vol. 107, 1999.

[109] J. Campbell, “Complete Casting Handbook: Metal Casting Processes, Metallurgy, Techniques and Design: Second Edition,” *Complete Casting Handbook: Metal Casting Processes, Metallurgy, Techniques and Design: Second Edition*, pp. 1–1028, Sep. 2015, doi: 10.1016/C2014-0-01548-1.

[110] J. C. Najmon, S. Raeisi, and A. Tovar, “Review of additive manufacturing technologies and applications in the aerospace industry,” *Additive Manufacturing for the Aerospace Industry*, pp. 7–31, Jan. 2019, doi: 10.1016/B978-0-12-814062-8.00002-9.

[111] T. DebRoy *et al.*, “Additive manufacturing of metallic components – Process, structure and properties,” *Prog Mater Sci*, vol. 92, pp. 112–224, Mar. 2018, doi: 10.1016/J.PMATSCI.2017.10.001.

Chapter 3: Bioinspired design methodologies and tools applied to an aeronautical assembly column

3.1 Introduction

With the emergence and development of new manufacturing methods and computational tools, there has been a democratization of advanced designs for component optimization. Today, it is uncommon not to encounter a component manufactured through additive manufacturing and optimized with an organic structure. However, these methodologies are not thoroughly studied nor often compared with each other. Therefore, this chapter addresses the need to begin with an overview of some design methodologies and tools that may be relevant for the developments in this manuscript. Once described, three tools will be selected for application in an example.

In this study, the question of how bioinspired design and advanced manufacturing methods can revolutionize the aeronautical industry by transforming the conception, creation, and utilization of tooling will be addressed. Exploration will be undertaken into how nature offers efficient and adaptable solutions that can inspire the design of more versatile and effective tooling. Additionally, examination will be conducted into how advanced manufacturing technologies, such as casting and additive manufacturing, can be employed to materialize these bioinspired designs, thereby enabling the creation of lighter, customizable, and sustainable tooling.

More precisely, this study aims to explore the effect of three bioinspired design methods on an aeronautic assembly tooling used to support large structural components such as fuselages and wings. In the end, the objective is to evaluate proposed designs and select the best one according to operational objectives. Additionally, the study investigates the manufacturing of the selected design at real dimensions using advanced manufacturing methods. The proper operation of the large-scale manufactured component will be assessed through operational testing.

In 2023, the aerospace and defense industry saw a resurgence in product demand, significantly driven by an increase in air travel and new geopolitical challenges. This surge in demand led to an increased need for new aircraft and after-market products and services. Notably, domestic commercial aviation surpassed pre-pandemic levels in most countries, marking a significant turning point for the industry. The recovery of the sector was reflected in a 3% increase in aerospace and defense industry revenues in 2022, reaching $741 billion, although this growth was tempered by production constraints due to supply chain challenges and labor shortages [1], [2].

In the tooling industry, the careful design and implementation of fixtures and jigs are paramount for ensuring precise alignment and robust structural assembly. These specialized tools serve as essential aids in aligning and securing components during assembly, contributing significantly to the overall quality and efficiency of manufacturing processes. By providing stable support and accurate positioning, well-crafted fixtures and jigs minimize errors and streamline assembly workflows. Their role in maintaining alignment and rigidity cannot be overstated, as they lay the foundation for the successful integration of components into final products. Across diverse manufacturing sectors, from automotive to electronics, the meticulous design and utilization of

fixtures and jigs are instrumental in achieving reliable and high-quality assembly outcomes. The main characteristics that future tooling must possess are:

1. Precision in measurements and alignment of the tooling
2. Repeatability and consistency in the assembly of each product
3. Improvement in efficiency and productivity
4. Quality and reliability of the assembled product
5. Safety and ergonomics for workers and the integrity of the factory
6. Innovation and complex design

In the realm of aeronautical industry, where precision and efficiency are deemed imperative, the tooling utilized along assembly lines plays a pivotal role in ensuring the quality and safety of aircraft. These devices, traditionally designed to be rigid and highly specialized, have been considered essential for decades. However, in an ever-evolving world characterized by the need for agility, flexibility, and efficiency, a fundamental question arises: Can a redefinition and revitalization of aeronautical tooling to adapt to shifting industry demands be achieved?

The current status of tooling within the aerospace industry is characterized by inherent rigidity and a high degree of specialization, which can lead to considerable challenges. The production of highly specialized tooling incurs significant costs in terms of time and resources. Furthermore, a requirement for skilled personnel to operate and maintain these systems is deemed essential but costly. In a world where the mobility of assembly lines and adaptability to different projects are crucial, a dependence on rigid and specialized tooling can be perceived as an impediment to efficiency and profitability.

This statement raises an imperative need for the democratization and standardization of tooling used in the aerospace industry while aiming for greater reconfigurability and versatility in design. The redesign and reinvention of aerospace tooling are seen as essential components to sustain competitiveness in a highly dynamic global market. Within this context, an opportunity arises to leverage the principles of bioinspired design and advanced manufacturing methods to realize significant advancements in the evolution of aerospace tooling.

After a deep state-of-the-art study, not a lot of information has been found about comparisons of bio-inspired optimization methods applied to a certain use case; however, there exist some review studies that mention some of them with different classifications [3], [4]. Instead, there is a lot of information on application of lattices [5], [6], topology optimization [7], generative design [8], and the use of Voronoi patterns and other bioinspired geometries [9], [10], [11]. The comparative study can be of great interest to know how three different methods are applied in the same research and at the same time to observe the results applied to a case study. Although a method's turning out to be the best for the specific case studied here does not mean that it is the best methodology for other studies, it may provide clues for future research.

In this chapter, the fabrication method used to create a large structure (800 × 500 × 2100 mm) with complex topology due to its bioinspired design will be discussed. No literature was found regarding the fabrication of components with such complexity (topology and large size). However, there have been some studies mentioning the potential of 3D printed sand molds for complex

topology parts [12], [13]. Additionally, tests have been performed to certify that the digital model and the fabricated part behave identically in terms of vibration modes.

3.2 Theoretical framework

Engineering systems that have mass and elasticity are capable of relative movement. When such movement repeats over a time period, it's referred to as vibration. Generally, vibration is a way to expend energy and is considered an undesirable effect in most machinery because it leads to noise generation, component failure, and the transmission of unwanted forces and movements to adjacent objects [14].

Understanding the nature and definition of this phenomenon is crucial to prevent unwanted damage to machines. To begin, a simple case is considered: a dynamic system with one degree of freedom consisting of a mass and a spring subjected to an internal force as seen in **Figure 3.1**.

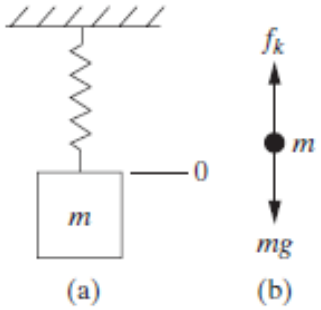

Figure 3.1. *Single degree of freedom dynamic system of a mass and a spring subjected to gravitational force* [15]

Ignoring the weight of the ideal spring, two forces act on the body: the gravitational force mg and the elastic force of the spring f_k. Where this force can be defined as:

$$f_k = kx \tag{1}$$

Where k is the stiffness factor and x the displacement forced by the gravitational load. If Newton's second law is applied:

$$m\ddot{x}(t) = -kx(t) \tag{2}$$

If that differential equation is solved:

$$\begin{cases} x(t) = A\sin(\omega_n t + \varphi) \\ \dot{x}(t) = \omega_n A\cos(\omega_n t + \varphi) \\ \ddot{x}(t) = -{\omega_n}^2 A\sin(\omega_n t + \varphi) \end{cases} \tag{3}$$

Where $\dot{x}(t)$ is the velocity of the system, $\ddot{x}(t)$ the acceleration, A constant is the amplitude, ω_n is the angular natural frequency and φ is the phase. Substituting the equations into the movement equation:

$$-m{\omega_n}^2\, A\, sin(\omega_n t\, +\, \phi)\, =\, -kA\, sin(\omega_n t\, +\, \phi) \tag{4}$$

Operating further, the following equation is obtained:

$$\omega_n{}^2 = \frac{k}{m} \tag{5}$$

The natural frequency of a mechanical system is defined as the frequency at which the system tends to oscillate in the absence of any type of external force acting on it, except when subjected to an initial disturbance. In simpler terms, it's the inherent vibration frequency of a system when it's neither damped nor driven by external forces.

This property is a fundamental characteristic of mechanical and structural systems, ranging from simple mass-spring setups to complex aeronautical structures. The natural frequency directly stems from the physical properties of the system, such as mass, stiffness, and for more complex systems, the geometrical and material properties of the structure.

However, real mechanical systems are generally not as simple as the example described here. In reality, oscillatory systems tend to reduce their motion until they stop completely, indicating that the model described is not entirely realistic. There is always a phenomenon known as viscous damping, which causes this motion to decay and is defined proportionally to the system's velocity and can be defined as follows:

$$f_c = c\dot{x}(t) \tag{6}$$

Where c is the constant called damping coefficient. This coefficient cannot be measured as simply as the mass or the stiffness of a system. If we study this new force in a common example known as damped single-degree-of-freedom system seen in the next **Figure 3.2**.

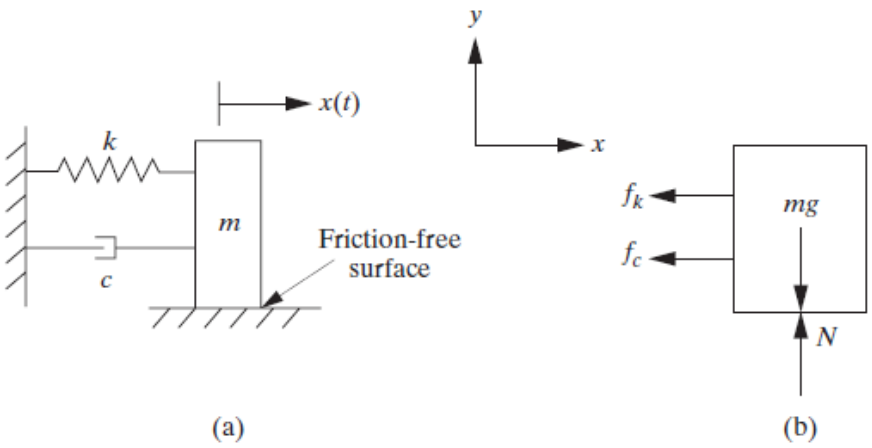

***Figure 3.2**. Damped single degree of freedom dynamic system subjected to a displacement.* [15]

We get that:

$$m\ddot{x}(t) = -c\dot{x}(t) - kx(t) \tag{7}$$

To solve this damped equation it is necessary to define the initial conditions which are $x(0) = x_0$ and $\dot{x}(0) = v_0$. This equation will be solved as the previous problem has. In this case $x(t) = ae^{\lambda t}$.

$$(m\lambda^2 + c\lambda + k)ae^{\lambda t} = 0 \tag{8}$$

As $ae^{\lambda t} \neq 0$ this reduces to the equation:

$$m\lambda^2 + c\lambda + k = 0 \tag{9}$$

Which leads to two solutions:

$$\lambda_{1,2} = -\frac{c}{2m} \pm \frac{1}{2m}\sqrt{c^2 - 4km} \tag{10}$$

Depending on the value of $c^2 - 4km$ the solution would be real or complex. Therefore it can be noticed that there exist a value of c that will define a limit for real numbers which can be defined from $c^2 - 4km > 0$.

$$c_{cr} = 2\sqrt{km} = 2m\omega_n \tag{11}$$

Where ω_n is the undamped natural frequency. To understand this it is necessary to define the non dimensional term ξ known as damping ratio.

$$\zeta = \frac{c}{c_{cr}} = \frac{c}{2m\omega_n} = \frac{c}{2\sqrt{km}} \tag{12}$$

What would lead to rewrite the solution to:

$$\lambda_{1,2} = -\zeta\omega_n \pm \omega_n\sqrt{\xi^2 - 1} \tag{13}$$

Depending on the damping ratio value the damping of the system will behave differently as explained here and illustrated in **Figure 3.3**.

In an **underdamped motion**, the system lacks sufficient damping to prevent oscillations, meaning the system will vibrate around its equilibrium position with an amplitude that gradually decreases over time. The damping ratio ζ for this scenario is less than 1 ($\zeta < 1$), indicating that the damping is not adequate to halt the oscillatory movement immediately. While damping reduces the system's energy over time, allowing it to eventually settle, oscillations persist for a period before the system fully stabilizes. This behavior is common in many mechanical systems where a balance is sought between quick return to equilibrium and minimizing vibrations, such as in vehicle suspension systems.

In contrast, **overdamped motion** is defined by a system possessing a level of damping that exceeds what is necessary to prevent any oscillation. In this scenario, the damping ratio ζ is greater than 1 ($\zeta > 1$), indicating that the system will return to its equilibrium position without oscillating. This type of movement results in a slower return to equilibrium compared to underdamped motion, as the excess damping suppresses oscillations but also restricts the system's dynamics. Such behavior is preferred in situations where oscillations, even of small amplitude, could be detrimental, or where the priority is to prevent relative movement between parts of the system.

Critically damped motion represents the transitional point between underdamped and overdamped movements, where the system possesses precisely the amount of damping required to return to its equilibrium position in the shortest time possible without oscillating. In this scenario, the damping ratio ζ equals to 1 ($\zeta = 1$), indicating a perfect balance between minimizing the return time to equilibrium and avoiding oscillations. This level of damping is ideal for applications that demand rapid stability following a disturbance, such as in certain control systems and safety devices where time efficiency is critical.

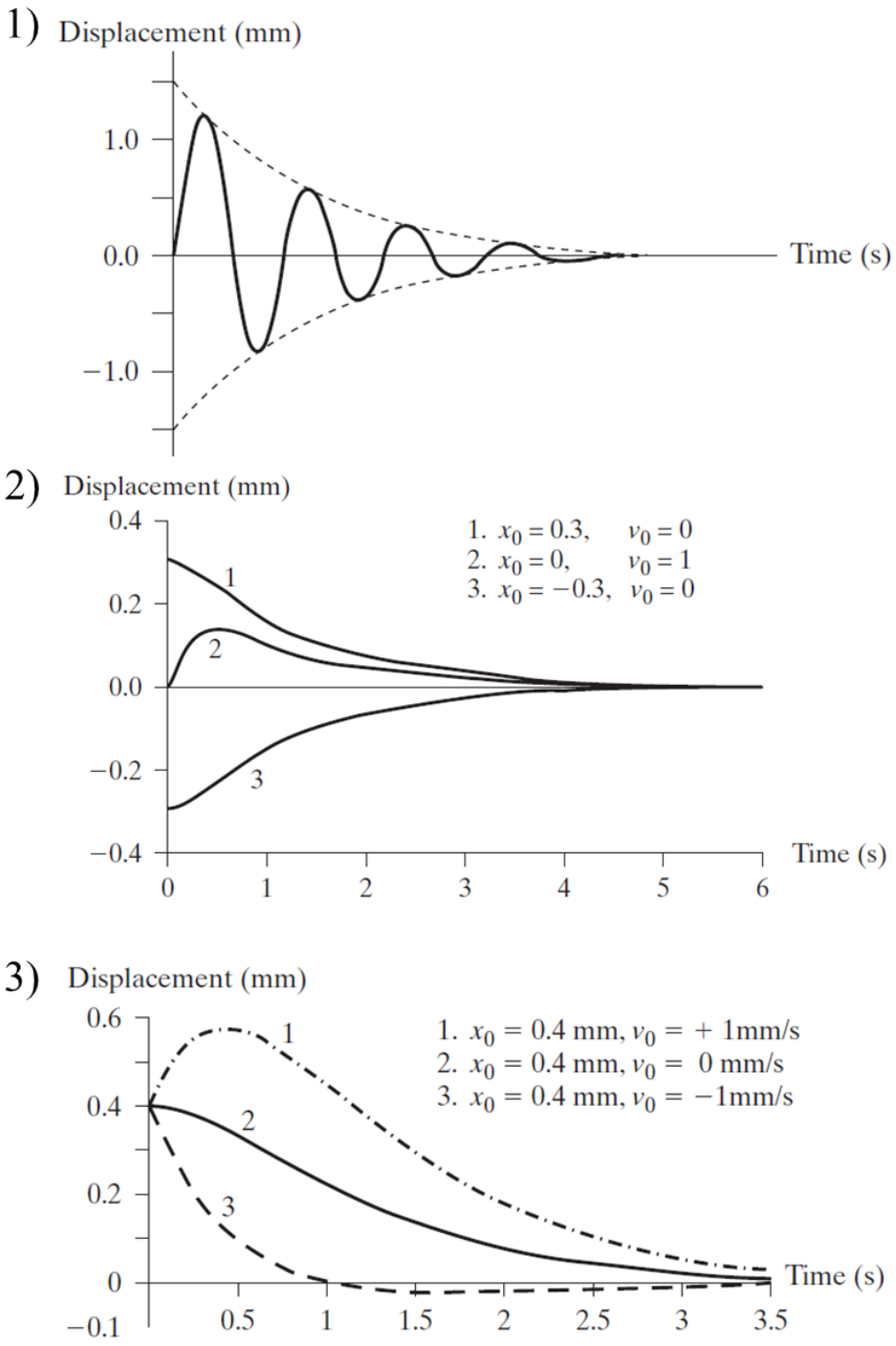

Figure 3.3*.Graphic expression of the three types of damped systems based on the damping critical value. 1) Underdamped 2) Overdamped 3) Critically damped* [15]

Understanding natural frequency is critical in engineering because the phenomenon of resonance occurs when the frequency of applied external forces matches the system's natural frequency, potentially leading to catastrophic failures due to the amplification of vibrations. To grasp this

concept, it's essential to consider a basic case known as the undamped harmonically excited system, which is illustrated in **Figure 3.4**.

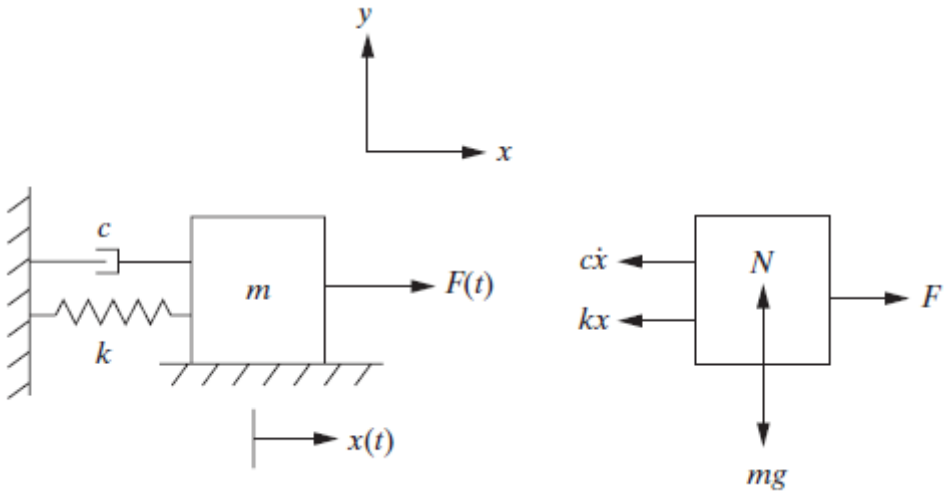

Figure 3.4. *Schematic view of a single degree of freedom dynamic system subjected to a harmonic external force* [15].

The harmonic force is defined by:

$$F(t) = F_0 \cos \omega t \tag{14}$$

Where F_0 represents the amplitude of the force applied and ω is the input frequency. In the case showed above the displacement must satisfy:

$$m\ddot{x}(t) + kx(t) = F_0 \cos \omega t \tag{15}$$

If this expression is divided by the mass:

$$\ddot{x}(t) + {\omega_n}^2 x(t) = f_0 \cos \omega t \tag{16}$$

Where $f_0 = F_0/m$. Now, to obtain the solutions to this differential equation, the particular solution must be defined, which is:

$$x_P(t) = X \cos \omega t \tag{17}$$

After substituting and other operations the following amplitude expression is obtained:

$$X = \frac{f_0}{{\omega_n}^2 - \omega^2} \tag{18}$$

In the case of harmonic excitation of damped systems something similar happens but in this case the following expression for the amplitude is obtained:

$$X = \frac{f_0}{\sqrt{({\omega_n}^2 - \omega^2) + (2\zeta\omega_n\omega)^2}} \tag{19}$$

After some operations the expression can be written by:

$$\frac{Xk}{F_0} = \frac{X{\omega_n}^2}{f_0} = \frac{1}{\sqrt{(1^2 - r^2) + (2\zeta r)^2}} \tag{20}$$

Where that ratio is known as the normalized amplitude and $r = \omega/\omega_n$ is known as the frequency ratio. In the following **Figure 3.5** can be seen the effect of resonance where $r = 1$. In poorly damped cases, the amplitude grows exponentially and if the $c = c_{cr}$ or $\zeta = 0$, an asymptote would define the amplitude in the nearby values of r.

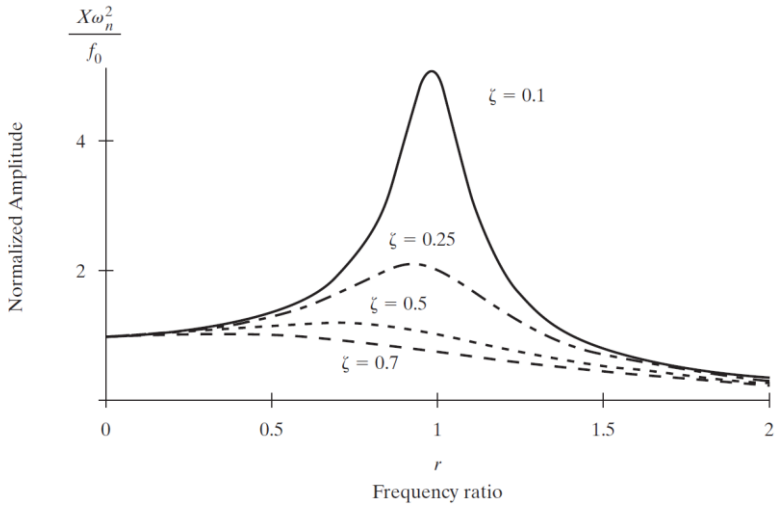

Figure 3.5. *A plot of the normalized amplitude by the Frequency ratio that illustrate the resonance phenomenon* [15]

3.2.1 Experimental Modal Analysis (EMA)

EMA is a technique utilized to determine the natural frequencies, modal shapes, and damping factors of a vibratory system. This information is crucial for the dynamic characterization of the structure or component being studied. The process begins with exciting the structure at various points across a range of frequencies, followed by measuring the responses. The collected data is then analyzed to identify the system's vibration modes.

The specific methodology to conduct EMA involves several steps, including the selection of appropriate hardware for measurement and data analysis. The hardware typically comprises exciters (such as an impact hammer or shaker), accelerometers, data acquisition systems, and specialized software for signal processing and modal parameter extraction.

Vibration testing and EMA are essential tools in the design and evaluation of mechanical and structural systems. These analyses enable engineers to better understand the dynamic behavior of systems, identify potential issues, and make modifications before large-scale production or final implementation. Additionally, they contribute to design optimization, enhancing the reliability, safety, and performance of components and systems [15].

3.3 Methodology

This section shows the selection process for the tools and methodologies utilized in the optimization of the component, defining the problem comprehensively to accurately confine the scope of concern. It describes the steps executed with each tool for obtaining optimized geometries, presents the outcomes, and identifies the best solution based on predetermined success metrics. The chapter concludes by delineating the approach adopted for the design for

manufacturing and conducting an ecodesign analysis of the final result, thereby evaluating the sustainability aspect of the study.

3.3.1 Design methodology and selection

To initiate, conducting a review of current design tools and methodologies proves insightful for selecting three distinct methodologies to achieve the best possible outcome. Research has been directed towards three promising avenues: generative design, topology optimization, and a nature-mimicking approach, as will be further explained.

The first method to be applied to the case study is generative design. This is a broad concept and has several definitions. However, ASSESS Initiative, a multi-industry organization whose objective is to bring together key players to guide and influence software tool strategies for performing model-based analysis, simulation, and systems engineering, defined generative design as “a tool that uses algorithmic methods to generate feasible designs or outcomes from a set of performance objectives, performance constraints, and design space for specified use cases” [16]. In this sense, generative design can be considered a bio-inspired design method because, as in the evolution process, different designs are explored to obtain the best result and the component is customized for specific boundary conditions.

The generative design can be based on several optimization methods such as topology optimization [17], cellular automata [18], genetic algorithms [19], or artificial intelligence systems [20].

To choose the most suitable generative design tool for this study, a review of the commercial software was performed. In order to be as precise as possible, the tools were compared based on the key capabilities indicated by ASSESS Initiative. This organization, backed by NAFEMS (International Association for the Engineering Modelling, Analysis and Simulation Community) defined 15 key points to rate generative design tools with the specific requirements each software item must accomplish to reach a rating of from 1 to 5, avoiding the subjectivity of this qualification. It should be mentioned that with the information that is publicly available for each of the tools it was not possible to qualify the 15 key points defined by the initiative. Thus, **Table 3-1** shows the 7 points that could be evaluated with the 8 commercial tools to be compared. It should be noted that this rating was made by the authors of this study and with public information without having access to any of the software. It may happen that some features of the software items are not publicly available and therefore not regarded in this qualification. In addition, it may happen that at the time of publication of this study these tools are updated; therefore, the ratings could change in some of the mentioned parameters [16].

Table 3-1. *Evaluation criteria of the 8 commercial software.*

	Handling appropriate objectives and constraints	Handling transitions from solid to lattice	Handling multiple manufacturing processes	Handling cost as an objective constraint	Enabling informed, comprehensive and efficient exploration of the viable design alternatives	Enabling efficient & effective transformation to detailed design analysis	Enabling broad accessibility to generative design	Mean rating
Ansys Discovery 2022 R2 (Canonsburg, PA, USA)	3	2	1	1	3	1	3	2.0
Autodesk Fusion 360 v2.16490 (San Francisco, CA, USA)	4	3	4	3	3	3	5	3.6
nTopology 3.45 (New York, NY, USA)	3	5	2	2	4	3	4	3.3
Dassault Systèmes CATIA Generative Design V5-6R2017 (Paris, France)	3	2	4	1	3	3	3	2.7
Altair inspire (Troy, MI, USA)	3	3	1	1	1	1	3	1.9
NX by Siemens v41.0 (Plano, TX, USA)	3	2	1	1	1	1	3	1.7
Paramatters CogniCAD 4.0 (Ontario, Canada)	3	5	2	2	2	1	5	2.9
Apex MsC 2021.3 (Stocholm, Sweden)	3	4	1	1	3	1	3	2.3

As can be seen in the table the highest scoring commercial tool is Autodesk Fusion 360. Moreover, it is not only that it has the best score, it has unlimited access for all tools for students for a limited time which is why it was also chosen. So, the first methodology to be analyzed in this work is Fusion 360, based on topology optimization by the level-set method [21]. To support the choice of this tool, IntrinSIM LLC did a review of the software on the market and came to the conclusion that AutoDesk Fusion 360 was strongly competitive with its competitors which also support the choice of the tool [22].

As a second technique, a pure topology optimization tool was employed to present a more traditional perspective. Topology optimization is iterative and boundary-condition-driven, similar to the evolutionary strategies observed in nature. This process involves an adaptive refinement of the design to meet specified loading conditions, similar to how natural structures evolve over time to adapt to environmental stresses but in a short time frame. The optimization algorithm iteratively removes material that does not significantly contribute to the structural stability, resulting in an optimized, often organic-looking form [3]. This tool is solely based on the loading conditions applied to the structure, independent of fabrication methods or design variations. Depending on the method used, elements that do not significantly contribute to the stability of the part are eliminated. As a result, a mesh with a reduced number of elements is obtained. The number of elements to be retained can be chosen by selecting an isovalue. However, exporting the final geometry can be challenging and often requires post-processing to convert the mesh into a solid. Altair Optistruct was selected as the commercial topology optimization tool due to its established heritage of utilizing traditional methods such as SIMP [23]. Additionally, the tool offers the capability to apply various objectives and constraints, including first natural frequency and volume constraint, among others.

For direct mimicking perspective, Synera was selected as the tool of choice. Synera, is a generative engineering software that utilizes algorithmic and parametric design. This allows for the reuse of design algorithms and the generation of complex geometries such as natural patterns and features. Additionally, Synera can interface with other software for topology optimization, FEA and other simulations and also has its own solvers for FEM analysis. As such, it can be considered a hybrid tool that combines true biomimicry with simulation-driven design. True biomimicry is achieved through the tool’s ability to generate and modify complex structures using geometric patterns and structures observed in nature. Within Synera, there are methods to use Voronoi cells, tree-like structures, skeleton-like structures, and some types of lattice structures. For the simulation-driven design aspect, Synera has connectors to other software to import results of different optimizations and has its own meshers and solvers for FEM analysis. It also has an optimizer based on MIDACO (Mixed Integer Distributed Ant Colony Optimization) for multi-objective optimizations based on the geometrical parameters of the part [24].

3.3.2 Eco-design analysis

This analysis delves into the environmental impact of the final product, meticulously examining the entire lifecycle from the procurement of materials and manufacturing processes of the constituent elements to the usage phase and the end-of-life disposal. This comprehensive approach underscores the study's commitment to evaluating the sustainability of the proposed solution.

The focus on ecodesign is based in a detailed pre-study, gathering essential data on aeronautical components, with a particular emphasis on the rudders and elevators of average-sized,

commonly used in commercial aircrafts. This preparatory work lays the groundwork for an informed analysis of potential environmental impacts and sustainability considerations.

A cornerstone of this study is the adoption of bioinspired design principles aimed at reducing the weight of traditional tooling without compromising mechanical properties or rigidity, particularly concerning vibrational stress. The innovative inclusion of two high-precision hexapods facilitates the adaptability of the tooling geometry to various products, marking a significant advancement in assembly technology as seen in **Figure 3.6**. The resulting design achieves a 70% reduction in weight through the use of a monolithic aluminum structure. This not only enhances efficiency but also promotes the standardization of tooling across different aircraft models, simplifying assembly line processes.

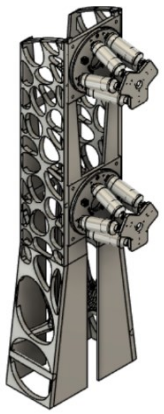

Figure 3.6. *The bioinspired outcome with the hexapods attached.*

Fig. 5. The proposed outcome with the configurable hexapods.

To initiate the comparative study, an examination of Boeing and Airbus aircraft components that matched the dimensions of the assembly column was conducted. However, certain components of the horizontal stabilizer, such as the elevator, due to their larger size, fall outside the scope of the tooling studied here. Despite this, the rudder of these aircraft could fit the criteria, and these elements have been chosen for the ecodesign study analysis.

***Table 3-2**. Rudder dimensions for different Airbus and Boeing airplanes [46].*

Airplane type	*Rudder av. Width (m)*	*Rudder height (m)*	*Rudder width bottom (m)*
A380	1.74	13.14	4.10
A340	1.40	8.49	3.31
A330	1.49	7.60	3.51
A320	0.95	5.63	2.25
B747	2.11	9.14	4.98
B767	1.42	8.11	3.36
B737	0.94	5.54	2.22

The reference tooling, as previously mentioned, is constrained by its requirement for a unique form for each component to be assembled. Each assembly line column has different curvatures to accommodate the specific part being mounted. However, the proposed bio-inspired solution, featuring two hexapods at each of its anchor points, is capable of mounting various elements while maintaining a consistent, lightweight, and optimized geometry for improved assembly operation performance.

To conduct the study, Granta Edupack software was utilized to assess the environmental impact of the component throughout its lifecycle, from raw material acquisition through energy consumption during use, and ultimately to disposal. Unfortunately, I can't display the image here, but the results comparing the two solutions—the reference design and the bio-inspired solution with hexapods—highlight significant differences in their environmental footprints.

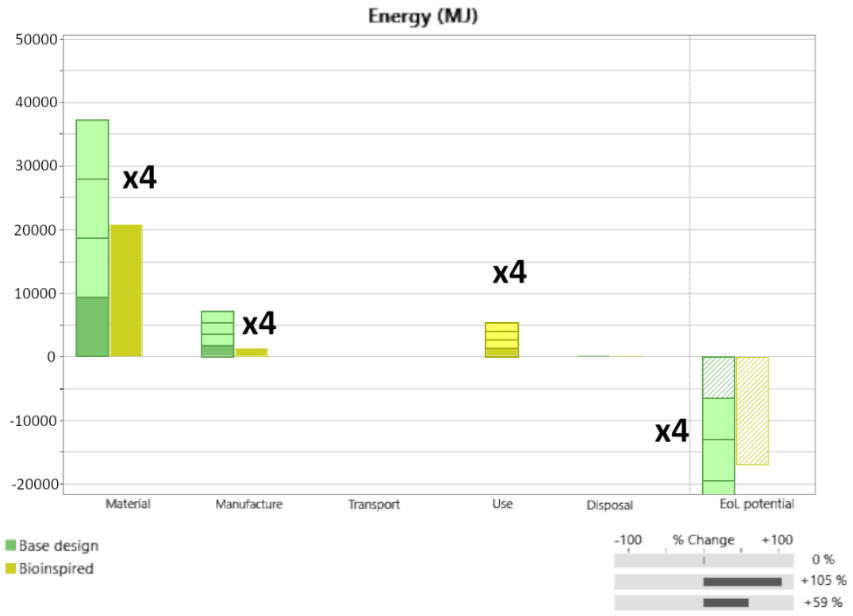

Figure 3.7. *The graphic of the results of the ecodesign analysis for two solutions.*

The analysis of energy consumption for each tooling solution considers various lifecycle stages, including material selection, manufacturing, transportation, operation, and end-of-life disposal. Analysis indicates that assembling four Airbus rudders with the reference design incurs a higher energy demand, as unique tooling geometry is required for each rudder. This aspect positions the reference design unfavorably in terms of material and manufacturing efficiency. However, unlike the passive nature of the reference design, which incurs no operational energy costs, the proposed bio-inspired solution with hexapods demands additional energy due to its active configuration capabilities for accommodating diverse geometries. Despite this, the bio-inspired solution demonstrates an overall enhancement in energy efficiency across aeronautical assembly lines, potentially reducing the carbon footprint. It's pertinent to highlight that the bio-inspired approach is presently in a prototype stage, suggesting that optimization of manufacturing processes could yield further improvements in energy consumption.

3.3.3 Problem definition

The focus of this chapter revolves around the innovation and optimization of an aeronautical assembly column, a fundamental component envisioned to revolutionize future jigless assembly tools. This advancement aims to significantly enhance assembly line flexibility, markedly reducing the necessity for a multitude of tools, shimming practices, and associated costs. By transitioning from traditional jigs to more sophisticated fixtures and ultimately to a metrology-assisted assembly approach, aerospace assembly companies can navigate towards more efficient processes. The aerospace assembly, characterized by the integration of large structures necessitating precise tolerances alongside extensive drilling and riveting operations, currently relies heavily on fixed toolings or jigs. These are crucial for positioning and assembling components accurately according to stringent specifications, consuming about 5% of the total manufacturing costs of an aircraft, or 10% of the aircraft structure's cost.

A primary objective within the assembly sector is to curtail costs and assembly times linked to fixed toolings through diminishing their use and augmenting their reconfigurability and reusability. The ultimate vision is to minimize tooling dependence to the extent where the most efficient tooling is essentially nonexistent, leveraging the inherent benefits of increased flexibility and reduced necessity for physical tooling.

Challenges in optimizing the assembly column are multi-faceted, encompassing the reduction of tooling mass while ensuring consistent part quality and enhancing rigidity. Achieving a sufficiently high first eigenvalue is critical to prevent catastrophic failures during vibrational activities such as drilling. The envisioned optimization aims to not only lighten the fixed structure, thereby improving its rigidity and vibrational response characteristics but also to introduce mobility and adaptability into the structure.

The introduction of a hexapod system into the optimized structure marks a pivotal innovation, enabling the assembly column to be auto-aligning and readily movable across various product assembly lines.



Figure 3.8. *The wing skin panels for Boeing's first 737 MAX airplane are loaded on fixtures into an automated assembly machine in the company's plant in Renton, Wash., on 2 June 2015 (source:* [25]*) [**left**]. The simplified reference design of the assembly column based on the fixtures used in assembly lines [**right**].*

The reference design is built by welded and bolted parts of structural steel, with a total weight of 344 kg and its first eigenfrequency is 42 Hz. The design envelope used for the optimization in this study would be the volume filled by the reference design. Which its bounding box has the following dimensions: 300x600x2200mm.

Loads, constraints and objectives

A common goal of the design of structures is to avoid resonance of the structure in a given interval for external excitation frequencies. This can be achieved by maximizing the fundamental eigenfrequency [26], [27]. For drilling processes in the aircraft industry, the speed for a 6 mm drill bit is approximately 3000 rpm for materials such as aluminum or Carbon Fiber Reinforced

Polymers (CFRPs) [28], [29]. This equates to a rotational speed of 50 turns per second or 50 Hz. To ensure an acceptable safety margin, the limit for this case is set at 60 Hz.

The structure must be capable of supporting different load cases. Operational loads, which account for mounting operations such as drilling and riveting, and structural loads, which are defined by the weight of the supported structure (vertical loads in fixations), must both be considered.

Operational loads are more complex to predict and can be more detrimental than structural loads. Therefore, for design purposes, various configurations of operational loads have been selected with a value of 1000 N per fixation (each column has two). Since the loads can come from different directions as seen in **Figure 3.9**, the load cases to be studied are:

1. 1000 N for each fixation in −X direction
2. 1000 N for each fixation in +X direction
3. 1000 N for each fixation, upper fixation with −X and the lower fixation with +X direction
4. 1000 N for each fixation, upper fixation with +X and the lower fixation with −X direction

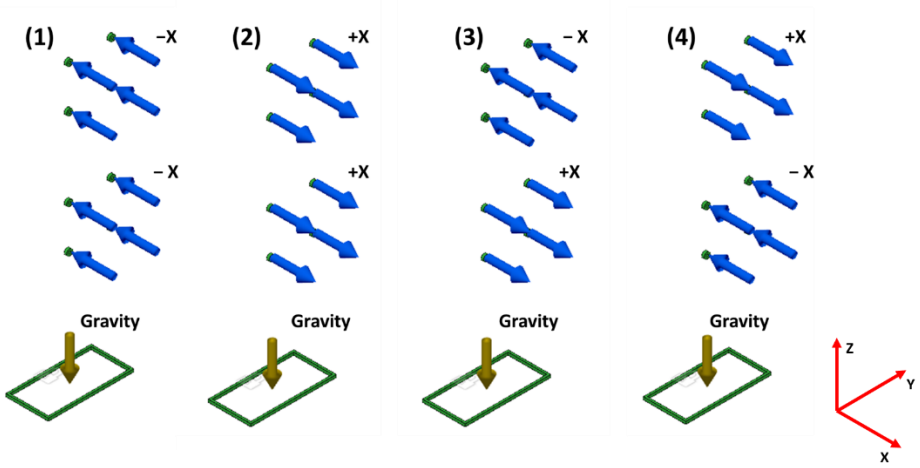

Figure 3.9. *Operational load case graphic expression.*

Suppose that this assembly column will be used to assemble the wing of a Boeing 737, having a total span of 35.8 m (according to [30]) and knowing that the wings are assembled separately, half of this span is taken, 17 m. It is also known that the wing area of this aircraft is 124 m^2 and it is assumed that the average thickness of the covering of the structure is 5 mm (it can vary between 1 and 10 mm). The total volume of the material of the wing's covering would be:

$$V = S \times t \times 2 = 62\text{m}^2 \times 0.005\text{m} \times 2 = 0.62\text{m}^3 \quad (21)$$

where *S* is the surface area and *t* is the average thickness of the soffit. The cladding material can be aluminum or CFRP with densities of 2700 kg/m^3 and 1550 kg/m^3, respectively. Therefore, the weight in aluminum would be 1674 kg and in CFRP 961 kg. In addition, it would be necessary to add the stringers and ribs that can also be of both materials, which are usually 400 kg for aluminum and 250 kg in CFRP. The total weight of the wing would be 2074 kg in aluminum and 1211 kg in CFRP. The assembly columns of this type are usually placed one every meter; therefore, 17 + 1 should be placed. The weight distribution for each column would be 115 kg if the wing was made of aluminum and 67 kg if it was made of CFRP. This translates into 1130 N and 657 N,

respectively. As the system is intended to be as flexible as possible, the most restrictive value will be taken and a safety factor of almost double will be applied. This value will be 2000 N to be supported by each column. The safety factor for the whole study is defined as a ratio between the reference maximum admissible value and the value we want to compare with.

Manufacturing process

Designs inspired by nature often feature complex topologies. Manufacturing these components poses the greatest challenge in the process. Often, such designs are costly in terms of both computational time and labor. However, executing them also presents an additional technological challenge. Therefore, design methods that take into account the manufacturing process have a significant advantage over other design methods.

Traditional manufacturing processes are often not suitable for parts with bioinspired topologies, especially when dealing with large and complex pieces. In the case of the project under consideration, traditional machining methods were not feasible due to the size and complexity of the desired component. Therefore, manufacturing was limited to casting or additive manufacturing processes, with machining used only to achieve specific tolerances on certain surfaces or holes.

Casting is an ancient yet still highly versatile method for metal fabrication. There are various casting methods, some of which require expensive, durable molds but come with design limitations, such as the injection molding process. Injection molding is often efficient for large parts, while for more complex parts, expendable wax or sand molds can be used, although this can be costly per part.

Additive manufacturing encompasses a variety of methods, some of which allow for great complexity in design. However, this process is often expensive and time-consuming, especially for large parts like the one in the project being considered. Therefore, additive manufacturing was not a viable option.

In summary, given that traditional machining methods and additive manufacturing were ruled out, the remaining option was casting. Given the complexity and size of the part, casting with expendable sand molds appears to be the best option. Additionally, gravity will be used as the method of mold filling. Manufacturing such a complex sand mold will require additive manufacturing of multiple parts, specifically through binder jetting.

Material selection

Focusing on the manufacturing process of gravity sand casting, selecting a consistent alloy suitable for this specific method becomes crucial. Given the objectives of mass reduction and recyclability, a Si-based aluminum alloy was chosen for its favorable characteristics tailored to gravity sand casting. This alloy's relatively low viscosity is particularly advantageous, facilitating the flow and fill of the mold in the gravity sand casting process [31]. The mechanical properties of this alloy, including a Young's modulus of 71 GPa, a density of 2700 g/cm^3, a Poisson's Ratio of 0.33, and a yield stress of 170 MPa, are considered [32]. While Cu- or Zn-based Al alloys might offer superior properties, their higher viscosity could complicate the casting process, potentially affecting the quality and integrity of the cast parts. Therefore, the chosen Si-based aluminum alloy represents an optimal balance between processability and performance for gravity sand casting, aligning with the goals of efficient manufacturing and sustainability.

3.3.4 Design and optimization

In the next sections, the already presented use case is going to be used as an example so the reference design is optimized with different bio-inspired design methods. The methodologies are going to be precisely described so the outcomes can be resembled for future studies.

Generative Design with Level-Set Topology Optimization (Fusion 360)

In Autodesk Fusion 360 v2.0.16490 (F360), the available design space is also divided into two different sections as shown in Figure 4, comparable to the approach in Altair Optistruct. The preserved geometry, or non-design geometry, refers to the parts of the design that must be included in the generative design outcome. In this case, this includes the base of the column and the holes for the fixations. The obstacle geometry defines the boundaries of the design and sets the limits for the outcome generated by the software. The design and non-design can be seen in **Figure 3.10**.

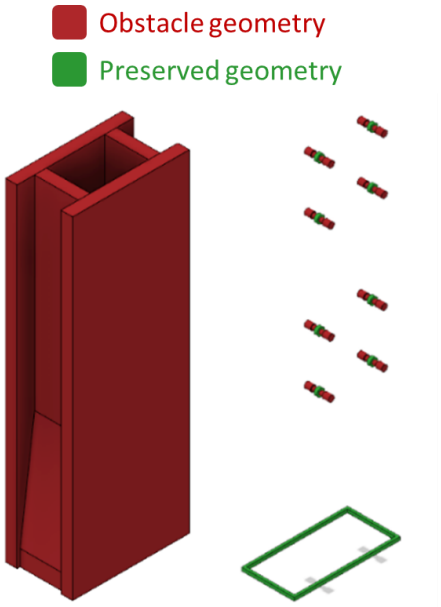

Figure 3.10. *Outside boundary of the obstacle geometry (**left**) and preserve geometry and tool clearance obstacle geometry (**right**) of the Fusion 360 simulation.*

Fusion 360 has the option to select the manufacturing method and the objectives and limits of the design. For this study, as the main objective was to have the best design no matter the manufacturing process, the unrestricted mode was selected. The objective of the design can be set as minimize mass or maximize stiffness. And as limits, a minimum safety factor, a minimum first frequency mode, or/and a minimum displacement can be imposed. Vibrational stability is crucial for an assembly column, so a constraint was set to ensure that the first mode is above 60 Hz. To achieve symmetric designs without geometric singularities, the outcomes from Fusion 360 must be post-processed. A graphic view of the outcome can be seen in **Figure 3.11**.

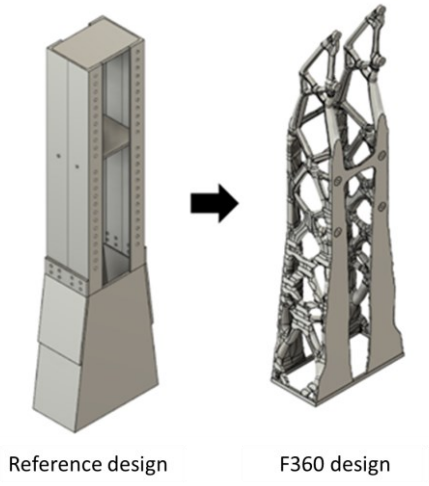

Figure 3.11. *Evolution of designs in Fusion 360. Reference design and F360 design.*

SIMP Topology Optimization (Altair Optistruct)

To perform this SIMP Topology Optimization analysis, the design geometry and a non-design geometry is defined, as shown in the **Figure 3.12**. The design space occupies the same volume as the reference design and has holes that allow assembly tooling, the so-called tool clearance. The non-design space consists of a base of the structure and the holes where the fixations are screwed.

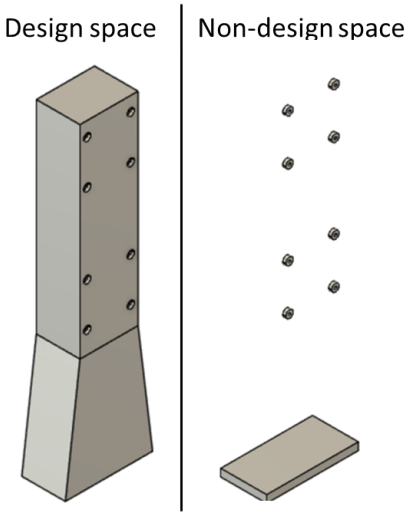

Figure 3.12. *Design space (**left**) and non-design geometry (**right**) for Altair Optistruct Topology Optimization.*

To mesh the two geometries, 7 mm trias elements were selected. A static structural study was defined as an FE simulation. The topology design variable was defined with symmetry on the XZ plane, as there are no asymmetric loads on the structure. To determine the type of result to be obtained, the constraints and objectives of the simulation were selected. The volume fraction of removed material was constrained to be less than 6.25% and the first vibration mode of the system was required to be higher than 60 Hz. The objective of the optimization was to minimize compliance while considering a weighted response of the four operational load cases. The result of the topology optimization is shown in **Figure 3.13**.

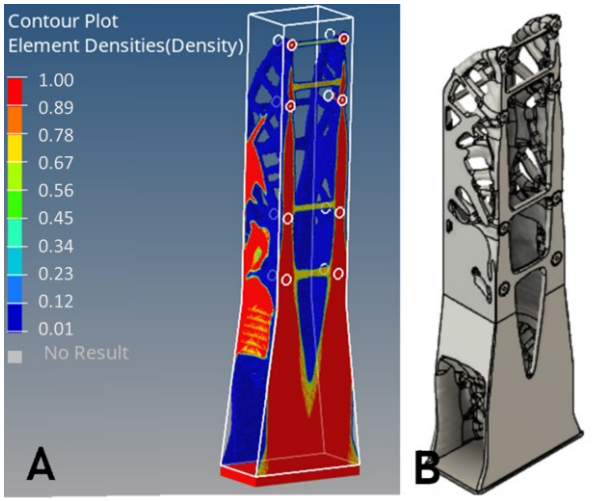

Figure 3.13. *(**A**) Optistruct topology optimization result in element density plot. (**B**) Outcome of the simulation translated into a solid.*

Hybrid Method (Generative Engineering) (Synera)

The method used in this case study is a hybrid method called generative engineering. With the help of the Synera commercial tool, which has capabilities for parametric design, connectivity with different engineering software items, i.e., Hypermesh and optimization, and natural geometrical patterns can be optimized and guided towards specific functionality. Two different designs were obtained for this case study: one based on the skeleton method and the other on the Voronoi pattern. Both designs are partially based on the results of topology optimization but apply these true biomimicry perspectives and enhance the result with parametric optimization.

To ensure efficient stress distribution, the unions between elements in both cases are based in the morphology of joints seen in nature, specifically in diatoms [33]. Notably, these natural structures often employ rounded and smooth joints between structural elements, a design feature critical for mitigating stress concentrations. Such configurations are instrumental in distributing mechanical loads more evenly, thereby enhancing the overall structural integrity. The structural efficiency of diatoms was studied experimentally and with FEM in [34] showing a remarkable ability to withstand applied forces.

The parameter optimization, as mentioned earlier, is based in the MIDACO solver. In the approach presented in this study, the optimization process involves the careful selection of various geometrical parameters of the design. These parameters are then subjected to a series of optimization steps, where different responses are evaluated to converge on what we define as the 'optimal result.' This process is not just about optimizing a single objective; instead, it entails balancing multiple objectives to achieve a design that represents the best compromise among these various goals.

The skeleton method involves extracting load lines from topology optimization analysis and assigning diameters to these lines to create a strut-like structure. Parameter optimization is conducted on the diameters of the stiffeners to achieve the optimal geometry for the design. In this process, the lateral skeletons are assigned a uniform diameter along their length, which is included as a key parameter in the optimization. Conversely, the vertical skeletons are designed with a gradient-based decreasing diameter as their height increases, a specification also determined through parameter optimization as seen in **Figure 3.14**. The parameters thus

comprise the constant diameter of each lateral skeleton element and the range (initial and final diameters) for the vertical skeletons. This optimization is informed by critical factors such as maximum stress, maximum deformation, and the first eigenfrequency. The integration of these parameters facilitates the setup of a comprehensive study, culminating in the precise dimensioning of the Skeleton design. The skeleton method design was selected for its known structural stability in natural organisms such as diatoms and radiolarians [33].

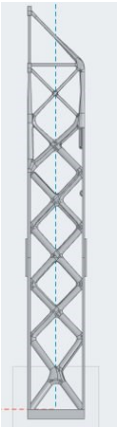

Figure 3.14. *Skeleton diameter distribution after parameter optimization.*

The Voronoi pattern is also based on topology optimization results but is applied based on the voids appearing in the extracted load lines; see **Figure 3.15**. The Voronoi option was selected based on its similarity to the dragonfly wing structure which flaps its wings at 32.3 Hz during hover flight and has a first vibration mode of 154 Hz—4.8 times higher—potentially providing greater stiffness and raising the first vibrational mode [35]. In this design, reinforcement was achieved through the incorporation of skeleton-based features, which were strategically aligned with the internal load lines of the structure for optimal stability. The optimization parameters were carefully chosen to include the thickness of the Voronoi cell separations and the thickness of the walls themselves, along with the diameter of the skeleton elements. The selection of the final design was informed by a detailed analysis of stress and deformation, as well as the first eigenfrequency results for these specified parameters, ensuring a design that is both structurally sound and efficient.

These two outcomes are referred to as Skeleton design and Voronoi design, respectively. Both can be seen in **Figure 3.16**.

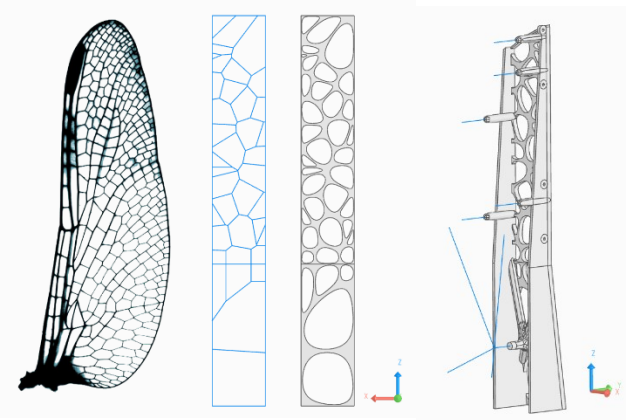

Figure 3.15. *The Voronoi distribution according to the load lines from Topology Optimization (**left**). Skeleton lines extracted from the Topology Optimization (**right**).*

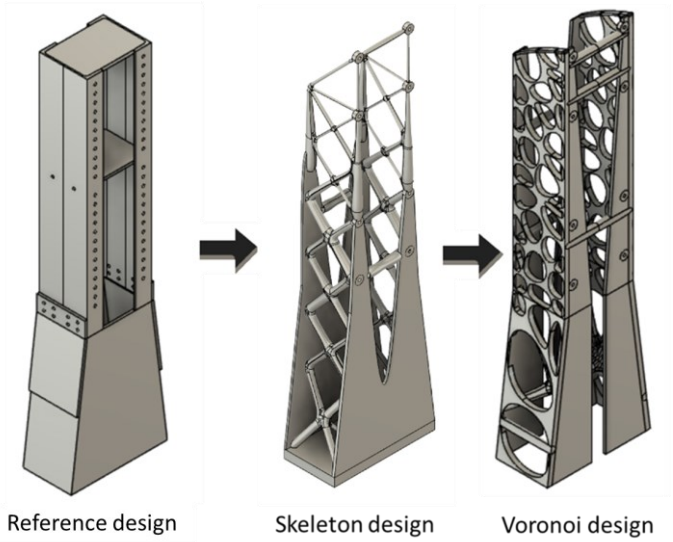

Figure 3.16. *Evolution of designs in Synera. Reference design, Skeleton design, and Voronoi design.*

3.3.5 Outcome selection and validation

The section initiates with the exposition of simulation outcomes for products developed from varied design methodologies. The purpose is to systematically evaluate the performance of each product, utilizing simulation as a critical assessment tool. Following the comprehensive examination of simulation data, a detailed analysis is conducted to identify the most advantageous solution.

Subsequently, attention is directed towards conducting a fatigue analysis of the selected design solution. This step is pivotal for assessing the design's endurance and reliability under conditions of repetitive stress and usage. The fatigue analysis aims to confirm the design's capability to meet and exceed established performance and longevity criteria, thereby affirming its feasibility for practical implementation. This process ensures that the final design choice is not only

theoretically sound but also validated for real-world application, emphasizing its scientific rigor and applicability.

Results

To perform the structural analysis of all outcomes, ANSYS Workbench 2020 software has been chosen. In this way, convergent conclusions are obtained due to the use of the same software for each solution. In the **Table 3-3**, the values of all the relevant factors are summarized.

Table 3-3. *Summary of the results of all designs where mass, first eigenfrequency, maximum Von Mises stress, maximum displacements and safety factor are shown. Note that SI stands for Skeleton Improved design.*

Name	*Mass (kg)*	*Max D. Eigenfreq (mm)*	*Eigenfreq. (Hz)*	*MaxVM Stress (MPa)*	*MaxD. Loads (mm)*	*SF*	*D/H1 Loads [x1000]*	*D/H2 Loads [x1000]*
Reference	344.76	4.14	42.08	0.90	0.009	277.78	0.004	1.939
F360	89.08	17.68	63.65	1.12	0.031	250.00	0.014	8.281
TO	153.05	14.63	61.8	3.88	0.026	72.16	0.012	6.852
Skeleton	85.23	22.06	64.63	2.65	0.064	105.66	0.030	10.331
Voronoi	90.61	8.98	60.80	1.87	0.021	149.73	0.010	4.206

Discussion

Table 3-3 shows the results of the modal and static-structural analyses performed on each of the designs. The reference design stands out for being the heaviest (344.76 kg) due to being the already existing one built with structural steel. In addition, the Skeleton design outcome stands out for being the lightest (85.23 kg). **Figure 3.17** compares the values of each of the five factors that determine the quality of the design divided by the maximum so that the graph is on a common percentage scale. The five factors that best define a successful design are mass, first natural frequency, Von Mises maximum stress safety factor, the maximum deformation ratio to total height of the structure for the load cases, and the same ratio for the resonance at the first natural frequency. The limit of each of these factors has been drawn (black dashed line) which the values cannot fall below or exceed depending on the magnitude being looked at. Therefore, the area shaded in yellow represents the areas where the design happens to be within acceptable margins.

- Mass: 100 kg to reduce the mass to 30% of the reference design. If the design is lighter than this limit; it would be accepted.
- First eigenfrequency: Minimum first natural frequency of 60 Hz. All the designs with a lower value are rejected.
- Safety factor: Limit of a minimum safety factor 40 as a sufficiently laudable value for tooling structures. Values below this limit are rejected.
- Deformation to height ratio: Two different values for two different studies, one for the load cases (operational and structural) and other for the case of resonance. The limit was set to a value a bit bigger than the average of all, so the most deviated deformations are discarded. Thus, the results above those limits are rejected.

Looking at the results concerning mass, it can be seen that two of the five designs are outside the acceptable area. That is, the reference (344.76 kg) and the TO (153.05 kg) would be discarded. The F360 (89.08 kg), the skeleton design (85,225 kg), and the Voronoi design (90.61 kg) would be

inside the margin. Regarding the first vibrational mode, being a factor of great importance in the acceptance of the designs, all designs achieved the established limit. The same occurs with the safety factor and the deformation-to-height ratio when supporting the load cases. Up to this point, based on mass criteria, two designs would have been discarded. Finally, observing the ratio of deformation per height of the structure for the first eigenfrequency, it can be seen that the F360 outcome and the skeleton results are outside the limit. The highest deformation was found for the Skeleton design and the F360 outcome, which a priori in terms of mass and structural characteristics seemed to be the best results obtained in this study.

The Voronoi-based design, situated uniquely within the defined margins, exhibits superior deformation characteristics in comparison to other designs. Significative enhancements in deformation behavior are observed across both scenarios—the first eigenfrequency and various load cases—distinguishing it as the second-best performer in the latter and the optimal choice under resonance, with the exception of the reference design, as can be observed in **Figure 3.17** and **Figure 3.18**. This finding suggests that, analogous to the structural attributes observed in dragonfly wings [35], Voronoi structures—as the results demonstrate—show a remarkable stiffness, surpassing even designs explicitly tailored to fulfill precise vibrational criteria.

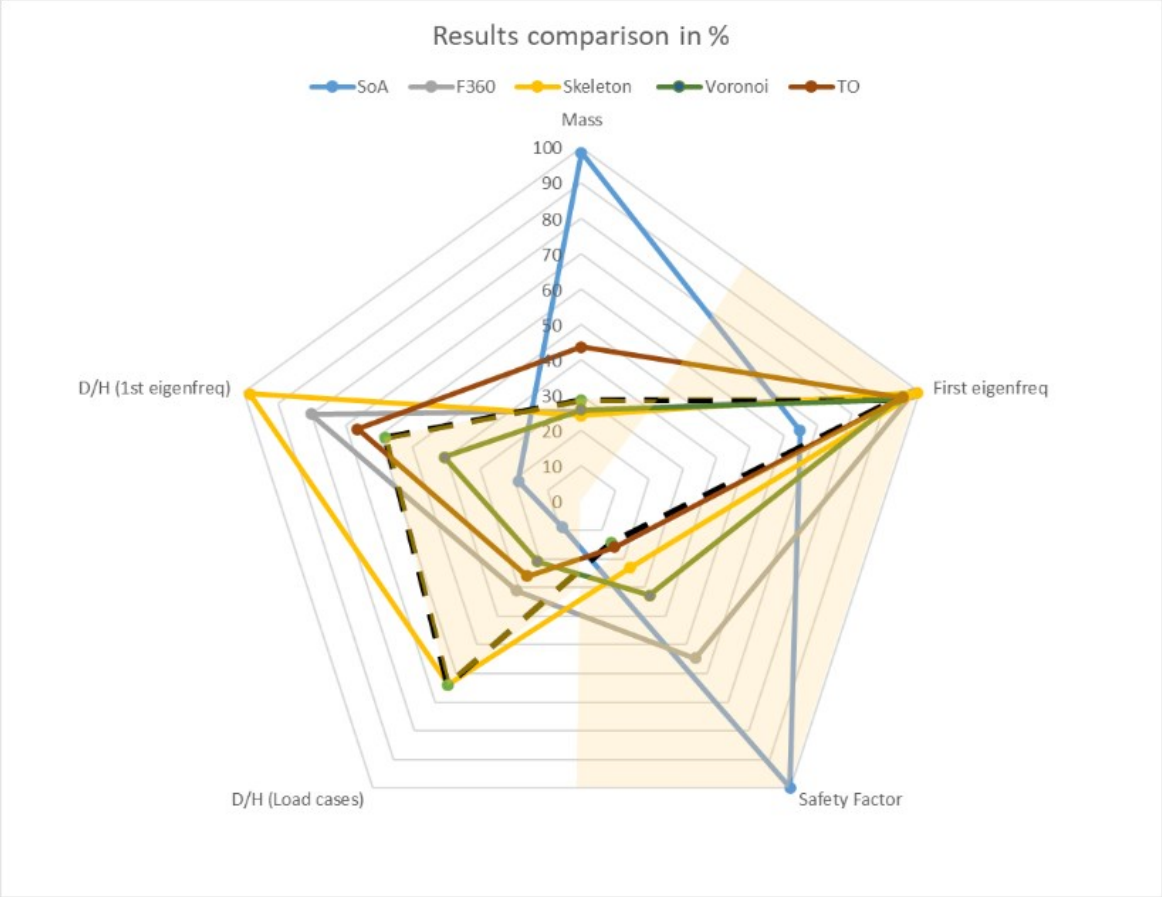

Figure 3.17. *Representation of the results in a percentage scale so it is possible to compare each of the designs with the others. Furthermore, a limit has been set to accept the outcomes. This limit is represented as a black dashed line and the yellow shaded areas are the ones that serve as graphic representations of acceptable values for each of the factors. Artwork made with MS Excel.*

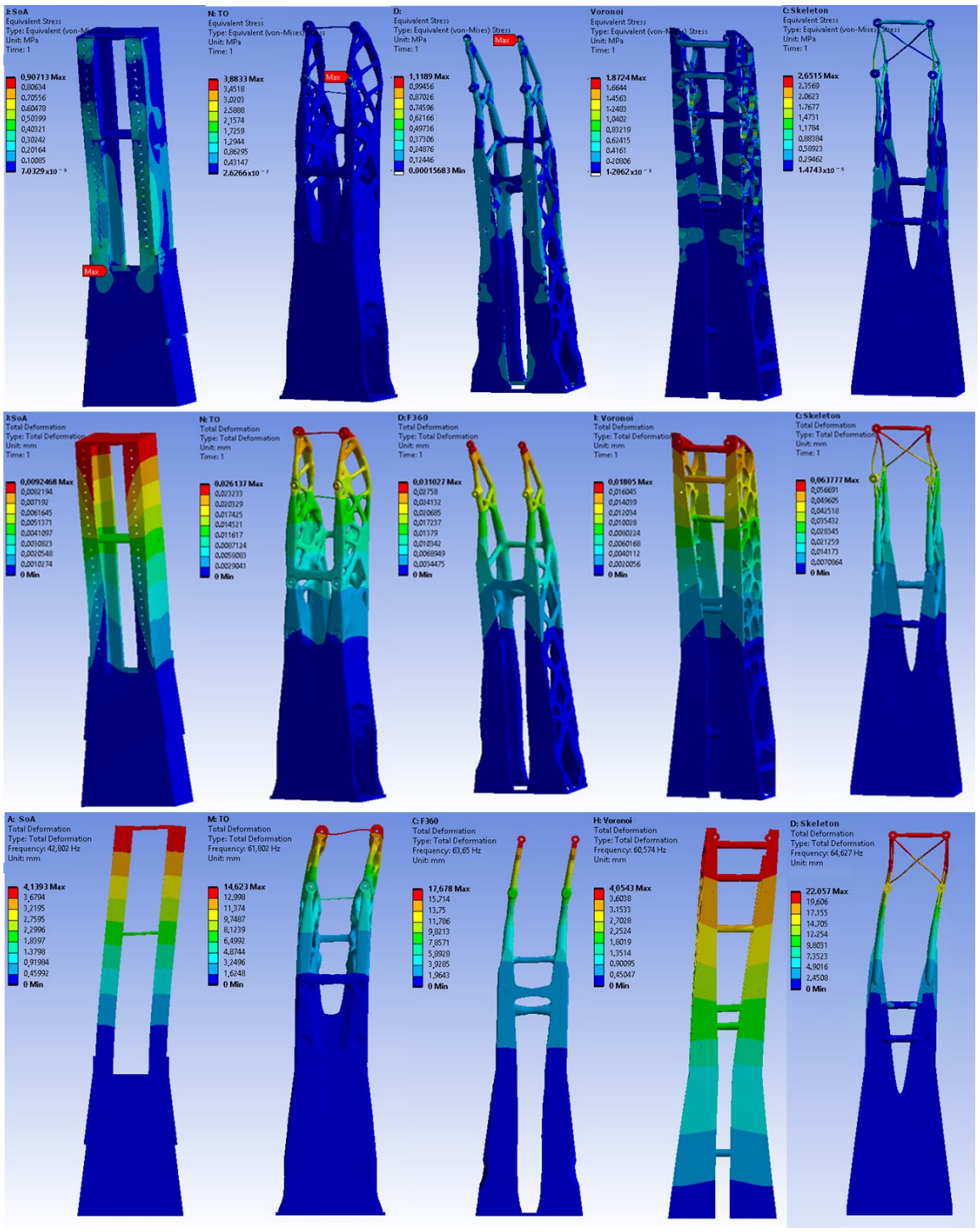

Reference design→ *TO design→* *F360 design→* *Voronoi design→* *Skeleton design*

Figure 3.18. *(**Top**) Von Mises equivalent stress diagram in MPa for the 5 solutions with the initial load cases. (**Middle**) Deformation in mm of the 5 solutions for the initial load cases (**Bottom**).*

In the realm of bioinspired design, understanding the long-term durability and resilience of structures under repetitive stress conditions is of great importance. This is particularly true for this study, where the goal is to optimize aeronautical tooling using bioinspired methods. To this end, a comprehensive fatigue analysis was incorporated into this research. This analysis is focused on the selected design, which, although generally exhibiting non-significant stress levels under standard operating conditions, may still benefit from a detailed evaluation of its fatigue properties. By examining the fatigue behavior of the selected bioinspired design, it is intended to provide a deeper insight on how the outcome is far from failure, which is of great importance in this kind of application.

The first step is to check which are the maximum and minimum stress values under the worst cases presented before. In this particular case, the maximum Von Mises equivalent stress is going to be the criteria to define the amplitude of the cyclic loading. The equivalent Von Mises stress is considered as a conservative method since it does not take into account the sign of the stress [36]. However, this case needs to be conservative for its application. As seen in **Figure 3.19**, the maximum Von Mises values for the worst case (loads of part weight and operations applied) is 3.1051 MPa and the minimum is 0 MPa.

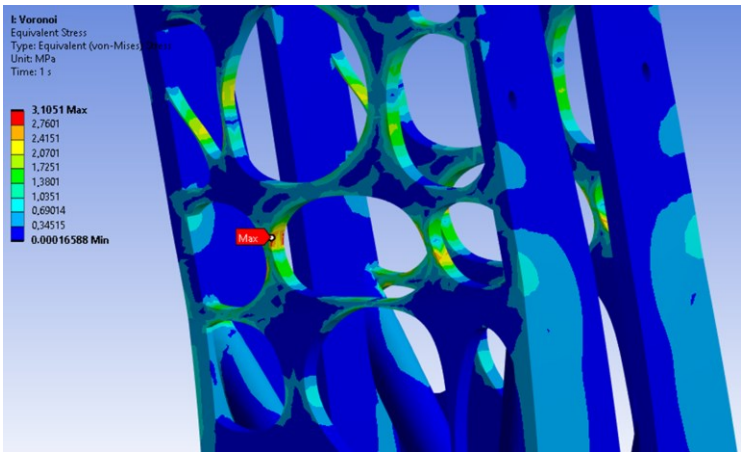

Figure 3.19. *Maximum equivalent Von Mises stress for the worst load case scenario in the Voronoi outcome.*

To study fatigue, the graphic from [37] has to be modified since the fatigue criteria are prepared for rotary samples and not axial tension samples. The modifying parameters for aluminum alloys are given by [38].

$$\sigma_e = \frac{1}{K_D}\sigma'_N \tag{22}$$

where σ_e is the modified fatigue limit and σ'_N is the stress for the rotary sample and $\sigma_N = 0.9 \cdot \sigma'_N$ where σ_N is the stress value for the axial alternating stress sample [39]. K_D is defined by:

$$K_D = \frac{K_F}{\beta\ \varepsilon} \tag{23}$$

where K_F is known as the fatigue notch coefficient, β is the surface quality factor, and ε is the size factor. Both ε and β are taken from empirical equations [40]; ε is supposed to be 1 as a first

approach, while β depends on the UTS of the material and the surface roughness. In this case, the structure would be a ground surface, so the coefficient is 0.961 for AlSi110 Mg.

K_F depends on q, notch sensitivity, and K_T, the stress concentration factor. q for aluminum alloys is 0.483 [41] and K_T is defined by the problem studied. For the purpose of calculating the stress concentration factor (K_T), the case study was simplified to represent the bending of a plate with an elliptical hole. This simplification serves as a proxy for the more complex geometries observed at the sides of the Voronoi structure, as seen in **Figure 3.20** [41].

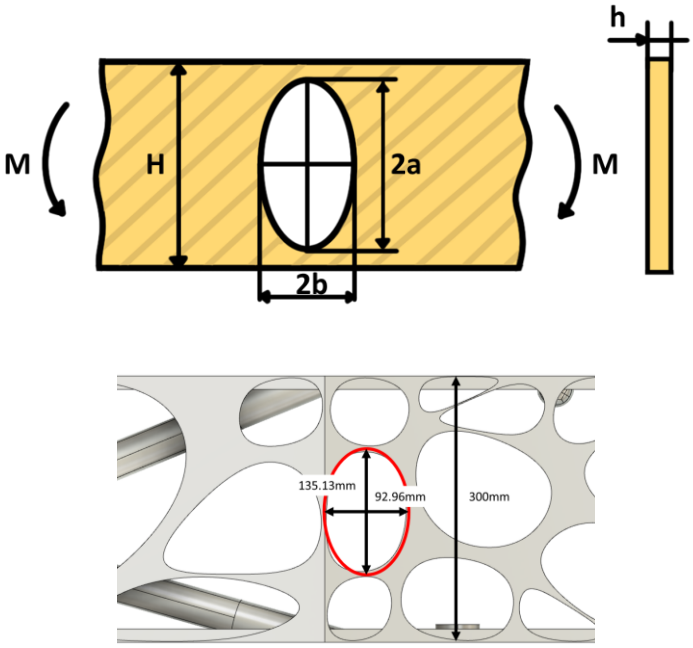

Figure 3.20. *Bending of an infinite and of a finite width plate with a single elliptical hole stress concentration factor case as defined by* [41] *(**top**). The case analyzed in this study with the real dimensions (**bottom**).*

Once all the correction parameters are defined, the new S-N curve for the AlSi10Mg alloy is given in the next **Figure 3.21**.

The fatigue is analyzed for 10^6 cycles and with the Goodman criteria, as can be seen in Figure 15. As predicted, with the load case studied here, the outcome is far from the Goodman line, which means that it is far from failure because of fatigue.

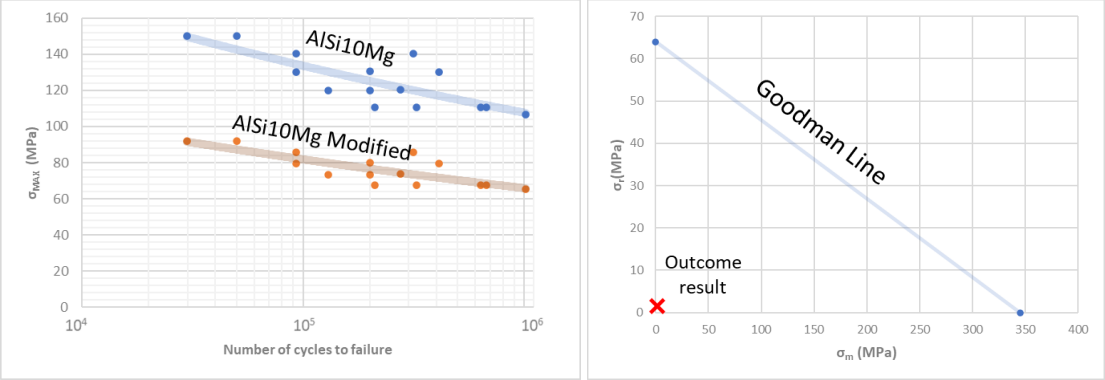

***Figure 3.21**. S-N curve for AlSi10Mg alloy and the modified curve to meet the axial tension samples (**left**). Goodman line and the situation of the outcome for the studied load case (**right**).*

3.3.6 Design for manufacturing

Following the determination of the optimized design and the selection of the manufacturing method, the next step involves refining the current geometry to ensure it is conducive to the chosen fabrication process. Given the selection of a casting method, this necessitates the careful design of the gating and feeding system. This process is critical as it ensures the molten material is adequately and efficiently directed into the mold, while also providing for the necessary paths for gases and excess material to escape or be stored until solidification occurs.

First the design had to be partially modified to be correctly casted. There were two constraints to be considered: a minimum thickness of 7 mm and to round all the sharp edges. Some ribs inside the Voronoi pattern needed to be modified, but the rest of the pattern was suitable for casting as seen in **Figure 3.22**. The geometrical changes did not change significantly, nor the weight, nor the structural behavior of the component.

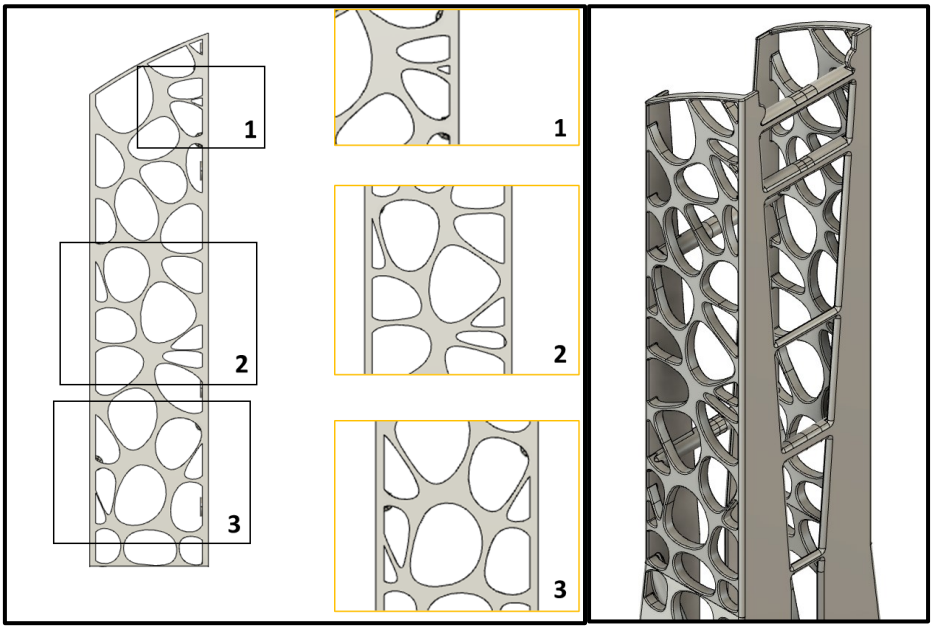

Figure 3.22. *Changes in the structure according to the manufacturing constraints. Wall thickness correction bigger than 7 mm (**left**) and rounding of sharp edges (**right**).*

Casting design

To conduct casting with a low risk of failure, accurately designing casting components is crucial. This means having well-sized filling and feeding systems to prevent surprises during the process. Parts with greater mass often lead to irregularities because the molten metal solidifies slower in those areas, resulting in porosity within the part. These defects often result from the material contracting unevenly as it solidifies (isolated molten areas), potentially leading to critical integrity issues.

Therefore, minimizing casting process defects necessitates a robust design of the filling and feeding systems, involving the following steps:

1. **Material Selection**: The first step is selecting the appropriate material for the part. For this project, an AlSi10Mg known commercially as Silafont-36 was chosen for its lightweight characteristics and suitable castability. This material's mechanical, thermal, and fluid dynamics properties align well with the project's requirements.

2. **Design of the Gating System**: The gating system comprises the network of channels guiding the liquid metal to the mold cavity. It includes the sprue, pouring cup, sprue well, runner, and gate or entry. The first task is to determine the optimal casting orientation, ensuring uniform and efficient filling by gravity. Vertical placements, as seen in scenarios A and B shown in **Figure 3.23**, extend the molten metal's travel distance, making these approaches impractical. Thus, casting with the part placed horizontally is preferred. Feeding from the bottom ensures even filling of the entire part, particularly important for the most voluminous sections where the molten metal should arrive first, making position C the most favorable for successful casting.

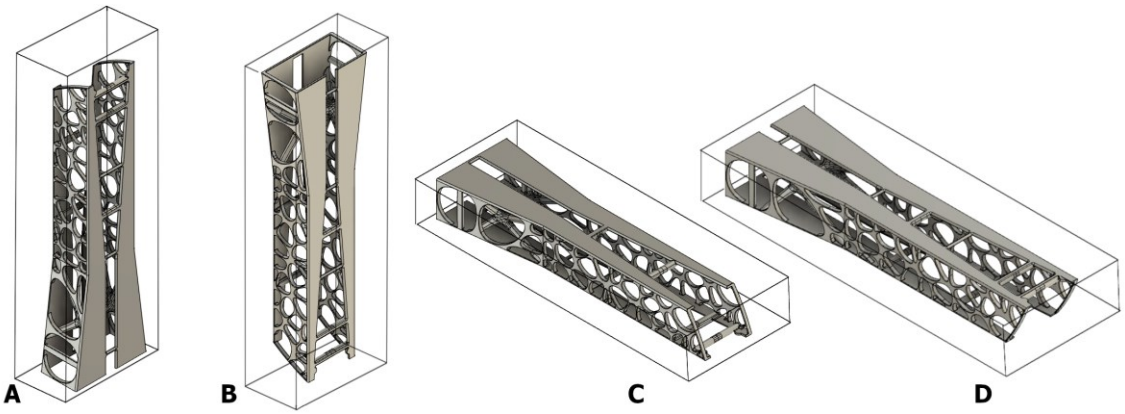

Figure 3.23. *All the possibilities of filling orientations for the part.*

In the process of designing for gravity sand casting, choosing the appropriate point for pouring the molten metal is crucial, especially since the pour will occur at a single point. Similar to selecting the orientation, the area where the most voluminous part of the casting is located needs to be considered to ensure the hottest molten metal reaches this critical point first. Consequently, the filling area must be positioned at the widest part of the casting to facilitate optimal Flow as seen in **Figure 3.24**.

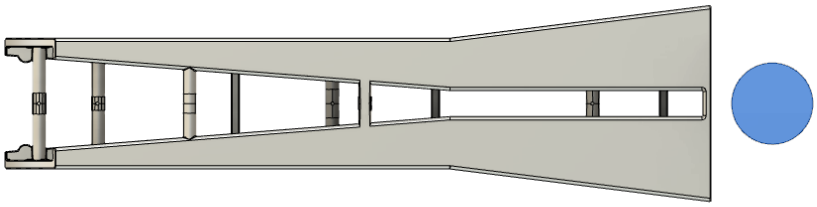

Figure 3.24*. Metal pouring point at the bottom of the area with bigger mass in blue color.*

Feeding channels should run parallel to the casting on both sides, with the gates positioned at the bottom as previously discussed. These channels will also be at the same height. The size of the gates is constrained by the thickness of the casting in the area where it will be fed. The placement points for these gates should be in areas that allow for the flow of molten metal across other parts of the casting, as illustrated in the **Figure 3.25**.

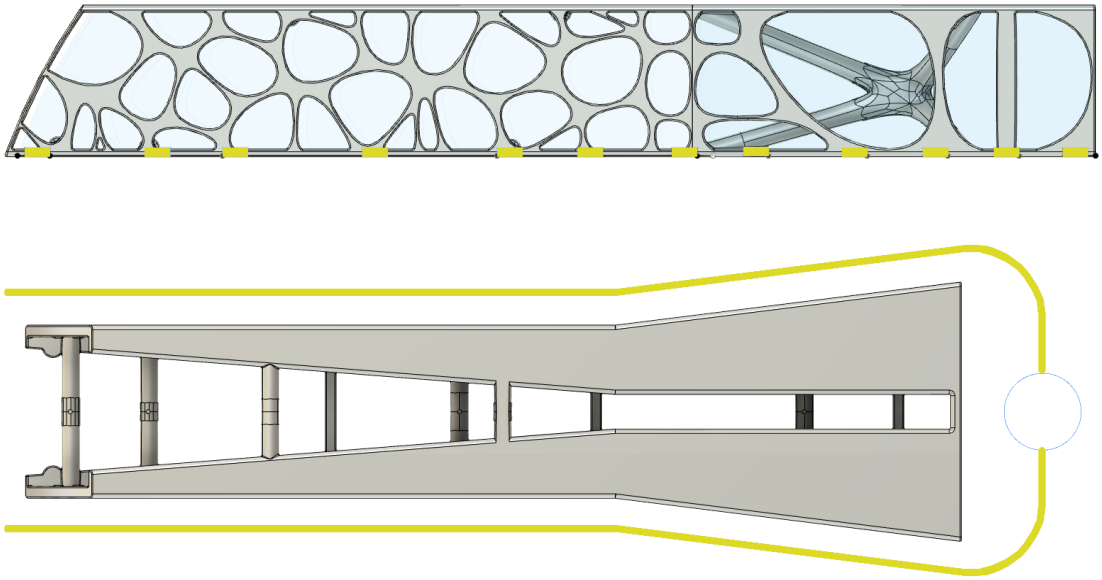

Figure 3.25. *Gating system layout in yellow.*

For the sprue, instead of designing the pouring cup, neck, and sprue itself, a commercial sleeve has been chosen. Given the large size of the casting, it's necessary to pour as much molten metal as quickly as possible to ensure the material fills the casting promptly. Assuming a desired flow diameter of 80mm, consulting the FOSECO catalog seen in the **Figure 3.26** reveals that the XTAE models are the only ones with a similar outlet diameter. To minimize turbulence, the XTAE 21/25 has been selected.

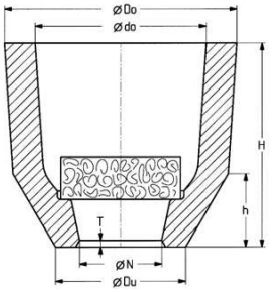

KALPUR Moldeable

Type	Module	Filter Ø	Nominal Dimensions (mm)							Vol.
	(cm)	(mm)	Du	N	Do	do	H	h	T	(dm^3)
ZTAE 10/12	2,50	70	76	48	136	100	120	43	4	0,68
ZTAE 12/15	3,00	90	96	60	157	120	151	45	4	1,29
ZTAE 15/18	3,70	125	120	70	191	152	181	55	5	2,57
ZTAE 18/20	4,30	150	130	86	221	174	200	80	6	3,78
XTAE 21/25	5,30	175	150	100	250	200	250	100	6	6,25
XTAE 23/25	5,80	200	160	110	278	225	250	110	6	7,75

Figure 3.26. *Sleeve of the sprue KALPUR model from FOSECO.* [42]

In calculating the gating system, it's essential to consider that the cross-sectional area of the sprue must be larger than that of the runners, and the runners must have a larger cross-section than the gates. This setup ensures the molten metal accelerates as it flows through the casting system, adhering to the principle:

$$S_{sprue} > S_{runner} > S_{gate} \tag{24}$$

Applying Bernoulli's principle and the continuity equation for flow, the flow velocity at the height of the runner is calculated to be 2590 mm/s, and the velocity at the gate is 17356 mm/s. Considering the runner must feed the entire length of the casting without solidifying, the velocity should not exceed double the flow velocity. Therefore, to achieve a desired runner velocity of 5000 mm/s, a runner diameter of 60 mm is calculated.

$$Q = ct \;\; ; \;\; P + \frac{\rho \cdot v^2}{2} + \rho \cdot g \cdot h = ct \tag{25}$$

To further ensure the quality of the casting by preventing impurities carried by the molten metal from entering the part, ceramic foam filters have been placed at the entrance of the two main gating channels. These filters effectively trap impurities while allowing the molten metal to pass, thereby enhancing the casting's integrity.

Additionally, to address the potential issue of gas entrapment within the mold, which can lead to porosity and weaken the casting, seven venting channels have been strategically integrated along the casting. These venting channels facilitate the escape of gases generated during the casting process, ensuring a denser and more uniform final product. The placement and design of these venting channels are critical for maintaining the quality of the casting by preventing gas pockets and ensuring the molten metal fills the mold cavity effectively.

1. **Riser system calculation**

Defining the position of risers requires identifying the locations of the most massive sections of the part. In this scenario, the surface area most capable of providing material to these sections would be the upper part of the casting.

The first step involves determining the type of riser needed for this application, which necessitates calculating the filling time using Chvorinov's rule.

$$t = B\left(\frac{V}{S}\right)^n \tag{26}$$

where:

- t represents the solidification time,
- B is the mold constant, reflecting the heat transfer properties of the mold material,
- V is the volume of the casting,
- S is the surface area of the casting in contact with the mold, and
- n is a constant that varies depending on the source, with Askeland suggesting a value of 2 [43].

And B comes from [44]:

$$B = \left[\frac{\rho_m L}{T_m - T_0}\right]^2 \left[\frac{\pi}{4k\rho c}\right]\left[1 + \left(\frac{c_m \Delta T_s}{L}\right)^2\right] \tag{27}$$

This includes the melting temperature of the material (T_m), the initial temperature of the mold (T_0), the pouring temperature minus the melting temperature (ΔT_s) which represents the

superheat, the latent heat of fusion (L), the thermal conductivity of the mold material (k), the density of the mold material (ρ), the specific heat of the mold material (c), the density of the casting material (ρ_m), and the specific heat of the casting material (c_m).

To ensure the solidification time of the riser is 20% greater than that of the casting, thereby facilitating the desired directional solidification and feed throughout the casting process, the following equation can be utilized to determine the modulus of the risers:

$$Mm = \sqrt{\frac{1{,}2t}{B}} \tag{28}$$

Turning to the FOSECO catalog (**Figure 3.27**) for a riser sleeve that aligns with the project requirements, the KALMIN* S series is identified as suitable for aluminum castings as well as for copper, iron, and steel alloys. According to the catalog, the solidification time of these sleeves is 2.0 to 2.2 times higher than that of a traditional sand riser, translating to a riser modulus increase of 1.4 to 1.5. When estimating the total mold cost based on the volume of the casting, a minimum safety margin of 2 is considered advisable. Consequently, a sleeve with a modulus of 2.25 of the open counter-conical type is selected to meet these criteria.

Type	Module (cm)		Nominal Dimensions (mm)					Vol. (dm3)
	KALMIN S	geom.	du	Du	do	Do	H	
KS 4/7	1,10	0,75	41,0	58,0	34,0	63,0	72,0	0,08
KS 4/95	1,20	0,80	42,0	58,0	35,5	63,5	93,5	0,11
KS 5/8	1,40	0,95	51,0	68,5	47,0	74,5	80,0	0,15
KS 6/9	1,55	1,05	57,0	74,0	51,0	80,0	91,0	0,21
KS 7/10	1,80	1,25	69,0	87,5	64,0	95,0	101,0	0,35
KS 8/11	2,05	1,40	77,5	97,5	70,0	104,0	108,0	0,46
KS 9/12	2,25	1,55	88,0	107,0	80,0	116,0	119,0	0,66
KS 10/13	2,55	1,75	97,0	118,0	89,5	128,0	128,0	0,89

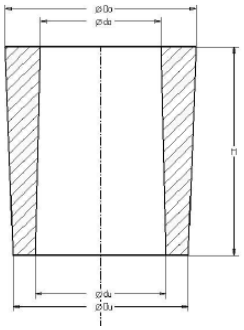

Figure 3.27. *Foseco catalogue for the riser's sleeves, model KALMIN.* [42]

To calculate the number of risers needed for a casting, the following equation can be utilized:

$$N_F = \frac{L}{d + F_D \cdot T} \tag{29}$$

where N_F represents the number of risers required, L is the length of the casting, d is the diameter of the riser, F_D is the feeding factor, and T is the thinnest section of the casting.

***Table 3-4**. Table showing the values of the feeding factor for different metal alloys [45].*

Alloy	Feeding factor
Steel (0.25% C)	4.0
Steel (0.20% C)	5.0
Steel (0.60% C)	4.5
Aluminum (99.99%)	10.0
Al Cu 4.5	6.0
Al Si 7	6.0
Al Si 12	10.0
Al Si (6-13)	5.0

After conducting the necessary calculations, it has been determined that the number of risers with the specified modulus required for this part should be 14. This indicates that these risers need to be strategically placed in various areas identified as critical. To achieve optimal results, it has been decided to position them in groups of 7 on each side of the part, as close to the edge as possible, to adequately cover the more massive zones. This placement strategy aims to ensure uniform feeding and solidification throughout the casting, particularly focusing on the areas prone to defects due to their mass and geometry. This methodical arrangement of risers is crucial for enhancing the overall quality of the casting by mitigating potential issues such as shrinkage porosity or incomplete filling, common challenges in complex or large castings.

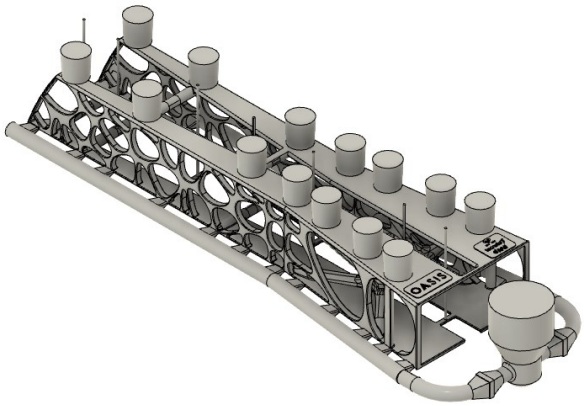

***Figure 3.28.** The geometry that define the mold cavity or the casting design and the part.*

3.4 Manufacturing process

3.4.1 Simulation

For the casting simulation, ESI Group's ProCast software was employed, offering a sophisticated approach to modeling and analyzing the casting process. To optimize the calculations, a strategy of refining the mesh in critical areas of the part for increased accuracy, while employing a coarser mesh in the outer regions of the mold, was adopted to balance detail against computational efficiency.

The boundary conditions set for this simulation included:

- An initial molten metal temperature of 700°C,
- An initial mold temperature of 25°C,
- The definition of 24 volumes as seen in ***Figure 3.29***, with one exhibiting the properties of resin-bonded sand (for the mold) and the remaining 23 adopting the properties of the chosen material, AlSi10Mg alloy.
- The convective heat coefficient in contact with the mold has been set as $h = 750W\ /\ (mm\ K)$
- A total filling time of 40 seconds.

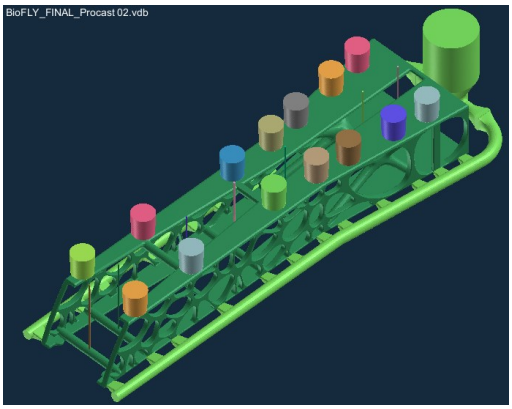

Figure 3.29. *Different volumes as defined in ProCAST.*

The simulation, as seen in **Figure 3.30.** *Solid fraction of the partially filled part at the further end of the filling (**left**). Temperatures of the melt when the part is fully filled (**right**).*, revealed significant temperature drops during the filling process, with variations in how closely different regions approached the alloy's solidification range. Notably, the area farthest from the gate began to solidify even before filling was completed. While the simulation indicated complete filling, the narrow margin suggests that slight deviations in temperature or filling velocity in real-life scenarios could lead to issues. However, considering that the simulation was run under conservative conditions specifically because of the alloy temperature and the filling time, it effectively presents a worst-case scenario.

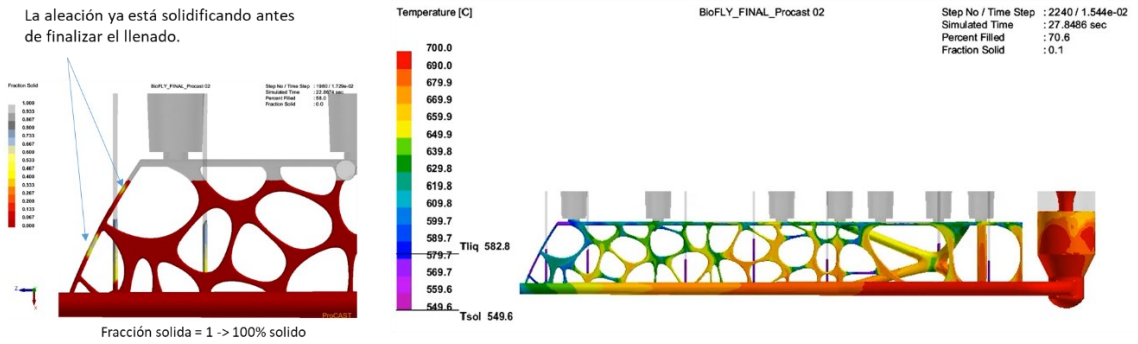

Figure 3.30. *Solid fraction of the partially filled part at the further end of the filling (**left**). Temperatures of the melt when the part is fully filled (**right**).*

The porosity prediction indicates areas that might exhibit some porosity due to the accumulation of isolated molten pools, as depicted in the provided **Figure 3.31**. It's crucial to investigate whether these porosity zones could adversely affect the structural performance of the part.

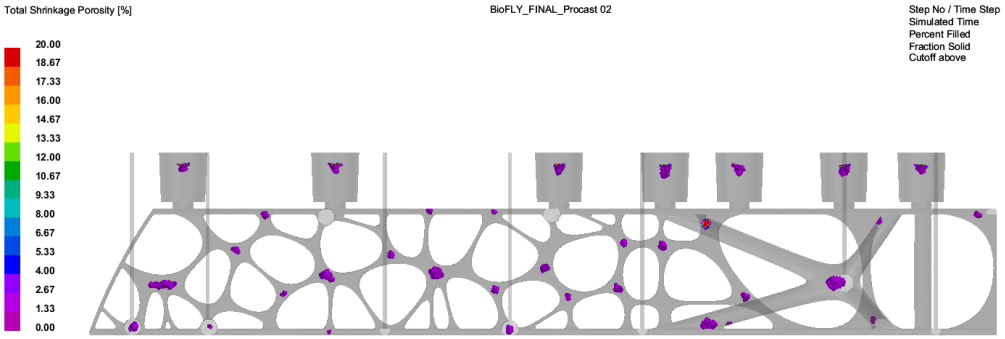

Figure 3.31. *Result of shrinkage porosity in the part after full solidification.*

According to the results, the part is entirely filled. However, there are areas where the molten metal cools more rapidly without fully filling the part, suggesting the process is on the verge of potential issues should there be slight deviations from the expected parameters. Nonetheless, it is important to note that the simulation was conducted under the most adverse conditions to ensure the capability of filling the part in the most conservative scenario. Despite this, particular attention should be paid to the filling temperature, as it could be a decisive factor for the complete and successful filling of the part.

3.4.2 Mold manufacturing

For manufacturing the part, it's necessary to design and fabricate the sand mold using binder jetting technology because of the geometrical complexity. When designing, it's crucial to account for the aluminum alloy's shrinkage factor of 1.2% as noted [47] This means the mold cavity's dimensions must be made 1.2% larger to achieve the correct sizes of the finished part. Moreover, since mold manufacturing isn't cost-effective, minimizing the volume of the mold produced by this method to achieve the desired geometry and casting conditions is essential. The remainder of the mold will be filled with the same type of sand to conserve resources.

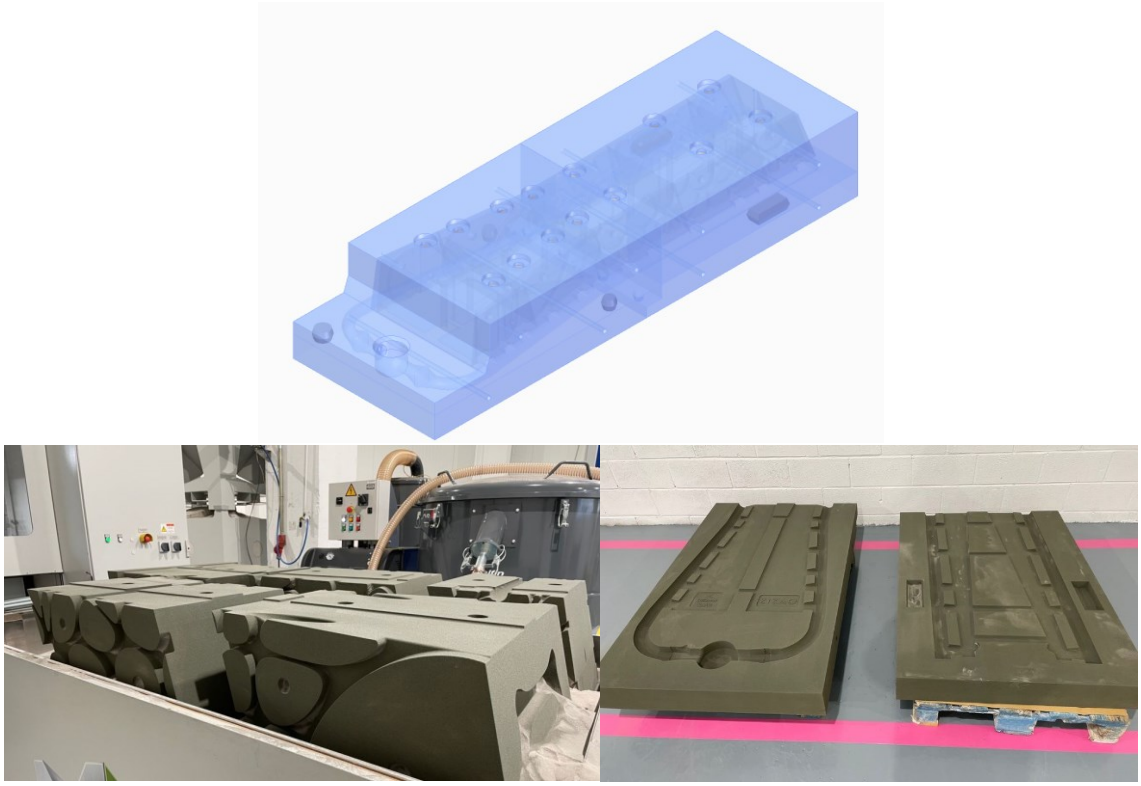

Figure 3.32. *Mold design for Binder Jetting (**top**). Mold parts as manufactured (**Bottom**)*

One of the major challenges encountered was the assembly of the mold due to very tight tolerances and the mold consisting of 24 pieces. This complexity required precision in both design and fabrication to ensure that the mold pieces fit together correctly and maintained the necessary tolerances to produce a casting that meets the design specifications.

3.4.3 Casting process

As shown in **Figure 3.33**, the casting process was successfully executed, and the part emerged without visible defects. The casting temperature was set at 750°C, with an ambient temperature of 25°C, and a filling time of 35 seconds. This scenario suggests that the simulation operated under conditions where not all parameters were fully controlled, which nonetheless assured the casting process's success. The next step involves conducting tests and trials to verify if the part's operational performance aligns with the outcomes observed in the simulations.

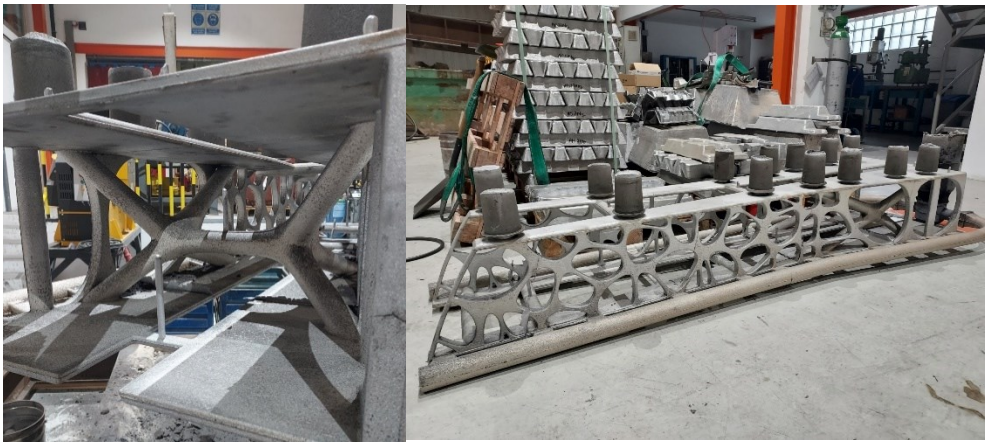

***Figure 3.33**. Outcome of the casting process. Inner surfaces (**left**) whole part (**right**)*

3.5 Physical Validation

To validate the design and manufacturing process, a modal test was conducted with the goal of ensuring that the first eigenfrequency of the structure was higher as supposed. A free vibration configuration was selected for this test in order to achieve maximum realism. In this study, a distinction between the configurations used in the FEA must be noted. The configuration employed for the FEA in the discussion section differs from that of the free vibration analysis. Due to the complexities associated with achieving perfect clamping of the structure, as assumed in the FEA for the discussion, the study opted for free vibration as a more practical configuration for validation purposes. Consequently, a supplementary FEA was conducted under this new configuration to ensure that the results were comparable and reliable. The structure was suspended from a crane using elastic ropes with negligible stiffness compared to that of the alloy (**Figure 3.34**). The acquisition device was an ICP 356A15 triaxial accelerometer of PCB and the impact device a 086C03 impulse force hammer of PCB. The impacts were performed in 20 different points in two directions. Those points were taken in 5 different heights so the different modes were noticed. In total, 40 runs were obtained.

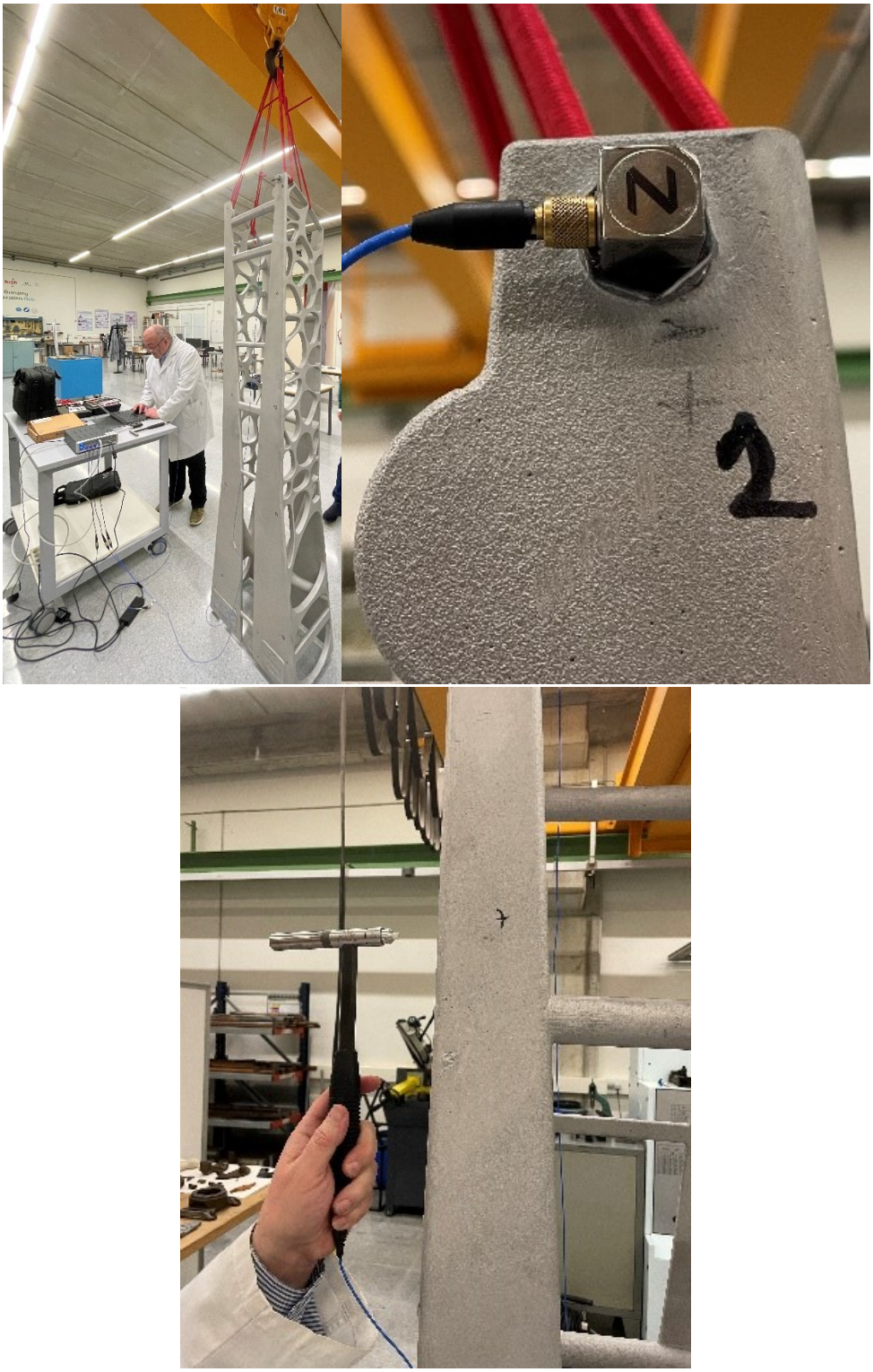

Figure 3.34. *Modal test configuration for free vibration conditions with the data-acquisition device, the accelerometer in the top right area of the part, and the hammer at UPV/EHU's facilities.*

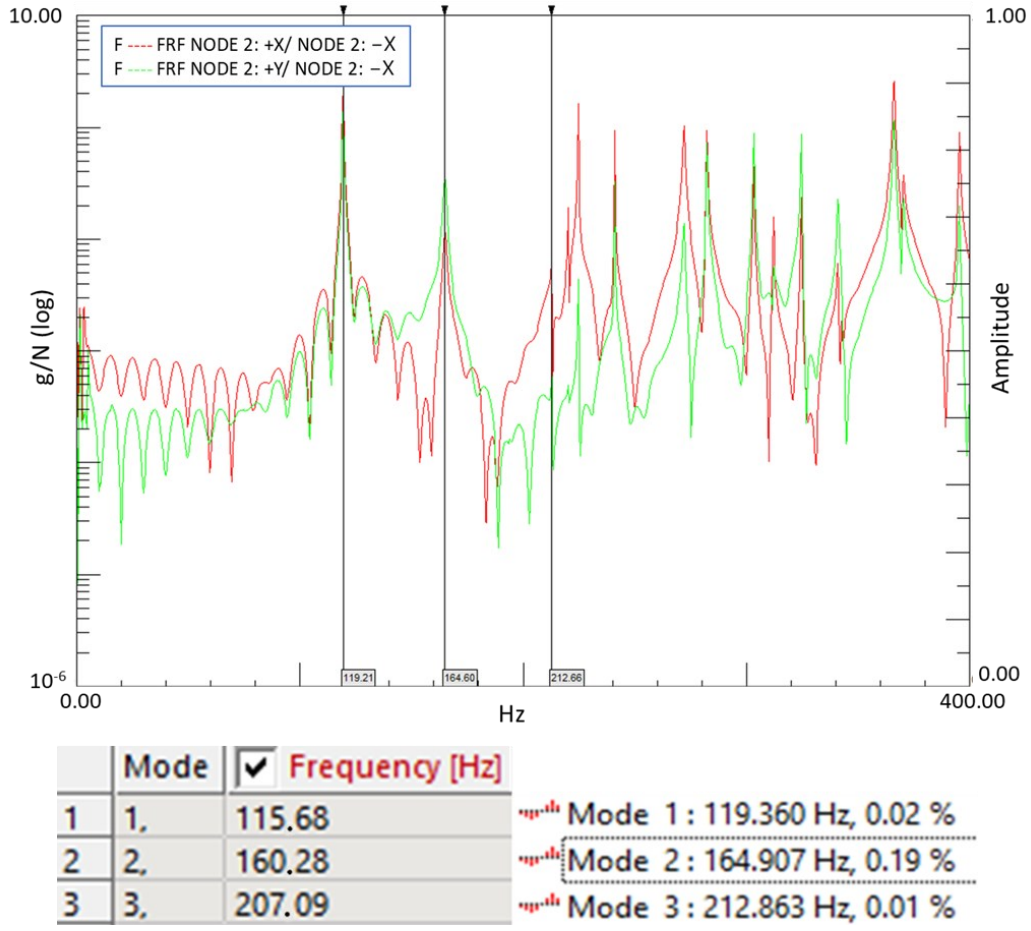

Figure 3.35. *The FRF of the signal from one of the acquisition nodes in two directions X and Y (**Up**). The results comparison of the generic material properties selected for the FEA (**left**) and the results of the modal test (**right**) (**Down**).*

The results of this test are shown in **Figure 3.35**. In order to compare these results with those obtained from finite element analysis, a free vibration FEA simulation was also performed using default aluminum alloy properties from ANSYS engineering data. The results showed a relative deviation, which may have been due to differences between the properties of the actual alloy used and those of ANSYS's default aluminum alloy properties. The modal testing data were analyzed with Siemens Simcenter Testlab.

To obtain more accurate results, samples were taken from the casting and their density was evaluated using an Archimedes balance. Finally, Young's modulus was corrected based on mathematical development [48] in order to obtain more reliable results. The final results are shown in **Table 3-5**. The first three modes of the experimental and corrected Young's modulus FEA were in free vibration configuration.

***Table 3-5**. Experimental and corrected Young's modulus FEA first three modes in free vibration configuration.*

Hz	Experimental	FEM (Corrected E)	Error
Mode 1	119.36	119.1	0.22%
Mode 2	164.907	165.01	0.06%
Mode 3	212.863	213.2	0.16%

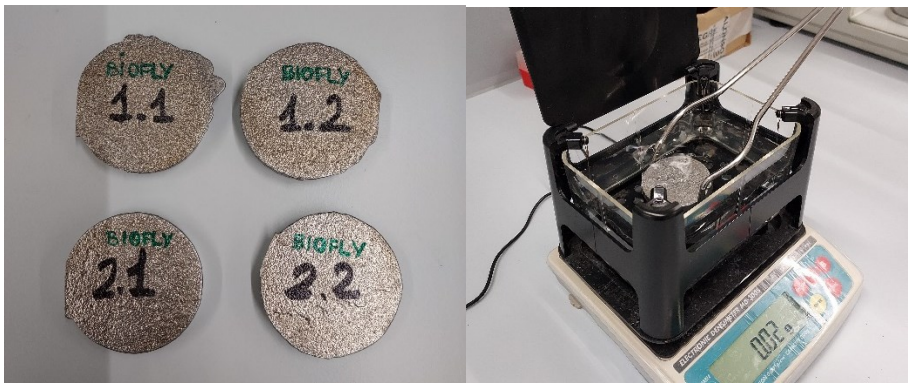

*Figure 3.36. Samples taken from the casting process of the part (**left**). Archimedes test for determining the density of the material (**right**).*

3.6 Conclusions

In this study, three different bioinspired design methods were selected and applied to a common use case: an aeronautic tooling that needed to be lightened and functionality directed optimized. The selection of these methods was made in order to have a broader study that included more classic methods such as traditional topology optimization, new emerging tools of generative design, and a novel method that mixed different bioinspired design methods. Four designs were evaluated in addition to the base design or reference design. As an overall conclusion, it can be said that all four bioinspired designs improved upon the reference design in some way. This demonstrates that mimicking nature in its different forms can be beneficial for improving upon what a human engineer can come up with based on their knowledge and experience. The findings of this study indicate that a hybrid approach, integrating simulation-driven design with true biomimicry, leads to a significant 74% reduction in mass and an enhanced first vibrational mode, effectively preventing resonance in aeronautical assembly operations. Additionally, the proposed bioinspired designs demonstrate their capability to withstand operational loads within an acceptable safety factor margin, highlighting their potential as a transformative solution in structural engineering. These results suggest that the efficacy of this hybrid method merits further investigation in diverse structural engineering applications.

The importance of design validation cannot be overstated. In this study, the digital models were compared with reality to ensure their accuracy. The first challenge in this process was the manufacturing process. To ensure the correct filling of the part, pertinent simulations were performed. All of this resulted in a high-quality casting. This has been a major milestone and

nothing similar has been found with this kind of design in terms of manufacturing process and size. To certify the good result, intensive modal testing was performed. The results of this study showed that the work proceeded as planned and all challenges faced in this project were successfully overcome. This represents a significant achievement in the field of bioinspired design.

Based on this study, the successful application of bioinspired design methodologies to an aeronautic tooling represents a significant achievement for structural engineering in various industries such as aerospace, automotive, and energy generation. The potential for lightweight, functionality-aimed, and manufacturable metallic components using bioinspired design is immense. In the aerospace industry, for example, the reduction of mass in aircraft components can lead to significant fuel savings and enhance new propulsion methods. In the automotive industry, lighter vehicles can improve fuel efficiency, electric vehicle range, and performance. In the energy-generation industry, lighter and more efficient components can improve the performance and longevity of power-generation equipment. The next steps for future research in this field should include further evaluation of the hybrid method of simulation-driven design and true biomimicry, as well as the exploration of other bioinspired design methodologies. Additionally, the manufacturing process and its potential for producing complex structures should be further investigated in terms of cost.

The ecodesign study conducted demonstrates that the integration of hexapods and weight reduction substantially enhances the environmental footprint of the current solution. Furthermore, this innovative approach suggests the inclusion of ecological analysis in engineering component feasibility studies, providing a valuable perspective for minimizing the carbon footprint in product design and manufacturing. This insight not only promotes more sustainable engineering practices but also encourages the development of green technologies, potentially setting new benchmarks for environmental responsibility in the engineering sector.

In conclusion, this study has demonstrated the potential of bioinspired design to improve upon traditional engineering methods and achieve significant advancements in structural engineering. Mimicking directly from nature can be a powerful method, as proven in this study.

3.7 References

[1] "Aerospace and defense (A&D) performance and outlook: PwC." Accessed: Mar. 28, 2024. [Online]. Available: https://www.pwc.com/us/en/industries/industrial-products/library/aerospace-defense-review-and-forecast.html

[2] "2024 aerospace and defense industry outlook | Deloitte Insights." Accessed: Mar. 28, 2024. [Online]. Available: https://www2.deloitte.com/us/en/insights/industry/aerospace-defense/aerospace-and-defense-industry-outlook.html

[3] A. du Plessis *et al.*, "Beautiful and Functional: A Review of Biomimetic Design in Additive Manufacturing," *Additive Manufacturing*, vol. 27. Elsevier B.V., pp. 408–427, May 01, 2019. doi: 10.1016/j.addma.2019.03.033.

[4] T. Vaneker, A. Bernard, G. Moroni, I. Gibson, and Y. Zhang, "Design for additive manufacturing: Framework and methodology," *CIRP Annals*, vol. 69, no. 2, pp. 578–599, 2020, doi: 10.1016/j.cirp.2020.05.006.

[5] J. Li, Z. Huang, G. Liu, Q. An, and M. Chen, "Topology optimization design and research of lightweight biomimetic three-dimensional lattice structures based on laser powder bed fusion," *J Manuf Process*, vol. 74, pp. 220–232, Feb. 2022, doi: 10.1016/j.jmapro.2021.12.007.

[6] Y. F. Zhao, S. Sun, P. T. Velivela, and N. Letov, "Challenges and Opportunities in Geometric Modeling of Complex Bio-Inspired Three-Dimensional Objects Designed for Additive Manufacturing," *Journal of Mechanical Design, Transactions of the ASME*, vol. 143, no. 12, Dec. 2021, doi: 10.1115/1.4051720.

[7] Y. Saadlaoui, J. L. Milan, J. M. Rossi, and P. Chabrand, "Topology optimization and additive manufacturing: Comparison of conception methods using industrial codes," *Journal of Manufacturing Systems*, vol. 43. Elsevier B.V., pp. 178–186, Apr. 01, 2017. doi: 10.1016/j.jmsy.2017.03.006.

[8] F. Buonamici, M. Carfagni, R. Furferi, Y. Volpe, and L. Governi, "Generative design: An explorative study," *Comput Aided Des Appl*, vol. 18, no. 1, pp. 144–155, 2020, doi: 10.14733/cadaps.2021.144-155.

[9] F. Breish, C. Hamm, and R. Kienzler, "Diatom-inspired stiffness optimization for plates and cellular solids," *Bioinspir Biomim*, vol. 18, no. 3, p. 036004, May 2023, doi: 10.1088/1748-3190/acc373.

[10] M. Al Khalil, H. Belkebir, N. Lebaal, F. Demoly, and S. Roth, "A Biomimetic Design Method for 3D-Printed Lightweight Structures Using L-Systems and Parametric Optimization," *Applied Sciences (Switzerland)*, vol. 12, no. 11, Jun. 2022, doi: 10.3390/app12115530.

[11] Y. L. Tee, T. Maconachie, P. Pille, M. Leary, T. Do, and P. Tran, "From nature to additive manufacturing: Biomimicry of porcupine quill," *Mater Des*, vol. 210, Nov. 2021, doi: 10.1016/j.matdes.2021.110041.

[12] H. Shangguan, J. Kang, C. Deng, Y. Hu, and T. Huang, "3D-printed shell-truss sand mold for aluminum castings," *J Mater Process Technol*, vol. 250, pp. 247–253, Dec. 2017, doi: 10.1016/J.JMATPROTEC.2017.05.010.

[13] J. Walker *et al.*, "3D Printed Smart Molds for Sand Casting," *International Journal of Metalcasting*, vol. 12, no. 4, pp. 785–796, Oct. 2018, doi: 10.1007/s40962-018-0211-x.

[14] W. W. Seto, *Schaum's outline of theory and problems of mechanical vibrations*. McGraw-Hill, 1964. Accessed: Mar. 28, 2024. [Online]. Available: https://search.worldcat.org/title/300310869

[15] D. J. Inman, "Engineering Vibrations 4th Edition," *Pearson*, pp. 170-180 532-572, 2014, Accessed: Mar. 28, 2024. [Online]. Available: https://search.worldcat.org/title/828332500

[16] J. Walsh and K. Meintjes, "Understanding a Generative Design Enabled Design Process Paradigm Shift Acknowledgements," 2019.

[17] B. Li, H. Liu, Z. Yang, and J. Zhang, "Thin-Walled Structures Sti ff ness design of plate / shell structures by evolutionary topology optimization," *Thin Walled Structures*, vol. 141, no. April, pp. 232–250, 2019, doi: 10.1016/j.tws.2019.04.012.

[18] S. Wolfram, "Cellular automata as models of complexity," no. I, 1984.

[19] M. Gen and L. Lin, "Genetic algorithms," *Wiley Encyclopedia of Computer Science and Engineering*, pp. 1–15, 2007.

[20] SJ. Russell and P. Norvig, *Artifcial intelligence: a modern approach*. 2010.

[21] R. Savage, "Fusion 360 Introduction to Generative Design," Autodesk University. [Online]. Available: https://www.autodesk.com/autodesk-university/article/Fusion-360-Introduction-Generative-Design-2020

[22] intrinSIM LLC, "A Vision for Generative Design - A market Report," pp. 1–34, 2019, [Online]. Available: https://intrinsim.com/PDFs/A VISION FOR GENERATIVE DESIGN V2_4.pdf

[23] J. Plocher and A. Panesar, "Review on design and structural optimisation in additive manufacturing: Towards next-generation lightweight structures," *Mater Des*, vol. 183, p. 108164, Dec. 2019, doi: 10.1016/J.MATDES.2019.108164.

[24] "MIDACO-SOLVER Numerical High-Performance Optimization Software."

[25] J. Dwyer-Lindgren, "Boeing says wing production has started for 737 MAX jets." Accessed: Nov. 14, 2023. [Online]. Available: https://eu.usatoday.com/story/todayinthesky/2015/06/02/boeing-says-wing-production-has-started-for-737-max-jets/28372587/

[26] G. I. N. Rozvany and T. Lewiński, "CISM International Centre for Mechanical Sciences 549 Courses and Lectures Topology Optimization in Structural and Continuum Mechanics International Centre for Mechanical Sciences." [Online]. Available: www.springer.com/series/76

[27] N. Kaiser, N. Goossens, A. Jimenez, I. Laraudogoitia, S. Psarras, and S. Tsantzalis, "Advanced manufacturing concept of a bio-inspired reaction wheel rotor for small- and medium-sized constellation satellites," *CEAS Space Journal*, vol. 1, pp. 1–14, Mar. 2023, doi: 10.1007/S12567-023-00489-W/FIGURES/12.

[28] A. Caggiano, L. Nele, and R. Teti, "Drilling of Fiber-Reinforced Composite Materials for Aeronautical Assembly Processes," *Intech*, vol. 32, no. July, pp. 137–144, 2013, [Online]. Available: http://www.intechopen.com/books/trends-in-telecommunications-technologies/gps-total-electron-content-tec- prediction-at-ionosphere-layer-over-the-equatorial-

region%0AInTec%0Ahttp://www.asociatiamhc.ro/wp-content/uploads/2013/11/Guide-to-Hydropower.pdf

[29] U. Alonso-Pinillos, F. A. Girot-Mata, R. Polvorosa-Teijeiro, and L. N. López-De-Lacalle-Marcaide, "Taladrado de materiales compuestos: problemas, prácticas recomendadas y técnicas avanzadas," *Dyna (Spain)*, vol. 92, no. 2, pp. 188–194, 2017, doi: 10.6036/8106.

[30] Boeing, "Boeing Next-Generation 737." [Online]. Available: https://www.boeing.com/commercial/737ng/

[31] M. Neuser, O. Grydin, Y. Frolov, and M. Schaper, "Influence of solidification rates and heat treatment on the mechanical performance and joinability of the cast aluminium alloy AlSi10Mg," *Production Engineering*, vol. 16, no. 2–3, pp. 193–202, Apr. 2022, doi: 10.1007/s11740-022-01106-1.

[32] "Aluminum 360.0-F Die Casting Alloy." Accessed: Nov. 27, 2023. [Online]. Available: https://www.matweb.com/search/DataSheet.aspx?MatGUID=46cc3a20683748718693cbb6039bec68

[33] C. Hamm, *Evolution of Lightweight Structures*, vol. 6. in Biologically-Inspired Systems, vol. 6. Dordrecht: Springer Netherlands, 2015. doi: 10.1007/978-94-017-9398-8.

[34] C. E. Hamm *et al.*, "Architecture and material properties of diatom shells provide effective mechanical protection," *Nature*, vol. 421, no. 6925, pp. 841–843, Feb. 2003, doi: 10.1038/nature01416.

[35] S. R. Jongerius and D. Lentink, "Structural Analysis of a Dragonfly Wing," *Exp Mech*, vol. 50, no. 9, pp. 1323–1334, 2010, doi: 10.1007/s11340-010-9411-x.

[36] A. Aid, M. Bendouba, L. Aminallah, A. Amrouche, N. Benseddiq, and M. Benguediab, "An equivalent stress process for fatigue life estimation under multiaxial loadings based on a new non linear damage model," *Materials Science and Engineering: A*, vol. 538, pp. 20–27, Mar. 2012, doi: 10.1016/j.msea.2011.12.105.

[37] J. N. Domfang Ngnekou *et al.*, "Fatigue properties of AlSi10Mg produced by Additive Layer Manufacturing," *Int J Fatigue*, vol. 119, pp. 160–172, Feb. 2019, doi: 10.1016/j.ijfatigue.2018.09.029.

[38] W. Dou, L. Zhang, H. Chang, H. Zhang, and C. Liu, "Fatigue Characterization on a Cast Aluminum Beam of a High-Speed Train Through Numerical Simulation and Experiments," *Chinese Journal of Mechanical Engineering (English Edition)*, vol. 34, no. 1, Dec. 2021, doi: 10.1186/s10033-021-00628-6.

[39] R. Avilés González, *Análisis de fatiga en máquinas*. Thomson-Paraninfo, 2005. Accessed: Nov. 22, 2023. [Online]. Available: https://dialnet.unirioja.es/servlet/libro?codigo=255311&info=resumen&idioma=SPA

[40] R. G. (Richard G. Budynas, J. Keith. Nisbett, and J. Edward. Shigley, *Shigley's mechanical engineering design*. McGraw-Hill, 2011.

[41] W. D. Pilkey and R. E. Peterson, *Peterson's stress concentration factors*. Wiley, 1997.

[42] "Foundry - Vesuvius." Accessed: Mar. 29, 2024. [Online]. Available: https://www.vesuvius.com/en/our-solutions/international/foundry.html

[43] D. R. Askeland, *The Science and Engineering of Materials*. Springer US, 1996. doi: 10.1007/978-1-4899-2895-5.

[44] J. S. Colton, “Casting Analysis-2 Solidification and cooling Surface tension Gas solubility and porosity,” *Georgia Institute if Technology*, 2011.

[45] INASMET, “Curso de formación sobre aluminio,” 2003.

[46] L. Jenkinsin, P. Simpkin, and D. Rhodes, *Civil jet aircraft design*. 1999.

[47] J. Campbell, “Complete Casting Handbook: Metal Casting Processes, Metallurgy, Techniques and Design: Second Edition,” *Complete Casting Handbook: Metal Casting Processes, Metallurgy, Techniques and Design: Second Edition*, pp. 1–1028, Sep. 2015, doi: 10.1016/C2014-0-01548-1.

[48] J. M. Sanchez, “Propiedades tribológicas y de fatiga de nuevas aleaciones de aluminio basadas en el concepto de alta entropía,” 2021.

Chapter 4: Reaction wheel for small- and medium-sized satellites

4.1 Introduction

The global space industry has experienced significant growth and transformation, with the total market value expanding to $546 billion as of 2023, marking a period of sustained growth and innovation across various sectors. This surge is a testament to the increasing commercial and government investment in space technologies and exploration, reflecting a broader interest in leveraging space for economic, strategic, and scientific advancements [1].

The commercial space sector has been particularly vibrant, driven by a surge of private investment and entrepreneurial ventures led by high-profile figures. These efforts have catalyzed advancements in reusable rocket technologies, satellite deployment, and even space tourism, which are reshaping the industry's landscape and setting the stage for future growth. The commercial segment alone is poised for significant expansion, with expectations to grow at the highest Compound Annual Growth Rate (CAGR) of over 8.0% through 2030 [2].

Technological advancements have been at the heart of this growth, with satellite technology playing a crucial role. In 2022, the industry witnessed the launch of 2,325 satellites, a historic high, with a significant portion supporting commercial communications. This boom in satellite launches underpins the critical role that satellite services play across various applications, from broadband internet access to Earth observation, highlighting the sector's robust dynamism and potential for further innovation and expansion [3].

On a regional level, North America has been a key driver of the space industry's growth, buoyed by supportive government initiatives, private investments, and the pioneering efforts of companies like SpaceX and Blue Origin. The region accounted for the highest market share in 2022, with over 54.0%, underscoring its leading role in space technology development and exploration. Meanwhile, Europe continues to strengthen its position with robust investment in satellite technologies and space exploration, marked by significant advancements by entities such as ESA and leading companies like Airbus and Thales Alenia Space. However, the Asia Pacific region is also emerging as a significant player, expected to record a CAGR of over 9.0% from 2023 to 2030, thanks to ambitious government initiatives and investments in countries like India, China, and Japan [2].

This dynamic growth trajectory of the global space industry, underpinned by technological innovation, strategic investments, and regional expansion, sets the stage for an exciting future. The industry's potential to reach a $1 trillion market value by 2030 highlights its strategic importance and the boundless opportunities it presents for exploration, development, and commercialization on a global scale [4].

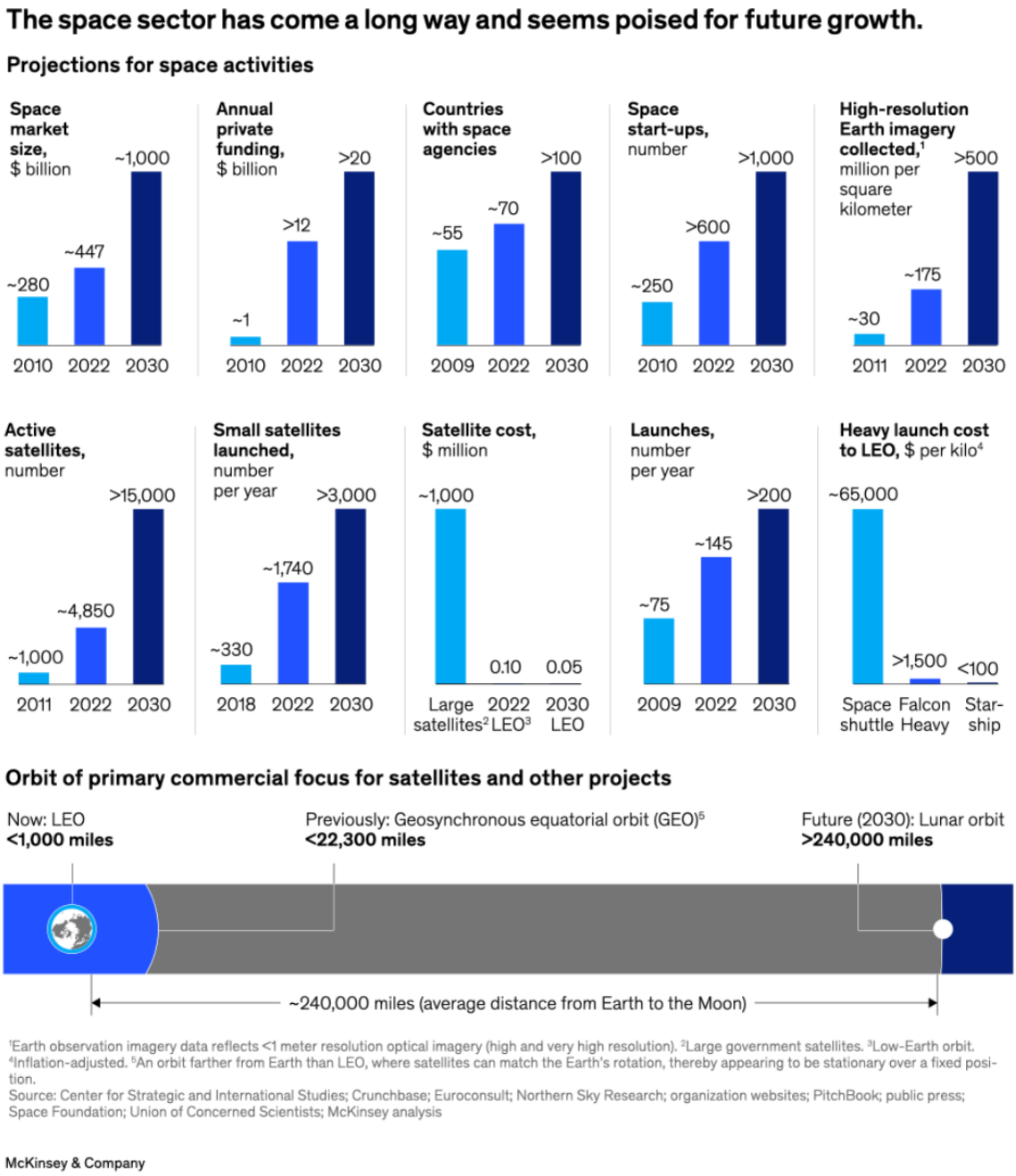

Figure 4.1. *Overview of the space sector by McKinsey & Company. Information from Center for strategic international studies; Curnchbase; Euroconsult; Northern Sky Research; organization websites; PitchBook; public press; Space Foundation; Union of Concerned Scientists; McKinsey Analysis* [4].

In the field of the global space industry, marked by growth and innovation, the significance of reducing spacecraft weight cannot be overstated. This principle is deeply intertwined with the core of rocket science and by the Tsiolkovsky's rocket equation. This equation, named after Russian scientist Konstantin Tsiolkovsky, who first derived it in 1903, quantifies the relationship between the mass of a rocket, the velocity of its exhaust gases, and the final velocity that the rocket can achieve. This equation is expressed as:

(1)

$$\Delta v = v_e \, ln \frac{m_i}{m_f}$$

Where Δv is the change in velocity, v_e is the exhaust velocity of the rocket's propellant, m_i is the initial total mass (including fuel), and m_f is the final mass (without fuel). The equation highlights the exponential nature of the relationship between the mass of a rocket and its final velocity, emphasizing the importance of every kilogram saved.

In practical terms, reducing the mass of a spacecraft—even by a single kilogram—can have profound implications. This is because the equation shows that the final velocity a rocket can achieve (which directly impacts its ability to reach orbit or escape Earth's gravity) is heavily dependent on the ratio of its initial mass to its final mass. Thus, every kilogram reduced from the spacecraft's mass allows for a more efficient use of fuel, increasing the payload capacity, or potentially extending the mission's range and capabilities.

To illustrate the discussed concept, suppose the goal is to transport a total payload of 5,000 kg to an orbit 400 km above Earth, within the Low Earth Orbit (LEO) range. To achieve this orbit, the payload must attain a velocity of 7,700 m/s, considering that the typical speed for chemically propelled rockets is 4,400 m/s [5]. It has been calculated that approximately 23,773 kg of fuel would be required. Therefore, to send 1 kg of mass into LEO orbit, around 4.75 kg of fuel is needed.

Reaction wheels are critical components within the Attitude and Orbit Control System (AOCS) of satellites, primarily tasked with managing satellite orientation. The rotor of a reaction wheel, which comprises several parts, represents the component with the greatest mass. Research indicates that reducing the mass of the rotor could substantially decrease the overall mass of the reaction wheel, as documented in studies [6], [7]. A reduction in mass not only impacts the reaction wheel but also significantly lowers mission costs. According to [8], a reduction of one kilogram in mass can decrease launch costs by approximately 5000€, underscoring the substantial financial benefits of even minor mass reductions. Currently, satellite reaction wheel rotors are constructed from multiple components, which increases assembly costs and can lead to rotor imbalance. By integrating these multiple components into a single part and optimizing the shape for load conditions, it is possible to achieve notable reductions in imbalance and enhance the overall performance of the reaction wheel system.

The optimization of rotors, particularly in the context of energy storage systems, is a well-covered topic in academic literature. Study [9] have explored the kinetic energy storage capabilities of various rotor geometries, while [10] introduced an innovative shape optimization strategy utilizing an evolutive system method. Additional research has focused on numerical shape optimization for even stress distribution [11], topology optimization to enhance energy density [8], and parametric geometry modeling for the same purpose [12]. Moreover, [13] has examined the optimal shape, size, and material of rotors in maximizing kinetic energy storage.

Despite the research on energy storage systems, literature specific to rotor optimizations for satellite reaction wheels remains relatively scarce. An exception is [14], which investigates an axis-symmetric topology optimization of a reaction wheel rotor for an Earth observation (EO) mission.

Furthermore, the field of bioinspired design presents a promising path for enhancing technical components by mimicking principles found in nature. This approach integrates natural solutions with technological advancements to foster improved designs, inspired by nature rather than directly copying it [15]. The underlying motivation for this methodology derives from nature's diversity, which offers a vast repository of inspiration [16], and from the evolutionary process, during which biological structures have been refined over 3.8 billion years. This evolutionary advantage has led to the development of organisms with lightweight structures that are highly optimized, representing near-optimal solutions achieved through millions of years of natural selection.

The advanced manufacturing process applied in the presented work is a hybrid method based on casting and 3D-printing. Using additive manufacturing for the production of the mold and an aluminum casting process for expendable molds as the main manufacturing process, higher geometric complexity and being cost effective at the same time is achievable. Compared to industries where expendable molds were not efficient because of the required number of parts, in space industry expendable molds are suitable regardless of the increased number of satellites launched because the mass restrictions outweigh the number of parts needed.

The objective of the present work is to describe a development process of a mass-optimized, single-part reaction wheel rotor with a bio-inspired design, made by advanced manufacturing and used in small to medium satellites, since the satellites size shifts towards this direction as they are frequently used in satellite constellations [17].

The presented work was part of LOBSTER, a 6-month subproject conducted in the framework of the EU-funded project OASIS (**O**pen **A**ccess **S**ingle entry point for scaleup of **I**nnovative **S**mart lightweight composite materials and components), which included the manufacturing of a demonstrator and first simplified analysis to identify potential for further studies.

4.2 Theoretical framework

In this chapter, we will discuss the theoretical foundations necessary to understand the design of a reaction wheel for the pointing of small and medium-sized satellites. The principles of flywheels and their specific application in reaction wheels will be explained. The theory of equilibrium in rotational motion will be covered, and finally, some of the loads specific to space structures and mechanisms that must be considered will be described.

4.2.1 Theory of reaction wheels

A flywheel is a mechanical device specifically designed to efficiently store rotational energy. It operates on the principle of conservation of angular momentum, meaning that as the flywheel

spins, it maintains its momentum until the energy is extracted from it for use. Flywheels are made with geometries with a high moment of inertia, materials with proper mechanical properties and density and spin on bearings with low friction. They can be found in various applications, from providing short bursts of energy for machines to smoothing out the power supply of electrical generators.

A reaction wheel is a type of flywheel used in spacecraft for attitude control without expelling propellant. It's essentially a flywheel with a motor, used to control the orientation of a satellite or spacecraft by utilizing the conservation of angular momentum principle. When a reaction wheel's speed is increased or decreased, the satellite rotates in the opposite direction to conserve angular momentum, allowing precise adjustments to its orientation in space.

Thus, understanding the operation and learning how to design these spacecraft components requires knowledge of their basic functioning. These components are fundamentally based on accelerated rotational movements.

Rotation about a fixed axis occurs when every particle of a rigid body follows a circular path centered on the axis of rotation. In this scenario, all lines within the body that are perpendicular to the rotation axis (including those not intersecting the axis) rotate through identical angles over the same time period. This uniform motion ensures that the angular displacement is consistent across the entire body [18].

The angular acceleration $\boldsymbol{\alpha}$ of a rigid body in three-dimensional motion is the time derivative of its angular velocity.

$$\boldsymbol{\alpha} = \dot{\boldsymbol{\omega}} \tag{2}$$

Angular momentum is the rotational analog to linear momentum. It is a important magnitude in flywheels because of its conservative nature. It can be defined as a vectorial product between the position vector $\boldsymbol{r}$ and its linear momentum vector $\boldsymbol{p}$**.** To conserve the angular moment is imperative to not have any external torque acting in the system. It can also be defined as:

$$\boldsymbol{L} = \boldsymbol{I} \cdot \boldsymbol{\omega} \tag{3}$$

Where $\boldsymbol{\omega}$ is the angular velocity and $\boldsymbol{I}$ is the mass moment of inertia. This last magnitude is a quantity that determines the torque needed for a desired angular acceleration about a rotational axis, akin to how mass determines the force needed for a desired acceleration. It depends on the body's mass distribution and the axis chosen, with larger moments requiring more torque to change the body's rate of rotation by a given amount.

The mass moment of inertia $\boldsymbol{I}$ is a measure of a body's resistance to changing its angular velocity around a particular axis. Specifically, it depends on how the body's mass is distributed relative to the axis of rotation. Mathematically, the moment of inertia for a rigid body in three dimensions is defined by the inertia tensor:

(4)

$$\boldsymbol{I} = \begin{pmatrix} I_{xx} & I_{xy} & I_{xz} \\ I_{yx} & I_{yy} & I_{yz} \\ I_{zx} & I_{zy} & I_{zz} \end{pmatrix}$$

where the elements I_{ij} are the components of the inertia tensor, calculated by considering the positions of the body's mass elements relative to the axis of rotation [18].

The equation of rotational motion for a rigid body rotating about an axis normal to its plane of motion involves an integral that reflects the distribution of mass relative to the axis of rotation. This integral is crucial because it represents the body's moment of inertia, which quantifies how the mass is distributed in relation to the rotational axis. Whenever a rigid body undergoes angular acceleration about its rotation axis, this integral becomes relevant. Therefore, understanding the dynamics of rotational motion requires proficiency in calculating the mass moments of inertia for rigid bodies, as these calculations determine how the body will respond to rotational forces.

For a rigid body, α is the same for all radial lines and it should be erased from the integral. The remaining integral is called the mass moment of inertia I of the body about the axis O-O and is:

$$I = \int r^2 dm \tag{5}$$

In the case analyzed in this chapter, exploring the moment of inertia of both a disk and a ring proves to be insightful. When considering a disk of radius R and mass m that rotates around an axis O-O, as illustrated in the **Figure 4.2**, it becomes essential to understand the following principles:

$$dm = \rho dV \tag{6}$$

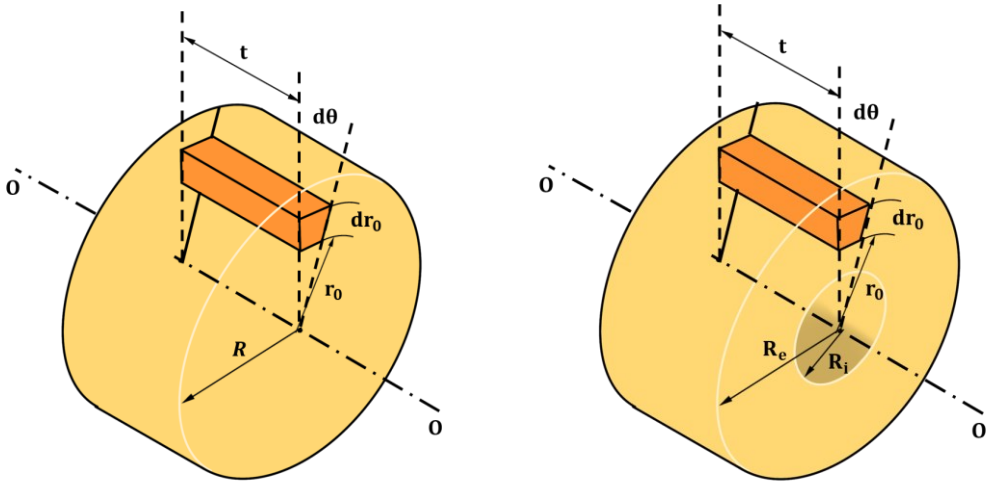

Figure 4.2. *An scheme of a disk with its O-O axis of rotation and relevant dimensions (**right**). An scheme of a ring with its O-O axis of rotation and relevant dimensions (**left**). Adapted from* [18].

And the volume of a disk in polar coordinates:

$$dV = r_0 dr_0 d\theta \tag{8}$$

And the moment of inertia can be defined as:

$$I = \int_0^{2\pi} \int_0^R {r_0}^3 dr_0 d\theta = \rho t \frac{\pi R^4}{2} = \frac{1}{2} m R^2 \tag{9}$$

If the same method is applied to the ring seen in the **Figure 4.2**:

$$I = \int_0^{2\pi} \int_{R_i}^{R_e} {r_0}^3 dr_0 d\theta = \rho t \frac{\pi}{2} ({R_e}^4 - {R_i}^4) = \frac{1}{2} m ({R_e}^2 + {R_i}^2) \tag{10}$$

By comparing both expressions, it is clear that mass close to the rotation axis contributes minimally to the ring's moment of inertia. The moment of inertia reaches its maximum value when the internal radius (R_i) is close to the external radius (R_e). Therefore, it could be assumed that ideally, a greater concentration of material should be on the outer part of the ring [18].

For the design of a reaction wheel rotor, it becomes pertinent to increase the mass at the external radius of the disk and ensure that the mass connecting to the rotation center is as minimal as possible to withstand the forces involved. Placing more material at the edge of the wheel increases the moment of inertia, which in turn enhances the efficiency of attitude control while reducing energy consumption.

To comprehend the functioning of a reaction wheel in a satellite, the concept of angular momentum conservation must be understood. This will involve considering a reaction wheel with mass m_R and radius R_R in the form of a disk, and a rectangular prismatic satellite with mass m_S and rectangular cross-section sides a_S and b_S as illustrated in the **Figure 4.3**.

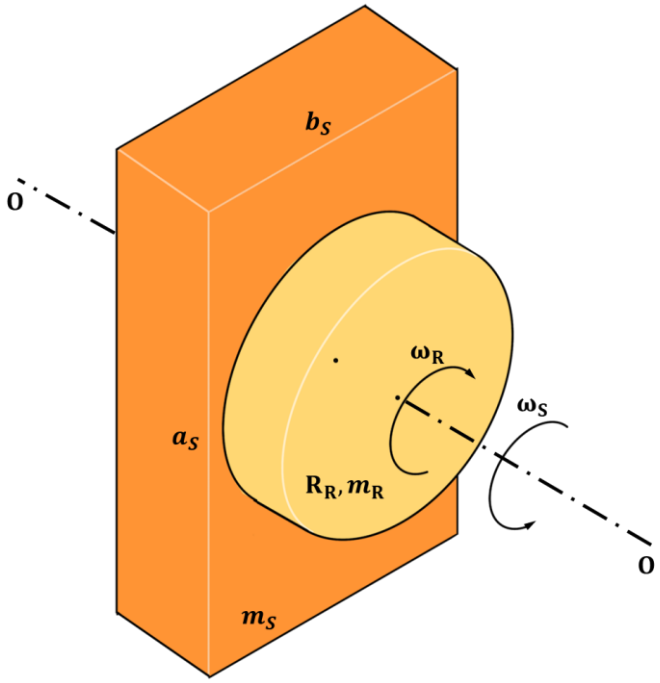

Figure 4.3. *Visual scheme of the motion of a reaction wheel and the satellite to which is attached.*

By equalizing the angular momenta of the satellite and the reaction wheel, and considering the moment of inertia of a rectangular prism as $I = \frac{1}{12}m(a^2 + b^2)$:

$$L_S = L_R \tag{11}$$

$$I_S\omega_S = I_R\omega_R \tag{12}$$

$$\omega_S = \frac{I_R\omega_R}{I_S} \tag{13}$$

In a case study similar to what this chapter will explore, with a reaction wheel of 3 kg mass, a moment of inertia of 0.05kg m^2 aiming to adjust a 200 kg satellite to an angular velocity of 1 RPM, it is calculated that the reaction wheel's angular velocity must be approximately 1400 RPM in the reverse direction to achieve this.

The kinetic energy of a reaction wheel is expressed as:

$$E = \frac{1}{2}I\omega^2 \tag{14}$$

The power required to reach a specified angular velocity in the reaction wheel is:

$$P = T\omega \tag{15}$$

Where T is the torque needed to move the reaction wheel to the necessary velocity in a certain time, therefore T can be expressed as:

$$T = I\alpha \tag{16}$$

4.2.2 Theory of balance in rotational motion

The theory of imbalance in the context of reaction wheel design is fundamentally anchored in the principles of rotational dynamics. According to Newtonian mechanics, the distribution of mass around the rotation axis of a body affects its moment of inertia. When there is an imbalance in this mass distribution, it results in a moment of inertia that varies, generating undesired torques around the axis of rotation. This imbalance disrupts the rotational motion that is intended, thereby impacting the precision with which orientation adjustments can be made in spacecraft.

Moreover, during the process of rotation, imbalanced masses give rise to centrifugal forces that are not perfectly balanced. These forces lead to mechanical vibrations and impose additional stresses on bearings and the structure's support mechanisms. This affects not only the stability of the device but also its operational longevity. The imbalance effectively causes forces that tug the rotating system in directions that were not anticipated, making the control of the system more complex.

In addition, the presence of imbalance introduces various modes of vibration that would not exist in a system that is perfectly balanced. These vibration modes depend on the wheel's geometry, the distribution of its mass, and its boundary conditions. Understanding and analyzing these modes is crucial for predicting the dynamic behavior of the reaction wheel. It also plays a key role in implementing measures to correct or mitigate these effects, ensuring the reaction wheel can perform its function with the required precision and reliability in controlling the attitude of spacecraft [19].

In the context of reaction wheel design, the distinction between **static** and **dynamic balancing** is crucial for ensuring the optimal performance of spacecraft attitude control systems. **Static balancing** refers to the correct distribution of mass around the rotation axis so that the center of mass coincides with the axis itself. This is fundamental to prevent the generation of centrifugal forces during rotation, which can lead to undesired vibrations and mechanical stresses. Ensuring static balance is about achieving a state where, when the wheel is not rotating, there is no tendency for it to start rotating on its own due to gravitational forces acting on an unevenly distributed mass [19].

Dynamic balancing, on the other hand, goes a step further by addressing the mass distribution not only to maintain the center of mass on the axis of rotation but also to minimize the gyroscopic forces and vibrations generated during rotation. This is particularly important at high rotation speeds, where even small imbalances can generate significant forces that affect the system's stability and precision. Dynamic balancing involves adjusting the mass distribution such that the wheel's rotation does not induce wobbling or oscillations, which could transmit through the spacecraft structure and interfere with its mission objectives [19].

Theory of space structures

When designing a structure or mechanism for use in space, it is crucial to consider factors that are not as critical on Earth. During launch, the intense vibrations of the rocket can impose mechanical loads that could potentially cause catastrophic damage to the structure. In addition, the space environment exposes materials to extreme temperatures, which can generate significant thermal loads due to expansion or contraction of the materials. Another important aspect is outgassing, which is the release of gases trapped inside materials when they are exposed to the vacuum of space. This phenomenon can affect the performance and integrity of materials used in the construction of space structures. Therefore, it is imperative to consider these and other factors specific to the space environment during the design process.

During the launch of space structures, such as satellites or parts of spacecraft, they are subjected to a variety of intense mechanical loads that can induce vibrations. These loads are primarily of two types: sine (sinusoidal) and random. Understanding these loads is crucial for designing structures that can survive the harsh conditions of launch and operate as intended in space [20].

Sine loads

Sine loads are characterized by their sinusoidal vibration patterns, which are typically a result of rotating machinery or the resonance effects within the launch vehicle as it ascends. These vibrations have a predictable pattern and are usually defined by specific frequencies and amplitudes. Engineers can predict sine loads using data from previous launches and simulations, allowing for the design of structures that can withstand these expected vibrational forces. Components and structures are tested with sine vibration tests to ensure they can endure the peak stresses experienced at these resonant frequencies without failure [20].

Random loads

Random loads, on the other hand, are less predictable and arise from a variety of sources, including aerodynamic turbulence as the vehicle speeds through the atmosphere, acoustic loads from the intense noise of the launch, and the complex interactions of structural elements of the vehicle itself. Unlike sine loads, random vibrations do not follow a simple, predictable pattern and are characterized by a broad spectrum of frequencies and amplitudes. These loads are often represented statistically, such as through power spectral density (PSD) functions, to understand their likely impact on spacecraft structures.

The challenge with random loads is their unpredictability and the wide range of frequencies involved, which can excite numerous natural frequencies of the spacecraft structure, potentially causing resonant amplification and fatigue issues. To ensure the integrity of spacecraft components under random loads, extensive testing, including random vibration tests, is conducted. These tests simulate the complex vibrational environment expected during launch, ensuring that every component can withstand the unpredictable nature of these forces [20].

Design and testing for vibrational loads

To design spacecraft structures capable of surviving both sine and random vibrational loads, engineers employ a combination of rigorous computational modeling and empirical testing. Finite element analysis (FEA) is commonly used to simulate the response of structures to these loads, allowing designers to identify potential weak points and optimize the design for both weight efficiency and structural integrity [20].

Thermal Loads

Spacecraft are subjected to extreme thermal environments, from the intense cold of deep space to the severe heat when exposed directly to the Sun or during re-entry into a planet's atmosphere for those that return to Earth. Thermal expansion and contraction can induce stresses in the structure and materials of the spacecraft [20].

4.3 Methodology

In this chapter, the methodology used to develop the reaction wheel is described in detail. First, the problem to be solved will be identified and explained, as well as the associated boundary conditions and the specific characteristics of the component intended for space use.

Subsequently, the design process that has been followed will be detailed, explaining how the optimization of the component has been carried out. This will include a review of the various design iterations that were performed, focusing on the modifications that contributed significantly to improving the performance of the component. This will be followed by the selection of the optimal design. This design was developed by the Alfred Wegener Institute and specifically the team of Bionic lightweight design together with the researcher writing this manuscript.

Finally, once the final geometry of the component has been defined, the design process of the elements required for manufacturing will be described, according to the selected production method.

4.3.1 Problem definition

This study is dedicated to the development of a mass-optimized reaction wheel rotor, designed to operate at high rotational speeds of up to 7500 RPM. The rotor aims for a maximum radius of 300 mm and a mass moment of inertia ranging from 0.051 kgm^2 to 0.06 kgm^2. This design specification enables a momentum storage capacity of at least 40 Nms. In comparison, existing rotors that achieve similar inertia and momentum storage capacity are typically constructed from materials like stainless steel A316 or the polymer PEEK. These rotors, however, often have a larger diameter of approximately 350 mm and operate at reduced rotational speeds ranging from 4500 to 6000 RPM, with a mass around 2.3 kg [6], [14]. According to [21], rotors of this design and capacity are suitable for small- to medium-sized satellites, emphasizing the need for innovations that accommodate higher performance within compact dimensions.

The primary goal of optimizing this component is to minimize its mass while maximizing the mass moment of inertia within a specified range. Achieving this balance is critical to enhancing the performance of the reaction wheel rotor, especially in terms of its efficiency and functionality in satellite applications. Additionally, it is imperative to ensure mechanical stability for the rotor under all specified load cases. These load cases, which will be detailed throughout this chapter, represent various operational conditions the rotor will encounter, including launch vibrations, thermal stresses, and operational loads during its deployment in space. Ensuring stability across these scenarios is crucial not only for the longevity and reliability of the rotor but also for the overall safety and success of the satellite mission [22].

Loads, constraints and objectives

The rotor must be able to withstand the loads during operation in-orbit as part of a satellite and additionally during launch to space. Therefore, two different load and boundary conditions were considered as these are in no way similar. The assumed load amplitudes and frequency have been average values for earth observation mission given by the project beneficiary.

During launch, the rotor of the satellite's reaction wheels experiences dynamic loads, as discussed in the previous chapter. These dynamic loads are simplified into acceleration loads using the Miles equation. The Miles equation is a statistical method used in engineering to estimate Root Mean Square (RMS) of the random vibration response of a structure subjected to a broadband random input, such as the environment experienced during a rocket launch. It translates these complex dynamic loads into simplified, quantifiable acceleration loads of 20 g, which are applied separately in the X-, Y-, and Z-directions [22].

The method of mounting the rotor during launch is crucial for its stability. Specifically, the rotor is fixed to the inner surfaces of the connection elements, an arrangement that functions similarly to securing the rotor with launch locks. The positions of these launch locks are strategically selected to ensure that the rotor experiences minimal loading, thereby enhancing the satellite’s durability and performance during the intense conditions of launch.

Furthermore, to mitigate the risk of critical vibrations that could impair the satellite's structural integrity, the design requirements specify that the first natural frequency at launch must be greater than 150 Hz. This frequency threshold is critical for avoiding resonances that could lead to catastrophic failure. The mounting points used during the launch phase differ from those in operational mode, reflecting the different mechanical stresses and requirements between these two phases [22].

In the operation of satellites in orbit, different forces and torques affect the satellite's stability and performance. Firstly, centrifugal forces arise due to the reaction wheels spinning at a high speed of 7500 RPM around the satellite's vertical Z-axis. These forces result from the outward push experienced by the mass of the wheel as it rotates [22].

Separately, a disturbance torque of 3.56Nm is applied around the satellite's horizontal X- or Y-axes to simulate external disturbances such as maneuvering or environmental interactions. Additionally, a specific value of 1.85 Nm, derived from an assumed coupled imbalance of 30 gcm² multiplied by the rotational speed, is considered within this disturbance torque. This represents the effect of any non-ideal distribution of mass in the reaction wheel affecting the satellite's dynamics [22].

The satellite's movement, known as 'slew,' which occurs at a rate of 1 degree per second, introduces a gyroscopic torque of 0.52 Nm. This torque results from the interaction between the satellite's rotation and the inertia of the spinning reaction wheels [22].

$$\tau_{gyro} = \omega_{slew} \cdot L \tag{17}$$

Boundary conditions for these scenarios are assumed to be fixed at the rotor surfaces that contact the bearings, which alters the required minimum natural frequency to 190 Hz under in-orbit conditions. This adjustment is crucial for ensuring the structural integrity and operational stability of the satellite.

Moreover, the analysis includes a safety factor of 1.5, enhancing the robustness of the satellite by ensuring it can handle greater stresses than those typically expected during operation. In total, three different static load cases for launch conditions and two for operational conditions are considered. These cases are essential for assessing the satellite's resilience and control accuracy across various scenarios.

The defined constraints are [22]:

$$0.051kg\ m^2 \leq I_{rotor} \leq 0.06kg\ m^2 \tag{18}$$

$$L \geq 30Nms \tag{19}$$

$$f_{n,launch} \geq 150Hz \tag{20}$$

$$f_{n,operation} \geq 190Hz \tag{21}$$

Manufacturing process selection

Designs that mimic nature often have complicated forms. Making these parts is the biggest challenge in their creation. These designs also tend to be expensive in terms of both computational time and work needed. Additionally, actually producing them introduces extra technical difficulties. Thus, design strategies that factor in how something will be made are significantly more advantageous than those that do not.

Casting can satisfy small-scale serial productions associated with the increasing demand for small- and medium sized satellites and at the same time, provide complex shapes like it can been seen in mass optimized parts.

The advanced manufacturing process applied in the presented work is a hybrid method based on casting and 3D-printing. Using additive manufacturing for the production of the mold and an aluminum casting process for expendable molds as the main manufacturing process, higher geometric complexity and being cost effective at the same time is achievable. Compared to industries where expendable molds were not efficient because of the required number of parts, in space industry expendable molds are suitable regardless of the increased number of satellites launched because the mass restrictions outweigh the number of parts needed.

Material selection

Within the scope of this project, there is a notable interest in evaluating the performance of a nano-reinforced aluminum alloy, specifically recycled AlSi10Mg reinforced with Al2O3 nanoparticles, for use in the rotor design. The chosen material for the rotor simulation has a density of 2600 kg/m^3, a yield strength of 80 MPa, a Poisson's ratio of 0.33, and a Young's modulus of 71.5 GPa. These material characteristics suggest that the nano-reinforced aluminum alloy could offer significant advantages in terms of strength-to-weight ratio, crucial for aerospace applications where reducing weight while maintaining structural integrity is paramount.

Design space

Within the framework of the project, the maximum allowed design envelope corresponds to a cylinder with a diameter of 300 mm and a height of 150 mm. As discussed in the theoretical section, the moment of inertia of a ring significantly increases when the inner radius closely matches the outer radius. This phenomenon results in a moment of inertia superior to any disk of equivalent dimensions and mass. For this reason, it was considered optimal to use all available mass at the minimum thickness allowed by the manufacturing method, while also occupying the maximum possible height within the outer diameter, that is, 150 mm [22].

Since the material connecting the center of the rotor to the inertial ring does not significantly contribute to the moment of inertia, it is designed to have the least possible mass while still being able to withstand the defined loads. The final design and non-design space can be seen in **Figure 4.4**.

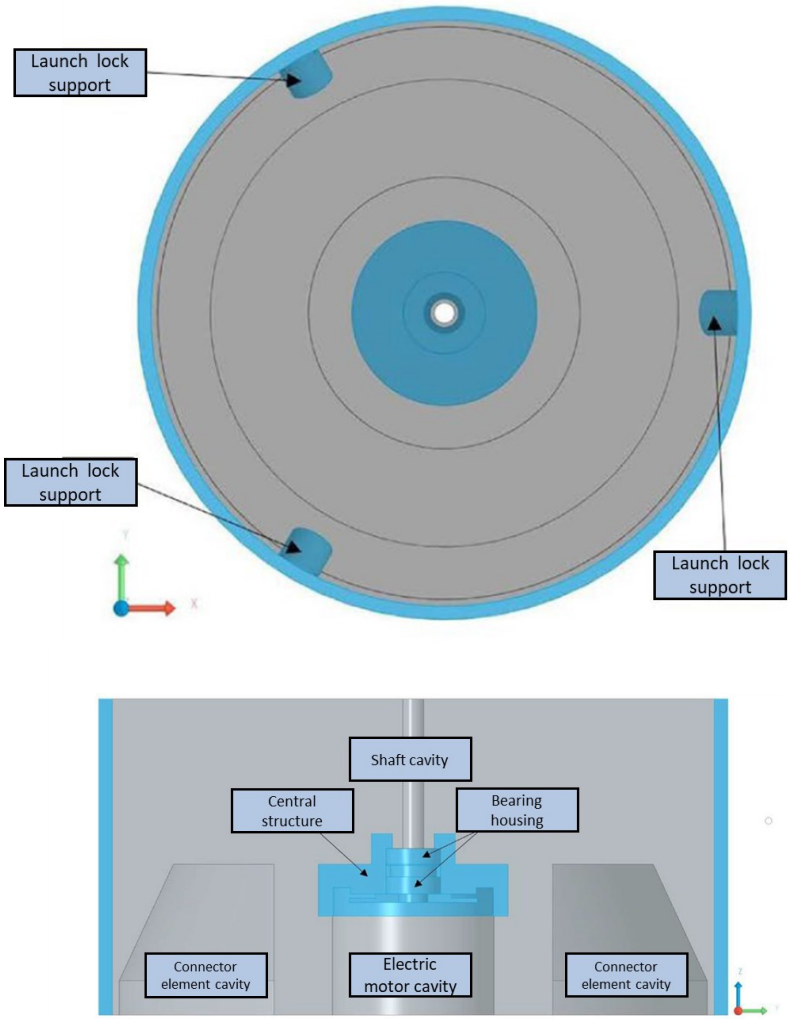

Figure 4.4. *Top view and cross-section of the design space (**grey**) and non-design space (**blue**) used for topology optimization* [22].

4.3.2 Design and optimization

The rotor design was optimized using a bio-inspired design process, leveraging principles observed in nature to achieve an optimal mass distribution. This approach aimed to create structures that are lightweight, highly adapted to defined loads, and capable of generating the required mass moment of inertia with the least amount of material. The design methodology was rooted in a generative, algorithm-based workflow.

The process adapted from the problem-driven bio-inspired design approach referenced in [23] and the technology pull method cited in [24], involved several key steps. These steps included defining the problem, searching for biological role models, and implementing abstracted principles [22].

For the practical execution of the design, the software Synera (Synera GmbH, Bremen, Germany) was utilized, which facilitates the development of complex CAE models through an automated, algorithm-based process. Additionally, for topology optimization, the combination of Altair

HyperMesh software and the OptiStruct solver (Altair Engineering Inc, Michigan, USA) was employed. This enabled the creation of a refined structural topology that meets the design criteria with enhanced efficiency and material utilization.

Topology optimization

Topology optimizations were carried out to identify the areas where the material should be placed for supporting all load cases with the defined constraints and objectives. These provided the basis for the new design. As defined before, the rim was mainly responsible for the mass moment of inertia, so that it remained solid and unaffected by the topology optimization (non-design space). In addition, a simplified structure at the center of the rotor, which is used to cover and attach wheel components like ball-bearings and the motor, was also defined as non-design space; the three connection elements for launch locks were also considered as non-design space. All non-design spaces are shown blue-highlighted in **Figure 4.4**, while the design space is shown in grey.

Due to the given rotational symmetry, a rotational symmetry criterion was selected for the optimization, with the aim of generating a new design by rotating identical cylinder sectors (analogous to circle sector). Two different settings were considered, 3 or 6 sections. Both setups were complemented by a minimize weighted compliance objective considering all load cases equally weighted with a factor of 1, and constraints for a volume fraction of 0.2 as well as minimum first natural frequencies.

Due to the different boundary conditions, the frequencies differ between launch (150 Hz) and operation (190 Hz) [22]. The results of the optimization are shown in **Figure 4.5**.

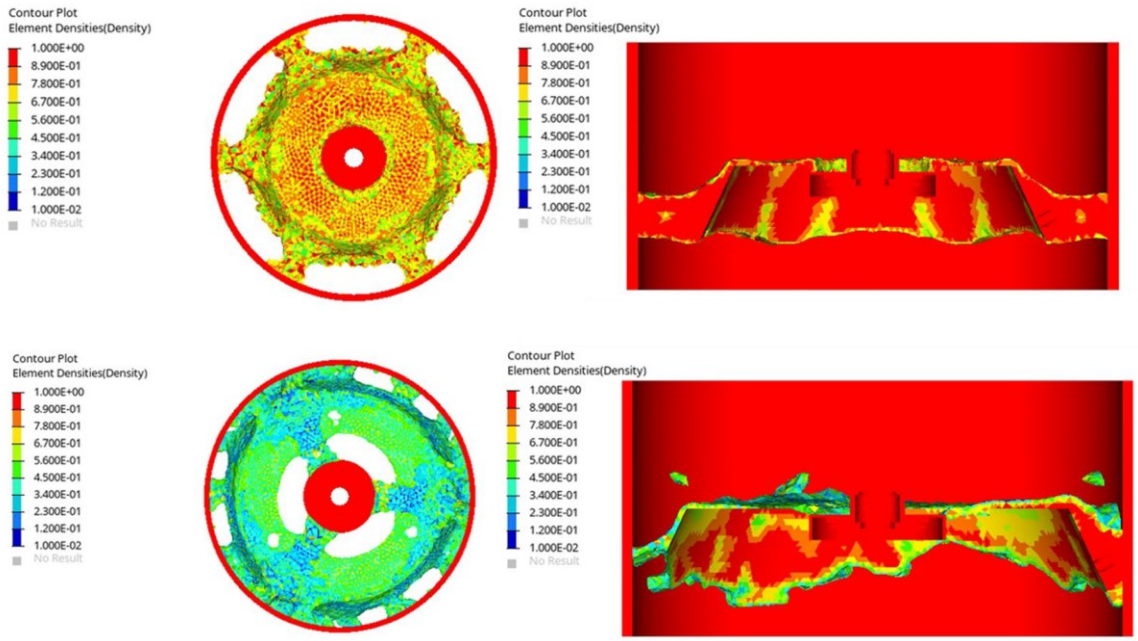

Figure 4.5. *Topology optimization result using 6 (**top**) or 3 (**bottom**) rotational symmetric sectors* [22]

Bioinspired design

To initiate the development of a preliminary bioinspired design for a rotor, the process began with the selection of biological examples that could serve as inspirations for structural design. This selection is crucial because the biological example chosen must possess structural integrity and operate within a similar work regime to the rotor intended for design. For instance, diatoms are recognized for their exoskeletons that exhibit a variety of shapes, with spherical or circular forms being among the most prevalent [25].

Drawing from nature, analogies can be made either to the overall organism or to specific features within individual sections of their structures. The analogies considered were categorized into three distinct fields: Function, Requirement, and Form. The Function and Requirement analogies were directly derived from the specifications necessary for the new rotor component, ensuring that the bioinspired design would meet the operational and functional needs of the project. The Form analogy, however, was influenced by the results from the design's topology optimization (as illustrated in **Figure 4.5**). This approach allowed for the incorporation of topology-optimized areas into the new design, guiding the structural layout and feature selection.

The proposed design for the rotor incorporated rotational symmetric cylinder sectors. The central area of the rotor was designed to include a few robust struts featuring large, trapezoidal cavities, which contribute to both strength and mass reduction. The main body of the rotor was envisioned to contain flat structures that could be optionally reinforced with rib structures to enhance durability and load-bearing capacity. In areas where further weight reduction was feasible, these flat and ribbed structures could be replaced with comb-like or lattice structures, which offer significant advantages in terms of lightweight design without compromising on strength. In summary, the analogies were defined as:

- Function: Mass concentration in outer areas, loading due to rotation, loading due to vibration.
- Requirement: Load transfer and distribution from center to outside, areas with less or no mass, connection structures with low mass, combination of load carrying and load transferring sections, smooth connections
- Form Cylindrical, rotational symmetry, struts and cutouts, flat structures, horizontal symmetry

Drawing inspiration from biological role models, bio-inspired structures were synthesized and integrated with non-design spaces identified through topology optimization to create a preliminary parametric design, which was subsequently refined and optimized. The right half of the new design, schematically shown in **Figure 4.6**, exhibits a two-part, radially-symmetric structure that mirrors the shell shapes of *Asterolampra marylandica* and *Roccella schraderi*.

In line with the structural characteristics of these biological models, the centrally located area of the rotor was designed to contain larger, robust structures that anchor the design. Progressing outward, the rotor transitions into regular, comb-like structures, which increase in size towards the periphery, similar to the features observed in various diatoms such as *Thalassiosira sp*.

Through the design process, these comb-like patterns were rounded off and the ribs that run between them thickened, rendering them less distinguishable as individual combs in the final design. Instead, this outer area evolved into a ring featuring irregularly shaped oval cavities, which contributes to an overall reduction in material while maintaining structural integrity.

The structural ribs, originating from substantially thicker elements at the rotor's center, branch outward, effectively directing and distributing loads from the center to the peripheral areas. This design strategy not only optimizes load handling but also mirrors the efficient load distribution systems observed in nature. Moreover, the entire design incorporates smooth or rounded transitions and variations in structural thickness, adhering closely to the adaptive and resilient features of the biological role models.

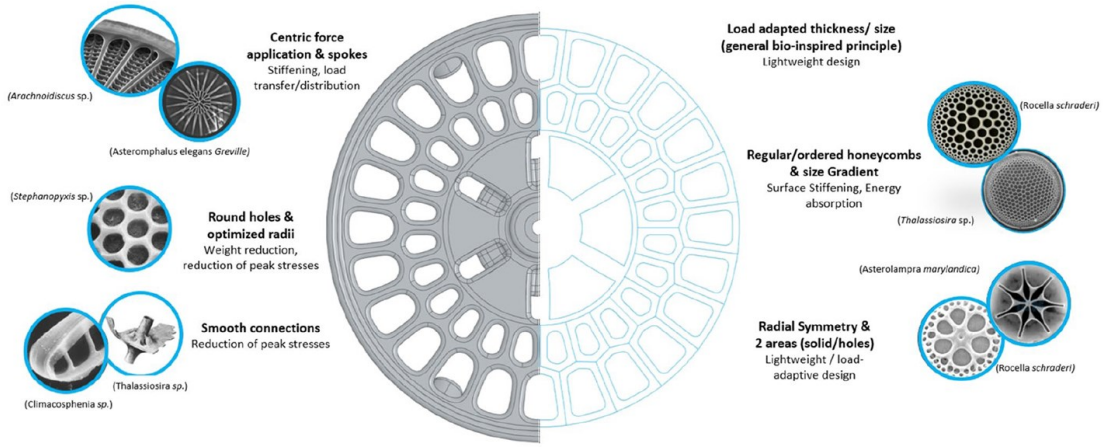

Figure 4.6. *Final design of the rotor in a rendered (left) and schematic (right) representation, including an overview about the marine microorganisms used to abstract bio-inspired design principles and structures (modified according to [*[22], [26], [27],*)*

Parameter optimization

To optimize the integration of bio-inspired design principles, an automated parameter optimization was conducted using the MIDACO solver, a Mixed Integer Distributed Ant Colony Optimization tool. This solver employs a derivative-free, evolutionary hybrid algorithm suitable for both single- and multi-objective optimization, handling potentially thousands of variables and hundreds of objectives [28]. For instance, adjustments were made to the number, arrangement, and dimensions of comb-like structures as well as the robustness of their fillets to tailor the design precisely to the prevailing load conditions.

FEM simulations accompanied each new iteration of the design to ensure that the stress values remained below the material's yield strength, thereby upholding the structural integrity of the design under operational loads. Details of all parameters adjusted during the optimization process are documented in **Figure 4.7** and **Table 4-1**.

The design process was facilitated by Synera software, which allowed for the incorporation of manufacturing-relevant design constraints through a parametric and algorithm-based design

environment. This included implementing fillets with a minimum radius of 3 mm at each edge and ensuring a minimum material thickness of 7 mm to enhance manufacturability while maintaining structural integrity. To avoid excessive weight and simplify manufacturing processes, designs incorporating massive solid areas were avoided, and transitions between different structures were smoothed.

Due to the constraints on minimum material thickness, designs that relied on lattice structures or rib-reinforced surface structures were ultimately not feasible. The finalized rotor design, which incorporated these considerations and optimizations, is presented from various perspectives in **Figure 4.8**, showcasing the results of this comprehensive design and optimization process.

***Table 4-1**. Parameter definition for discretizing geometry and perform a parameter optimization*

#	**Parameter**	**Range**	**Explanation**
1	Maximum diameter	280-300 mm	Lower bound due to launch locks and requested moment of inertia
2	Cylinder sectors	3 or 6	Number of structures in the center area
3	Cylinder sector width	0-1	0 represents a width of 14mm and 1 the maximum possible width
4	Outer radius	0.1-0.8	Radius of the inside structure in relation to the maximum possible radius
5	Cylinder sector bending	0-1	0 is related to “straight” and 1 to the maximum bending
6	Cylinder sector rounding	1.5-3 mm	Fillet radius for rounding vertical edges of inner structures
7	Combs	12, 18 or 24	Number of combs within one row
8	Comb rib thickness	3.5-5 mm	Rib thickness between honeycombs
9	Central radius	23-45.2 mm	Based on the size of the non-design space
10	Top bearing position	-11 to 64	Z coordinate of the upper bearing center of gravity
11	Bearing distance	0-1	0 is related to no distance, and 1 represents the maximum distance
12	Comb rows radial	2, 3 or 4	Number of combs in radial direction

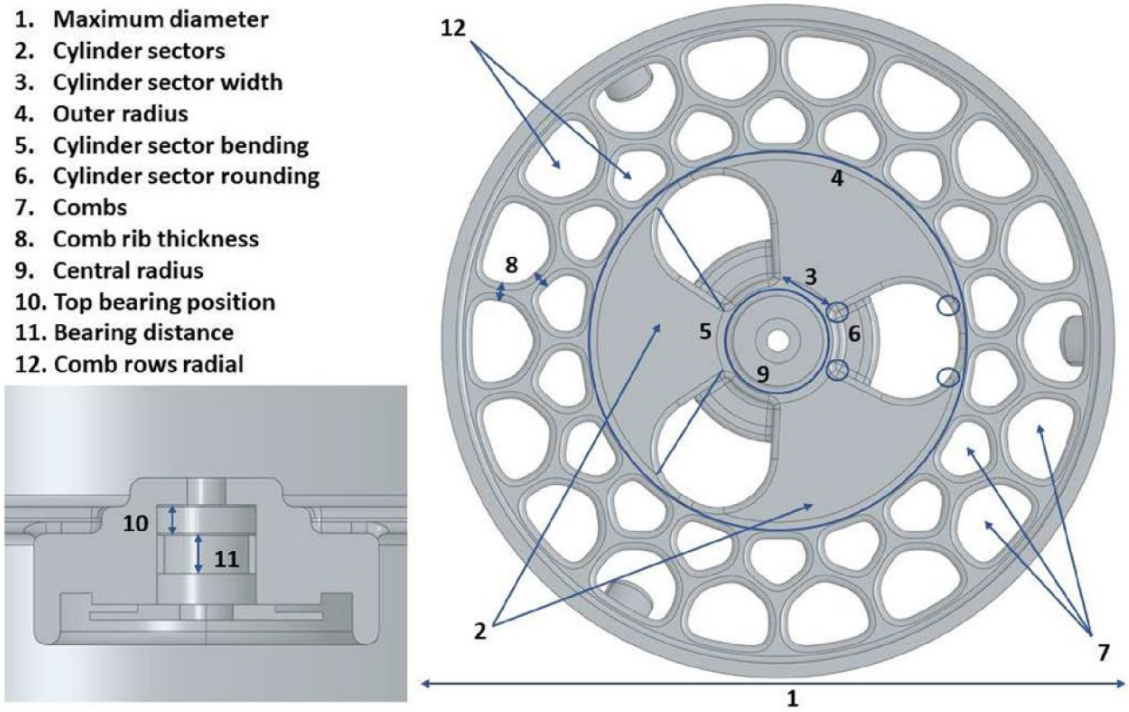

Figure 4.7. *Visual representation of the parameters taken into account for the parameter optimization* [22].

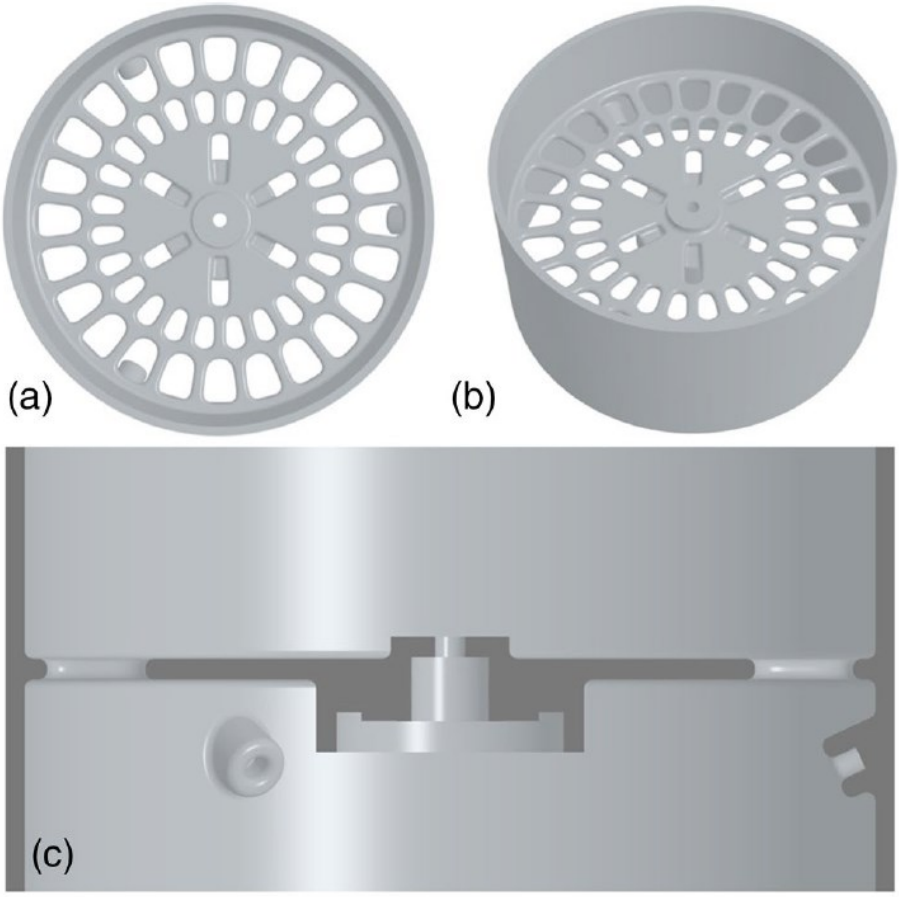

Figure 4.8. *Different views of the bioinspired rotor* [22].

4.3.3 Outcome selection and validation

To assess the performance and potential of the new bio-inspired rotor design, comparative analysis was conducted using data from a commercially available rotor, specifically the RSI25-220/45 from Rockwell Collins Inc., Cedar Rapids, Iowa, USA, and a conceptual topology-optimized rotor referenced in [14]. Since specific data for the commercial rotor's wheel were unavailable, a simplified model with comparable properties derived from data in [6] was utilized. In addition to the rotor properties already mentioned, the inertia to mass ratio I_m , the angular momentum L and the energy density e as kinetic energy E_{kin} to rotor mass ratio were considered for the performance evaluation, calculated based on the CAD-model, where:

$$I_m = \frac{I_{rotor}}{m_{rotor}} \tag{22}$$

$$e = \frac{E_{kin}}{m_{rotor}} \tag{23}$$

The bio-inspired rotor, designed with a diameter of 282 mm and a maximum rim height of 150 mm, had a mass of 3.375 kg. It boasted a moment of inertia of 0.051 kgm² and an inertia to mass ratio of 0.0151 m²/kg. At a rotational speed of 7500 RPM, the rotor achieved an angular

momentum of 40 Nms and an energy density of 4661 J/kg. Comparative performance metrics for the commercial and conceptual models were compiled in Table 2, with the new design's superior metrics highlighted in bold and any subpar values underlined.

Additional performance metrics included the first natural frequency in launching configuration, where the new rotor design exhibited 658 Hz at that condition, significantly surpassing the required 150 Hz. During operation, the frequency was 210 Hz, again above the necessary 190 Hz. Stress analysis revealed that the maximum occurring stress was approximately 18% below the yield strength criterion of 53.3 MPa, affirming the structural robustness of the rotor. This calculation took into account a safety factor of 1.5, derived from multiplying a factor of 1.25 for critical yield strength consideration in metallic parts [29] with an additional factor of 1.2 to compensate for coarse manufacturing tolerances associated with casting processes [30].

Table 4-2. *CAD-model based reaction wheel rotor performance of the bio-inspired design, a simplified commercial design* [6] *and a conceptual design* [14]*. Improved values of the new design are written in bold and less-performable values are underlined.*

Component	**Diameter [mm]**	**Rim height [mm]**	**Mass [kg]**	**Inertia [kg m^2]**	**Inertia to mass ratio [m^2]**	**Inertia ratio [-]**	**Energy density [J kg^{-1}]**	**Angular momentum [N m s]**	**Nominal RPM**
Topology	350	99	2.24	0.041	0.0183	0.5971	3610	26	6000
Commercial	347	99.2	2.34	0.053	0.0227	0.7532	2517	25	4500
Bionspired	**282**	**150**	<u>3.375</u>	0.051	<u>0.0151</u>	**0.7584**	**4661**	**40**	**7500**

4.3.4 Design for manufacturing

In the development process using Synera software, an algorithm-based design environment, manufacturing-relevant design constraints were seamlessly integrated through parametric design principles. This method utilized logic and mathematical rules to ensure the manufacturability of the rotor. Key design adjustments included applying a minimum fillet radius of 3 mm to each edge to reduce stress concentrations and enhance mechanical integrity. The rotor maintained a minimum material thickness of 7 mm across all sections. Large, massive solid areas were avoided in the design to avoid isolated melt areas. Additionally, smooth transitions between different structural features were implemented to decrease stress concentrations.

Once the main geometrical constraints have been established, this chapter will focus on the development of a specific design for the selected manufacturing process, which in this case is

centrifugal motion assisted gravity casting using 3D printed sand molds. The necessary simulations will be carried out to evaluate the feasibility and effectiveness of the design in this manufacturing method. Subsequently, the results obtained will be analyzed and appropriate conclusions will be drawn for each case, ensuring that the design meets the manufacturing requirements. This approach will allow the design to be optimized for production, respecting the limitations and taking advantage of the benefits offered by casting with 3D printed sand molds.

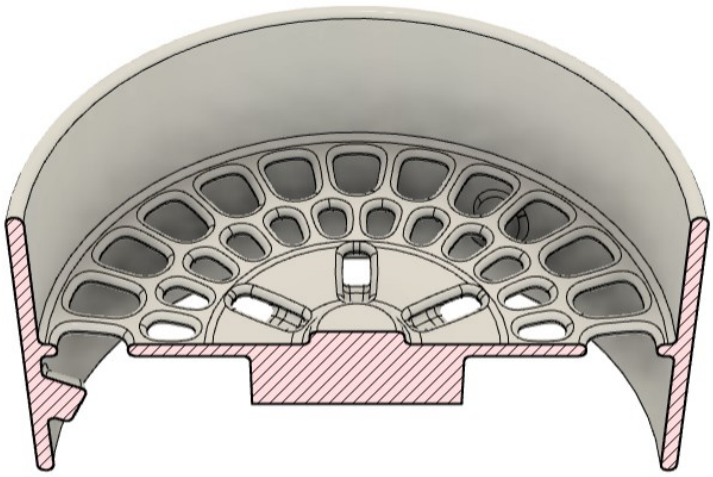

Figure 4.9. *Section of the outcome with the manufacturing constraints applied.*

Casting design

The chosen manufacturing method for this part was gravity casting in sand, selected due to the complexity of the geometry. To aid the filling of the axially symmetrical part, the mold was rotated during the metal pouring process. The successful execution of this casting method required the design of an effective filling system to guide the liquid metal through the mold cavity accurately.

The efficiency of the filling system largely depends on the orientation of the part within the mold. As seen in **Figure 4.10**, orientation C, which is vertical, was immediately discarded due to its inability to ensure homogeneous filling across the part's radius, leading to potential axial imbalance. Regarding filling from the outside, this approach was rejected for all orientations because of the complex post-processing challenges it presents, such as the removal of flutes and hit points, which could exacerbate axial imbalance.

Among the remaining choices, orientation B was selected over orientation A primarily because it offers a larger area for placing the sprue collar. This larger area is critical for ensuring a more rapid and effective metal flow into the mold, enhancing the overall quality of the casting. The design of orientation B not only facilitates a better setup for the sprue system but also simplifies the casting and post-processing stages by minimizing potential defects and simplifying material handling.

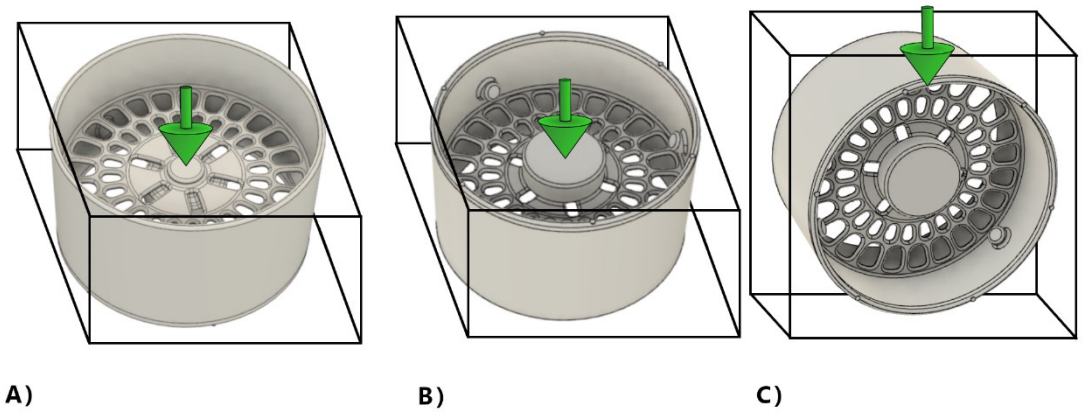

Figure 4.10. *Three orientations possible for filling the part.* ***A)*** *Part filled horizontally placed and upwards.* ***B)*** *Part horizontally placed and filled downwards.* ***C)*** *Filling in vertical* [22].

Once the optimal orientation for the casting process was determined, the next critical step involved dimensioning the sprue to ensure efficient and clean metal flow into the mold. The filling system designed needed to control the melt flow effectively, preventing splashing or impactful flows, avoiding the dragging of impurities, ensuring complete filling of the part, and being straightforward to disassemble.

To simplify the design process and incorporate a reliable filter, a decision was made to use a commercial sleeve as a sprue. Given that the surface where the electric motor is to be housed has a maximum allowable channel width of 84mm, the selection of the appropriate sprue size from a commercial catalog became essential.

After reviewing the FOSECO catalog seen in **Figure 4.11**, which included options with the specified shape, six sleeves were available within a range of D2 diameters from 48 mm to 110 mm. The sleeve chosen had a D2 diameter of 70 mm, a D1 diameter of 152 mm, an h1 diameter of 126 mm, and an h2 diameter of 181 mm. This size was selected because the next size up with a D2 diameter of 86 mm would exceed the maximum allowable channel width, thus not fitting within the specified 84 mm limit.

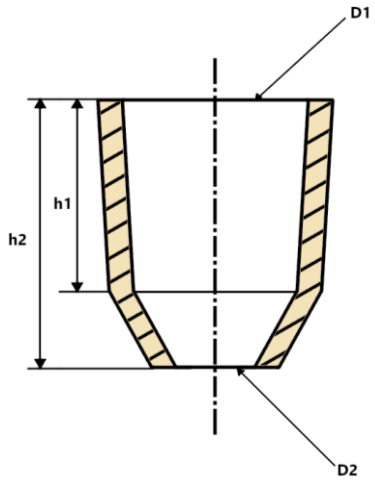

KALPUR Moldeable

Type	Module	Filter Ø	Nominal Dimensions (mm)							Vol.
	(cm)	(mm)	Du	N	Do	do	H	h	T	(dm^3)
ZTAE 10/12	2,50	70	76	48	136	100	120	43	4	0,68
ZTAE 12/15	3,00	90	96	60	157	120	151	45	4	1,29
ZTAE 15/18	3,70	125	120	70	191	152	181	55	5	2,57
ZTAE 18/20	4,30	150	130	86	221	174	200	80	6	3,78
XTAE 21/25	5,30	175	150	100	250	200	250	100	6	6,25
XTAE 23/25	5,80	200	160	110	278	225	250	110	6	7,75

Figure 4.11. *Geometric parameters for commercial sprue selection. In the present case D2 is 70 mm, D1 is 152 mm, h1 is 126 mm and h2 is 181 mm (**top**). Sleeve dimensions for the sprue (**bottom**)* [31].

For the initial casting design, it was decided to proceed with just the sprue and exclude any risers, hypothesizing that the geometry might not necessitate them due to its thinness. To validate this decision and examine the flow dynamics and solidification, relevant simulations were conducted using ESI Group's ProCast software. These simulations incorporated both the gravitational force and the centrifugal force resulting from the rotation of the mold at 30 RPM, as previously described.

The simulation results, depicted in **Figure 4.12**, revealed a critical issue: isolated melt pockets were present in the regions of the three launch lock bumps. This outcome indicates that this melt pockets could generate significant shrinkage in those critical areas making necessary to use some risers.

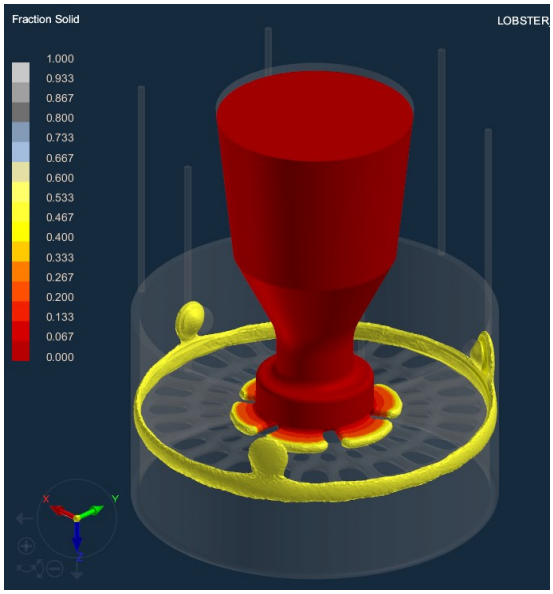

***Figure 4.12**. Solid fraction of the casting design without feeders.*

Therefore, it has been decided to design three risers capable of feeding these three protrusions to avoid shrinkage. The risers are used to feed the parts during the solidification period, in order to compensate the metal shrinkage and to avoid the formation of porosity in the parts, as in this case it seems that it can occur in the three areas of the bumps. To start with the calculation, the filling time must be calculated using Chvorinov's rule [32].

$$t = B\left(\frac{V}{S}\right)^{n} \tag{24}$$

where:

- t represents the solidification time,
- B is the mold constant, reflecting the heat transfer properties of the mold material,
- V is the volume of the casting,
- S is the surface area of the casting in contact with the mold, and

n is a constant that varies depending on the source, with Askeland suggesting a value of 2 [33].

And B is given by:

$$B = \left[\frac{\rho_m L}{T_m - T_0}\right]^2 \left[\frac{\pi}{4k\rho c}\right]\left[1 + \left(\frac{c_m \Delta T_s}{L}\right)^2\right] \tag{25}$$

This includes the melting temperature of the material (T_m), the initial temperature of the mold (T_0), the pouring temperature minus the melting temperature (ΔT_s) which represents the superheat, the latent heat of fusion (L), the thermal conductivity of the mold material (k), the

density of the mold material (ρ), the specific heat of the mold material (c), the density of the casting material (ρ_m), and the specific heat of the casting material (c_m).

Considering a cylindrical shape of the risers and a given height, their radius could be calculated with the riser module (M_r) equation and the Chvorinov's rule.

$$M_r = \sqrt{\frac{1{,}2t}{B}} = \frac{V}{S} \tag{26}$$

Assuming a 20 % longer solidification time for the risers compared to the casting part [40] and a safety margin of 4, the radius of the risers was set to 32 mm. The safety margin was defined based on foundry experience, the effort to produce as many defect-free parts as possible despite very low quantities and the placement of the risers in a cold zone.

Once the sprues were dimensioned, the filling and solidification simulation was carried out using ESI Group's ProCast software, improving the previous result as can be seen in **Figure 4.13**. The melt is still gathered in the bumps but with the sprues it is still possible to feed these areas due to their late solidification.

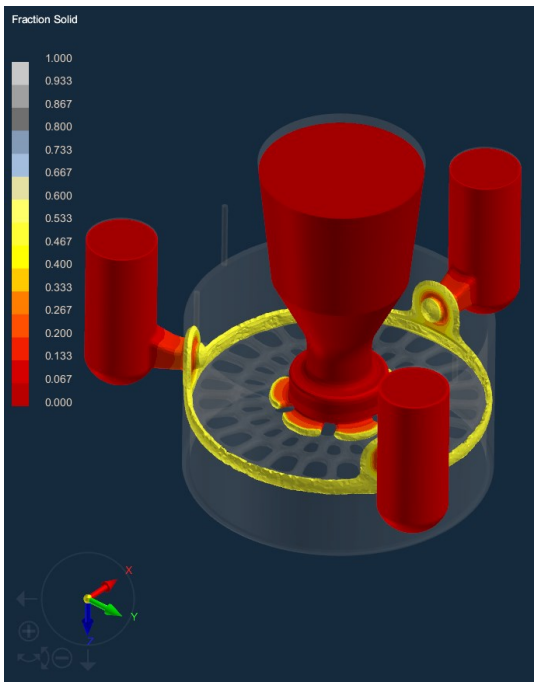

Figure 4.13. *Solid fraction of the casting design with feeders in the launch lock cavities.*

Mold design

Once all components necessary for the casting have been dimensioned and the design validated through relevant simulations, attention must be turned to accommodating the shrinkage that occurs during the solidification of aluminum. This shrinkage takes place after the metal has

solidified and cools down to room temperature, typically resulting in the part being slightly smaller than the mold. This dimensional change is generally expressed as linear shrinkage, and for aluminum sand casting processes, a shrinkage coefficient of 1.2% is commonly applied [32].

Given the complex geometry of the part, the sand mold is fabricated using the Binder Jetting additive manufacturing method. This technique allows for the creation of sand molds by building up layers of bonded sand with a resolution equivalent to the grain size of the sand used, approximately 100 µm. This method is particularly advantageous for producing molds with complex cavities and shapes, which would be challenging with traditional sand mold manufacturing that uses physical models of the part.

The placement of the parting line, where the two halves of the mold meet, is crucial as it influences the molding process and the structural integrity of the mold. A poorly placed parting line can leave fragile parts of the mold exposed, increasing the risk of breakage. Although a horizontal line in the middle plane of the disk might seem the simplest solution for a horizontal molding, considerations regarding access to the necks of the risers and the thickness of the cantilevered flanges have led to the selection of a parting line as shown in **Figure 4.14**.

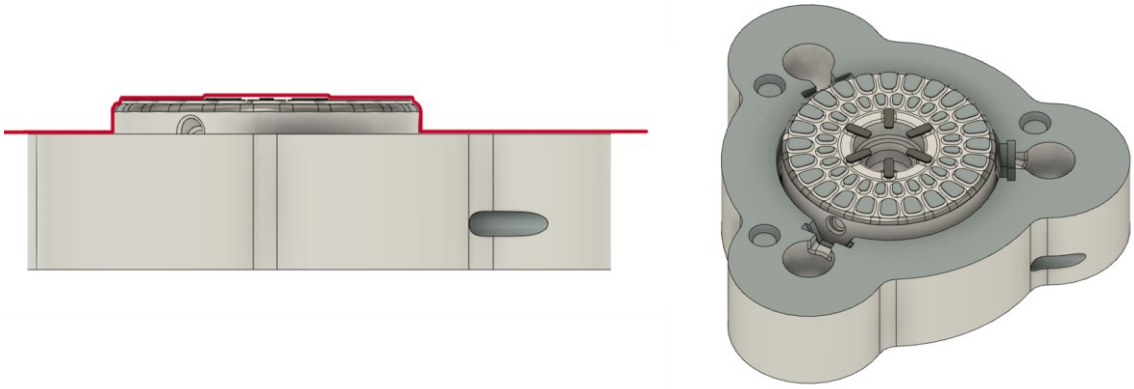

Figure 4.14. *Mold parting line in red and geometry in grey* [22].

4.3.5 Eco-design analysis

To support the choice of the selected manufacturing process, and considering that the end-of-life of the part involves disintegration in the atmosphere—an appropriate behavior for the chosen material as will be explained later—an eco-design analysis was conducted. This analysis compares the energy consumption and carbon footprint of the part depending on the manufacturing method. It is also noted that, in the case of casting, the use of recycled aluminum is possible, whereas for the other methods, this is not as evident. Three manufacturing methods were considered: gravity casting, additive manufacturing via SLM, and machining. Additionally, it was assumed that 10 kg of material would be produced. The results for both energy consumption and carbon footprint obtained from the analysis made in Granta Edupack software are shown in **Figure 4.15** and **Figure 4.16**.

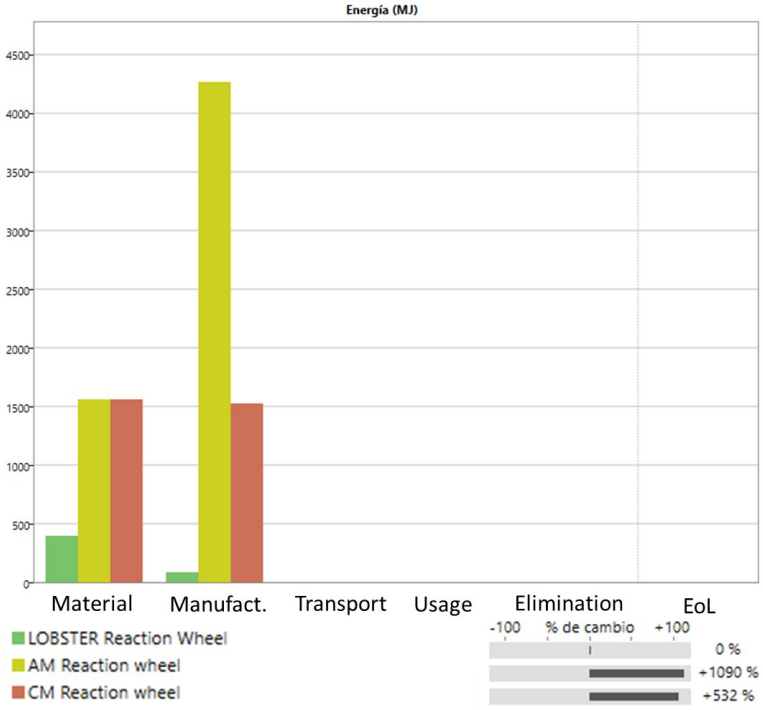

***Figure 4.15**. Eco-design analysis comparing energy consumption (in MJ) for different manufacturing methods: gravity casting, additive manufacturing via SLM, and machining.*

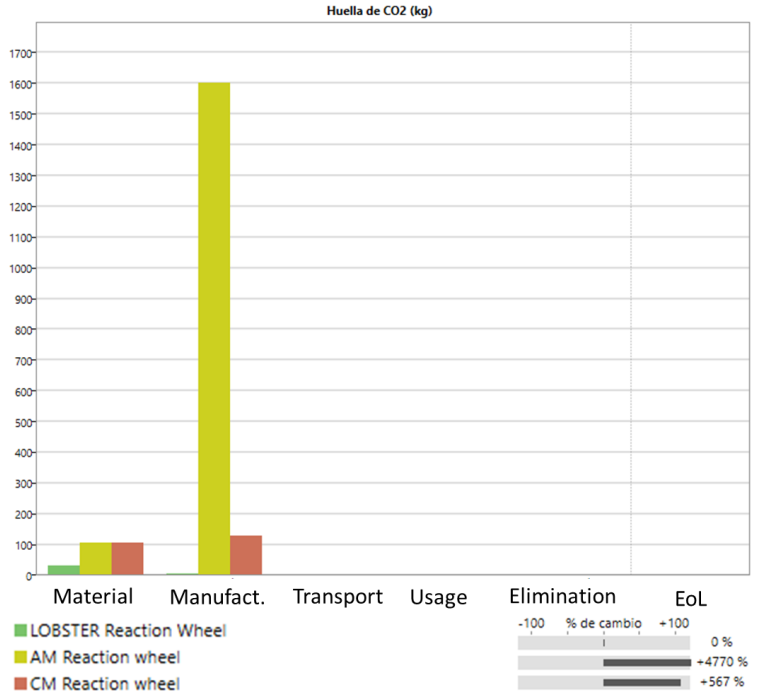

***Figure 4.16**. Eco-design analysis comparing the carbon footprint (in kg CO2) for different manufacturing methods: gravity casting, additive manufacturing via SLM, and machining.*

As shown in these graphs, the chosen method of gravity casting is the most suitable. In terms of energy consumption, additive manufacturing would require an order of magnitude higher energy, and traditional machining would require five times more. When analyzing the carbon footprint,

the difference is even greater: the carbon footprint of the piece manufactured by additive manufacturing is 47 times higher, and by traditional machining, five times higher. This outcome is due to the significant differences in energy consumption and carbon footprint produced by each manufacturing process. Specifically, the energy consumed per kg of material in the SLM process for aluminum is ten times greater than that of casting, and the carbon footprint is 150 times higher [34], [35], [36]. This demonstrates that the chosen manufacturing method, and consequently the part, is clearly superior in terms of environmental sustainability.

4.4 Manufacturing process

To initiate the casting process, the first step involved assembling the mold with its various components inside a demolding box. The necessary sand was then added around the mold manufactured using the binder jetting technique. Following this, the mold assembly and box were placed on a rotary table, set up for the pouring stage, as depicted in the designated **Figure 4.17.**

Subsequently, 25 kg of the chosen aluminum alloy were melted, and Al2O3 nanoparticles were incorporated into the molten metal to enhance its properties. With all preparations complete, the molten material was poured into the rotating mold at the specified angular speed. The casting process proceeded smoothly, and upon demolding, the part was found to be free of any visible defects, as illustrated in the referenced **Figure 4.17**.



Figure 4.17. *Molten metal pouring into the mold (**top**). The area where the riser has been removed (**bottom-left**). The overall view of the manufactured part (**bottom-right**).*

The post-processing of the cast part involved turning and milling operations, necessary to address any distortion and achieve the required surface quality, particularly at the component interfaces. The addition of nano-reinforced particles in the aluminum alloy improved its machinability and helped reduce the occurrence of flow chips typically associated with machining aluminum.

To ensure the part was properly balanced, twelve M3 screw threads were created at both the upper and lower sections of the rim. This design decision was crucial for distributing the weight evenly and enhancing the overall stability of the part during operation. Since this project was conceptualized as a proof of concept, it was determined that a lower grade of balancing would be sufficient for the initial testing and evaluation phases.

4.5 Physical validation

The physical evaluation of the component is a key step to validate the operation of the developed part. This step was fully investigated and performed by Zarm Technik AG.

To ensure the reliable operation of the rotor, it is critical to evaluate the strength of vibrations that arise during its use. In the investigation of micro-vibrations caused by the rotor at various rotational speeds, an experimental setup was employed. This setup involved mounting three uniaxial acceleration sensors of the type PCB 333B50 onto the rotor's stator, as illustrated in **Figure 4.18**, which depicts the measurement configuration [22].

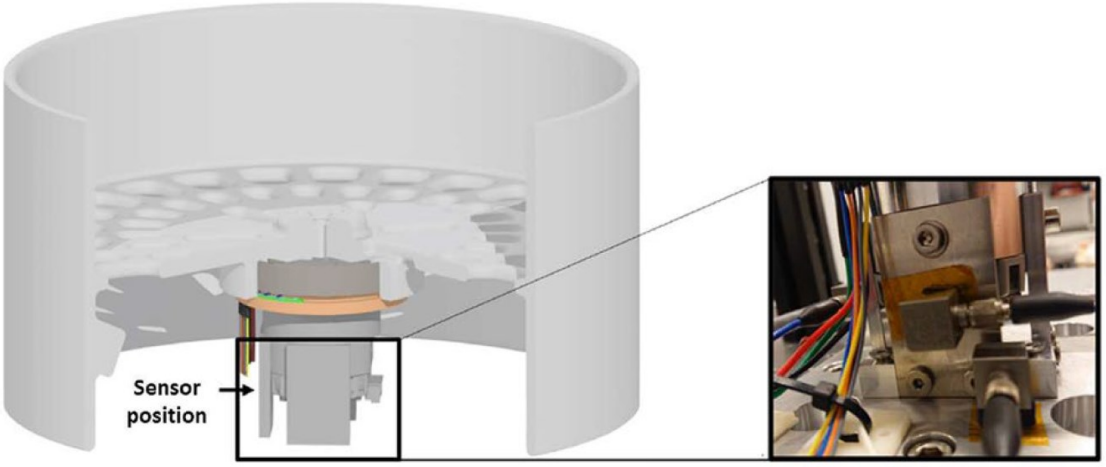

***Figure 4.18**. Physical validation setup* [22].

A mass transfer function was applied to convert the measured accelerations into forces, which were then analyzed in relation to the resonance of the component. Two types of resonance were identified: dynamic resonance and static resonance. Dynamic resonance may be caused by factors such as rotor imbalance or issues with the ball bearings, while static resonance refers to the natural frequencies of the components within the setup. **Figure 4.19** presents the measurement results for dynamic and static resonance across a range of rotational speeds from 1000 RPM down to 0 RPM. An initial calibration was performed using a disc-shaped calibration rotor, which also exhibited static resonance, as shown in **Figure 4.19**. This indicates that the static resonance is related to both the test setup and the rotor mounting, highlighting that static resonances can amplify dynamic resonances [22].

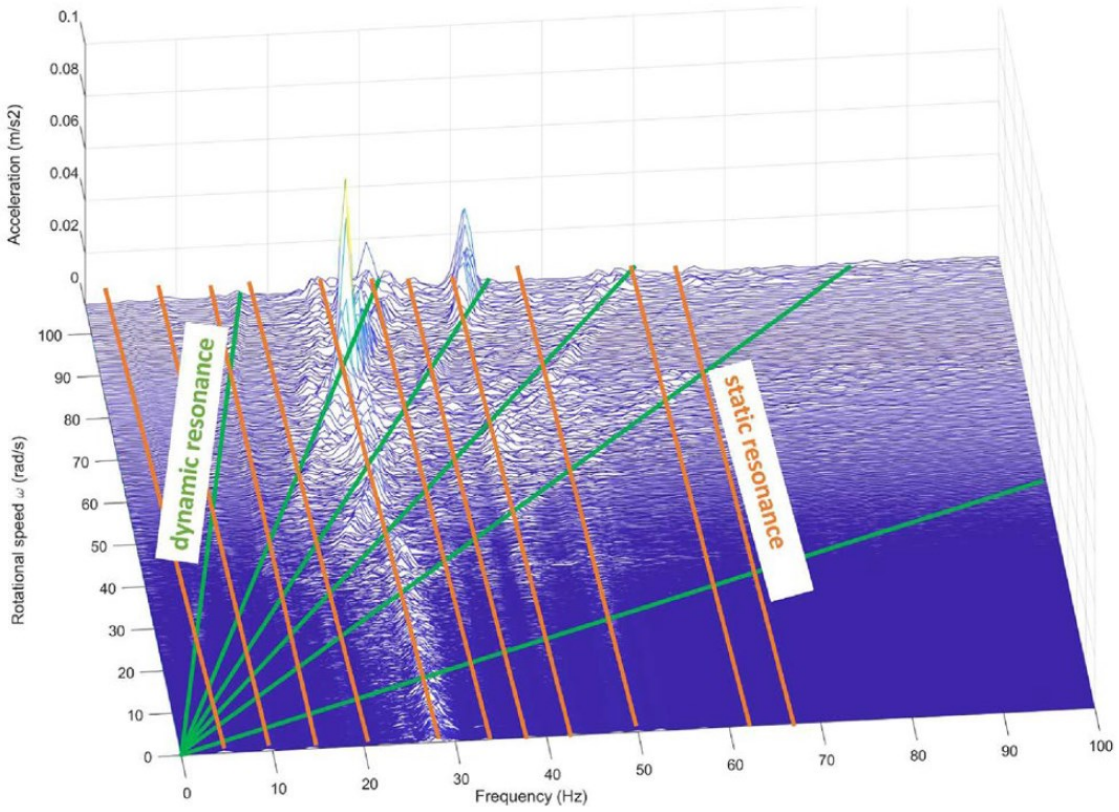

Figure 4.19. *Rotor vibrational measurements for 1000 RPM rotation down to 0 RPM* [22].

During operation, a three-point balancing technique in a single plane was implemented to mitigate the disturbance amplitude. To achieve the displayed level of static imbalance, a balancing mass of 30 g was required. The relatively high level of imbalance restricted the maximum allowable rotation rate, as the bearings were unable to fully compensate for the rotor's eccentric motion. The electric motor's air gap dictated the tolerable extent of eccentric motion. However, the significance of the disturbance amplitude value displayed in **Figure 4.19** is limited by the unknown transfer function, indicating that further analysis is necessary to accurately quantify the vibrational impact. This highlights the complex interplay between various factors in rotor dynamics and emphasizes the need for precise balancing and resonance analysis to ensure optimal performance and longevity of the rotor system [22].

4.6 Discussion

This section will provide a comprehensive evaluation of the various stages of the process that have been described throughout the chapter, starting from the initial design phase through to the validation of the final product. Each step will be analyzed in detail to identify how each contributed to the success of the project and how they interrelate to form a cohesive and effective process.

4.6.1 Bioinspired design process

The analysis of rotor performance seen in **Table 4-2** reveals an unexploited potential for mass savings based on the stress levels observed. The maximum stress encountered is approximately 18% lower than the material's yield strength, suggesting that the rotor's material could be further reduced. This reduction would result in a lower mass while bringing stress levels closer to the maximum allowable value. However, any reduction must still maintain the necessary mass moment of inertia, comply with manufacturability requirements, and adhere to yield strength constraints.

Comparing the bio-inspired design to a topology optimized concept design [14] and a simplified commercial reference model [6], several considerations emerge. The bio-inspired design is 44% heavier and has an inertia to mass ratio that is approximately 19% worse than that of the concept design. Despite these drawbacks, it offers a 30% improvement in energy density and a 27% increase in inertia ratio, suggesting significant enhancements in these areas. Moreover, the design is more compact, featuring a smaller rotor diameter, although it has a greater maximum rotor height.

The rotor inertia of the concept design is about 20% lower, and its design is highly simplified, lacking structural interfaces for bearings, launch locks, or similar features. The incorporation of such features and an increase in inertia would inevitably lead to a higher mass, making comparisons with the concept design somewhat limited.

In contrast, the comparison with the commercial model is more pertinent since it includes similar functionalities of the initial component, despite being simplified according to [6]. Like the concept design, the bio-inspired design is more compact and operates at similar inertia and inertia ratio levels, yet its inertia to mass ratio is 34% lower. Additionally, the bio-inspired design allows for up to 67% faster speeds and an 85% increase in energy density. It also offers advantages in terms of demisability since it is made of aluminum, unlike the commercial stainless steel rotor.

This comparison highlights that the bio-inspired design achieves a comparable performance in terms of mass distribution, as indicated by the inertia ratio, but with a significantly higher energy density. Although a "lightweight" design was not extensively implemented due to manufacturing constraints, the ongoing development of materials and hybrid manufacturing techniques suggests a high potential for substantial improvements. Future adaptations could see reduced material thicknesses, particularly in centrally located, low-stress areas, which would minimally affect inertia that predominantly depends on the rim of the rotor. Furthermore, replacing the comb-like area with finer patterns or lattices could save additional mass.

4.6.2 Material selection

The selection of an aluminum alloy for the rotor was driven by its ability to achieve higher specific energy densities at smaller rotor radii and higher speeds, a critical advantage in applications where performance optimization is essential. This lightweight characteristic of aluminum is not

only essential for achieving high performance in space applications but also facilitates the engineering of components that are easier to transport and integrate into various systems. Moreover, aluminum alloys are favorable in design contexts where weight reduction is as crucial as performance, enhancing the overall energy efficiency of the system.

As a beneficial property, aluminum alloys are capable of fast burn-up during re-entry into the atmosphere, which contributes to reducing space debris—an increasingly important consideration in satellite missions. This attribute ensures that parts made of aluminum pose less risk of contributing to orbital debris, aligning with sustainable practices in space exploration.

Despite these advantages, the use of nano-reinforced aluminum did not appear to offer significant improvements in the analyzed rotor properties, suggesting limitations in the context of mass savings when using bio-inspired design principles. Conversely, higher density materials like Inconel 718, currently in use, offer benefits in terms of rotor mass efficiency and the ability to withstand higher mechanical stresses, potentially enabling further size reduction.

Additionally, Inconel alloys have higher fatigue strength, but from a post-processing perspective, nano-reinforced particles in aluminum alloys have improved machinability and reduced the occurrence of flow chips, which is advantageous in manufacturing processes.

4.6.3 Casting process

During the casting process, several challenges were encountered that potentially affected the quality of the castings and highlighted opportunities for improvement. The mold required rotation, as detailed in previous sections, utilizing a rotating table with a manually set speed of 0.5 RPM. A critical issue encountered was aligning the center of rotation with the center of gravity of the mold, which was complicated by the assembly's weight. This misalignment could lead to uneven distribution of the molten metal, potentially resulting in defects or inconsistent thickness in the casting.

Furthermore, the rapid solidification of the metal posed a significant challenge. The metal needed to be poured quickly enough to fill the entire part before it began to solidify. Given the thinness of the part, the alloy solidified almost immediately, which made it difficult to ensure complete filling without premature solidification.

The complexity of the part's geometry also increased the effort and complexity required in post-processing. Specifically, the central area where the feeder is attached, and the launch lock connections at the inside of the rim were cast as solid geometries without cavities, necessitating extensive material removal during post-processing.

Additionally, the casting quality was compromised by the presence of pores ranging in diameter from 0.5 to 1 mm, observed during post-processing. These defects could have been caused by

inadequate degassing, issues with the mold material, or a suboptimal casting design. These factors need further investigation to improve the outcomes of the casting process.

In discussions about the bio-inspired design process, it was noted that using lattice or fractal honeycomb structures could lead to improvements in rotor performance. However, the fabrication of these structures would require reducing the minimum material thickness, which presents a challenge for traditional casting methods. An alternative fabrication method, such as additive manufacturing, could accommodate the complex geometries of these structures. While additive manufacturing could preserve the integrity of such intricate designs, it may not be suitable for nano-reinforced materials and could reduce the feasibility of manufacturing large quantities compared to traditional casting methods.

To enhance the casting process and the quality of the resulting parts, a thorough evaluation of current casting design, materials, and post-processing methods is necessary. This evaluation should also explore improvements in mold design and alignment techniques for rotational casting.

4.6.4 Physical validation

In evaluating the new rotor, it is important to note that no tests were conducted on a commercial rotor for comparison purposes. The primary objective of these measurements was to verify if the rotor met the specified frequency requirements.

The results of these measurements underscored the importance of the balancing process in achieving low vibration emissions. Furthermore, a detailed analysis of the casting deformations proved crucial for effective post-processing to minimize imbalance. However, the measurements provided only a qualitative evaluation of rotor performance due to the limitations imposed by the mass transfer function. This function, which is challenging to predict, depends on the reaction wheel's components and the setup used for mounting during measurements. For a more precise evaluation, the function should be determined using direct force measurements.

Additionally, modal analysis of the rotor indicated that the detected resonance originated from the measurement setup rather than the rotor itself. Finally, to thoroughly assess the rotor's performance across its entire operational range, it is recommended to test the rotor at higher rotational speeds, extending up to the maximum speed of 7500 RPM. This would allow for more comprehensive conclusions about its behavior under various operational conditions.

4.7 Conclusions

In this chapter, the development of a reaction wheel within the framework of a collaborative project involving multiple entities has been detailed. Each entity significantly contributed to the success of the study. The main goal was to optimize a reaction wheel for small to medium-sized

satellites, aiming to maximize the moment of inertia within a required range while minimizing mass, ensuring load case endurance, and avoiding specific natural frequencies to prevent unwanted resonances.

Although a direct comparison with a rotor in an identical operational environment was not possible, the findings demonstrated that the proposed rotor could be a viable option for redesigning many of the rotors currently on the market. Despite operating in an environment with less favorable rotational speeds, the rotor exhibited higher energy density and improved inertia ratios compared to other rotors analyzed. This study supports the applicability of bio-inspired design methodologies in component manufacturing, promising to be a valuable alternative across various industries, particularly in the space industry where resource optimization is crucial.

Additionally, paralleling developments in the aerospace tooling chapter, the effectiveness of sand casting molds produced via binder jetting technology was highlighted. This technique proves to be an efficient option for prototype manufacturing and, at a moderate production scale, can be an interesting alternative to direct additive manufacturing of highly complex geometric components.

The physical validation of the part revealed some balance issues in the reaction wheel, potentially due to a lack of optimization in the design and casting process. The use of possibly excessive safety margins was a precaution taken to minimize defects, but future experiences could allow for these margins to be adjusted to enhance performance. Regardless of the manufacturing process used, an appropriate post-process will always be necessary to mitigate the effects of manufacturing defects.

For future developments stemming from this project, exploring the use of more complex bio-inspired patterns, such as cellular structures, could further optimize the component, albeit at the expense of the advantages of the current manufacturing process. Additionally, a detailed study using FEM simulations of the thermal behavior of the component would be valuable, considering the extreme thermal conditions of space, ranging from -65°C to 125°C [37]. It would also be beneficial to collaborate with tier 1 entities in the European space industry to certify this type of manufacturing process for application in real spaceflight components.

4.8 References

[1] "Space Foundation Releases The Space Report 2023 Q2, Showing Annual Growth of Global Space Economy to $546B." Accessed: Apr. 22, 2024. [Online]. Available: https://www.spacefoundation.org/2023/07/25/the-space-report-2023-q2/

[2] "SpaceTech Market Size & Growth Analysis Report, 2030." Accessed: Apr. 22, 2024. [Online]. Available: https://www.grandviewresearch.com/industry-analysis/space-technology-market-report

[3] "2023 SIA Report: Space Business Revenue Globally | Hughes." Accessed: Apr. 22, 2024. [Online]. Available: https://www.hughes.com/resources/insights/industry/2023-sia-report-satellite-industry-contributes-73-space-business

[4] "A giant leap for the space industry." Accessed: Apr. 22, 2024. [Online]. Available: https://www.mckinsey.com/featured-insights/sustainable-inclusive-growth/chart-of-the-day/a-giant-leap-for-the-space-industry

[5] "Rocket Science 101: Operating Principles | Aerospace Engineering Blog." Accessed: Apr. 22, 2024. [Online]. Available: https://aerospaceengineeringblog.com/rocket-science-101-operating-principles/

[6] S. H. Park, S. Mischler, and P. Leyland, "Re-entry analysis of critical components and materials for design-for-demise techniques," *Advances in Space Research*, vol. 68, no. 1, pp. 1–24, Jul. 2021, doi: 10.1016/J.ASR.2021.03.019.

[7] M. Spel, E. Constant, P. Van Hauwaert, J. Dumon, S. Galera, and J. Annaloro, "DEMISABILITY STUDY OF INDUSTRIAL TEST CASES WITH THE SPACECRAFT-ORIENTED CODE PAMPERO," 8th European Conference on Space Debris. Accessed: Apr. 22, 2024. [Online]. Available: https://conference.sdo.esoc.esa.int/proceedings/sdc8/paper/278

[8] Bernd. Klein, *Leichtbau-Konstruktion : Berechnungsgrundlagen und Gestaltung*. Friedr. Vieweg & Sohn Verlag, 2007. Accessed: Apr. 22, 2024. [Online]. Available: https://books.google.com/books/about/Leichtbau_konstruktion.html?hl=es&id=9t4L99lJt_4C

[9] M. A. Arslan, "Flywheel geometry design for improved energy storage using finite element analysis," *Mater Des*, vol. 29, no. 2, pp. 514–518, Jan. 2008, doi: 10.1016/J.MATDES.2007.01.020.

[10] L. Pedrolli, A. Zanfei, S. Ancellotti, V. Fontanari, and M. Benedetti, "Shape optimization of a metallic flywheel using an evolutive system method: Design of an asymmetrical shape for mechanical interface," *https://doi.org/10.1177/0954406216682054*, vol. 232, no. 2, pp. 217–230, Nov. 2016, doi: 10.1177/0954406216682054.

[11] G. R. Kress, "Shape optimization of a flywheel," *Structural and Multidisciplinary Optimization*, vol. 19, no. 1, pp. 74–81, Mar. 2000, doi: 10.1007/S001580050087/METRICS.

[12] L. Jiang, W. Zhang, G. J. Ma, and C. W. Wu, "Shape optimization of energy storage flywheel rotor," *Structural and Multidisciplinary Optimization*, vol. 55, no. 2, pp. 739–750, Feb. 2017, doi: 10.1007/S00158-016-1516-0/TABLES/8.

[13] V. Kale, M. Thomas, and M. Secanell, "On determining the optimal shape, speed, and size of metal flywheel rotors with maximum kinetic energy," *Structural and Multidisciplinary*

Optimization, vol. 64, no. 3, pp. 1481–1499, Sep. 2021, doi: 10.1007/S00158-021-02935-X/FIGURES/12.

[14] L. M. Lottes, N. Kaiser, N. Goossens, H. W. Oelze, and C. Braxmaier, "TOMARES: Topology optimization of an additive manufactured reaction flywheel designed for an Earth-observation satellite," *CEAS Space Journal*, vol. 13, no. 4, pp. 521–532, Oct. 2021, doi: 10.1007/S12567-020-00343-3/TABLES/11.

[15] H. Hashemi Farzaneh and U. Lindemann, "A Practical Guide to Bio-inspired Design," *A Practical Guide to Bio-inspired Design*, 2019, doi: 10.1007/978-3-662-57684-7.

[16] R. Müller *et al.*, "Biodiversifying bioinspiration," *Bioinspir Biomim*, vol. 13, no. 5, p. 053001, Jul. 2018, doi: 10.1088/1748-3190/AAC96A.

[17] B. Lal *et al.*, "Global Trends in Small Satellites," 2017.

[18] J. L. (James L.) Meriam and L. G. (L. G. Kraige, *Engineering Mechanics: Dynamics*. Wiley, 2012.

[19] F. F. Ehrich, "Handbook of rotordynamics," 1992.

[20] M. D. Griffin and J. R. French, "Space Vehicle Design, Second Edition," *Space Vehicle Design, Second Edition*, Dec. 2005, doi: 10.2514/4.862403.

[21] G. Borque Gallego, "Performance and Micro-Vibrations in Magnetic Bearings for Space Actuators," 2021, doi: 10.5075/EPFL-THESIS-8425.

[22] N. Kaiser, N. Goossens, A. Jimenez, I. Laraudogoitia, S. Psarras, and S. Tsantzalis, "Advanced manufacturing concept of a bio-inspired reaction wheel rotor for small- and medium-sized constellation satellites," *CEAS Space Journal*, vol. 16, no. 1, pp. 73–86, Jan. 2024, doi: 10.1007/s12567-023-00489-w.

[23] M. Helms, S. S. Vattam, and A. K. Goel, "Biologically inspired design: process and products," *Des Stud*, vol. 30, no. 5, pp. 606–622, Sep. 2009, doi: 10.1016/J.DESTUD.2009.04.003.

[24] G. Pohl and W. Nachtigall, "Biomimetics for Architecture & Design," *Biomimetics for Architecture & Design*, 2015, doi: 10.1007/978-3-319-19120-1.

[25] C. Hamm, *Evolution of Lightweight Structures*, vol. 6. in Biologically-Inspired Systems, vol. 6. Dordrecht: Springer Netherlands, 2015. doi: 10.1007/978-94-017-9398-8.

[26] F. E. (Frank E. Round, R. M. Crawford, and D. G. Mann, *The Diatoms : biology & morphology of the genera*.

[27] "ANSP Diatom New Taxon File." Accessed: Apr. 22, 2024. [Online]. Available: http://symbiont.ansp.org/dntf/

[28] "MIDACO-SOLVER." Accessed: Apr. 22, 2024. [Online]. Available: http://www.midaco-solver.com/

[29] "ECSS-E-ST-32-10C Rev.1 – Structural factors of safety for spaceflight hardware (6 March 2009) | European Cooperation for Space Standardization." Accessed: Apr. 22, 2024. [Online]. Available: https://ecss.nl/standard/ecss-e-st-32-10c-rev-1-structural-factors-of-safety-for-spaceflight-hardware/

[30] D. G. Ullman, *The mechanical design process with case studies*.

[31] "Foundry - Vesuvius." Accessed: Mar. 29, 2024. [Online]. Available: https://www.vesuvius.com/en/our-solutions/international/foundry.html

[32] J. Campbell, "Complete Casting Handbook: Metal Casting Processes, Metallurgy, Techniques and Design: Second Edition," *Complete Casting Handbook: Metal Casting Processes, Metallurgy, Techniques and Design: Second Edition*, pp. 1–1028, Sep. 2015, doi: 10.1016/C2014-0-01548-1.

[33] D. R. Askeland, *The Science and Engineering of Materials*. Springer US, 1996. doi: 10.1007/978-1-4899-2895-5.

[34] M. R. Jolly and K. Salonitis, "Investigating the energy consumption of casting process by multiple life cycle method," 2014. [Online]. Available: https://www.researchgate.net/publication/281207786

[35] Z. Y. Liu, C. Li, X. Y. Fang, and Y. B. Guo, "Energy Consumption in Additive Manufacturing of Metal Parts," Elsevier B.V., 2018, pp. 834–845. doi: 10.1016/j.promfg.2018.07.104.

[36] C. van Sice and J. Faludi, "Comparing environmental impacts of metal additive manufacturing to conventional manufacturing," in *Proceedings of the Design Society*, Cambridge University Press, 2021, pp. 671–680. doi: 10.1017/pds.2021.67.

[37] J. Plante, "Environmal Conditions for Space Flight Hardware-A Survey For the NASA Electronic Parts and Packaging", Accessed: Apr. 22, 2024. [Online]. Available: http://arioch.~sfc.nasa.lzov/302/~evs-se/toc.htm

Chapter 5: Scaled gear for wind turbines

5.1 Introduction

The dawn of the 21st century has witnessed an unprecedented surge in global energy demand, propelled by rapid industrialization, technological advancements, and population growth. This escalating demand poses a significant challenge, highlighting the dependency on traditional energy sources such as fossil fuels. The reliance on coal, oil, and natural gas has long been the backbone of the world's energy grid, powering everything from industries to everyday household needs. However, these conventional sources are finite and have raised serious environmental concerns, primarily due to their contribution to global warming and pollution.

In response to these challenges, there has been a global shift towards exploring and implementing alternative energy sources. This shift is marked by a growing interest in energy harvesting -a concept that revolves around harnessing energy from renewable sources like the sun, wind, water, and geothermal heat. Unlike traditional methods, these renewable sources offer an inexhaustible supply of energy, presenting a sustainable solution to meet the world's growing energy needs. Furthermore, advancements in technology have made it possible to efficiently capture and utilize these sources, making renewable energy more viable and accessible than ever before.

The transition to renewable energy sources is not just a technological shift but a necessary step towards environmental stewardship and sustainability. As the world continues to deal with the effects of climate change, the role of renewable energy in mitigating these impacts becomes increasingly crucial. The move towards energy harvesting signifies a profound change in how energy is perceived and utilized, marking a pivotal moment in the history of energy production and consumption.

The renewable energy sources, unlike their fossil fuel counterparts, offer plenty of benefits, chief among them being their inexhaustibility and lower carbon footprint.

Solar energy, harnessed from the sun, is a cornerstone of renewable energy. It utilizes photovoltaic cells to convert sunlight directly into electricity, or solar thermal technology to use the heat from the sun for water heating or power generation. Wind energy, another key player, captures the wind's kinetic energy through turbines to produce electricity. Hydroelectric power, generated by harnessing the energy of moving water, typically from rivers or dams, is a well-established renewable source. Geothermal energy, though less widespread, utilizes the heat from the Earth’s interior for heating and power generation.

Biomass, including biofuels derived from organic materials, is used for heating and as an alternative to fossil fuels in transportation. Additionally, tidal and wave energy, although in earlier stages of development, harness the energy of ocean tides and waves, respectively.

In Europe, the commitment to renewable energy is evident in its increasing share in the overall energy mix. In 2022, approximately 23% of the energy consumed in Europe came from renewable sources [1] as seen in **Figure 5.1**. This significant proportion reflects the continent's concerted efforts in transitioning towards more sustainable energy practices. The trend in Europe is a testament to the potential of renewable energy sources in transforming the global energy landscape, offering a blueprint for other regions aiming to reduce their reliance on non-renewable energy sources. This shift not only represents a response to environmental concerns but also an adaptation to the evolving energy needs of a growing population.

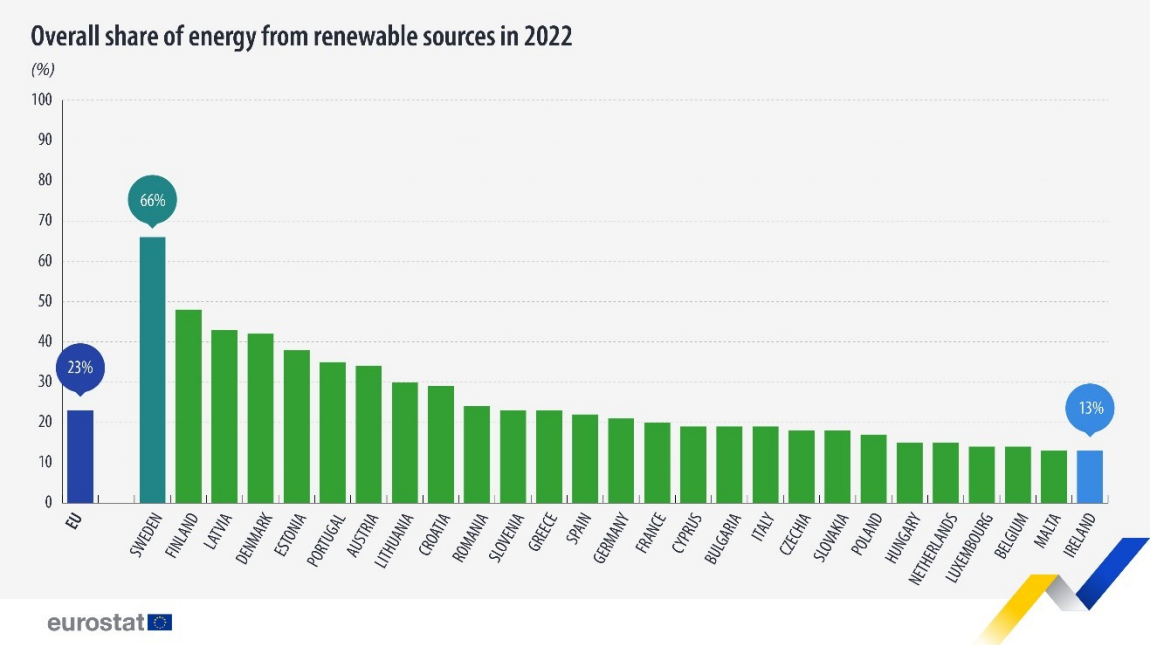

***Figure 5.1**. Overall share of energy from renewable resources in 2022 by Eurostat. Source:* [1]

This focus on renewable energy is not just an environmental consideration; it's a strategic move towards energy independence and long-term sustainability. The diverse range of renewable energy sources offers a multifaceted approach to meeting the world's energy needs, marking a significant shift from the traditional reliance on fossil fuels. As technology advances and the efficiency of renewable energy sources improves, the potential for a complete transition to a greener, more sustainable energy system becomes more tangible.

The transition towards renewable energy sources, while crucial, also underscores the need for efficiency in energy harvesting devices. The effectiveness with which these devices capture, convert, and store energy is paramount to maximizing the potential of renewable sources. Solar panels, wind turbines, and other renewable energy technologies are continually undergoing refinements to enhance their efficiency and output. This is crucial because the more efficiently

these devices operate, the more viable renewable energy becomes as a replacement for traditional fossil fuels.

The efficiency of wind turbines, for instance, is a critical aspect of renewable energy technology, directly influencing the effectiveness and economic viability of wind energy. Wind turbines convert the kinetic energy in wind into mechanical power, which is then turned into electricity. The efficiency of this process depends on several factors, including the design of the turbine, the materials used, and the characteristics of the wind at the installation site.

Modern wind turbines are marvels of engineering, designed to maximize energy capture. The blades are shaped to extract the maximum amount of energy from the wind, and advancements in materials have led to lighter, more durable blades. These improvements enable turbines to operate in a wider range of wind speeds and conditions, increasing their overall effectiveness.

Moreover, technological advancements in wind turbine design continue to push the boundaries of efficiency. Innovations like improved gearbox designs, advanced control systems, and predictive maintenance using AI and IoT technologies contribute to enhancing turbine performance, reducing downtime, and extending their operational lifespan.

A modern wind turbine is composed of several key components, each playing a crucial role in converting wind energy into electricity which can be observed in **Figure 5.2**. The main parts include:

1) **Foundation**: This is the base of the wind turbine, providing stability and support. For onshore turbines, it's a large concrete block buried in the ground, while offshore turbines have foundations underwater or floating structures.

2) **Tower**: Made primarily of steel, the tower supports the rest of the turbine components and is tall enough to allow the blades to operate efficiently. Its height typically matches the diameter of the blades' rotation circle.

3) **Rotor and hub**: The rotor includes the blades and the hub, which connects them. These blades, usually three in number, are designed to capture wind energy efficiently. They are airfoil-shaped, lightweight, and strong, often made of composite materials.

4) **Nacelle**: Sitting atop the tower, the nacelle houses several crucial turbine components like the gearbox, braking systems, generator, and electrical power transmission systems. It's the 'head' of the wind turbine.

    a) **Gearbox assembly**: Transforms the rotor's slow rotation into a higher speed suitable for generating electricity.

    b) **Braking systems**: Includes aerodynamic and mechanical brakes to control the turbine's speed and stop it when necessary.

c) **Turbine generator**: Converts the rotational energy into electrical energy through electromagnetic induction.

d) **Yaw system**: Align the turbine's rotor with wind direction.

5) **Generator**: Converts the mechanical energy from the rotor into electrical energy, typically located within the nacelle.

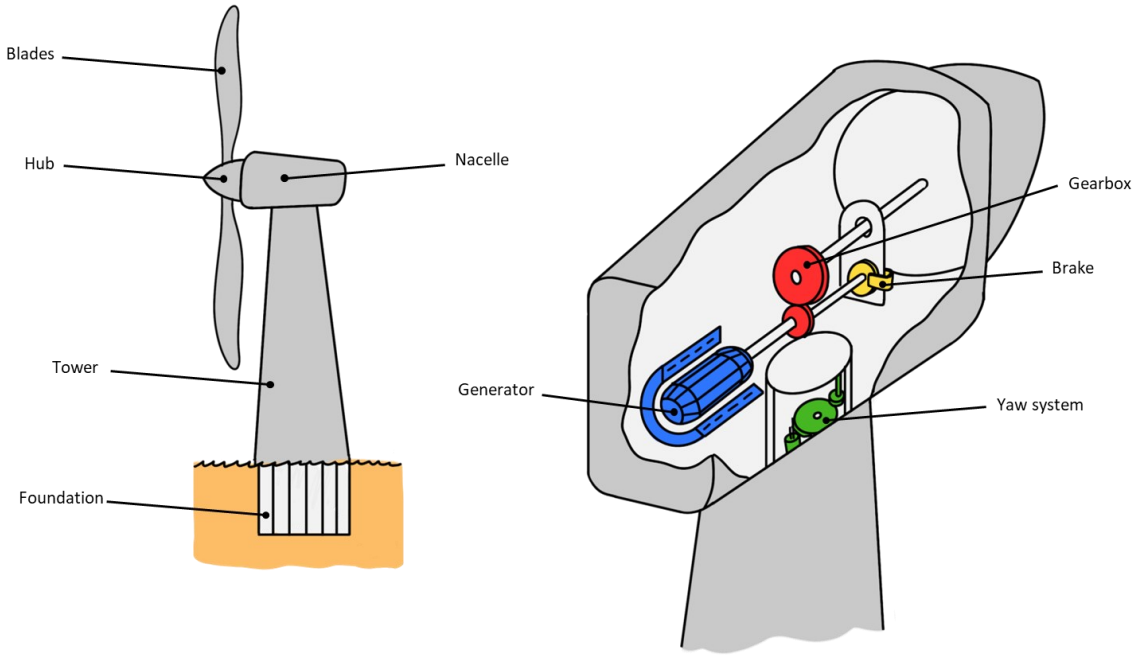

***Figure 5.2**. Drawings of a wind turbines from outside (left) and from inside (right).*

As observed, two of the four main elements within the nacelle of wind turbines are comprised of gear systems, highlighting their critical role in the efficient functioning of this energy generation hardware. The gearbox is primarily responsible for converting the rotor's slow rotation into a speed sufficient for effective electricity generation. Consequently, the gears within it must be robust and designed to withstand heavy loads, cyclic stresses, and wear and tear. Similarly, the gears in the yaw system are crucial for accurately and reliably moving the nacelle to align with wind direction. These gears also need to be robust, as they bear both the weight of the nacelle and the dynamic forces exerted by the wind.

As we delve into the future of renewable energy, the focus on redesigning and optimizing wind turbine gear systems stands as a key topic in this ongoing narrative. Gears are key for the overall operation of a wind turbine. Therefore, enhancing the design and functionality of these gears is not just a matter of mechanical improvement but a step forward in harnessing wind energy more effectively and sustainably. This pursuit underscores a broader commitment to refining renewable energy technologies, aligning with global efforts to mitigate climate change and reduce reliance on fossil fuels. The innovative advancements in gear technology within wind

turbines represent a key aspect of this evolution, promising a future where renewable energy is not only more prevalent but also more efficient and reliable.

In this chapter, the focus will be on the investigation of redesigning a gear wheel using the methodology proposed throughout the manuscript, specifically tailored to the unique operating conditions of this component in wind turbines. Before diving into the practical aspects, the chapter will provide a theoretical context covering relevant topics not yet addressed. This theoretical groundwork is essential for understanding the complexities involved in gear redesign and the specific challenges faced in wind turbine applications. After the practical redesign process, the chapter will analyze the results obtained, discussing their implications and the derived conclusions. This comprehensive approach, from theory to practical application and analysis, aims to offer a deeper understanding of gear wheel redesign in wind turbines, highlighting its significance in enhancing the efficiency and sustainability of renewable energy technologies.

5.2 Theoretical framework: gear theory, failure mechanisms

Gears are used in most types of machinery. They are used to transport kinetic energy from one place to another with different speeds, directions and torques. Gear design is a highly complicated art. The constant development to build less expensive, quieter running, lighter, and more powerful machinery has resulted in a steady change in gear designs. At present much is known about gear load-carrying capacity, and many complicated processes for making gears are available.

5.2.1 Fundamental gear theory

First, it is essential to understand the dimensions and characteristics of gears. To this end, the following list will enumerate all the pertinent concepts [2], with some of them illustrated in **Figure 5.3**:

- Pinion. When two gears mesh together, the smaller is called the pinion. The larger is called the *gear*.
- Ratio. Ratio is an abbreviation for gear tooth ratio, which is the number of teeth on the gear divided by the number of teeth on its mating pinion.
- Module (m). A measure of tooth size in the metric system. In units, it is millimeters of pitch diameter per tooth. As the tooth size increases, the module also increases.
- Circular pitch (p). The circular distance from a point on one gear tooth to a like point on the next tooth, taken along the pitch circle. Two gears must have the same circular pitch to mesh with each other.
- Pitch diameter (D). The diameter of the pitch circle of a gear.
- Addendum (h_a). The radial height of a gear tooth above the pitch circle.
- Dedendum (h_f). The radial height of a gear tooth below the pitch circle.

- Whole depth (h). The total radial height of a gear tooth (whole depth = addendum + dedendum).
- Pressure angle (α). The slope of the gear tooth at the pitch-circle position. (If the pressure angle is 0º, the tooth is parallel to the axis of the gear which is a spur-gear tooth.)
- Helix angle (β). The inclination of the tooth in a lengthwise direction. (If the helix angle is 0º, the tooth is parallel to the axis of the gear which is a spur-gear tooth.)
- Outside diameter (D_o). Diameter of the gear, measured from the top of the tooth.
- Root diameter (D_R). Diameter of the gear measured from the base of the tooth.

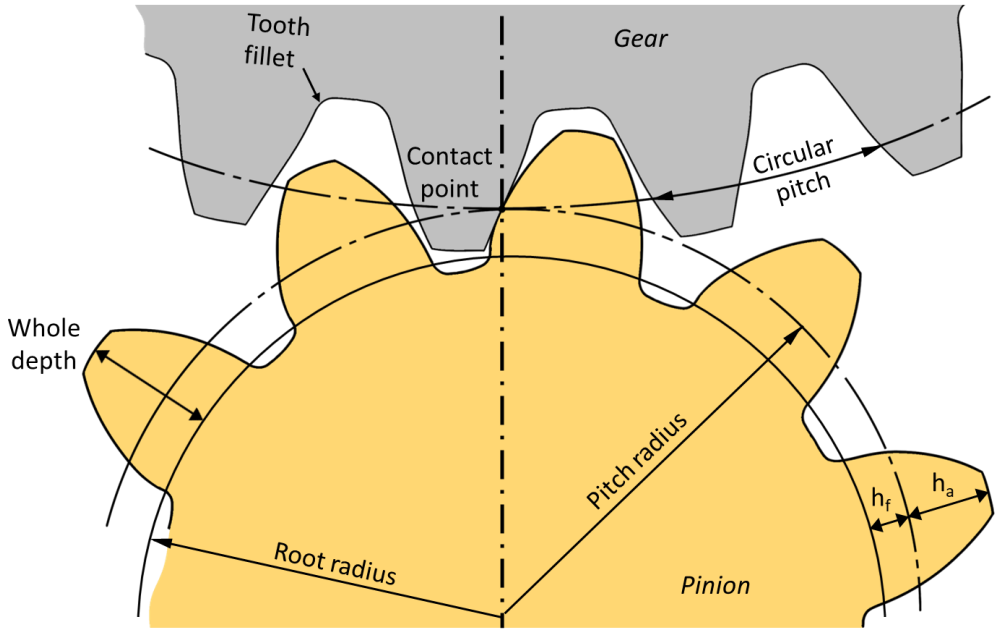

***Figure 5.3**. Spur gear nomenclature* [2].

There are some basic formulas in gear design that need to be explained to understand the dimensions of these components. The module of a gear can be defined as:

$$m = \frac{p}{\pi} \tag{1}$$

Knowing also that the pitch diameter can be defined as:

$$D = N \cdot m \tag{2}$$

Being N the number of teeth on the gear. Therefore, the addendum and the dedendum can be defined as:

$$h_a = \frac{1}{2}(D_o - D) \tag{3}$$

$$h_f = \frac{1}{2}(D - D_R) \tag{4}$$

5.2.2 Movement and load transmission fundamentals

Gear ratio represents the ratio of the speeds at which the two gears rotate. The gear ratio can tell you how much the gear system will amplify torque or speed from the input (driving gear) to the output (driven gear). As mentioned before, this gear ratio is also defined by the number of teeth of each of the components of the gear system.

Gearing allows for significant reduction or increase in speed without a strict limit, but achieving high ratios can lead to complex component arrangements. In a basic gear setup, a maximum ratio of around 8:1 to 10:1 is feasible. The speed change is determined by comparing the pitch diameters of the gears; this ratio can also be calculated by dividing the number of teeth on the larger gear by the number on the smaller gear. The smaller gear, often referred to as the pinion, plays a key role. To achieve a 10:1 ratio, the gear needs to be ten times larger than the pinion, but exceeding this ratio may pose stress or geometric challenges for the pinion. To reach even higher ratios in parallel shaft gearing, multiple stages of gear meshes are combined. Therefore, the gear ratio can be defined as follows:

$$GR = \frac{D_2}{D_1} = \frac{N_2}{N_1} = \frac{\omega_1}{\omega_2} = \frac{T_1}{T_2} \tag{5}$$

Where 1 is the driver gear and 2 is the driven gear.

The ratio of a gearbox is usually referred to the maximum power and torque capacity for which a gearbox is designed. Therefore, gearbox rating is determined by the loads the gearbox components are capable of transmitting. In some cases where a system is operating continuously at a uniform load such as an electric motor driving and fan, the loading is simple to predict and component analysis can be based on a continuous horsepower transmitted at steady speed. Some applications, however, experience variable loading such as high starting torque or shock loads and these conditions must be considered in the gearbox design.

Load Transmission

It is interesting to know what mechanisms are involved in the transmission of motion and loads in gear systems:

- **Contact Stress**: Gears transmit loads through contact between their teeth. The shape and material of the teeth determine the maximum load they can handle without failure.
- **Power Transmission**: The power transmitted by gears is a function of the torque applied to the gear's shaft and the angular velocity. Gear design aims to maximize power transmission while minimizing losses due to friction and wear.
- **Efficiency**: Gear efficiency is the ratio of the output power to the input power. It is influenced by factors such as friction, the material properties of the gears, and the precision of their manufacturing.

To calculate gear and shaft loads, the gear tooth loads must be developed. **Figure 5.4** illustrates the load diagram on a spur gear tooth.

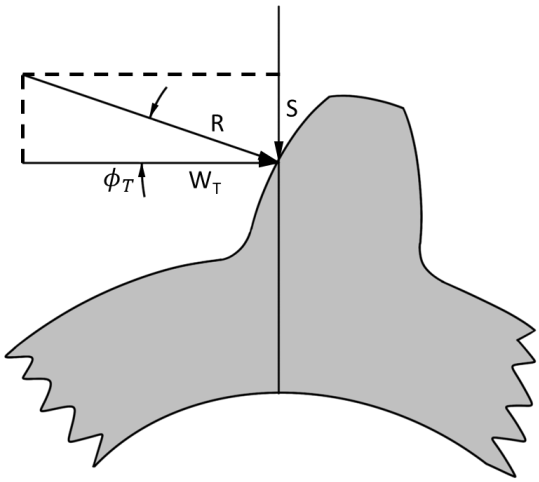

***Figure 5.4**. Spur gear's load transmission drawing.*

The torque transmitted by the gears can be defined by [3]:

$$T = \frac{P}{\omega} \tag{6}$$

Where T is torque in $N \cdot m$, P is power in W and ω is rotational speed in rad/s. The tangential load is defined as [3]:

$$W_T = \frac{2 \cdot T}{D} \tag{7}$$

Where W_T is tangential load and D is the pitch diameter. Therefore, the total load transmitted can be calculated by [3]:

$$R = \frac{W_T}{\cos \phi_T} \tag{8}$$

The maximum tensile stress at the tooth root, which should not exceed the allowable bending stress of the material, is crucial for evaluating the bending strength of gear teeth. This stress is concentrated in the "tension fillets" of the active tooth surfaces. If cracks due to loading develop, they typically initiate in the "compression fillets" of the inactive surfaces where compressive stress is present. In cases of unidirectional tooth loading with standard tooth shapes, these cracks usually do not progress to failure. Failures from crack propagation are more likely to originate in tension fillets. [4]

Loads and Stresses in Wind Turbine Gears

Compared to standard gears, wind turbine gears face a more complex and variable load regime, necessitating specific design considerations and materials to ensure reliable and durable operation under these conditions [5].

1. Torque Loads: The torque in wind turbine gears fluctuates with wind power. Therefore, the design should be sized for the maximum power the wind turbines are rated for.

2. Static and Dynamic Loads: Gears experience static loads from the weight of structures and components, as well as dynamic loads from wind turbine operation. Dynamic loads are particularly significant due to variations in wind speed and direction, making it crucial to study fatigue in these components.

3. Bending and Contact Loads: Bending loads on gear teeth arise from force transmission along the axes. Additionally, contact loads impact tooth surfaces, potentially leading to failures from surface fatigue or abrasive wear.

4. Misalignment Loads: Shaft misalignment, whether due to ground settlement, tower deflection, or thermal expansion, imposes additional loads on gears, resulting in increased contact forces at non-ideal points on the teeth.

5.2.3 Failure analysis and wear mechanisms

It is of particular importance to mention the failure mechanisms that gears can experience, as most are intrinsic to the operation of these components. First, it is essential to consider the commonly accepted definition of failure:

"A gear has failed when it can no longer efficiently perform the task for which it was designed." [6].

While this statement holds true, determining the specific cause of gear failure can often be complex. In many instances, multiple failure causes can overlap. Nevertheless, it is vital to understand the individual failure mechanisms of gears separately.

Fatigue

Fatigue failure, characterized by cracking under repeated stresses significantly lower than the ultimate tensile strength, is typically influenced by the number of stress cycles within a specific stress range rather than the total time under load. This type of failure does not occur below the stress amplitude known as the "fatigue limit." The presence of notches, grooves, surface irregularities, and subsurface imperfections can greatly increase the risk of fatigue failure by reducing the stress amplitude endurance for a given number of cycles. Additionally, elevating the average tensile stress during loading cycles significantly raises the likelihood of fatigue failure.

- **Tooth bending fatigue** is the predominant form of fatigue failure in gearing systems. While there are various manifestations of this failure mode, understanding the classic failure scenario can shed light on its different variations. The classic failure occurs when a tooth is in operation, and after multiple loading cycles in the root fillet radius where the highest tensile stress concentration exists, a crack initiate. This crack propagates towards the zero-stress point in the central region of the tooth (path of least energy) before ultimately reaching the opposite root where the highest compressive stress concentration occurs.
- **Surface contact fatigue** or **pitting** is known as a material-fatigue mode of failure. It happens at and near the contact surface area of the teeth where cyclic compressive stresses occur. Plastic and elastic deformation happen indifferently in the microstructure of the material. The differences of plasticity between grains will encourage fatigue cracks to initiate. The material hardness is a key property to avoid this failure mechanism, the bigger the hardness the more difficult will be that component to fail.
- **Rolling contact fatigue** is a phenomenon that occurs when surfaces of gears roll over each other under a loading condition. The stresses occurring during this rolling action may be within the material properties' margins. However, due to the nature of cyclic loading it can lead to the initiation and propagation of cracks. Surface finish as a key feature for avoiding this failure.
- **Contact fatigue** or **spalling** is not considered a crack initiation method but rather a propagation mechanism of pitting and rolling. Spalling is characterized by the flaking or chipping off of material from the surface, leading to roughness, noise, and eventually, mechanical failure.

Impact

Impact failure mechanisms in gears encompass the damage and failures resulting from sudden or repeated impact forces applied to gear teeth during operation. These failures can stem from tooth bending, tooth shear, and various other phenomena of differing natures.

Wear

Surface deterioration of the active profile of the gear teeth is called "wear." There are two distinct modes of wear abrasive and adhesive.

- **Abrasive wear** occurs when surface is being damaged, or material removed by hard abrasive particles. It only happen when two surfaces are in sliding contact. This type of wear is common in environments where gears are exposed to contaminated lubricants, debris, or when the gear materials themselves are of different hardness levels.
- **Adhesive wear** occurs on sliding surfaces when the pressure between the contacting asperities is sufficient to cause local plastic deformation and adhesion. This adhesion causes the removal of the material of one or both surfaces.

In conclusion, certain failure modes are more prevalent than others. Through the compilation of findings from numerous failure analysts across different fields of expertise, it has been established that fatigue is the most common failure mode, followed by impact (tensile or shear), and wear (abrasive or adhesive). An analysis of over 1500 studies revealed that the top three gear failure modes were tooth bending fatigue (32%), tooth bending impact (12.5%), and abrasive tooth wear (10%) [6].

5.3 Methodology

In this chapter, the methodology employed for developing the optimized design of a scaled gear for a wind turbine will be elucidated. The optimization objective has been to lighten the component in a manner that it can withstand defined loads effectively, exhibit adequate response to cyclic loads arising from operation, all while considering material selection and manufacturing method.

5.3.1 Problem definition

As previously explained, this chapter will focus on the optimization of a gear for a wind turbine. As a proof of concept, the aim is to manufacture this gear using additive manufacturing, specifically utilizing the Selective Laser Melting (SLM) method. Given that the build volumes of most machines for this type of manufacturing are limited, and considering the gear has an outer diameter of 700mm, it has been decided to scale both the size of the gear and the applied load by a factor of 1:5. This decision was made because the available print bed had a maximum range of 155mm. This approach will address the issue as if the gear had that dimension, facilitating the exploration of solutions within the constraints of the manufacturing equipment.

This gear is inside a gearbox that is often used to increase the rotational speed from a low-speed rotor to a high-speed electric generator [7]. According to [8] a 2MW wind turbine has a gear ratio of 115.2:1 with 3 stages of gear sets, and knowing that the maximum torque on the rotor is 1350 kNm, the maximum load that the gear would have to withstand can be calculated. Considering that the design will be scaled to 1:5, we can determine that the scaled force would be:

$$T_{GEAR} = \frac{T_{ROTOR}}{GR} \tag{9}$$

$$F = \frac{2 \cdot T_{GEAR}}{D} \tag{10}$$

Always considering that this load is intended for a gear made of 16NCr5 with a tensile strength of 450MPa, we can use a proportion to determine the equivalent load for AlSi10Mg with a tensile strength of 190MPa. the equivalent load for AlSi10Mg would be 3337.8N.

Considering that the minimum safety factor for bending force should be 1.56 according to [5], the design driving load is set at 5207N. This load can be applied on both sides of the tooth for design purposes.

Design space

The designated design space is defined by a chosen safety margin of 2mm on the tooth portion to allow for optimization of the interior of the tooth, and 8mm in the central part to securely accommodate the key that will connect it to the shaft and leaving a comparable safety margin between the key and the rest of the component. This design space can be visualized in **Figure 5.5**.

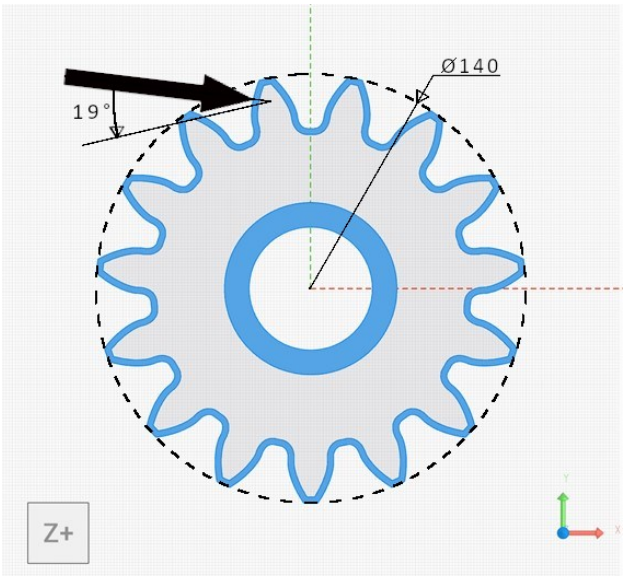

***Figure 5.5**. Design space and boundary conditions of the defined problem.*

Manufacturing process

The use of Selective Laser Melting (SLM) is proposed, an AM technique that utilizes a high-power laser beam to melt metal powder layer by layer to create solid parts [9]. This method has been chosen as a proof of concept for several reasons:

- It allows flexibility in design, providing a higher degree of optimization.
- It enables the use of materials more efficiently, reducing waste.
- It facilitates rapid prototyping.

Wind turbine gears necessitate smooth tooth surfaces to ensure optimal load capacity, particularly concerning pitting and wear resistance. However, achieving comparable smoothness with this manufacturing method can be challenging. Therefore, it would be essential to perform some machining for the finishing of the contact surface. For external gears, the maximum flank surface roughness should be Ra = 0.8µm.

Material

Taking into account that SLM additive manufacturing has been selected for this development and as the mass reduction and recyclability are considered key aspects of this optimization, a Si based aluminum alloy was chosen. This aluminum alloy has relatively low viscosity, which helps the

processability for different manufacturing methods [10]. The mechanical properties of this alloy in SLM are a Young's modulus of 71 GPa, density of 2680 g/cm^3, Poisson's Ratio of 0.33, a yield stress of 190 MPa and a Vickers Hardness of 127HV which can be regarded as moderate [11]. Cu- or Zn-based Al alloys could show better properties, but their viscosity is higher, putting the manufacturing process at risk.

5.3.2 Design and optimization

Topology optimization

The first step involves using a simplified topology optimization approach with a pre-defined load case. This allows designers to create a simplified model of the structure and determine where material can be removed to create a more efficient design. This is made by defining a design space and non-design space as seen in **Figure 5.5**. The whole geometrical envelope of the scaled gear is 140x140x40mm.

To begin the design process and having all the information about the boundary conditions of the component, a topology optimization can be carried out. This optimization will be based on the Solid Isotropic Material with Penalization (SIMP) method, which is the method in which Altair Optistruct solver bases its optimization process [12].

First, the problem needs to be presented. This is done by defining the design space and identifying where material cannot be placed (non-design space). The geometries are meshed, and the properties of each existing volume are defined. Then, the load case to be applied is specified (in this case, the load previously mentioned and only on one tooth) in terms of both its value and the elements to which it will be applied. The inner ring would be clamped in this particular case. The design objectives are to maximize stiffness while the volume of the component is considered a constraint. The result obtained for the load on one tooth is shown in the **Figure 5.6**. According to the boundary conditions, the load can be applied in both rotational directions of the gear and will be applied equally across all teeth. If the geometry obtained from topology optimization is taken and the most "dimensioned" side, or where the most stress seems to pass with the main axis the middle of the tooth, is mirrored, we would have the optimized geometry for one tooth. If this is multiplied by the 15 teeth, we would have the geometry observed in **Figure 5.6**.

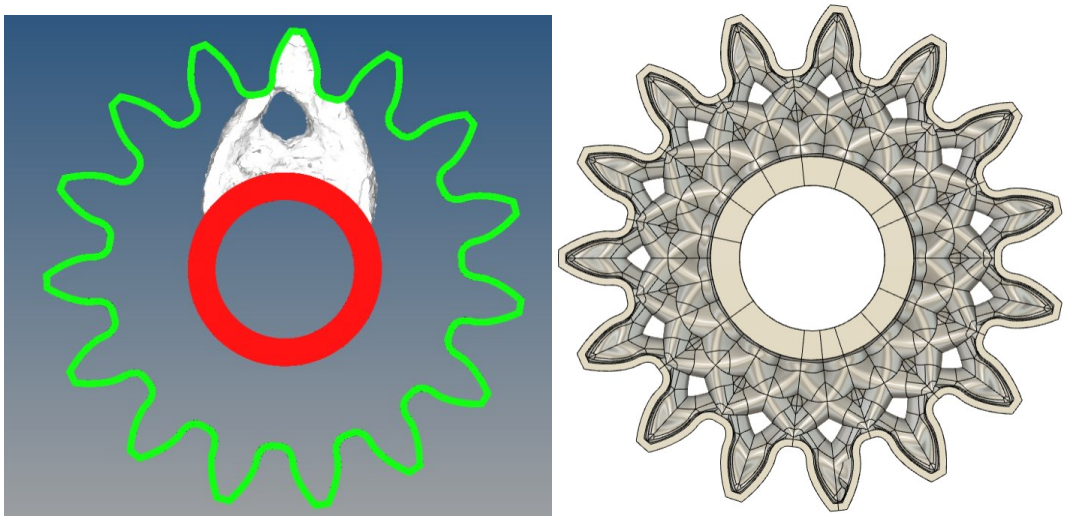

Figure 5.6. *Topology optimization result for one tooth (left). The most restrictive side of the topology optimization result mirrored and multiplied for 15 teeth (right)*

Bioinspired design

As seen in the multiplied topological optimization result, there are resultant reinforcements that aim to channel loads through a geometric pattern with cells that increase proportionally with the radius of the component. To apply a bio-inspired design of direct imitation, it's necessary to look for an example in nature that has sufficient structural integrity and a similar work regime to the case under study. Diatoms, for example, have exoskeletons of various shapes, but one of the most common is the spherical/circular [13], as seen in **Figure 5.7.**

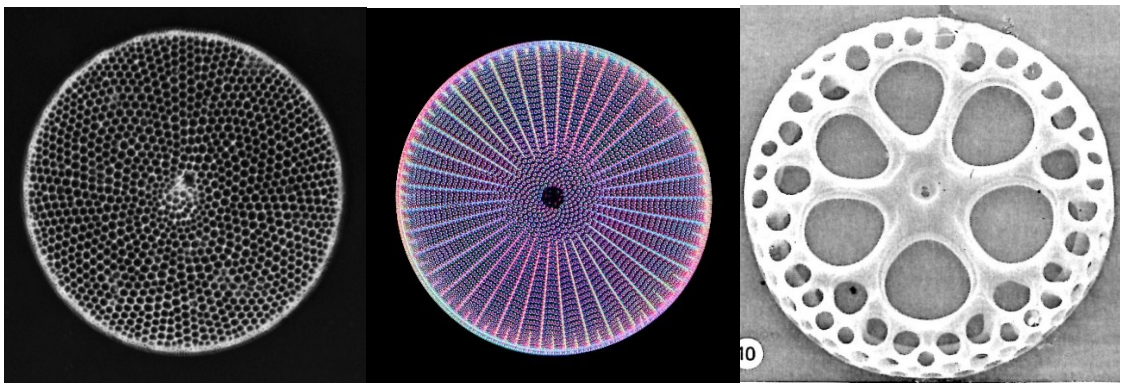

Figure 5.7*. Pictures of different diatom species: Thalassosira* [14]*, Arachnodiscus* [15] *and Rocella* [16] *from left to right respectively.*

One of the most common space division methods in these types of microorganisms is the division by the Voronoi pattern, which, as previously explained, is the geometric pattern that can divide space using the least amount of material, as also seen in honeycombs. The key to this, as observed in the exoskeletons of these diatoms, is that Voronoi patterns can adapt to the shape and the loads applied to them. Therefore, in addition to having a directional pattern as in *Thalassiosira*, a pattern based on topological optimization like in *Rocella* can be applied. The use of radial patterns

that act as stiffeners, as in *Arachnoidiscus*, may prove interesting, as seen in **Figure 5.8**. Consequently, this leads to the phase of parameterization of these models.

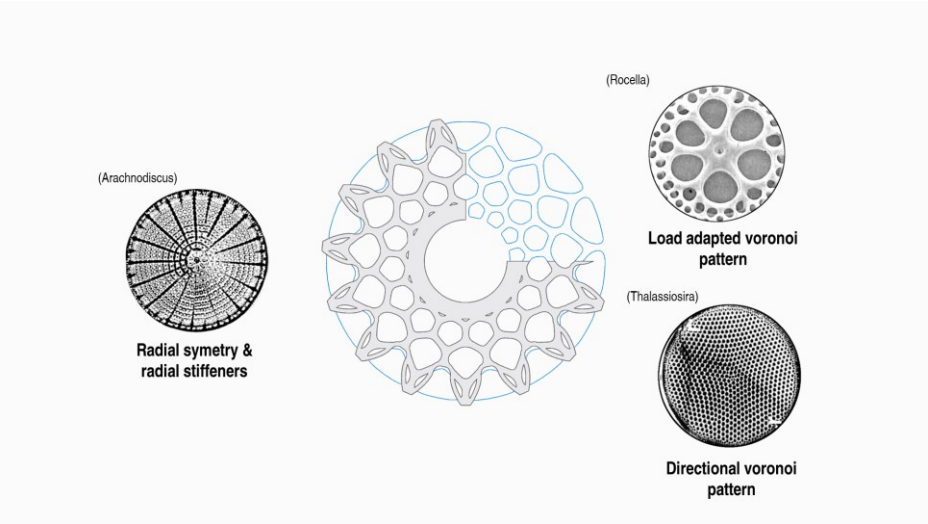

***Figure 5.8**. Design of the radial Voronoi pattern of one solution of the gear wheel in the center. In the outer images the examples of the diatoms for which several features have been applied* [16]

Parametric design

The third and final step involves parameterizing the natural pattern to conduct a parameter study of hundreds of potential solutions. This process entails varying the design parameters to evaluate their impact on the structure's performance. For this purpose, the low-code programming design platform SYNERA will be employed, which facilitates parameterization and automation of geometry generation while integrating various engineering software tools into a single platform. The optimal design solution is then chosen based on achieving the lightest designs while staying within the yield stress margins of the selected alloy.

In this case, two main parameters were selected to determine the final geometry: the radial size of each cell and the average thickness of the material between different cells. Although it would have been possible to choose the number of cells circumferentially or the number of cells radially as parameters, these were already established in the previous phase of topological optimization.

Moreover, it is crucial to acknowledge that the design process incorporated considerations for the SLM manufacturing method. This approach entails designing the structure with specific manufacturing constraints to ensure its manufacturability using SLM. The main manufacturing considerations included maintaining a minimum space between geometries greater than 0.3mm to prevent low hole accuracy and avoiding sharp edges as much as possible. The 0.3mm restriction was specified by the machine's provider Renishaw. Additionally, an "extrudable" design was sought to eliminate the need for support structures (overhang angles), thereby obviating the need for post-processing to remove them. Some of the results of the parameter optimization are shown in **Figure 5.9**.

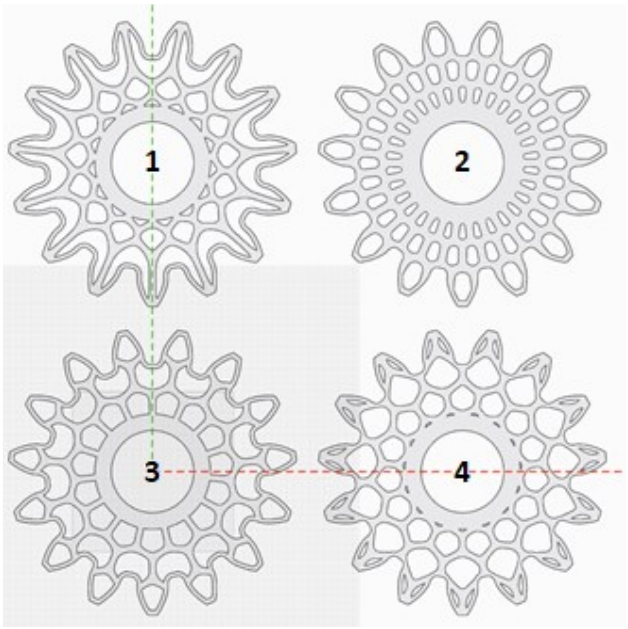

***Figure 5.9**. Several designs extracted of the parameter study performed to the gear wheel (4 out of 150).*

Result

For the selection of the best design, an optimization is carried out using the MIDACO solver included in SYNERA. This solver evaluates designs chosen by the user, utilizes the results of simulations defined by the user, and ranks the outcomes based on their characteristics. The number of geometries to be studied is defined by the user. In this study, a parameter optimization of 150 designs was conducted. In this case, since the final result could not exceed the yield stress of 190MPa, and almost an adequate safety factor was available, the lightest design with a value below 190MPa was chosen. The result is the design number 4 of the **Figure 5.9**.

5.3.3 Validation

Structural analysis

The optimal design was selected based on its mass and the maximum classical Von Mises equivalent stress, ensuring it remained under the yield stress value of the chosen alloy. The next step involves validating that the proposed design meets all specified requirements. To achieve this, a structural analysis simulation was conducted using the Altair Optistruct solver, as illustrated in **Figure 5.10**.

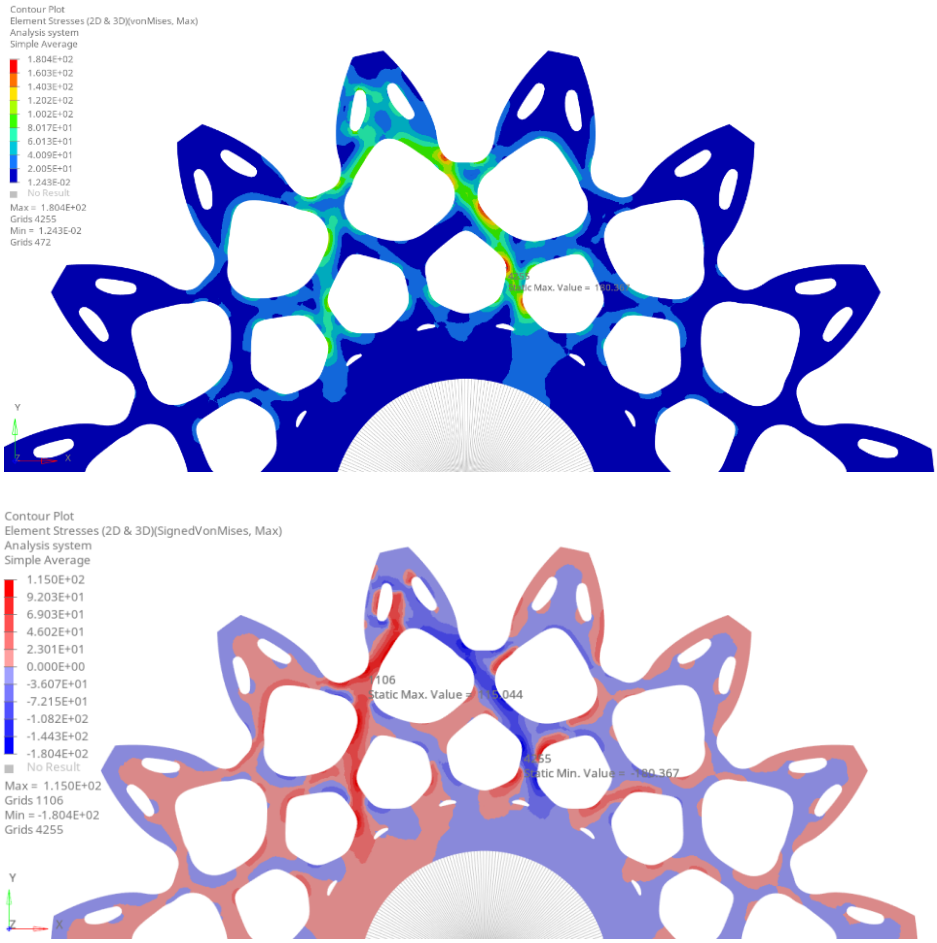

***Figure 5.10**. Von Mises stress result from the structural analysis simulation (Top) Signed Von Mises stress result from the structural analysis simulation (Bottom)*

The analysis results indicate that the final design can withstand the design load in a static case, exhibiting a maximum stress of 180.4 MPa in compression and 115 MPa in tension.

Fatigue analysis

In the previous paragraph, it was mentioned that the static load applied and the maximum stress identified assure that if the load is not cyclic, the gear would support the load. However, fatigue should be analyzed because in a gear the loads are periodic. In this case, the maximum stress according to Von Mises is not in the tooth root (static case, for optimization), but in the nearest hole to the center made for lightening the design (fig. 4). However, if the Signed Von Mises stress graphic is analyzed (dynamic case, for fatigue life), it can be seen that that maximum equivalent non signed stress is in compression. For the fatigue life analysis, the highest tensile stress has to be analyzed (Max tensile stress 115.044MPa). The static load and material selection have been done considering that the gear is made with AlSi10Mg. However, as the fatigue properties of AlSi10Mg may not be sufficient, both AlSi10Mg and Scalmalloy® will be studied. To study fatigue, graphics from [17] and [18] have to be modified since the fatigue criteria are prepared for rotary

samples and not axial tension samples. The modifying parameters for Aluminum alloys are given by [19].

$$\sigma_e = \frac{1}{K_D}\sigma'_N \tag{11}$$

Where σ_e is the modified fatigue limit and σ'_N is the stress for rotary sample and $\sigma_N = 0.9 \cdot \sigma'_N$ where σ_N is the stress value for axial alternating stress sample [20]. K_D is defined by:

$$K_D = \frac{K_F}{\beta\ \varepsilon} \tag{12}$$

Where K_F is known as fatigue notch coefficient, β is surface quality factor and ε is the size factor. Both ε and β are taken from empirical equations [21] ε is supposed as 1 as a first approach while β depends on the UTS of the material and the surface roughness. In this case, the gear would be a ground surface so the coefficient is:

$$\begin{cases} (AlSi10Mg)\ 0.961 \\ (Scalmalloy)\ 0.930 \end{cases} \tag{13}$$

K_F depends on q, notch sensitivity and K_T, stress concentration factor. q for aluminum alloys is 0.483 [22] and K_T is defined by the problem studied. It is supposed that the case studied is bending of a gear tooth as seen in **Figure 5.11** [23]

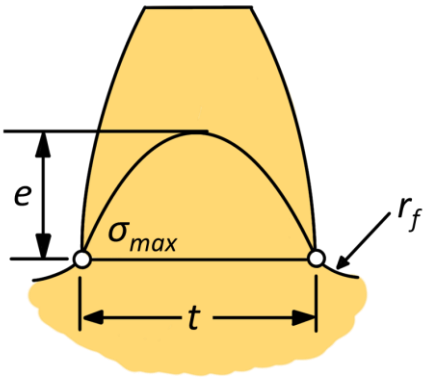

$$K_t = 0{,}18 + \frac{t}{r_f}^{0{,}15} + \frac{t}{e}^{0{,}45}$$

***Figure 5.11**. Bending of a gear tooth of 20º pressure angle for stress concentration factor as defined by* [23]

Once all the correction parameters are defined, the new S-N curves for both materials is given in the next **Figure 5.12**.

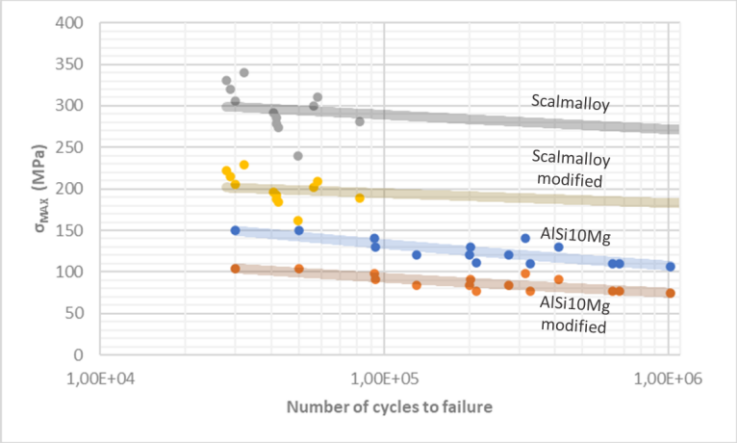

***Figure 5.12**. S-N curve for both materials studied and their modified curves to meet with the fatigue criteria.*

The fatigue is analyzed for 10^6 cycles and with the Goodman criteria.

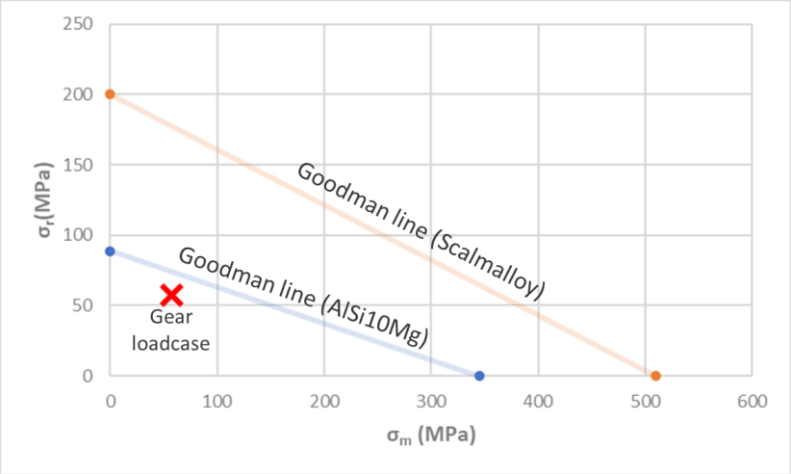

***Figure 5.13**. Goodman diagram for both materials and the gear situation for the studied load case.*

As shown in **Figure 5.13**, the load case study for the gear was found to be suitable for both materials based on the Goodman criteria for fatigue analysis. While AlSi10Mg would have a lower safety factor Scalmalloy® could be more secure. But as the load already had its safety factor included it can be said that AlSi10Mg is suitable enough for this purpose at least at this scale.

5.3.4 Manufacturing

In the manufacturing of the gear using the SLM additive manufacturing method, the component was produced according to the planned design specifications without the need for support structures or additional post-processing. This result demonstrates the precision and efficiency of SLM technology in producing complex geometry parts efficiently.

The SLM process enabled the creation of the gear at the desired scale, highlighting the capability of this additive manufacturing technique to minimize material waste and optimize resource usage. The absence of immediate post-processing requirements underscores the achieved manufacturing quality, though the implications of the resulting surface texture for specific applications must be considered.

From a technical perspective, the surface finish of components manufactured via SLM can exhibit significant levels of roughness due to the inherent characteristics of the manufacturing process. For a gear, whose efficiency and durability depend on the interaction of its contact surfaces, surface roughness can adversely affect its operation, increasing the risk of wear phenomena such as pitting and erosion under repetitive operational conditions.

In scenarios where the component is designed for regular use under constant mechanical loads, the adoption of post-processing techniques is advisable. These techniques might include surface finishing processes to diminish roughness and heat treatments to enhance the material's mechanical properties, including hardness and wear resistance. The integration of such post-processing measures can be vital to guarantee the gear's optimal function and prolong its service life in its intended application. However, in this specific case, as no physical testing was planned, the post-processing workflow and operations were not established.

The final as-manufactured component is depicted in **Figure 5.14**.

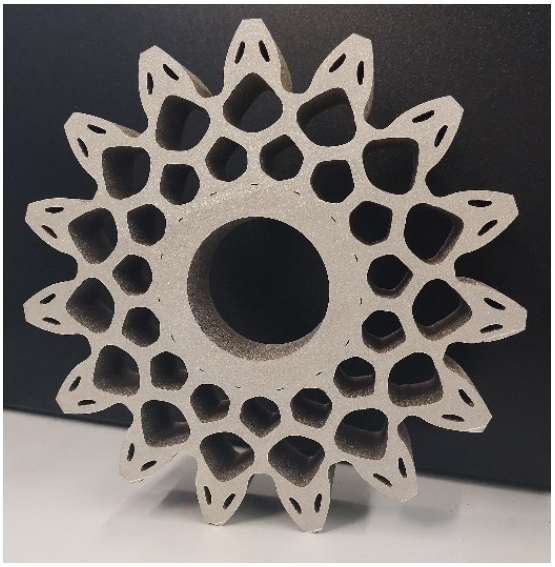

***Figure 5.14**. Final part manufactured by SLM AlSi10Mg additive manufacturing.*

5.4 Conclusions

The conclusion drawn from the study indicates that the methodology used in the research is promising for the future of engineering design. The study demonstrates that SYNERA, as a tool, can be used for designing all types of components and can reuse the design algorithms. The use

of bio-inspired designs is considered a breakthrough in engineering design, thanks to advancements in manufacturing methods and computational power. The study also suggests that bio-inspired designs can benefit from parametric design optimization for a more genuine and comparable result to those found in nature.

The significance of having a tool that can unify all stages of design, operation, and manufacturing is emphasized. The ability to reduce iterations, design, operation and manufacturing defects, and extra expenses that may be involved in manufacturing new components without being previously verified is considered a major advantage. This conclusion can be extrapolated to imply that the methodology used in the study has the potential to revolutionize the field of engineering design by streamlining the process and reducing costs.

As the gear moves into further testing phases and potential full-scale production, consideration must be given to the manufacturing tools necessary for such a product. While current SLM machines may not have the necessary envelope for full-scale production, new generation machines, such as the NXG XII 600E with an extended Z axis of 1500mm, the FormUp 350 Evolution or the TruPrint 1000 Next Gen, may be able to accommodate larger sizes [24]. Alternatively, other additive manufacturing (LMD) or casting methods (such as sand casting with 3D printed sand molds) may also be considered for larger sizes. Ultimately, the choice of manufacturing tool will depend on a variety of factors including cost, time, and desired product specifications.

It would have been beneficial to conduct a physical validation of the component to substantiate the theoretical and simulation results further. However, due to resource limitations, such validation, including static and fatigue testing, was not performed. Static testing could have provided insight into the component's ability to withstand applied loads, while fatigue testing would have assessed its durability under repeated stress conditions. Additionally, a tomography analysis could have offered valuable information regarding potential defects arising from the SLM manufacturing process, ensuring the component's integrity and performance. The absence of these tests leaves a gap in the comprehensive assessment of the component's suitability for real-world applications, highlighting an area for future investigation and validation efforts.

Furthermore, the conclusion suggests that the study's findings could inspire new research avenues for the use of different bio-inspired designs methodologies in engineering. It also indicates that future research could focus on exploring the potential for bio-inspired designs in other areas of engineering, such as civil engineering or aerospace engineering.

5.5 References

[1] "23% of energy consumed in 2022 came from renewables - Eurostat." Accessed: Mar. 13, 2024. [Online]. Available: https://ec.europa.eu/eurostat/web/products-eurostat-news/w/ddn-20231222-2

[2] S. P. Radzevich, "Dudley's Handbook of Practical Gear Design and Manufacture," *Dudley's Handbook of Practical Gear Design and Manufacture*, Jun. 2021, doi: 10.1201/9781003126881/DUDLEY-HANDBOOK-PRACTICAL-GEAR-DESIGN-MANUFACTURE-STEPHEN-RADZEVICH.

[3] P. Lynwander, "Gear Drive Systems : Design and Application," *Gear Drive Systems*, Jan. 2019, doi: 10.1201/9780203755075.

[4] "ISO 6336-3:2019 - Calculation of load capacity of spur and helical gears — Part 3: Calculation of tooth bending strength." Accessed: Mar. 03, 2024. [Online]. Available: https://www.iso.org/standard/63822.html

[5] "IEC 61400-4:2012 - Wind turbines — Part 4: Design requirements for wind turbine gearboxes." Accessed: Mar. 03, 2024. [Online]. Available: https://www.iso.org/standard/44298.html

[6] L. E. Alban, "Systematic Analysis of Gear Failures," 1985.

[7] W. Hu, *Advanced Wind Turbine Technology*. Springer International Publishing, 2018. doi: 10.1007/978-3-319-78166-2.

[8] G. Liu, H. Liu, C. Zhu, T. Mao, and G. Hu, "Design optimization of a wind turbine gear transmission based on fatigue reliability sensitivity," *Frontiers of Mechanical Engineering*, vol. 16, no. 1, pp. 61–79, Mar. 2021, doi: 10.1007/S11465-020-0611-5/METRICS.

[9] J. Michaud, "Additive manufacturing and gears," *Gear Solutions*, 2022.

[10] M. Neuser, O. Grydin, Y. Frolov, and M. Schaper, "Influence of solidification rates and heat treatment on the mechanical performance and joinability of the cast aluminium alloy AlSi10Mg," *Production Engineering*, vol. 16, no. 2–3, pp. 193–202, Apr. 2022, doi: 10.1007/s11740-022-01106-1.

[11] K. Kempen, L. Thijs, J. Van Humbeeck, and J. P. Kruth, "Mechanical Properties of AlSi10Mg Produced by Selective Laser Melting," *Phys Procedia*, vol. 39, pp. 439–446, Jan. 2012, doi: 10.1016/J.PHPRO.2012.10.059.

[12] J. Plocher and A. Panesar, "Review on design and structural optimisation in additive manufacturing: Towards next-generation lightweight structures," *Mater Des*, vol. 183, p. 108164, Dec. 2019, doi: 10.1016/J.MATDES.2019.108164.

[13] C. Hamm, *Evolution of Lightweight Structures*, vol. 6. in Biologically-Inspired Systems, vol. 6. Dordrecht: Springer Netherlands, 2015. doi: 10.1007/978-94-017-9398-8.

[14] "Diatomee / Diatom (fossile) - Thalassiosira sp. - 400x | Flickr." Accessed: Mar. 13, 2024. [Online]. Available: https://www.flickr.com/photos/picksfromoutthere/14281808022/

[15] "Arachnoidiscus deficiens diatom - www.photomacrography.net." Accessed: Mar. 13, 2024. [Online]. Available: https://www.photomacrography.net/forum/viewtopic.php?t=46946

[16] "ANSP Diatom New Taxon File." Accessed: Mar. 13, 2024. [Online]. Available: http://symbiont.ansp.org/dntf/index.php

[17] J. N. Domfang Ngnekou *et al.*, "Fatigue properties of AlSi10Mg produced by Additive Layer Manufacturing," *Int J Fatigue*, vol. 119, pp. 160–172, Feb. 2019, doi: 10.1016/j.ijfatigue.2018.09.029.

[18] M. Raab and M. Bambach, "Fatigue properties of Scalmalloy® processed by laser powder bed fusion in as-built, chemically and conventionally machined surface condition," *J Mater Process Technol*, vol. 311, Jan. 2023, doi: 10.1016/j.jmatprotec.2022.117811.

[19] W. Dou, L. Zhang, H. Chang, H. Zhang, and C. Liu, "Fatigue Characterization on a Cast Aluminum Beam of a High-Speed Train Through Numerical Simulation and Experiments," *Chinese Journal of Mechanical Engineering (English Edition)*, vol. 34, no. 1, Dec. 2021, doi: 10.1186/s10033-021-00628-6.

[20] R. Avilés González, "Análisis de fatiga en máquinas," 2005, Accessed: Mar. 03, 2024. [Online]. Available: https://dialnet.unirioja.es/servlet/libro?codigo=255311&info=resumen&idioma=SPA

[21] R. G. (Richard G. Budynas, J. Keith. Nisbett, and J. Edward. Shigley, *Shigley's mechanical engineering design*. McGraw-Hill, 2011.

[22] A. Ojha, WJ. Lai, C. Engler-Pinto, and X. Su, *Notch Sensitivity of AlSi10Mg Aluminum Alloy Produced by Laser Powder Bed Fusion Process*. in The Minerals, Metals & Materials Series. Cham: Springer International Publishing, 2021. doi: 10.1007/978-3-030-65261-6.

[23] W. D. Pilkey and R. E. Peterson, *Peterson's stress concentration factors*. Wiley, 1997.

[24] All3DP, "Top 3D Printers Launched at Formnext 2022," Nov 18, 2022.

Chapter 6: Supplemental airfoil for low-speed aircraft

6.1 Introduction

Urban mobility holds a paramount significance in today's society, particularly within the context of sprawling metropolises. The proliferation of vehicles on roadways has turned into traffic gridlocks, frequent accidents, noise pollution and escalating environmental degradation. These issues collectively underscore the pressing need for a comprehensive and sustainable solution. Electrification seems to be a transformative force that has the potential to reshape the urban mobility landscape. Electric vehicles (EVs) offer a ray of hope in mitigating the adverse impacts of conventional combustion engines. By producing zero tailpipe emissions and running quieter, EVs have the potential to alleviate urban air quality concerns and decrease noise pollution levels.

As urban mobility evolves, the concept of Unmanned Aerial Vehicles (UAVs) playing a pivotal role in transporting goods and individuals between locations is gaining traction. However, the integration of UAVs into urban airspace demands a meticulous regulatory framework to ensure safety, efficiency, and minimal disruption. The management of urban airspace to accommodate UAV traffic needs innovative approaches that account for both traditional aircraft and emerging aerial technologies. Addressing concerns such as noise pollution becomes critical, as the incessant hum of UAVs could exacerbate the existing urban noise environment. Furthermore, achieving full autonomy for these airborne vehicles is a key milestone. The development of reliable autonomous systems would not only enhance the feasibility of UAV-based transportation but also ensure optimal navigation, collision avoidance, and efficiency in a complex urban environment. Balancing the promise of UAVs with the complexities of urban dynamics requires a delicate equilibrium between technological advancement and regulatory precision.

In the context of technological advancement, there are two driving challenges that have to be developed. Those are the reliability and the autonomy within these urban aircrafts. Reliability stands as a key milestone for safety and efficiency in modern aviation Achieving greater reliability involves several key aspects:

1. **Development of Engines and Propulsion Methods:** Advancements in engines are essential to ensure the reliability of an aircraft. This entails improvements in the efficiency of electric motors and increased operational lifespan.

2. **Aircraft Control and Flight Electronics:** The ability to control the aircraft and its flight electronics are critical aspects of safety. Here, efforts focus on developing advanced control systems that allow precise, real-time responses to various situations, including emergencies. Redundancy of systems and intelligent automation are key approaches to improving reliability.

3. **Structural Components:** The aircraft's structure must be robust and resilient to withstand the stresses and loads experienced during flight. Advances in composite materials, manufacturing techniques, and inspection methods significantly contribute to the construction of more reliable and lightweight structural components.

Flight autonomy is a crucial goal in modern aviation, especially in applications such as drones and UAVs in general. To enhance autonomy, various strategies have to be explored:

1. **Weight Reduction:** Reducing the aircraft's weight is essential for extending autonomy. This involves the ongoing search for lighter and stronger materials, as well as optimized structural design to minimize resource usage without compromising safety.

2. **Battery Improvement:** Batteries are critical components in electric aircraft and drones. Research is focused on developing batteries with higher energy density, longer lifespan, and improved thermal management to achieve longer flight durations.

3. **Complementary Elements:** In addition to improvements in engines and batteries, complementary elements such as complementary wings and secondary propulsion methods are under investigation. These elements can provide additional lift and increase autonomy by reducing the load on the primary propulsion system.

In light of these considerations, the objective of this study is to contribute to the technological advancement of urban electric aircraft, focusing on a specific aspect. These aircraft operate at lower speeds and altitudes compared to commercial aviation, and there is a belief that bioinspired designs can offer valuable insights. In this case, the focus is on enhancing autonomy through the development of a complementary flight system—a wing capable of providing additional lift to the aircraft. The wing's redesign is rooted in bioinspired designs, and the process begins with a thorough examination of natural flight types. This examination identifies aerodynamic profiles available in existing literature, which are subsequently subjected to a 2D analysis under specific boundary conditions. Based on the results, two profiles are selected for further 3D analysis. In this final phase of the study, the profiles derived from the initial analysis are transformed into three-dimensional wing shapes, incorporating various bioinspired configurations believed to enhance aerodynamic performance.

6.2 Types of flight

To fully grasp the content presented in this chapter, it's essential to provide context regarding two key aspects: the types of aircraft based on their principles of flight and the various flight patterns found in nature. Understanding these elements will help pinpoint the specific aircraft types discussed in this study and shed light on why certain flight profiles were selected. This context is vital for interpreting the study's findings and appreciating the relationship between aviation design and the intricacies of the natural world.

6.2.1 Aircraft types

Aircraft can be classified based on the physical principle responsible for their lift:

Aerostats: These are aircraft lighter than air, distinguished by containing a gas of lower density than the surrounding air, such as hydrogen or helium. They were the earliest developed aircraft and ascend according to the principle of Archimedes.

- **Hot Air Balloons**: Hot air balloons consist of an envelope containing hot air and a basket at the bottom for carrying passengers. They lack any form of propulsion and rely on air currents for movement. However, they often have devices for controlling their ascent.
- **Dirigibles**: Dirigibles are powered aerostats equipped with maneuvering capabilities, allowing for controlled flight like conventional aircraft. Similar to hot air balloons, they feature an envelope filled with a gas lighter than air to achieve lift.



Figure 6.1. *Hot air balloons* [1] *(**left**) and a Zeppelin airship* [2] *(**right**).*

Aerodynes: Aerodynes are aircraft that are heavier than air and generate lift through aerodynamic forces produced by lifting surfaces, typically wings. These aircraft have been key in the development of modern aerial vehicles.

Further, aerodynes can be classified based on the type of wings they employ for lift production. While the majority fall under the category of fixed-wing aircraft, there are also rotary-wing aircraft.

- **Fixed-Wing Aircraft**: Fixed-wing aircraft have wings that are permanently attached to the rest of the aircraft structure and do not possess independent motion. This category includes airplanes, gliders/sailplanes, hang gliders, paragliders, powered paragliders, and ultralights.



***Figure 6.2**. Aircraft types: Commercial airplane* [3] *(**top**), glider* [4] *(**middle left**), hang glider* [5] *(**middle right**), paraglider* [6] *(**bottom left**), paramotor* [7] *(**bottom right**).*

- **Rotary-Wing Aircraft**: Rotary-wing aircraft have wings, in this case referred to as rotor blades that rotate around an axis to generate lift. This category encompasses autogyros, gyrodyne, helicopters, compound aircraft, and convertibles.



***Figure 6.3**. Rotorcraft types: Helicopter* [8] *(**top left**), autogyro* [9] *(**top right**), compound helicopter* [10] *(**bottom left**), tiltrotor* [11] *(**bottom right**).*

6.2.2 Natural flight types

In the same way that there are aircraft that require propulsion for flight, there are living organisms that possess the ability to utilize evolved attributes for powered flight but also unpowered flight. Below, we have presented the types of flight found in nature, explaining the basis of each:

- **Gliding** is a form of unpowered flight where animals use their body structures to move through the air without flapping their wings. Gliders can cover horizontal distances while losing altitude gradually, using air currents to stay aloft. There exist many examples of gliding animals, however, gliding has evolved among rainforest animals, especially in the rainforests in Asia (most especially Borneo) where the trees are tall and widely spaced. Flying squirrels, flying fish, flying lizards, sugar gliders [12].



***Figure 6.4**. Gliding animals: Flying squirrel (**left**), flying fish (**right**).*

- **Ballooning** is a form of unpowered flight where animals use their body structures to increase drag forces, slowing their descent as they fall or even becoming airborne thanks to air currents. Some small mammals, insects, and spiders (e.g., ballooning spiders) [13].
- **Soaring** is a form of energy-efficient flight where animals, primarily birds, use rising air currents to maintain altitude without flapping their wings. It can also be considered as a type of gliding flight. Soaring birds can travel long distances with minimal energy expenditure by exploiting thermals, orographic updrafts, and other air currents. Albatrosses, vultures, condors, eagles, frigatebirds [14].



***Figure 6.5**. Albatross in flight* [15].

- **Powered flight** is a form of active flight where animals generate lift, drag, and thrust by flapping their wings in various forms. This type of flight has evolved independently in

insects, birds, bats, and pterosaurs. Insects (e.g., bees, dragonflies), birds (e.g., crows, hummingbirds), bats [16].

6.3 Theoretical Framework: Fluid Mechanics, Aerodynamics, and CFD Fundamentals

6.3.1 Fluid mechanics fundamentals

- **Continuity Equation:** The continuity equation expresses the principle of mass conservation, which stipulates that, within a fixed control volume in space bounded by a surface, the net flow of mass through the control volume's surface must be equal to the time rate of change of mass contained within the domain. In other words, the incoming mass flow must equal the outgoing flow. As we can observe, the continuity equation demonstrates that if the inlet area increases, the velocity of the flow decreases, and vice versa. This fundamental concept underscores the relationship between mass, volume, and flow dynamics, providing essential insights into the behavior of fluid systems [17].

$$\left.\frac{dM}{dt}\right|_{System} = 0 \tag{1}$$

$$M_{System} = \int_{M_{System}} dm = \int_{V_{System}} \rho \cdot dV \tag{2}$$

$$\frac{dM}{dt} = \frac{\partial}{\partial t}\int_{CV} \rho \cdot dV + \int_{CS} \rho v \cdot dV \tag{3}$$

$$\rho_{in} \cdot v_{in} \cdot A_{in} = \rho_{out} \cdot v_{out} \cdot A_{out} \tag{4}$$

- **Bernoulli's equation:** Bernoulli's theorem demonstrates that in an ideal fluid (one without friction, incompressibility, and constant flow), the total energy remains constant along a streamline. Consequently, an increase in flow velocity corresponds to a decrease in pressure.

$$\frac{P}{\rho} + \frac{V^2}{2} + gz = constant \tag{5}$$

In this equation, P represents static pressure. The Greek letter rho (ρ) stands for fluid density, and V denotes flow velocity. The second term, $\frac{V^2}{2}$, represents dynamic pressure.

When air particles increase their velocity, it comes at the cost of a decrease in pressure, and vice versa. In other words, for any parcel of air, high velocity implies low pressure, while low velocity corresponds to high pressure. This relationship holds true at speeds below the speed of sound, as beyond this threshold, other phenomena come into play that significantly affect this relationship. Bernoulli's equation provides valuable insights into the interplay between velocity, pressure, and density in fluid dynamics [17].

- **Venturi effect*:*** The Venturi effect, named after the 17th-century Italian physicist Giovanni Venturi, was discovered through an experiment involving a tube that now bears his name.

This Venturi effect can be explained by the two previously mentioned principles: Bernoulli's theorem and the continuity equation. When a fluid flows through the interior of a conduit, its velocity increases, and the pressure decreases when it passes through a narrower section.

This phenomenon, rooted in the laws of fluid dynamics, showcases the interconnectedness of fluid velocity and pressure, as elucidated by Bernoulli's theorem and the continuity equation. The Venturi effect finds applications in various fields, including fluid mechanics, engineering, and even in the design of devices like carburetors, where it plays a pivotal role in optimizing fluid flow and pressure regulation [17].

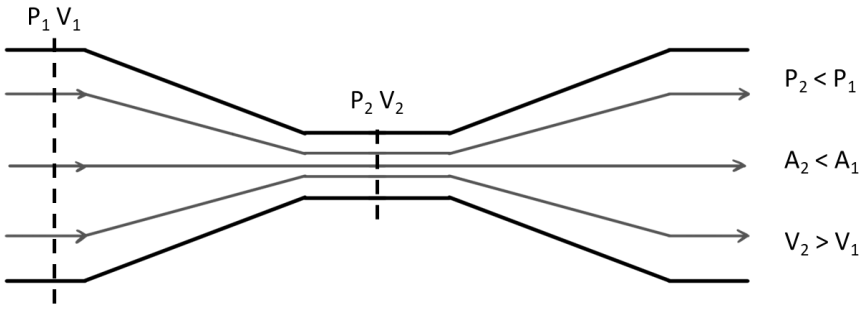

***Figure 6.6**. Descriptive diagram of the Venturi effect.*

6.3.2 Fundamentals of Aerodynamics

Lift and Drag Forces

After establishing the fundamentals of fluid mechanics, we can now delve into the aerodynamic principles that will serve as the foundation for comprehending the subject matter explored in this chapter.

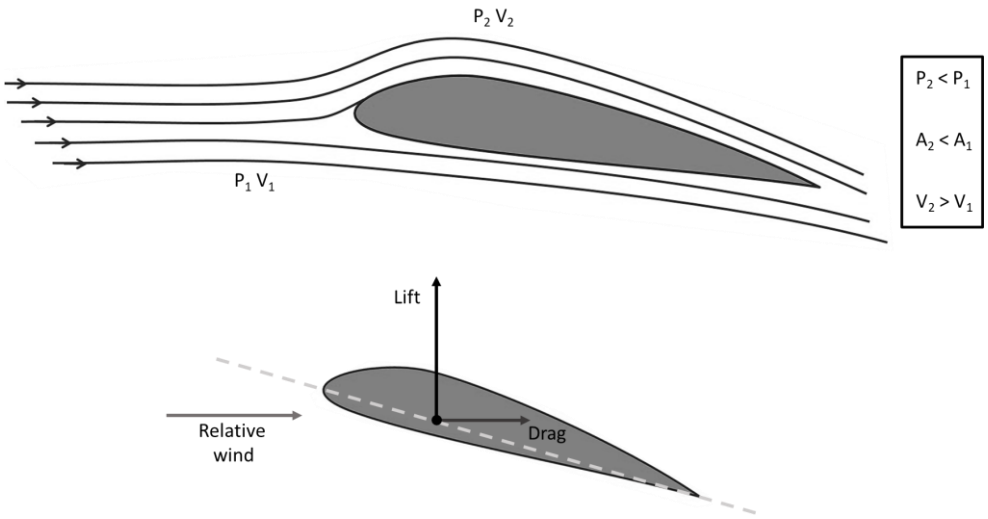

***Figure 6.7**. Aerodynamic study of airfoil shapes: airflow streamlines around an airfoil (**top**) and drag force acting on an airfoil (**bottom**).*

Consider the aerodynamic profile depicted in **Figure 6.7** and the air flowing around it as a closed volume. It becomes evident that the air passing over the upper surface (extrados) of the profile must traverse a longer path than the air traveling beneath the lower surface (intrados). Taking the Venturi effect into account, the fluid's velocity must be higher above the profile, creating a region of decreased pressure. This drop in pressure generates a force perpendicular to the flow direction, known as Lift [17]. The direction of this force always goes from high pressure to low pressure due to it being a suction force. Thus, the lift force is defined as follows:

$$F_L = \frac{1}{2} \cdot C_L \cdot \rho \cdot A \cdot v^2 \quad (6)$$

Here, F_L represents the Lift force (N), C_L is the Lift coefficient, ρ the fluid density(kg/m^3), A is the reference area (m^2) y v is the velocity (m/s).

On the other hand, we have the drag force, which is commonly referred to as "drag." Minimizing this force stands as one of the primary objectives for any fluid dynamics designer. To gain a comprehensive understanding of aerodynamic resistance, it is essential to not only delve into the physics governing its existence but also to classify its various manifestations. Aerodynamic resistance can be primarily categorized into two groups based on their immediate causes: viscous origin and potential origin. Within each group, there are two subdivisions, resulting in four distinct contributions to resistance:

- **Viscous Origin:** The two terms to consider are frictional resistance (or skin friction) and pressure resistance (form resistance). In bodies with attached flow that do not generate lift, moving through still air at subsonic speeds, frictional resistance often dominates. However, this is not the focus of our study in this document. In a real fluid, viscosity alters the pressure distribution on the body, giving rise to pressure resistance, which becomes the predominant type of resistance in configurations with detached boundary layers.
- **Potential Origin:** Strictly speaking, all aerodynamic resistance stems from viscosity because, without it, there would be no possibility of generating circulation around profiles. The two terms associated with this origin are induced resistance and wave resistance. Induced resistance results from velocity modifications near the vehicle due to the velocities induced by the trailing vortex wake extending downstream from the lifting profile.

It is worth noting that, based on the explanations provided, aerodynamic resistance is essentially the result of three distinct phenomena of very different nature: effects associated with the boundary layer (wall friction and separation), vortex wakes, and shockwaves. It is logical that the procedures employed to reduce a particular type of resistance may have little influence on other forms of resistance or may even prove counterproductive.

$$F_D = \frac{1}{2} \cdot C_D \cdot \rho \cdot A \cdot v^2 \quad (7)$$

Here, F_D represents the Drag force (N), C_D is the drag coefficient, ρ is the fluid density (kg/m3), A is the reference area (m2) y v is the velocity (m/s).

Finally, in practical terms for comparing airfoil profiles, dimensionless coefficients are utilized. This approach is preferred because the force depends on external factors such as density and the profile's cross-section. In contrast, dimensionless coefficients are independent of these factors and are determined solely by the shape and angle of attack of the profile itself. For each component of aerodynamic force, namely lift and drag, specific coefficients are employed, denoted as C_L and C_D respectively, with C_L representing the vertical coefficient and C_D the horizontal coefficient [17].

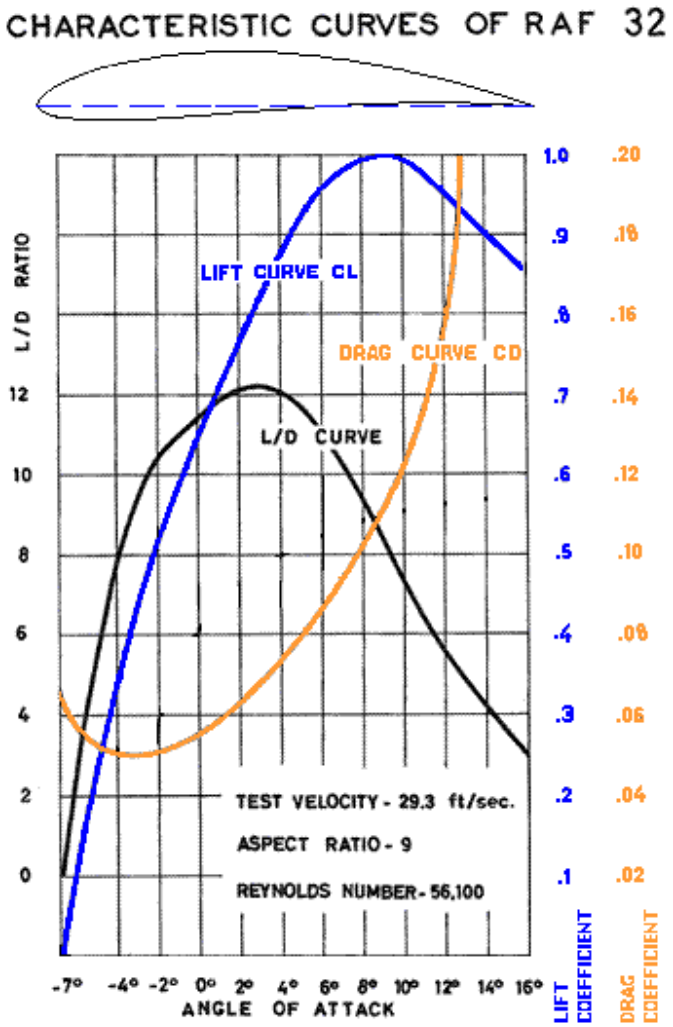

***Figure 6.8**. Characteristic curves of RAF 32 airfoil: lift curve, drag curve and lift-to-drag ratio (L/D) as a function of angle of attack* [18].

If the **Figure 6.8** is analyzed, the C_L graph exhibits an initial region where the slope is positive, reaching a point where it levels off at 0. Beyond this point, C_L decreases. This zone corresponds to boundary layer separation, where the air detaches from the profile as it is no longer able to follow its contours. This phenomenon marks the onset of aerodynamic stall, where the profile experiences a loss of lift.

In contrast, when we examine the graph of the coefficient of drag (C_D), we observe that it increases as the angle of attack of the profile increases. This graph consistently shows a rising

trend without reaching any critical point, unlike the negative slope observed in the coefficient of lift (C_L).

This divergence in behavior between C_L and C_D graphs highlights a crucial aspect of aerodynamics, where changes in the angle of attack influence lift and drag differently. While C_L eventually plateaus and then decreases as stall occurs, C_D continues to rise, indicating an increase in drag as the angle of attack grows. Understanding these relationships is essential for optimizing the performance and efficiency of aerodynamic profiles.

Aerodynamic efficiency

In the aircraft analyzed in this chapter, the goal is to maximize aerodynamic lift while minimizing drag as much as possible. The ratio between these forces is referred to as aerodynamic efficiency. This concept is defined by:

$$f = C_L / C_D \tag{8}$$

Where:

- f represents aerodynamic efficiency.
- C_L stands for the coefficient of lift.
- C_D represents the coefficient of drag.

Aerodynamic efficiency serves as a fundamental metric in aircraft design and optimization, indicating how effectively an aircraft generates lift relative to the amount of drag it produces. Achieving higher values of aerodynamic efficiency is a key objective in the development of efficient and high-performance aircraft [17].

Boundary Layer

When studying fluid dynamics, there are several complex and challenging effects to consider. One of the most significant challenges in aerodynamics is turbulence, primarily because it is difficult to predict. Turbulence arises from the gradients in pressure and velocity around a surface.

In a turbulent flow, as we will explain later, there are significant fluctuations in pressure and velocity, particles move randomly and chaotically, forming vortices. In contrast, in laminar flows, the fluid moves continuously, in an organized manner, and in parallel layers [17].

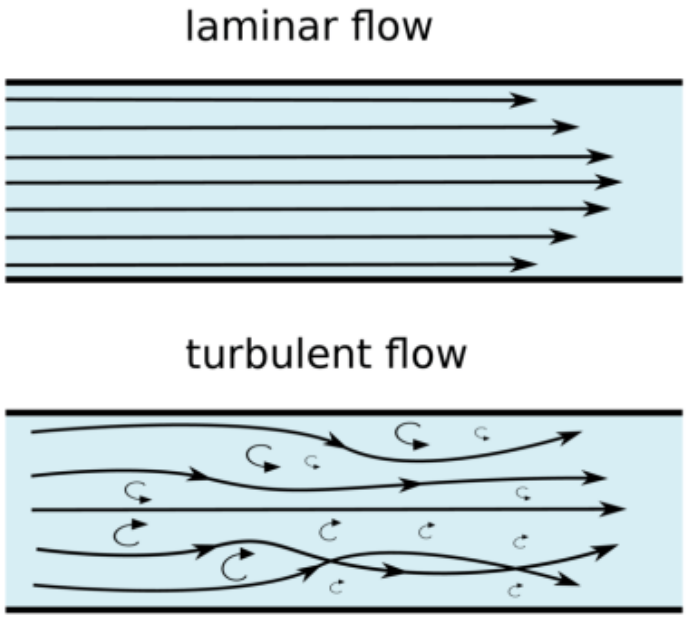

***Figure 6.9**. Comparison of laminar flow (top) and turbulent flow (bottom) illustrating the differences in fluid motion and behavior* [19].

A useful tool to determine whether a flow is laminar or turbulent is the Reynolds number, which depends on the density, velocity, characteristic length of the object in question, and the fluid's viscosity. This number relates the inertial forces to the viscous forces within a fluid and can be calculated using the following equation:

$$\mathrm{Re} = \frac{\rho V L}{\mu} \tag{9}$$

Where:

- ρ: Fluid density (kg/m3)
- V: Velocity (m/s)
- L: Characteristic length (for an airfoil profile, it's the chord length) (m)
- μ: Dynamic viscosity of the fluid (kg/m s)

The molecular layer of air in close contact with the surface of the airfoil remains adhered to it. Beyond this layer, there is a sliding motion between different layers, with increasing velocity as they get farther from the surface, eventually reaching the velocity of the free stream. The region between the airfoil's surface (where velocity is zero) and the point where velocity matches that of the free stream is known as the boundary layer. Its properties can be defined as follows:

- Pressure remains constant along lines perpendicular to the airfoil's surface.
- As the boundary layer advances along the surface of the obstacle, it widens for two reasons. Firstly, due to shear forces, each fluid layer within the boundary layer decelerates due to viscosity when compared to the immediate outer layer and accelerates when compared to the inner layer. The loss of momentum in the fluid is used

to balance the tangential action the wall exerts on it. The second reason for widening lies in adverse pressure gradients. When the boundary layer advances in the presence of an adverse pressure gradient, the loss of momentum is greater because, in addition to countering wall friction, it must also counteract the adverse pressure gradient. Conversely, when the pressure gradient is favorable, the boundary layer accelerates and gains momentum, which aids in balancing wall friction.

As a result of this mentioned deceleration, particles close to the wall eventually reverse their motion instead of advancing, leading to boundary layer separation in the region where this reversal occurs, as seen in **Figure 6.10**. In these conditions, viscosity influences the pressure field over the obstacle, and the first property mentioned ceases to be valid.

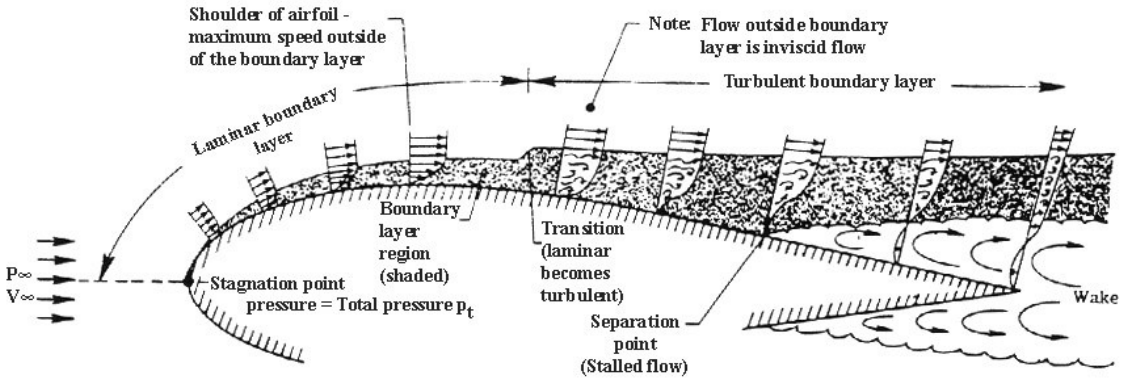

***Figure 6.10**. Diagram of boundary layer behavior over an airfoil, showing regions of laminar and turbulent flow, boundary layer transition, separation point, and wake formation* [20].

The laminar boundary layer is unstable and remains laminar only in the front portion of the airfoil. As disturbances introduced by the profile appear and amplify, the boundary layer transitions to turbulence through a nonlinear and complex process. In the case of a real airfoil with a partially turbulent boundary layer, the problem can only be numerically addressed, and even then, the treatment is highly complex. This complexity arises from the challenge of generating integration grids that adapt to all the peculiarities of the problem and from the intrinsic difficulty of handling turbulence models, which still do not faithfully reproduce the full complexity of turbulent motion in their formulations.

Adding to these challenges is the phenomenon of the laminar-to-turbulent boundary layer transition. Accurately predicting the point where this transition occurs is crucial for estimating frictional resistance more precisely. The key parameter determining the transition is the critical Reynolds number, which is the value at which this transition occurs.

In general terms, the mechanism leading to airfoil stall can be summarized as follows: when the angle of attack is large, a pronounced peak of negative pressure coefficient appears on the upper surface, near the leading edge of the airfoil. Underneath this suction peak, pressure increases, creating an adverse pressure gradient. This gradient can force the separation of the boundary layer, ultimately resulting in the airfoil entering a stall condition [17].

Turbulence Models

Let's begin by considering the flow of fluid over a flat plate. A uniform velocity profile strikes the leading edge of the flat plate, initiating the development of a laminar boundary layer. After a certain distance, small chaotic oscillations begin to form within the boundary layer, and the flow transitions into turbulence, ultimately becoming fully turbulent.

In the laminar regime, the fluid flow can be accurately predicted by solving the Navier-Stokes equations, which provide velocity and pressure fields. Let's assume initially that the velocity field remains steady with time. However, as the flow starts transitioning into turbulence, flow oscillations appear, even though the inflow rate remains constant over time. It is no longer possible to assume that the flow is time-invariant. In this case, solving the time-dependent Navier-Stokes equations becomes necessary, and the mesh used must be fine enough to resolve the size of the smallest eddies in the flow.

The scales of these eddies can vary from the largest, sometimes referred to as the integral length scale, indicating that the motion equations must be integrated at that scale to capture the behavior of the largest eddies, to the smallest, known as the Kolmogorov length scale. Kolmogorov's classical turbulence theory is based on the theory of self-similarity and suggests that the kinetic energy, represented by "k," of the larger eddies flows towards the smaller eddies through a cascade mechanism. Furthermore, this energy transfer is constant across different longitudinal scales of eddies and is determined by the dissipation rate, ε, of kinetic energy "k."

There are essentially three types of numerical simulations for turbulent flows. The simplest and most commonly used approach today is solving the Navier-Stokes equations with Reynolds-averaged Navier-Stokes (RANS) modeling for closing the equations. The next level of sophistication involves Large Eddy Simulation (LES), which directly simulates the movements of large-scale eddies while modeling the smaller-scale eddies with turbulence models. Lastly, there is Direct Numerical Simulation (DNS), which directly simulates all significant scales of turbulence. However, DNS and LES are currently limited due to the computational capacity required for these methods [21].

***Table 6-1**. Turbulence models with their particularities, pros and cons* [21].

Turbulence Model	Particularities	Pros	Cons
Laminar Model	No turbulence	Accurate for laminar flow	Inaccurate for turbulent flow
Reynolds-Averaged Navier-Stokes (RANS)	Governing equation and numerical method used to calculate turbulent viscosity	Widely used	Limited accuracy for complex flows
Spalart-Allmaras (RANS)	One-equation model	Accurate for boundary layer flows	Limited accuracy for separated flows
k-epsilon (RANS)	Two-equation model	Accurate for boundary layer flows	Limited accuracy for separated flows
k-omega (RANS)	Two-equation model	Accurate for separated flows	Limited accuracy for boundary layer flows
SST (RANS)	Two-equation model	Accurate for both boundary layer and separated flows	Computationally expensive

Wall law

Understanding the concept of the wall and the dimensionless variable y^+ is crucial to consider the effects near the wall, as it forms the basis for choosing a turbulence model. The dimensionless variable y^+ represents the distance from the wall in terms of viscous lengths.

To better understand this concept, you can think of it like a fishing net for catching fish. If you're trying to catch large fish, the mesh size of the net doesn't need to be very small. However, if the fish are relatively small, you need a finer mesh, and such a net can still catch larger fish.

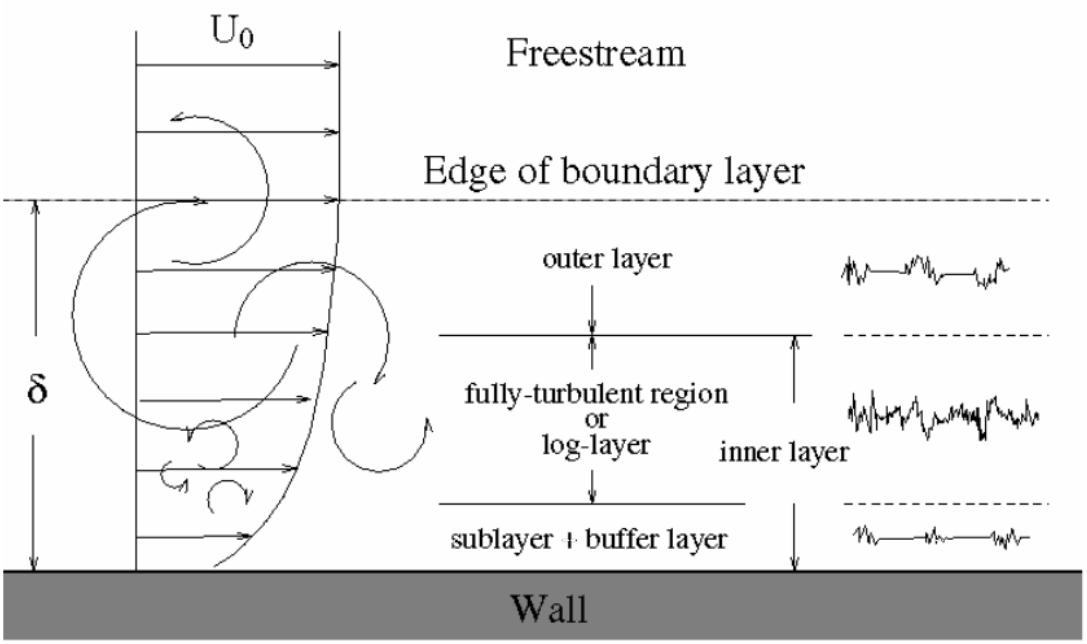

***Figure 6.11**. Diagram of the boundary layer structure near a wall, illustrating the freestream flow, edge of the boundary layer, outer layer, fully-turbulent region or log-layer, inner layer, sublayer, and buffer layer* [22].

Turbulent boundary layers are typically described in terms of various dimensionless parameters. The boundary layer thickness is the distance from the wall where viscous effects become negligible and marks the boundary of the boundary layer as can be seen in

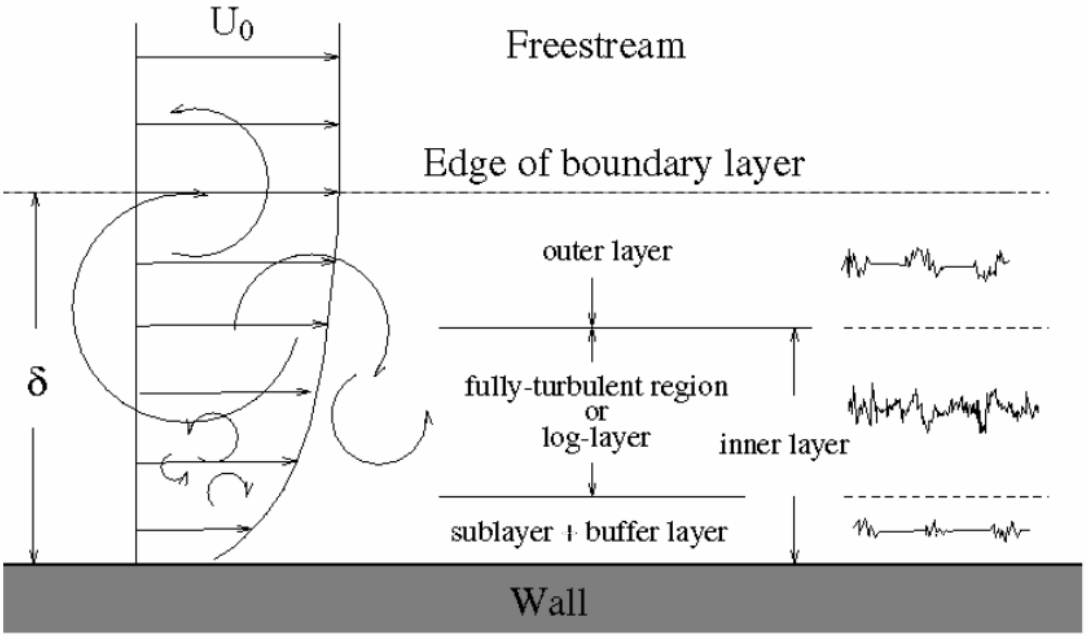

Figure 6.11. Near the wall, you can observe three different layers:

- The inner layer, where viscous shear predominates.
- The outer layer, where great scale turbulent predominates.
- The overlap layer, where velocity profiles exhibit a logarithmic variation.

Below are the sublayers found within the inner layer:

- **Viscous Sublayer**, also known as the linear sublayer: Close to the solid surface, the fluid is stationary, and turbulent motion must also cease very near the wall. In this sublayer where $y^+ < 5$ units, the variation of u^+ with y^+ is approximately 1: 1.
- **Buffer layer,** this is the damping layer that exists for values between $5 < y^+ < 30$. Notably, at $y^+ = 11$ the transition from linear to logarithmic behavior occurs. This means that the linear approximation is more accurate before y^+ reaches 11, and the logarithmic approximation should be used after that point.
- **Log-Law Layer**, in this region, both viscous and turbulent effects become significant. Within this inner region, the shear stress remains constant and equal to the wall shear stress but gradually varies with distance from the wall. Due to the logarithmic relationship between y^+ and u^+, this region is known as the logarithmic layer and is present where $30 < y^+ < 500$.

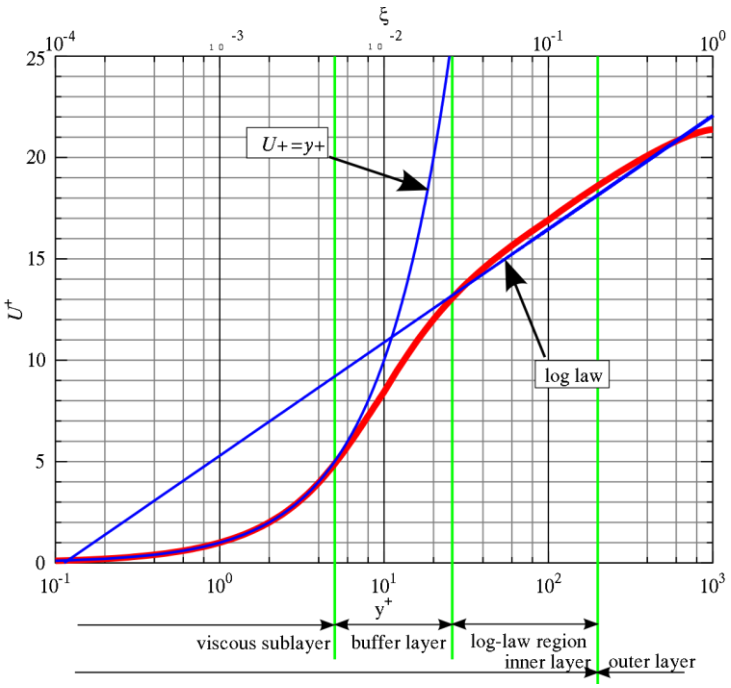

***Figure 6.12**. Velocity profile in a turbulent boundary layer near a wall, showing the relationship between velocity U+ and wall distance y+. The plot includes the linear region U+=y+ and the logarithmic region described by the log law* [23].

The accurate representation of flow in the region near the wall is crucial for successful predictions of bounded turbulent flows. Therefore, when dealing with complex geometries, refinement of the boundary layer may be necessary to ensure that the desired y+ value is achieved. In such

cases, mesh refinement or mesh adaptation techniques should be employed to attain the required value throughout the model as depicted in **Figure 6.12**.

It is essential to verify y+ values as part of your post-processing so that you can ensure that they fall within the valid range for flow physics and turbulence model selection. Therefore, it is advisable to resolve the boundary layer all the way to the wall with a finer mesh.

Airfoil geometry

The morphology of airfoils is a fundamental element in the design of aircraft and vehicles that interact with the air. These profiles, also known as wings or lifting surfaces, determine how the airflow behaves around them and ultimately influence the generation of lift and aerodynamic drag. Understanding the features and characteristics that define the geometry of these profiles is essential for optimizing the performance and efficiency of aircrafts. In this section, the parameters that define these components and how they affect to the aerodynamic efficiency will be discussed.

Wing profiles can take on a multitude of geometric shapes, and to precisely define the curves that make up these shapes, various parameters must be established which can be seen in **Figure 6.13**:

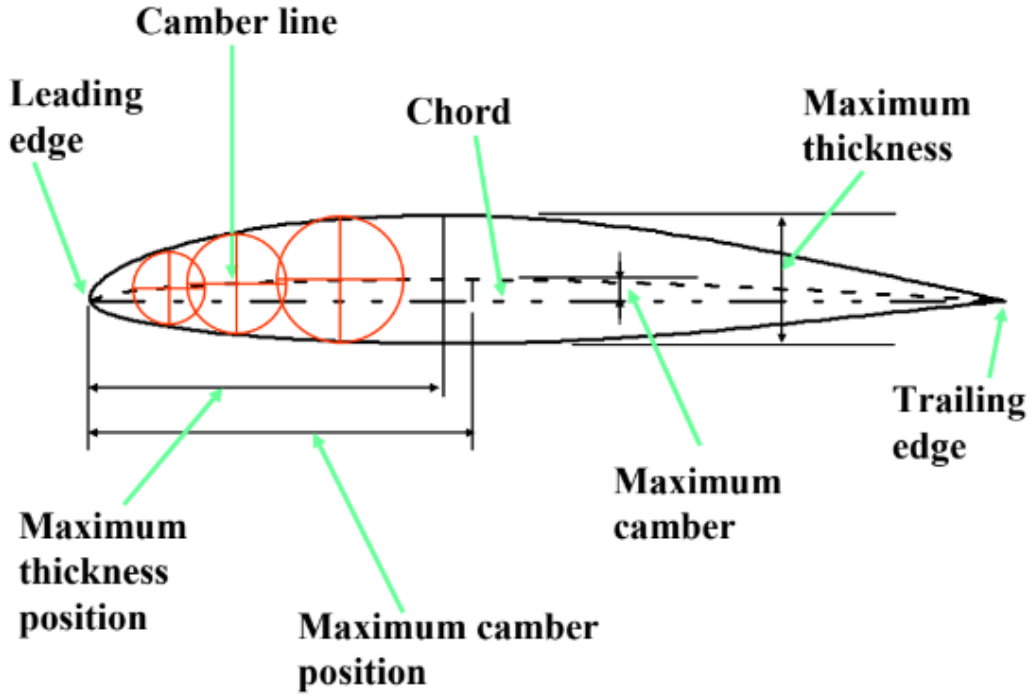

***Figure 6.13**. Diagram of an airfoil showing key geometric parameters* [24].

- Leading edge: The front edge of the airfoil. It is the first part to contact the air.
- Trailing edge: The edge where the airfoil ends or where the fluid flow of the upper and lower surfaces converge.

- Chord: The chord is the distance measured from the leading edge of the airfoil profile to its trailing edge.
- Camber line: The equidistant line to the upper and lower surface of the airfoil. Maximum camber is the maximum distance between the chord and the camber line. It is usually defined by the maximum camber position.
- Thickness: The thickness of the airfoil. The maximum thickness appears where the maximum thickness position is defined and it is the maximum distance between the upper and lower surfaces of the airfoil.
- Angle of attack: The angle between the chord and the relative direction of the fluid flow.

Understanding the effects of certain parameters on aerodynamic coefficient curves becomes valuable for anticipating the behavior of one profile compared to another. Below are analyzed some of these effects:

- **Effect of thickness** in C_L & C_D coefficients for different attack angles. The thinner the airfoil profile, the lower the angles at which boundary layer separation occurs. Conversely, when observing the effect at lower angles, it can be deduced that it has a relatively minor impact, and the lift remains nearly the same. However, when examining the C_D graph, it becomes apparent that at lower angles, thinner profiles exhibit less drag, but as the angle increases, thinner profiles show an exponential rise in the coefficient of drag at lower angles.

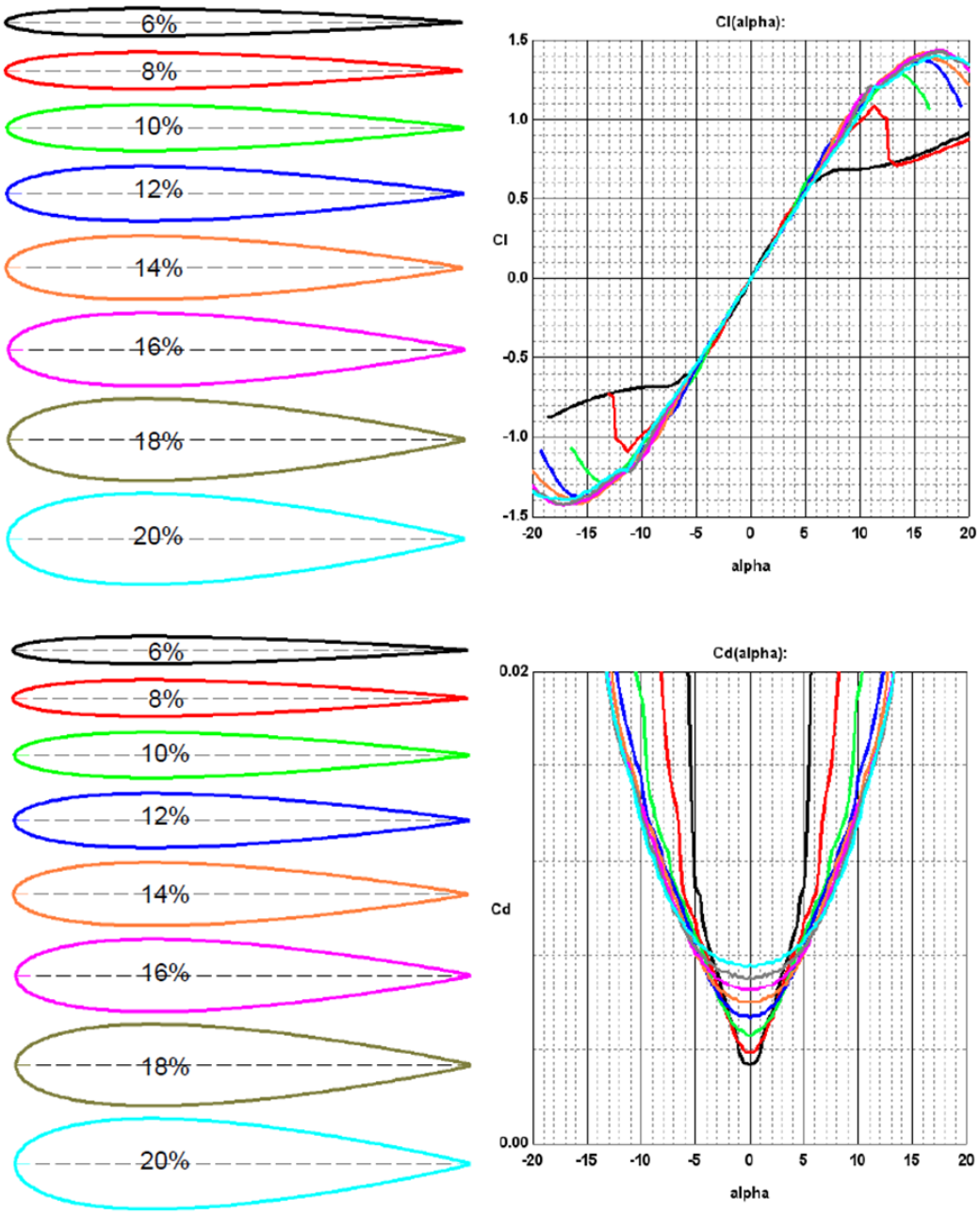

***Figure 6.14**. Comparison of airfoil shapes with varying thicknesses (6% to 20%) and their corresponding lift coefficient (**top**) and drag coefficient (**bottom**) as functions of angle of attack.*

- **Effect of camber** in C_L & C_D coefficients for different attack angles. If you look at the lift coefficient graph, you can see that as the angle of attack increases, especially for pronounced camber profiles, the lift increases. When examining the C_L-C_D graph, it becomes evident that the aerodynamic efficiency is higher for profiles with more pronounced camber.

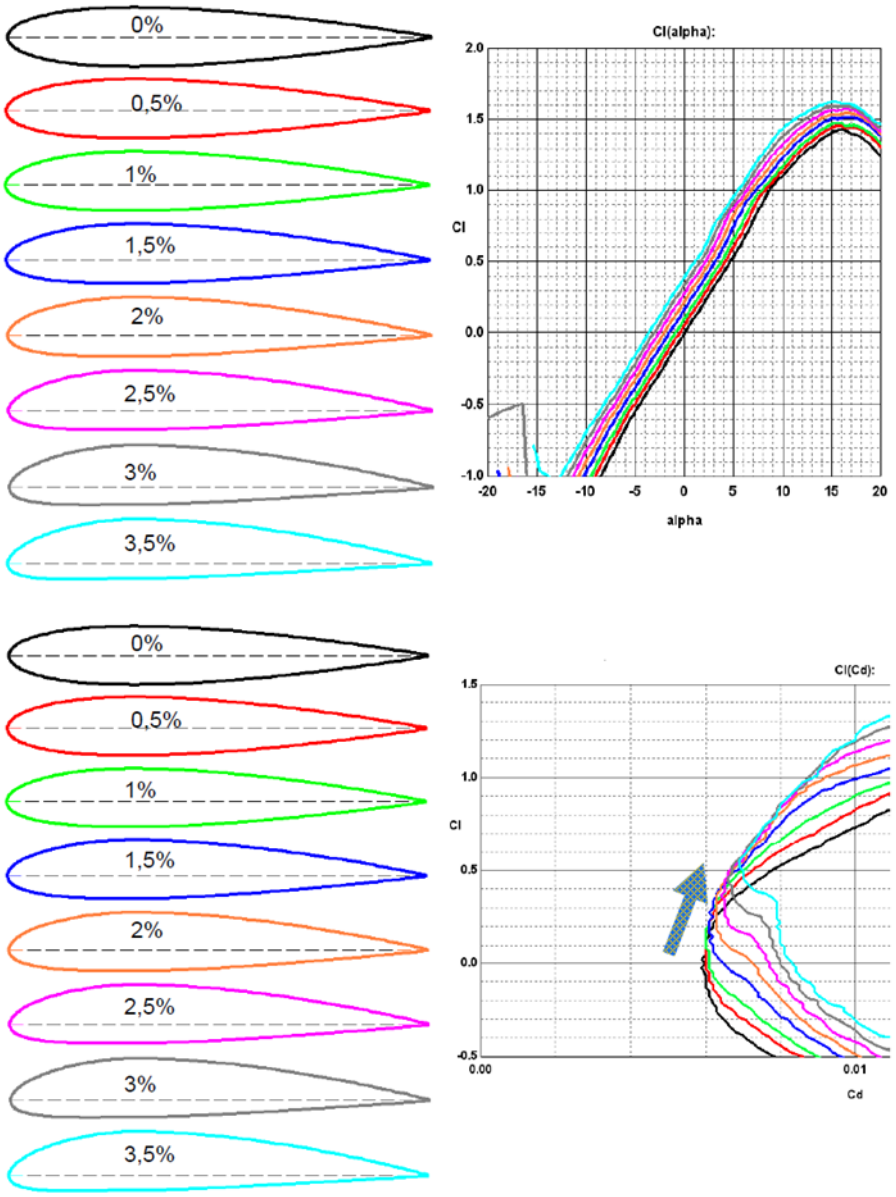

***Figure 6.15**. Comparison of airfoil shapes with varying camber percentages (0% to 3.5%) and their corresponding lift coefficient as a function of angle of attack (**top**), and lift coefficient versus drag coefficient (**Bottom**).*

6.3.3 Fundamentals of CFD

Computational Fluid Dynamics (CFD) is a branch of fluid mechanics that deals with flow problems using numerical methods. This approach arises from the impossibility of obtaining analytical solutions. To employ numerical methods, a process called discretization is applied, which approximates partial differential equations (PDEs) into systems of algebraic equations to be solved by a computer through iterations. These approximations are made in small subdomains, providing numerical solutions specific to a location and a moment in time. The accuracy of numerical methods depends on the discretization method used, always considering that the obtained solutions are approximations [17].

The essential components for proper numerical simulation include:

- **Mathematical Model**: Based on a set of PDEs, along with initial and boundary conditions.
- **Discretization Method**: CFD primarily involves converting PDEs into algebraic equations that computers can numerically solve. Three common methods are used: finite difference, finite volume, and finite element. Finite difference typically employs structured grids, while the latter two use unstructured ones.
- **Coordinate System**: A specific coordinate system is chosen; in this case, Cartesian coordinates are used.
- **Meshing**: The domain of study is divided into a finite number of subdomains called cells. The density of points in an area corresponds to the level of detail needed, known as mesh refinement. Two main types of meshing are structured and unstructured as seen in **Figure 6.16**.
    - **Structured Mesh**: Elements are organized in memory, facilitating quick access to neighboring cells.
    - **Unstructured Mesh**: Offers greater flexibility in handling complex geometries and requires less computational time for mesh generation.

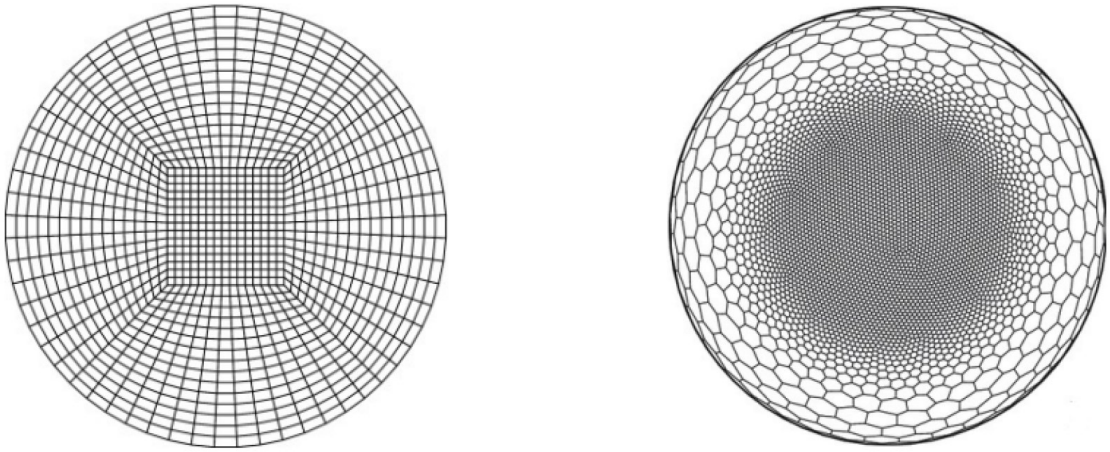

***Figure 6.16**. Comparison of two different mesh types used in CFD simulations: (a) structured mesh and (b) unstructured mesh* [25].

- **Convergence Criterion**: A problem is considered converged when the residual value of the algebraic equations solved by the computer approaches zero as the iteration progresses.

For this project, the finite volume method for discretization was chosen. The results obtained from any of these methods are linear or nonlinear algebraic equations, solved through iterative processes to achieve convergence. The main advantage of the finite volume method is that spatial discretization is carried out directly in the physical space of the problem. Consequently, there are no issues related to coordinate system transformations, as encountered in the finite difference method. Moreover, this method is highly flexible and can be applied to both structured and

unstructured meshes, making it the most suitable and recommended choice for handling complex geometries.

6.4 Use case description

After establishing a solid context for both aircraft and the known types of flight, as well as the physical laws governing the behavior of bodies in aerodynamics, it is the appropriate time to land on the central topic to be addressed in this chapter. As mentioned earlier, the primary focus of this study revolves around a specific category of aircraft known as rotary-wing aerodynes, also referred to as VTOL. The acronym VTOL stands for "Vertical Take-Off and Landing," signifying aircraft capable of taking off and landing vertically without relying on a conventional runway.

In general terms, we are talking about aircraft that operate at low altitudes and at subsonic speeds. This concept primarily applies to Unmanned Aerial Vehicles (UAVs) designed for the transportation of people and goods in urban environments. This technology has revolutionized the aviation industry by extending the range and maneuverability of UAVs, enabling them to access areas that would be inaccessible to traditional aircraft. The collective group of these UAVs is part of the "Urban Air Mobility" (UAM) concept. UAM is a technology-intensive industry that places significant emphasis on efficient performance and envisions safe transportation systems that leverage new vertical takeoff and landing electric aircraft to transport passengers or cargo within cities, between cities, or suburban areas using aerial routes [26].

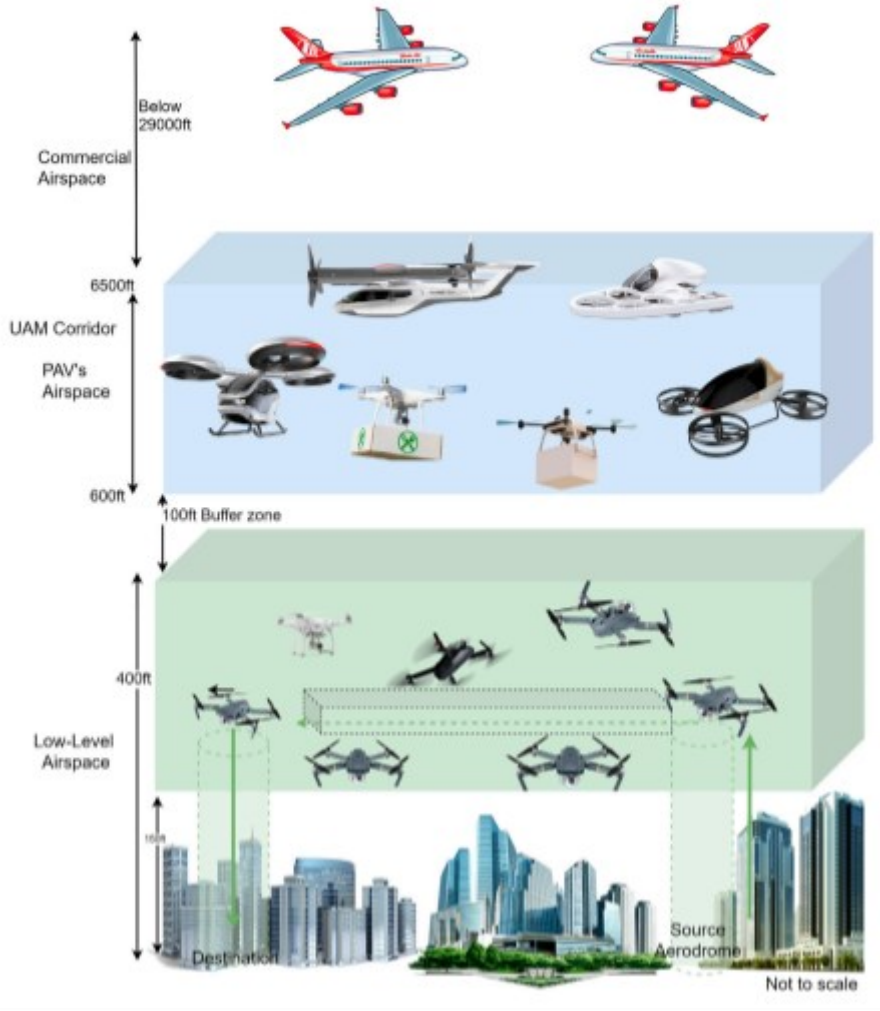

***Figure 6.17**. Airspace categorization for urban air mobility* [27].

When defining the values for the analysis, it is crucial to consider the parameters involved in calculating the Reynolds number to provide a coherent Reynolds value. The density of the air used is that which is found at sea level, i.e., 1.225 kg/m³ [28]. This density has been chosen because these aircraft will not reach high altitudes, and it is impossible to select a density that covers all possible situations. The dynamic viscosity of the air is 1.805×10^5 Pa·s, and this value has been used [29].

Regarding the aircraft's dimensions, it has been determined that the wing's chord should be approximately 0.5 meters, and the target velocity is around 150 km/h to suit this type of aircraft well. Rounding the Reynolds number to 1.6×10^6, a velocity of 42.7 m/s (equivalent to 153.72 km/h) and a chord length of 0.552 meters are used.

Finally, it is important to note that the mentioned pressure is gauge pressure. In this context, zero-gauge pressure is equal to atmospheric pressure, so the pressure used in the analysis is set at 0 Pascals (Pa).

The reference airfoil for this Reynolds number is DAE-11, obtained after a review of the Reynolds number of interest using the airfoil analysis tool at airfoiltools.com. Comparative analyses will be conducted using this reference airfoil in conjunction with 2D bio-inspired profiles. The DAE-11 airfoil was designed for human-powered aircraft [30].

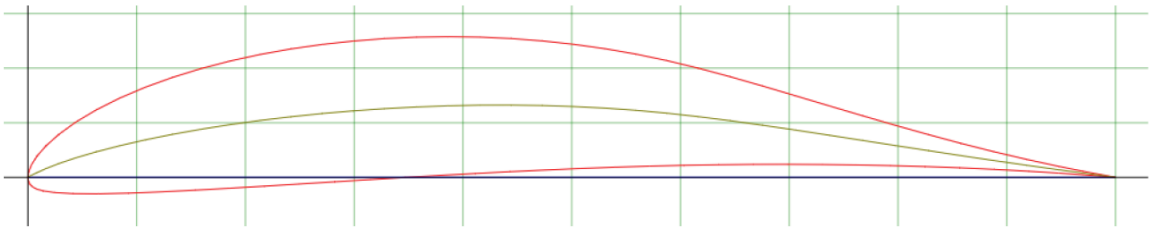

***Figure 6.18**. Geometry of the reference airfoil DAE-11 showing the camber line and thickness distribution* [31].

6.5 Methodology

Once the necessary context has been established for the study, it is time to provide a detailed explanation of what has been done and how it has been executed. In this section, an account will be given of how the bioinspired profiles to be studied were chosen and where their geometrical data was sourced. The methodology for the two-dimensional analysis will be outlined, and a thorough discussion of the results obtained will follow. These results have, in turn, guided the selection of the profiles believed to be the most suitable for the specific case under investigation. Subsequently, the different configurations of bioinspired wing designs to be examined using the profiles chosen in the preceding analysis will be explained. Finally, a description of how the three-dimensional analysis was conducted will be provided, along with the presentation of the obtained results.

6.5.1 Bioinspired airfoil selection

The process of selecting bioinspired airfoil profiles for comparison with the reference profile involved using the classification of natural flight types outlined in the introduction. Emphasis was placed on examining a diverse range of profiles, particularly those associated with organisms capable of achieving a significant glide ratio. Such profiles were deemed advantageous for enhancing the flight efficiency of urban aircrafts.

The acquisition of bioinspired airfoil geometries was by no means a straightforward task. Many airborne creatures possess the ability to modify the morphology of their wing sections during different phases of flight. Furthermore, these wings often exhibit changing chord and shape characteristics. Given these complexities, simplifying these geometries and acquiring accurate representations would have required resources beyond the scope of this study. Consequently, all profiles used in this research were sourced from existing literature and the work of other research groups.

The first profile selected for analysis is that of the Albatross. Albatrosses are renowned for their highly efficient flight style known as dynamic soaring. This technique enables them to glide gracefully across some of the world's most turbulent oceans, utilizing gravitational and wind gradient forces to maintain efficient trajectories. Remarkably, an albatross can traverse vast distances exceeding a thousand miles without flapping its wings once (source: Oceanographic Magazine). Furthermore, in a study of various bird profiles, including eagles, storks, falcons, and albatrosses "Numerical Investigation on Aerodynamic Performance of Bird's Airfoils," indicated that the albatross profile significantly outperformed others, particularly at angles near 0°. It exhibited superior performance in terms of minimal drag and high lift, distinguishing it from the profiles examined in the study. The form of this airfoil was derived from Airfoil Tools, where a predefined profile known as GOE-174, inspired by the Albatross's wing shape, was utilized. This profile has found application in numerous studies and practical implementations, particularly within the realm of bio-inspired unmanned aerial vehicles (Aerodynamic characterization of an Albatross wing for Bio-inspired unmanned aerial vehicle).

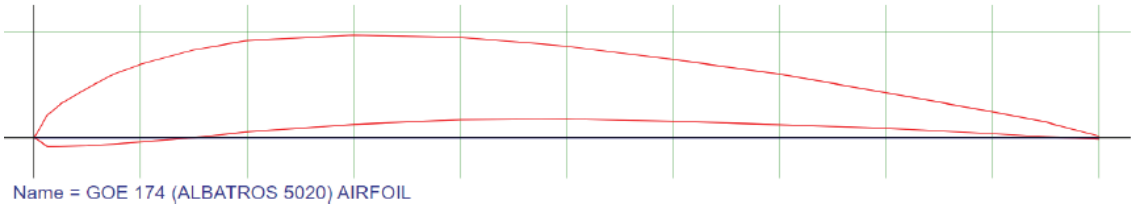

***Figure 6.19**. Geometry of the GOE 174 (Albatros 5020) airfoil, showing the camber line and thickness distribution* [31].

The second bio-inspired profile is that of an owl. Owls are renowned for their silent flight, allowing them to stealthily approach their prey. Their wings are notably broad with large surface areas, facilitating smooth gliding through the air with minimal flapping and noise generation. What sets owls apart in achieving silent flight is the unique design of the leading edges of their primary feathers, effectively minimizing turbulence-induced noise. Additionally, their secondary feathers feature soft fringes that further reduce turbulence behind their wings, while the trailing feathers at the wing's rear end are tapered to diminish noise. Owls are also adept at gliding, and their wing design is optimized to ensure silent flight and efficient gliding.

Noise reduction is a critical aspect for aircraft, especially those operating in proximity to residential areas. In the case of urban mobility aircraft, noise mitigation becomes even more crucial. Hence, the choice of this second profile is rooted in its potential to enhance efficiency, particularly gliding capabilities, and minimize noise emissions—a key consideration for aircraft of this type. The profile's geometry is derived from a study titled "Experimental Analysis of the Flow Field over a Novel Owl-Based Airfoil," which thoroughly investigates its aerodynamic performance [32].

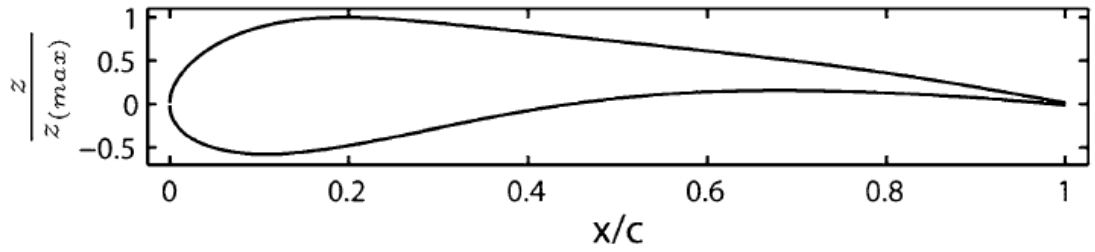

***Figure 6.20**. Geometry of the bio-inspired owl airfoil, showing the normalized thickness distribution along the chord* [32].

***Table 6-2**. Dimensional parameters of the owl-based profile* [32]

Description	Abbreviation	Value
Chord length	c	0.178 m
Span	l	0.5 m
Wing area	A	0.089 m^2
Max. thickness	Z_{tMAX}	14.77%
Location of z_{tMAX}	x_{tzMAX}	15%
Max. camber	Z_{cMAX}	3.80%
Location of Z_{cMAX}	x_{zcMAX}	50.40%
Nose radius	r_n	11.35%
Trailing-edge angle	alpha	4.53%

The third and final profile aims to compare a somewhat different morphology, as well as a profile that operates in a different medium—water. In this study, the goal was to analyze a profile inspired by an aquatic creature. Dolphins, well-known for their exceptional swimming abilities, are among the fastest and most efficient aquatic beings. Their pectoral fins provide them with remarkable stability during swimming while maintaining low drag. The profile of this animal has been sourced from a study titled "Hydrodynamic Analysis of Dolphin Fin Profiles" which hydrodynamically compares various fins from a dolphin specimen that had passed away naturally [33].

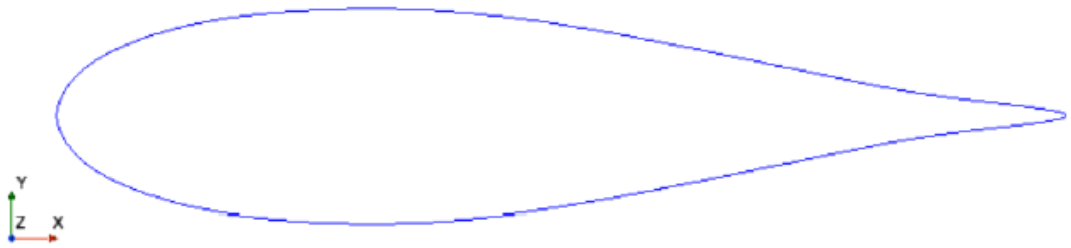

***Figure 6.21**. Geometry of the dolphin-inspired airfoil, based on the pectoral fin.*

***Table 6-3**.Dolphin fin offsets for different chord distance values* [33].

Distance from nose (% chord)	Fin semi-thickness (% chord)
0	0.00
2	3.97
5	6.07
10	8.05
15	9.28
20	9.96
30	10.53
40	10.17
50	8.98
60	7.20
70	5.22
80	3.16
90	1.57
100	0.23

Once all the profiles have been selected, they need to be compared based on the aerodynamic principles governing the chosen regime. To conduct the Computational Fluid Dynamics (CFD) study, Siemens Digital Industries Software's Simcenter STAR-CCM+ software will be employed. This software is well-suited for a wide range of engineering problems related to fluid flow, heat transfer, stress, particulate flow, electromagnetics, and related phenomena. It competes effectively with other industry-leading solutions like Ansys Fluent. Thanks to its modern interface, diverse applications, and compatibility with various hardware setups, Simcenter STAR-CCM+ is a favored choice among engineers and organizations across multiple industries.

In general, the performance of Simcenter STAR-CCM+ is on par with other leading CFD software such as ANSYS Fluent and OpenFOAM. The software choice may depend on various factors, including accuracy, computational cost, ease of use, and the specific problem being addressed. For the specific case under consideration in this study, and due to the ease of obtaining licenses in the institutions where the research was conducted, Simcenter STAR-CCM+ was selected for use.

6.5.2 Two-dimensional analysis

In this section, a comprehensive analysis will be conducted to outline the essential steps required for performing a correct and obtaining realistic results in a two-dimensional CFD analysis. Starting from defining the geometry, every subsequent step is crucial for ensuring that representative outcomes are obtained.

Model construction

To begin with, the boundary conditions that will serve as the foundation for the analysis are defined as follows:

- Chord = 0,552 m
- Velocity = 42,7 m/s
- Air density = 1,225 kg/m^3
- Dynamic viscosity = 1,805·10-5 Pa·s
- Manometric pressure = 0 Pa

Next, the steps that need to be followed to correctly construct the problem in Simcenter STAR-CCM+ will be detailed.

1. Importing the airfoil geometry

There are two options available for this step: either the airfoil profile coordinates can be imported directly from a data table or a CAD file with the desired geometry can be used. Importing via data tables is straightforward: the (X, Y) coordinates of the points forming the airfoil profile are obtained and then the format is adapted so that it can be understood by the software. This format is characterized by the addition of a column with a zero Z-coordinate. Despite the analysis being in 2D, the construction of the problem in Simcenter STAR-CCM+ is carried out in 3D until the mesh generation stage.

Importing via CAD geometry is also a simple process: the geometry is constructed using CAD software and is then imported into the 3D software.

In the case being studied, all the geometries for the 2D analysis were imported via data tables. The coordinates were obtained from airfoiltools.com.

2. Domain definition

The domain, which is the volume or geometry within which the fluid dynamics study will be conducted, is typically in the form of a rectangular prism. It is important to have a domain that is sufficiently large to encompass all the phenomena that may occur around the airfoil. While the area immediately surrounding the airfoil is of primary importance, phenomena occurring in more distant areas can have a significant influence on the events around the airfoil. Therefore, a larger domain results in a more realistic study, but it also comes with increased computational costs. There comes a point where the extra computational cost does not justify the effect of the additional volume on the study. Thus, finding the necessary compromise is essential.

Based on the provided data, a domain size of 12m in X, 6m in Y, and 1m in Z has been chosen. The airfoil is not centered because what occurs in the wake generated after the airfoil is more critical than what happens before the leading edge. Therefore, the leading edge is positioned 5m from the start of the domain and 7m from the end of the domain in the X direction.

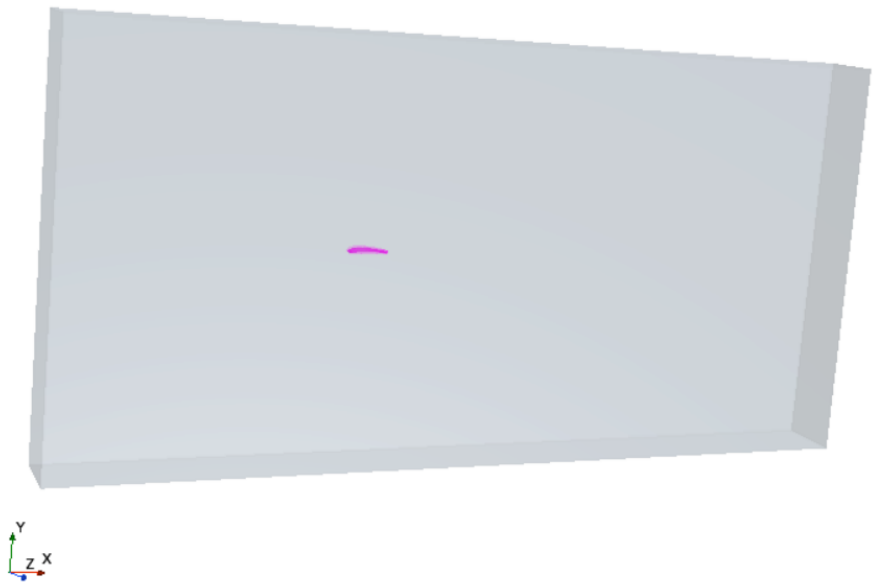

***Figure 6.22**. Domain definition for the 2D fluid dynamics study of the airfoils.*

3. Surface definition

Defining the surfaces that interact in the analysis is essential for the software to understand which is the airfoil profile, the direction of the fluid flow, and the volume of the defined domain. To achieve this, the geometry of the airfoil profile is first defined as "wing."

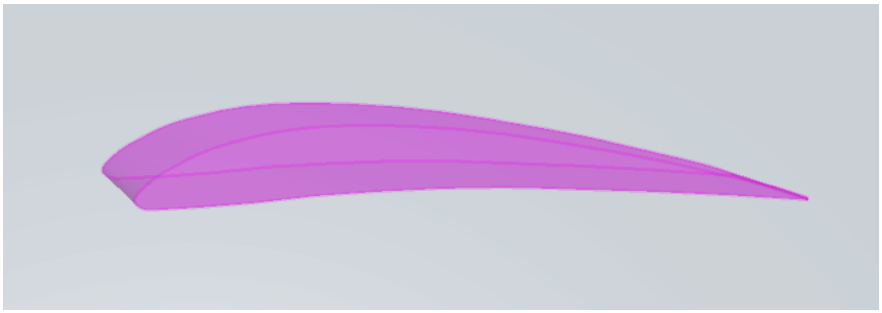

***Figure 6.23**. Surface definition for the fluid dynamics analysis, identifying the airfoil profile geometry as the "wing" to specify the interaction surfaces and the direction of fluid flow*

Next, the surfaces that delineate the domain are defined:

- Inlet: The surfaces defined here indicate where the air will enter. For this study, the chosen surfaces are the upper, lower, and initial surfaces of the domain. In any case, the air will enter in the direction previously defined (X+).

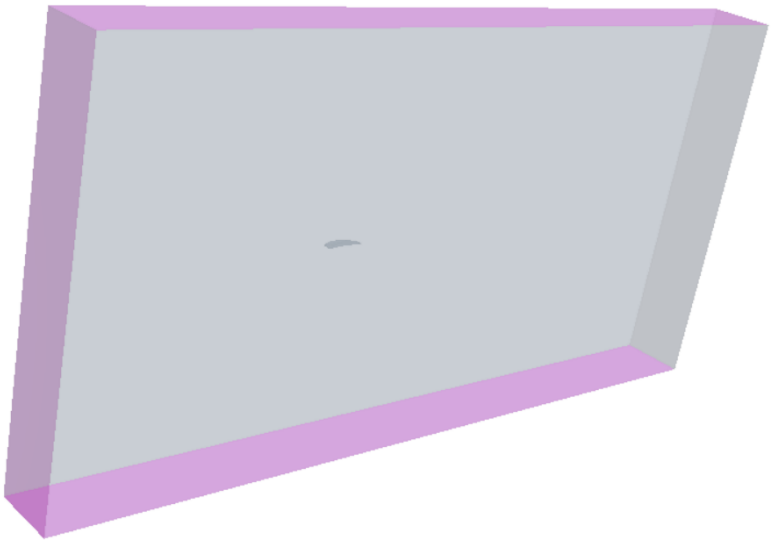

***Figure 6.24**. Definition of inlet surfaces, where the air will enter the domain, are indicated on the upper, lower, and initial surfaces of the rectangular prism.*

- Outlet: This surface defines the area through which air exits the domain.

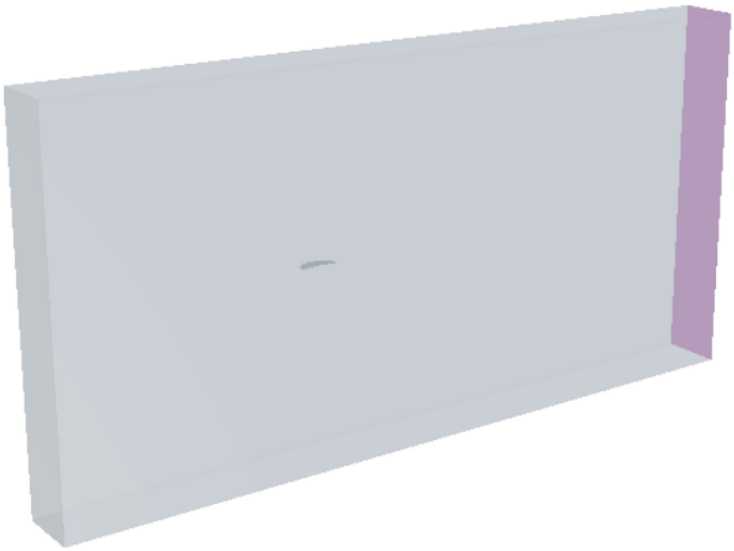

***Figure 6.25**. Definition of the outlet surface indicating the area through which air exits the domain.*

- Two independent walls: These surfaces delimit the domain in the Z direction. In this case, they are the surfaces located on either side of the airfoil profile.

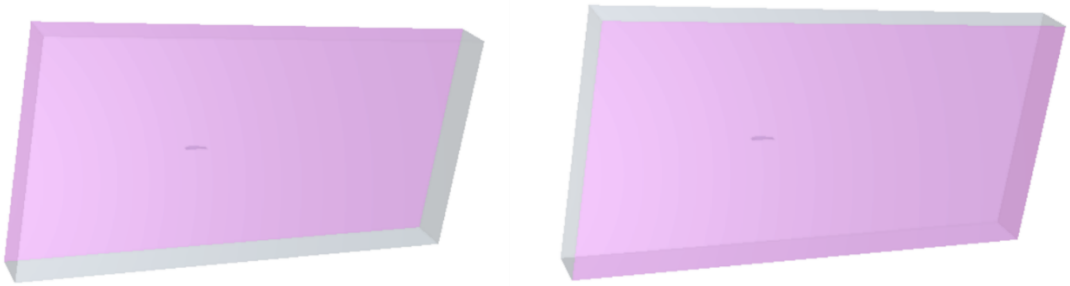

***Figure 6.26**. Definition of the two independent wall surfaces delimiting the domain in the Z direction.*

4. Mesh construction

As in all finite element studies, meshing plays a crucial role in obtaining reliable results in CFD analyses. The main challenge lies in finding a balance between a fine mesh and computational cost, as they are closely intertwined.

To define the mesh to be used in this study, we first need to determine the type of elements that will form our mesh. In the case at hand, the best choice appears to be polyhedral elements, which, unlike triangular and tetrahedral elements, adapt well to curved geometries. Nevertheless, for the boundary layer, prism elements have been used to more accurately capture the critical phenomena in that region. After several iterations, the parameters defining the mesh are as follows:

- base size = 0,1 m
- Number of prism layers = 25

- Prism layer stretching = 1,1
- Prism layer thickness = 0,00121 m
- Surface growth rate = 1,05
- Surface minimum size = % 25
- Surface target size = % 75
- Surface size = % 5

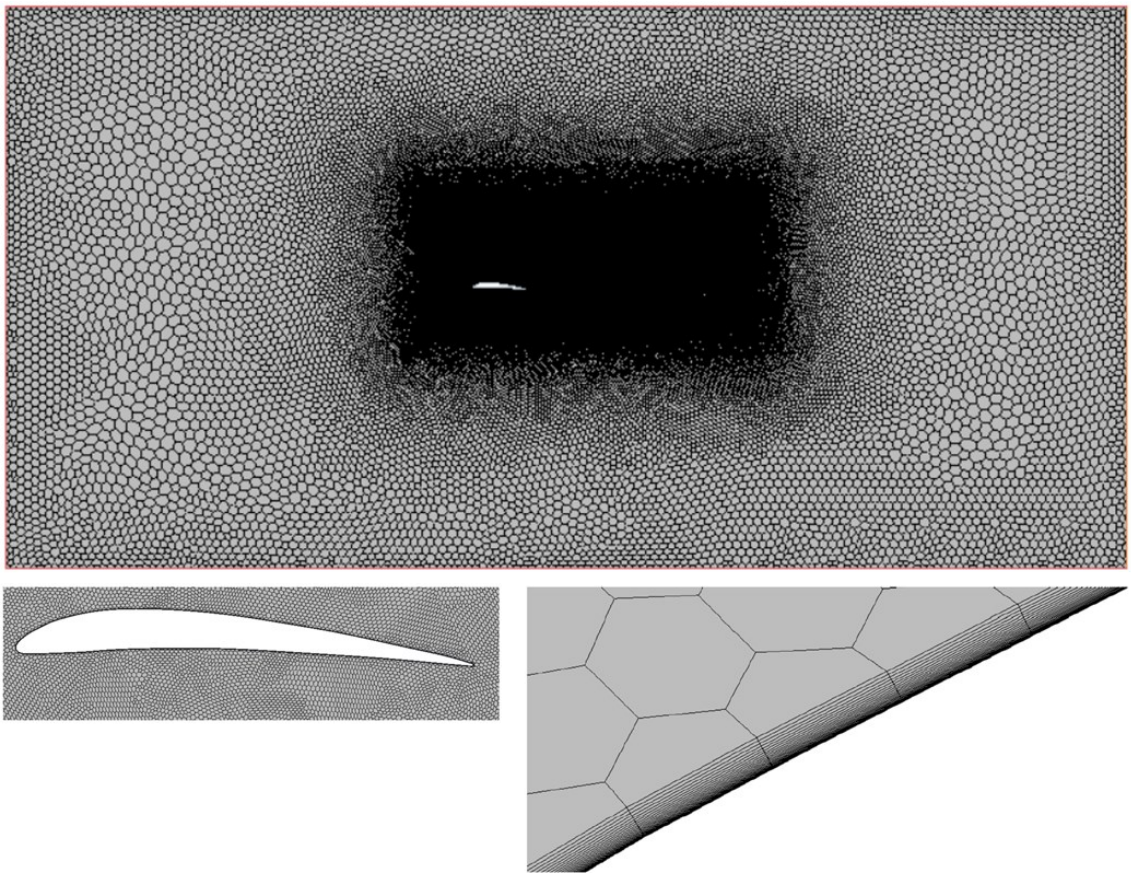

Figure 6.27*. Mesh definition using polyhedral elements for the main volume and prism elements for the boundary layer.*

5. Selection of model physics

To carry out the simulation, we need to define the physics that will govern our results. Here are the physics defined for the study being analyzed:

- Space: two dimensions
- Time: steady
- Material: Gas
- Flow: Segregated flow
- State equation: Constant density
- Viscous regime: Turbulent
- Average Reynolds turbulence: K-ω turbulent
- Transition: Gamma Transition

Given that the simulation is two-dimensional, the spatial dimension is also two-dimensional. The changes occurring in the simulation are smooth and regular, which is why a steady-state approach has been chosen. Since the fluid is air, the material must be a gas, not a liquid. In terms of flow, apart from separated flow, the other option is coupled flow, which is suitable for supersonic flow. However, as this is not a supersonic flow, the segregated flow option is preferred.

As seen in the force calculation formulas and force coefficient equations, fluid density is involved in the calculations. Therefore, a constant density has been selected in the state equation to ensure consistent values in all simulations.

With a Reynolds number of 1.6 x 10^6, which is greater than 5 x 10^5, it falls into the turbulent viscous regime, as explained in theory. Among the turbulence models, typically, K-epsilon or K-omega models are used in most cases because they are sufficient for normal computers and typical scenarios. Between these two, the K-omega model has been chosen because it provides better simulation results for curved geometries.

Lastly, for the transition models, the gamma transition model has been used. In fluid mechanics simulations, this model is employed to simultaneously simulate laminar flow, the transition from laminar to turbulent flow, and fully turbulent flow. It is the most suitable choice for this scenario.

Results analysis

After setting up the problem in Simcenter STAR-CCM+, the analysis is initiated, and the results are awaited to converge. Subsequently, it is essential to ensure that the mesh quality is decent and that the results in the scenes and plots appear to make sense. This means that, according to the results seen in the scenes, it can be ensured that the laws of aerodynamics that were anticipated are being met. Therefore, when observing the scenes in the 2D study of the Albatross GOE-174 airfoil profile, it is necessary to verify that at least the Venturi effect is being met because, if this holds true, the continuity and Bernoulli equations would also be satisfied. This implies that the problem should, in principle, be adequately formulated.

In the fluid velocity scenes, it can be noticed that the upper part of the profile has a higher velocity (~60 m/s), while the lower part has a lower velocity (~33.3 m/s). This makes sense because, for the continuity equation to be fulfilled, the fluid must take the same time to pass from one side of the profile to the other. Since the path is longer on the upper side than the lower side, the fluid must move faster on the upper side.

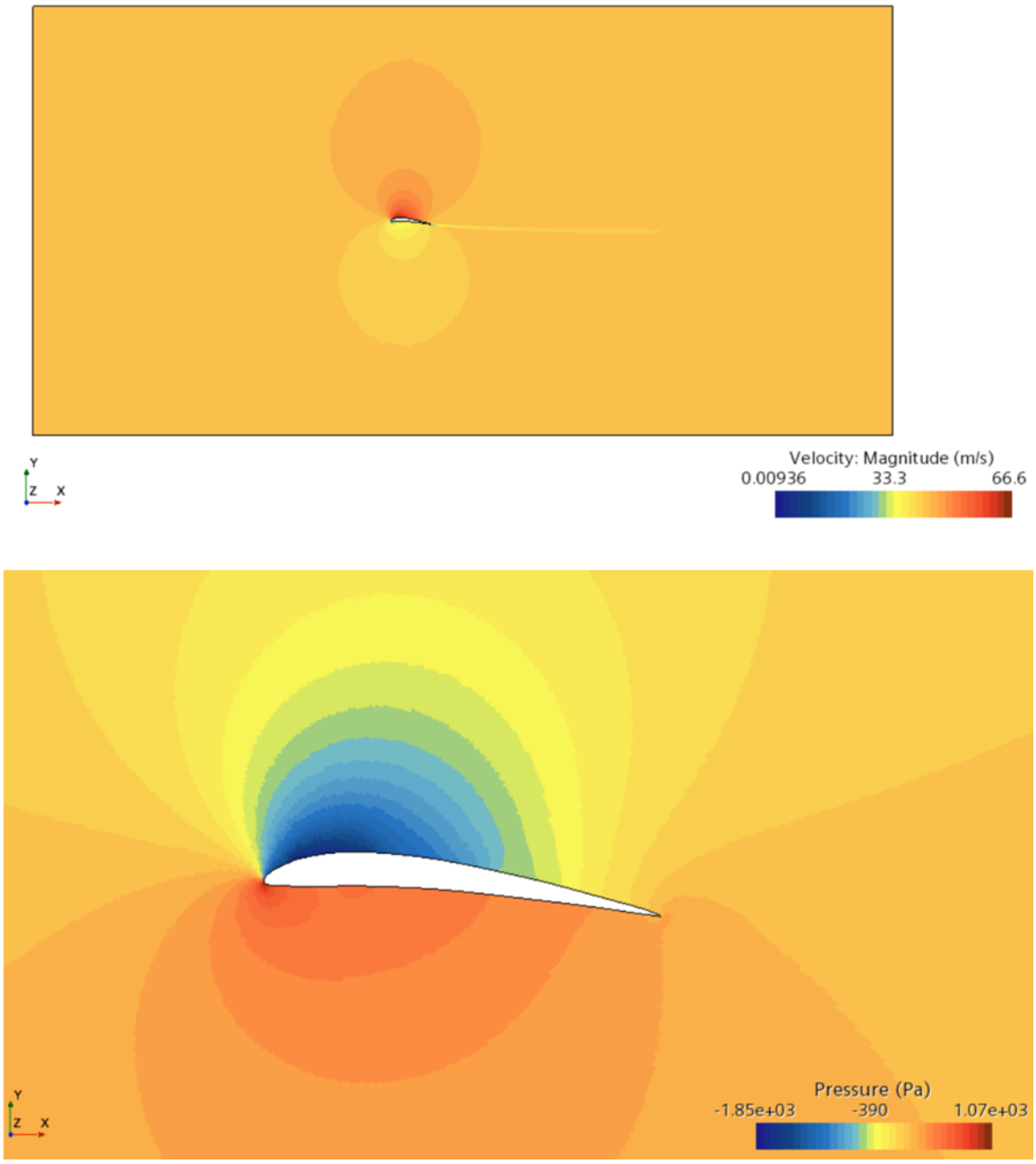

***Figure 6.28**. 2D CFD simulation results for the airfoil. Velocity magnitude distribution around the airfoil (**top**). Pressure distribution around the airfoil (**bottom**).*

In the case of pressure, due to the Venturi effect, the opposite occurs. As velocity increases, pressure must decrease, and vice versa. This confirms that Bernoulli's equation is also being satisfied throughout the volume.

In the **Figure 6.29**, you can observe that the velocity closest to the profile is almost zero, and as you move away from it, it increases. This indicates that the boundary layer has not separated in that area.

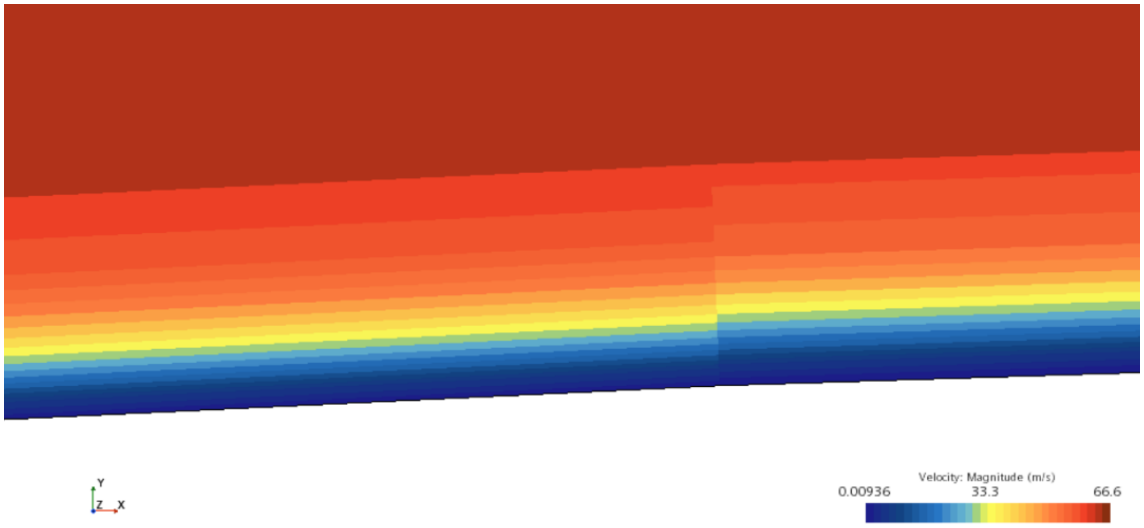

***Figure 6.29**. Velocity magnitude distribution in the flow field around the airfoil.*

Finally, in **Figure 6.30**, which displays the fluid velocity around the profile at a 10° angle of attack, it can be seen the boundary layer separation. Not only is it evident in the wake's velocity, but also turbulence is visible in the profile area where separation has occurred. This boundary layer separation can lead to a decrease in Lift and an increase in Drag, which is a highly critical phenomenon for aircraft that rely on their wings for lift and can worsen to the point of stall.

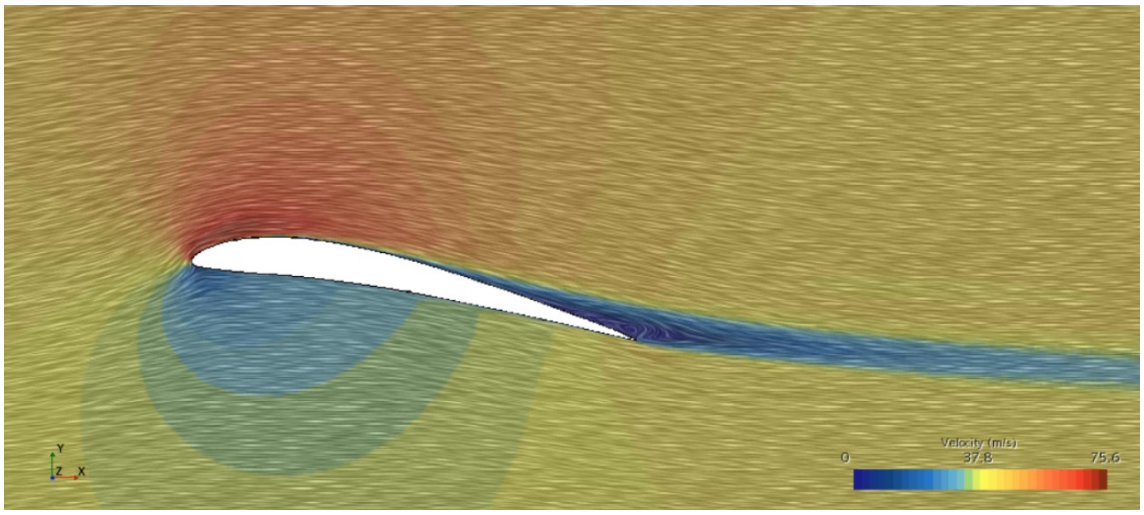

***Figure 6.30**. Fluid velocity distribution around the airfoil at a 10° angle of attack, illustrating boundary layer separation and turbulence in the wake.*

Once it is confirmed that the physics occurring around the profile appear to be correct, the next step is to examine the values of the aerodynamic coefficients, aerodynamic forces, and aerodynamic efficiency to choose among the previously selected airfoil profiles. The following tables show the results of the simulations with the mentioned physics for angles of attack ranging from 0° to 10°.

***Table 6-4**. Results of 2D analysis for DAE-11 airfoil.*

DAE-11

A(°)	C_L	C_D	C_L/C_D	Lift (N)	Drag (N)	Lift/Drag
0	0,65000	0,00757	85,87	400,80	4,67	85,82
1	0,75243	0,00677	111,14	463,94	4,18	110,99
2	0,85675	0,00646	132,62	528,20	3,98	132,71
3	0,96912	0,00684	141,68	597,50	4,22	141,59
4	1,08756	0,00723	150,42	670,60	4,46	150,36
5	1,18244	0,00860	137,49	729,10	5,3	137,57
6	1,29292	0,01028	125,77	797,20	6,34	125,74
7	1,38961	0,01248	111,35	856,80	7,69	111,42
8	1,45522	0,01516	95,99	897,30	9,35	95,97
9	1,48715	0,02035	73,08	916,96	12,55	73,06
10	1,40935	0,03159	44,61	868,99	19,48	44,61

***Table 6-5**. Results of 2D analysis for Albatross airfoil.*

ALBATROSS

A(°)	C_L	C_D	C_L/C_D	Lift (N)	Drag (N)	Lift/Drag
0	0,57168	0,00832	68,71	352,50	5,13	68,71
1	0,69360	0,00744	93,23	427,70	4,58	93,38
2	0,78430	0,00729	107,59	483,60	4,49	107,71
3	0,90879	0,00874	103,98	560,20	5,39	103,93
4	1,00150	0,00964	103,89	617,50	5,95	103,78
5	1,08760	0,01110	97,98	670,60	6,84	98,04
6	1,17510	0,01387	84,72	724,60	8,52	85,05
7	1,26926	0,01672	75,91	782,60	10,30	75,98
8	1,32730	0,01980	67,04	818,40	12,20	67,08
9	1,34987	0,02755	49,00	832,30	16,99	48,99
10	1,32260	0,03447	38,37	815,50	21,25	38,38

***Table 6-6**. Results of 2D analysis for Owl airfoil.*

OWL

A(°)	C_L	C_D	C_L/C_D	Lift (N)	Drag (N)	Lift/Drag
0	0,46240	0,00742	62,32	285,10	4,57	62,39
1	0,57000	0,00741	76,92	351,50	4,57	76,91
2	0,68500	0,0076	90,13	422,40	4,68	90,26
3	0,78780	0,008	98,48	485,70	4,93	98,52
4	0,89770	0,00835	107,51	553,50	5,15	107,48
5	1,00660	0,00921	109,29	620,60	5,68	109,26
6	1,11690	0,00979	114,09	688,60	6,03	114,20
7	1,21600	0,01093	111,25	749,80	6,74	111,25
8	1,32130	0,01190	111,03	814,70	7,34	110,99
9	1,43287	0,0138	103,83	883,50	8,51	103,82
10	1,53400	0,01559	98,40	945,90	9,62	98,33

***Table 6-7**. Results of 2D analysis for Dolphin airfoil.*

DOLPHIN

A(°)	C_L	C_D	C_L/C_D	Lift (N)	Drag (N)	Lift/Drag
0	0,01319	0,00646	2,04	8,13	3,98	2,04
1	0,10494	0,00659	15,92	64,70	4,06	15,94
2	0,21497	0,00672	31,99	132,50	4,14	32,00
3	0,33020	0,00697	47,37	203,60	4,3	47,35
4	0,46149	0,00743	62,11	284,50	4,58	62,12
5	0,55729	0,00815	68,38	343,60	5,02	68,45
6	0,64913	0,00945	68,69	400,20	5,83	68,64
7	0,73314	0,01017	72,09	452,00	6,27	72,09
8	0,84738	0,01130	74,99	522,50	6,97	74,96
9	0,92754	0,01222	75,90	571,90	7,53	75,95
10	1,01722	0,01357	74,96	627,20	8,37	74,93

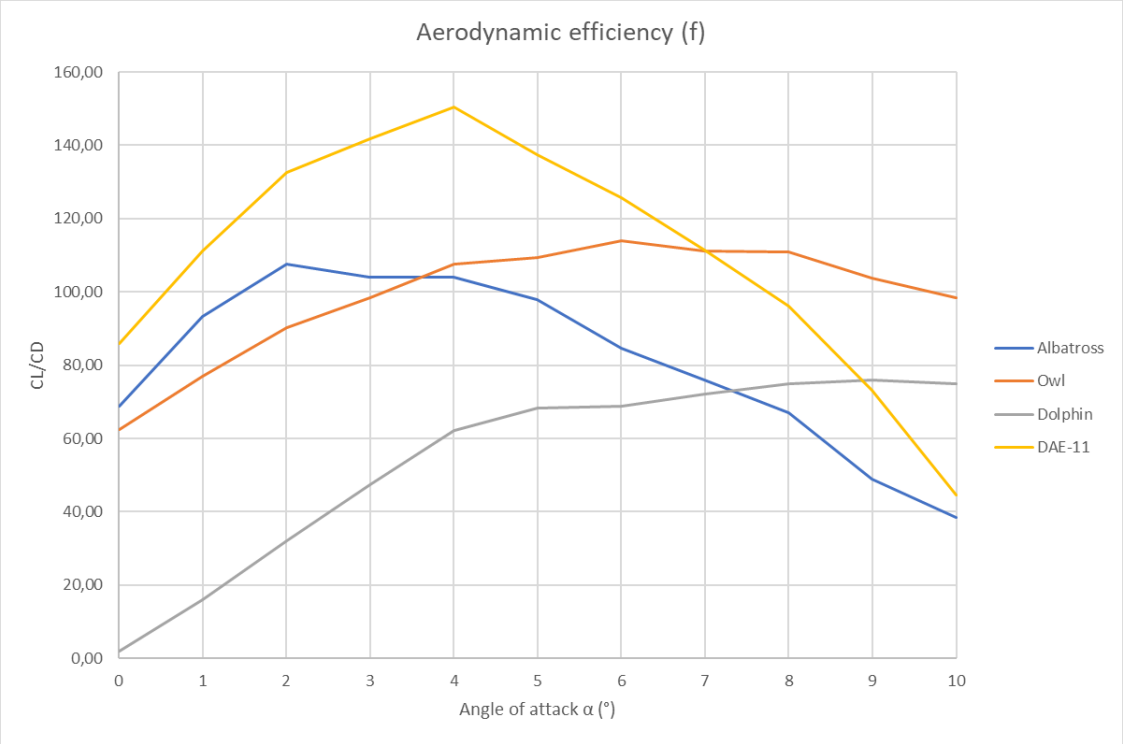

***Figure 6.31**. Aerodynamic efficiency (Cl/Cd) as a function of angle of attack for different airfoil profiles in the study.*

In **Figure 6.31**, the graph of the aerodynamic efficiency can be seen for each of the analyzed airfoil profiles. It is evident that the dolphin profile, with its unique symmetrical shape, lacks significance in this study due to its low efficiency in this regime. The reference profile DAE-11, chosen for its supposed suitability for the regime in question, performs better than any other from 0° to 7°, with its peak efficiency at 4°. The albatross profile exhibits relatively good performance at angles from 0° to 4°, with its maximum efficiency at 2°. Since the range from 0° to 5° is of the most interest, the albatross is the best-performing among the bio-inspired profiles. In fact, the owl profile shows good performance starting from 3°, with its peak efficiency at 6°. However, up to that point, the albatross profile outperforms it.

Due to the high computational cost of 3D analyses and resource limitations, it is necessary to choose the smallest number of examples to investigate. In this case, aside from comparing two of the best profiles in the 2D study, the goal is to test different configurations in 3D, including some bio-inspired elements. It is for these reasons and the observed results that the DAE-11 and albatross profiles have been selected for further study in a 3D simulation.

6.5.3 Bio-inspired 3D features selection and construction

3D analysis of aerodynamic profiles provides the opportunity to investigate different phenomena compared to 2D profiles, such as wingtip turbulence or even variable-section wings. In this case, as mentioned earlier, the goal is to study the two best-selected profiles in more depth through 3D analysis. To achieve this, three 3D wing configurations will be constructed for each of these profiles.

The first geometry will be a wing with variable chord from the root to the tip, decreasing by 15%. It has been chosen to keep the reduction in chord relatively mild along the 1.5m wingspan, as documented in the literature, higher aspect ratio wings have been shown to reduce drag [34]. However, in this case, a less pronounced reduction has been opted because the structural design has not been considered, and a slimmer wing would have less rigidity. The construction of this first type of wing can be seen in **Figure 6.32**.

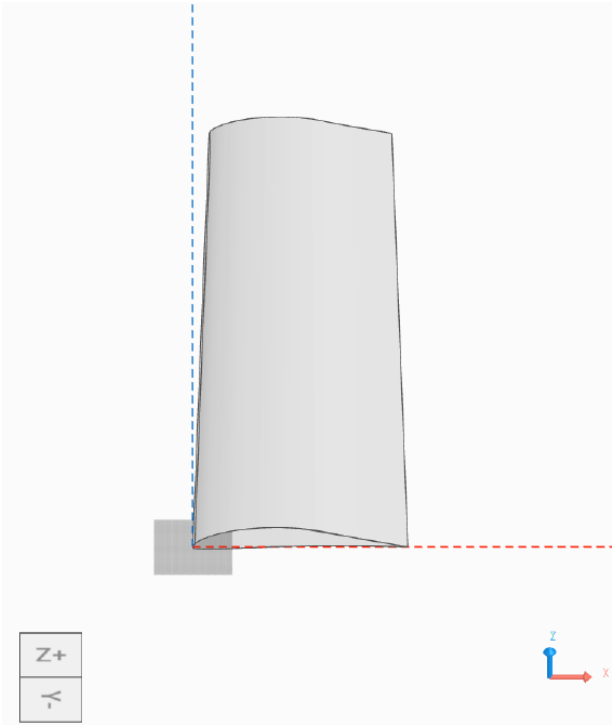

***Figure 6.32**. 3D wing configuration with a variable chord, decreasing by 15% from root to tip along the 1.5m wingspan.*

The second configuration will be the same wing with the chord reduction but with the addition of a 10° sweep. Sweeping the wings has been shown to have a detrimental effect on the performance of subsonic or low-speed aircraft wings [35]. Nevertheless, it has been deemed interesting to observe the effect of sweep on these wings because, as seen in nature, there are many examples of swept wings, including living organisms like the seeds of the Java cucumber or the wing end many gliding birds such as albatrosses or vultures. This aims to analyze the effect of sweep for the given regime.

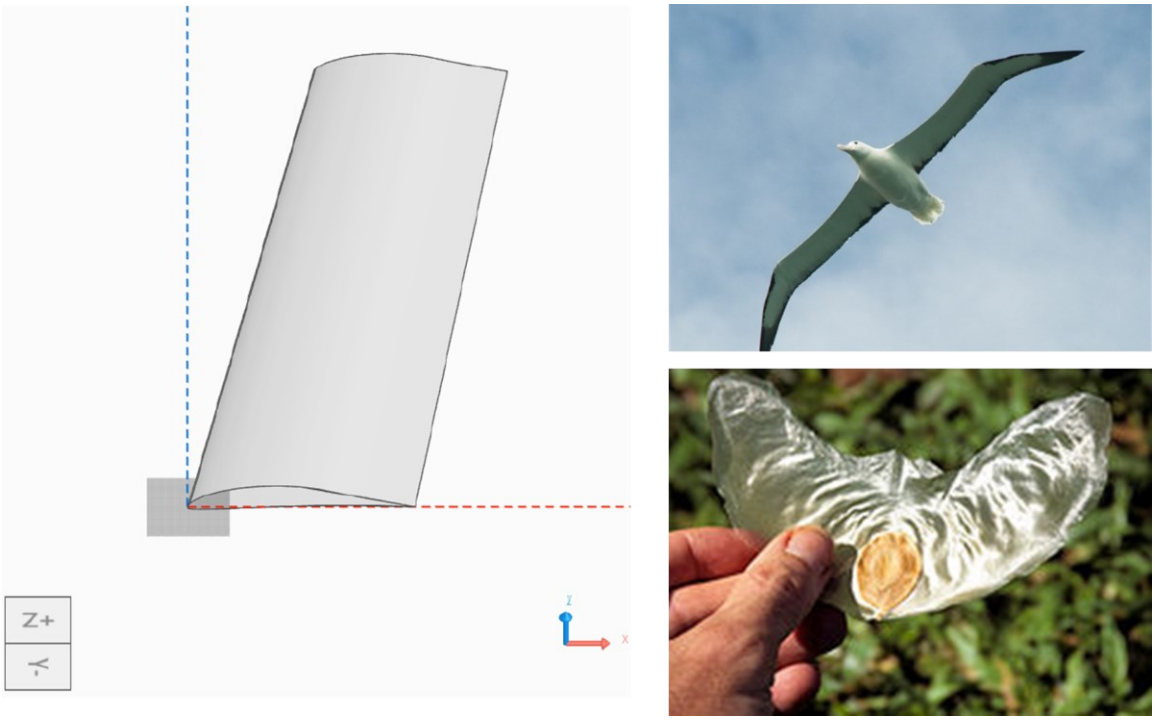

***Figure 6.33**. 3D wing configuration with a 15% chord reduction from root to tip and a 10° sweep. The sweep effect on subsonic or low-speed aircraft performance is analyzed, inspired by natural examples such as the Java cucumber seeds and the wings of gliding birds like albatrosses* [36][37].

The third and final configuration is based on applying protuberances inspired by the humpback whale's flipper, which have already been used in various bio-inspired applications but never for an aircraft of this type. The applications in which these protuberances have been seen include wind turbines and various aerodynamic elements (The Tubercles on Humpback Whales' Flippers: Application of Bio-Inspired Technology).

Humpback whales are known for their impressive swimming abilities and unique physical features. Their long pectoral fins, which can measure up to one-third of their body length, make them highly maneuverable and able to turn within their own body length, much like a dolphin. These fins have unique patterns of tubercles, which are knobby protuberances that help direct the flow of water over the fin, making it more efficient. Research has shown that these tubercles on the leading edge of the fins reduce stall, increase lift, and decrease noise in the post-stall regime (Effects of leading-edge tubercles on wing flutter speeds).

To build the model studied here, the first wing configuration (chord change without sweep) was used, and it was modified to add the protuberances or tubercles. To determine the geometry of these tubercles and the distance they should be from each other, inspiration was drawn from the study [38], which shows the graph that can be seen in **Figure 6.34**.

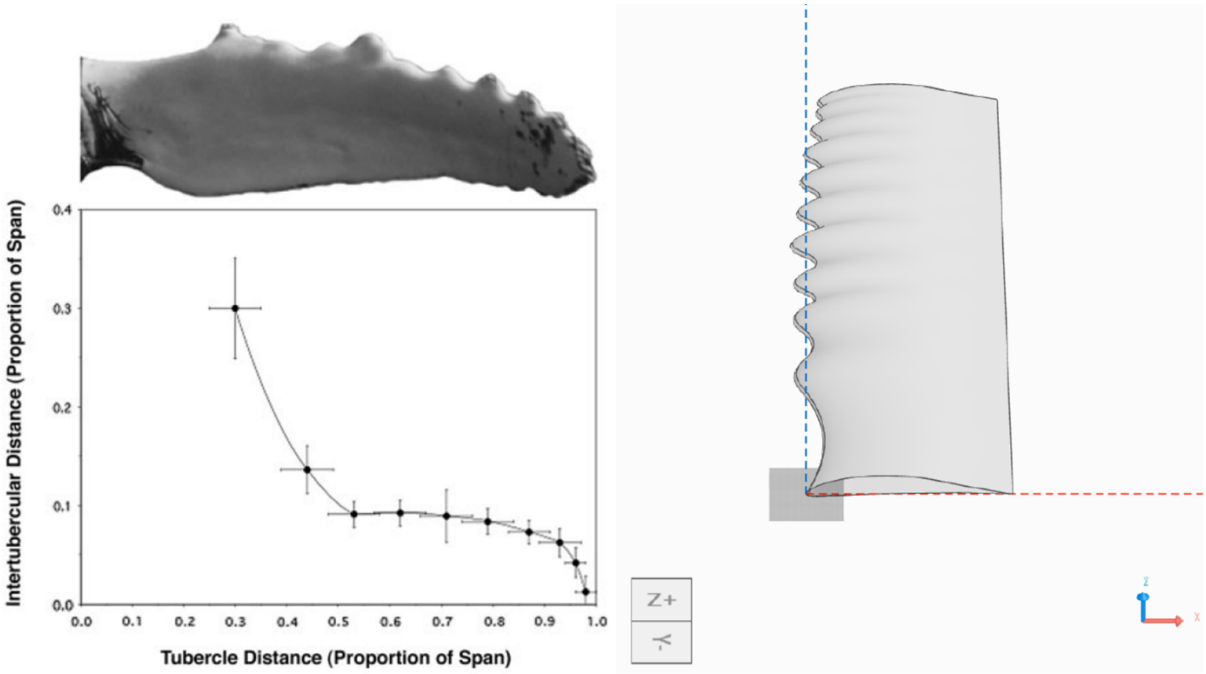

***Figure 6.34**. 3D wing configuration with variable chord and leading-edge tubercles inspired by the humpback whale's flipper. The graph indicates the tubercle distance proportion applied onto the design* [38].

6.5.4 Three-dimensional analysis

Once the geometries of the three wing configurations for the two profiles have been constructed, the problem needs to be set up in Simcenter STAR-CCM+ to carry out the three-dimensional study.

Model construction

To do this, the initial data are as follows:

- Chord = 0.552m
- Velocity = 42.7m/s
- Air density = 1.225kg/m3
- Dynamic viscosity = 1.805E-5 Pa·s
- Manometric pressure = 0Pa

1. Wing Importing

In this case, there is only one method for wing import. Build the geometry in a CAD program and import it as a solid into Simcenter STAR-CCM+. Once imported, it is only necessary to ensure that the axes coincide with the directions that will be defined for the fluid flow.

2. Domain Definition

To define the domain used in this analysis, the reference plane from the 2D analysis was utilized. Therefore, the XZ section of the domain is the same as in the two-dimensional analysis. However, unlike the previous study, the distance chosen on the Y-axis is important in this case. It needs to be sufficient to capture all the phenomena occurring at the wingtip and beyond.

For these reasons, a block-type domain has been defined with the following parameters:

- X Distance = 12m
- Y Distance = 6m
- Z Distance = 6m
- Center: (2,3,-3)m

Finally, the domain appears as shown in **Figure 6.35**. The wing is attached to one of the walls and offset in the X direction because, as mentioned earlier, phenomena occurring in the wake need more space to be captured. Furthermore, in this case, being a finite wing, it makes sense for the root to be attached to the surface simulating the body to which it will be connected, and the rest of the volume is sufficient at the tip to capture the phenomena occurring in that area.



***Figure 6.35**. Domain used for 3D analysis of wing configuration with tubercles.*

3. Domain Surface Definition

In this case, two types of surfaces are defined: the plane in contact with the wing called "symmetry" and the rest of the surfaces referred to as the "far field." There is also the "wing" surface, which encompasses the entire wing.

4. Mesh Construction

To create the 3D mesh, similar to the 2D analysis, the options of polyhedral meshing and prismatic meshing have been chosen to analyze the area closest to the wing's surface.

In this case, after conducting several tests, the following parameters have been selected to obtain a fine enough mesh for representative results:

- Base size = 0.1m
- Number of prism layers = 25
- Prism layer stretching = 1.1
- Prism layer thickness = 0.00121m
- Surface growth rate = 1.05
- Surface mínimum size = 25%
- Surface target size = 75%
- Surface size = 20%
- Attack volumetric control Surface size = 0.0025m
- Exit volumetric control Surface size = 0.0075m

In contrast to the 2D analysis, here the control volume has been increased from 5% to 20% due to the significant computational cost of this study. This change may imply that the wing geometry is not defined in sufficient detail. Therefore, in addition to the control volume covering the area, three others will be used to accurately define the leading edge, the trailing edge, and the wingtip, as shown in **Figure 6.36**. All of them are cylinders with a diameter of 0.2m.

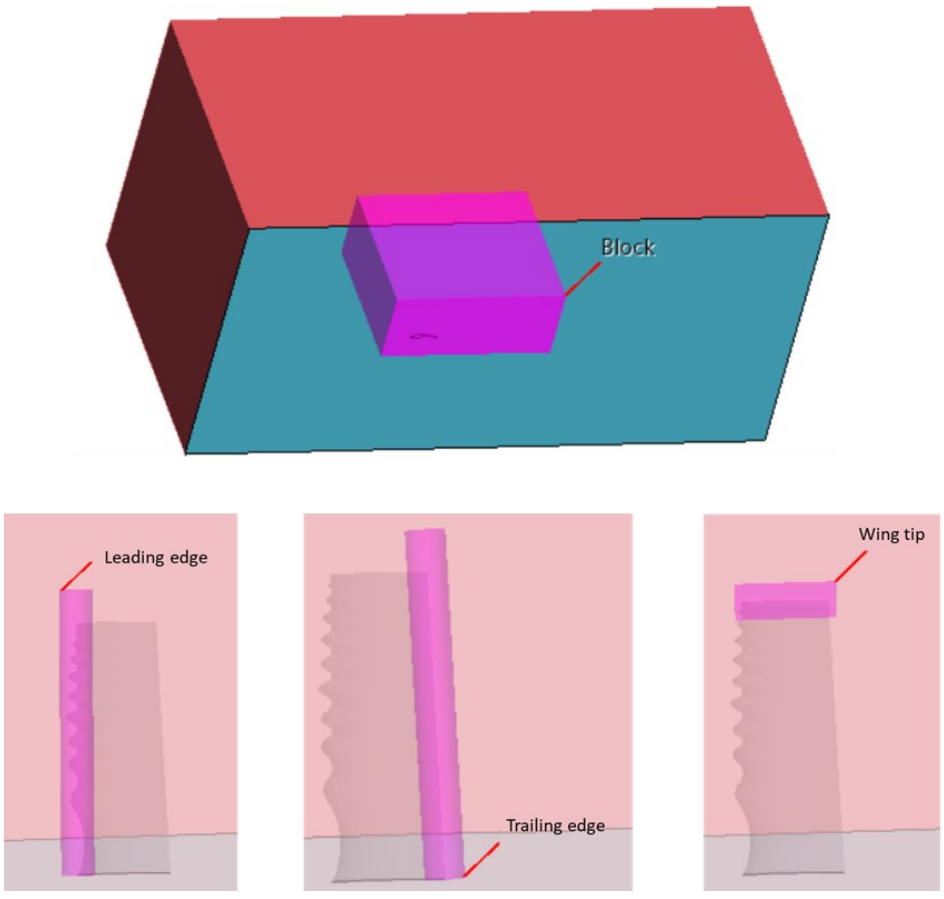

***Figure 6.36**. Definition of control volumes for meshing.*

With the selected parameters and control volumes, the mesh appears as shown in **Figure 6.37**. It should be fine enough to capture the most relevant phenomena for this study.

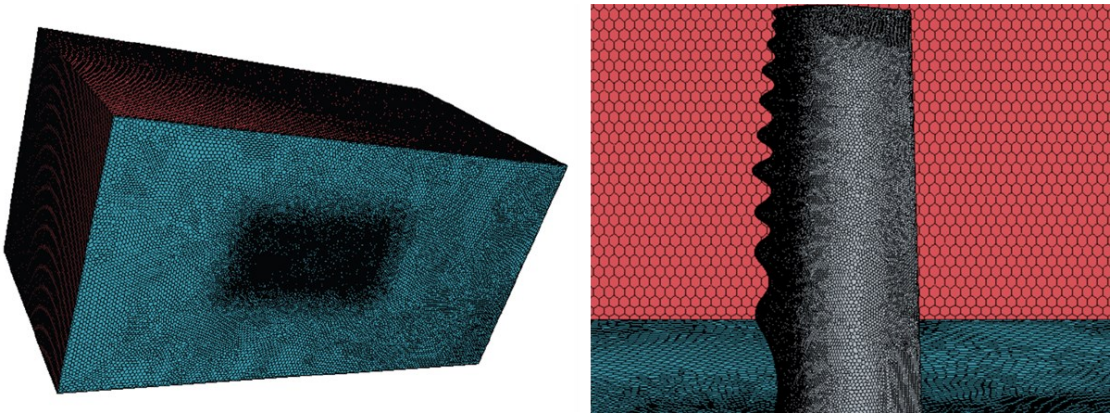

Figure 6.37*. Meshed 3D block defining the whole domain (**left**). Detailed view of element distribution of the wing model (**right**).*

5. Selection of Model Physics

To carry out the simulation, it is necessary to define which physics will govern our results. The following physics have been defined for the study analyzed here:

These are the physics that rule the problem here analyzed:

- Space: three dimensions
- Time: steady
- Material: Gas
- Flow: Segregated flow
- State equation: Constant density
- Viscous regime: Turbulent
- Average Reynolds turbulence: K-ω turbulent
- Transition: Gamma Transition

Results analysis

After setting up the problem in Simcenter STAR-CCM+, the analysis is initiated, and results are awaited to converge. Subsequently, it's essential to ensure that the mesh looks reasonable, and the results in scenes and plots appear to make sense. This means that based on the results seen in the scenes, it can be confirmed that the aerodynamic laws that were anticipated are being upheld. To do this, one can review the velocity and pressure scenes, **Figure 6.38** and **Figure 6.39**, respectively.

In the velocity diagrams, it can be observed that along the wing's surface, the fluid velocity is zero, which is an important detail indicating no boundary layer separation has occurred. Additionally, in the cross-sectional view, it can be seen that the fluid velocity is lower on the lower side of the profile and higher on the upper side, thus confirming the Venturi effect as previously explained.

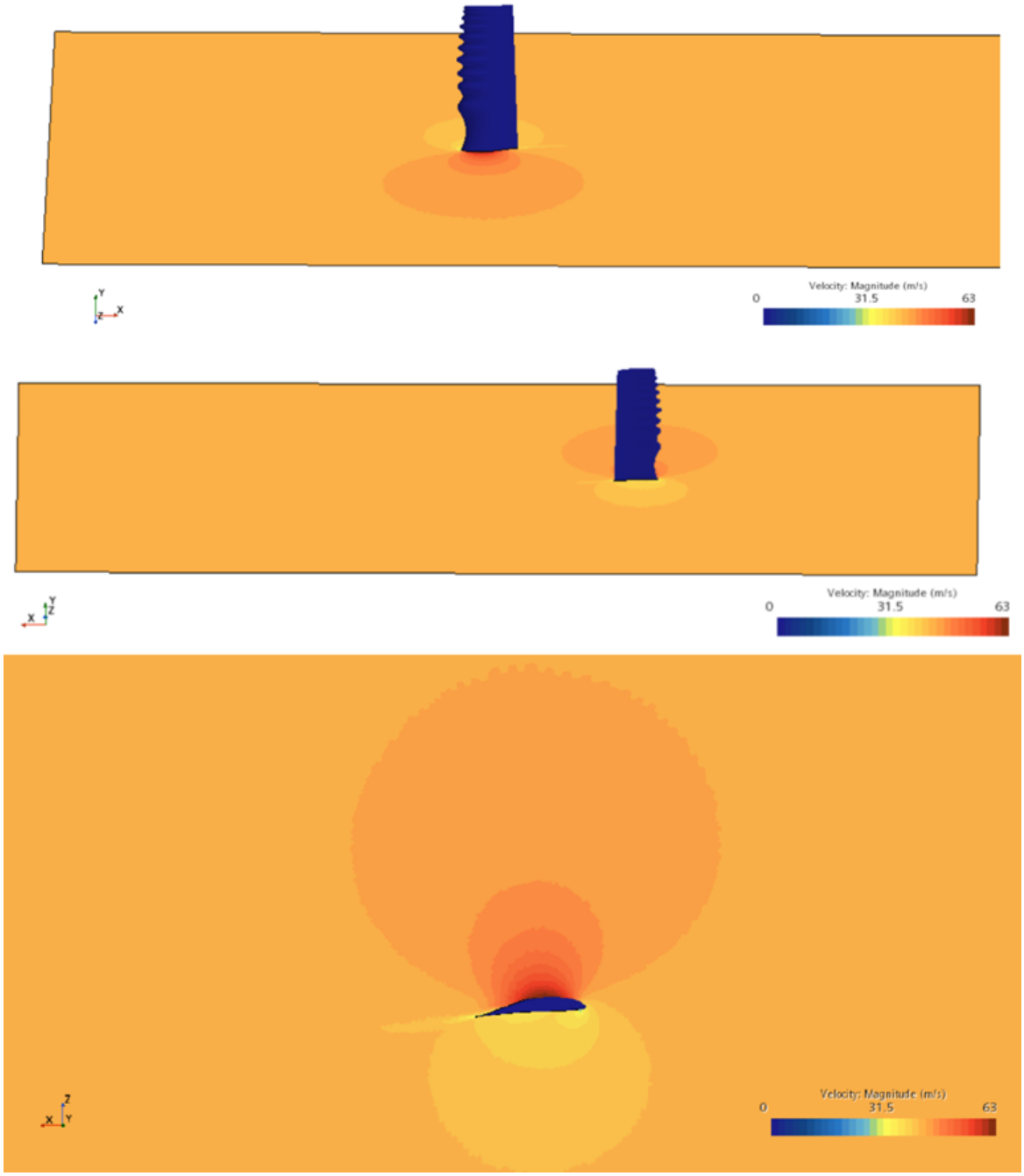

***Figure 6.38**. Velocity magnitude distribution around the 3D wing model with tubercles (side and top views).*

In the pressure diagrams, it can be verified the pressure difference between the lower and upper surfaces. Since you are referring to manometric pressure, all pressures appearing as negative values are those below 1 atm.

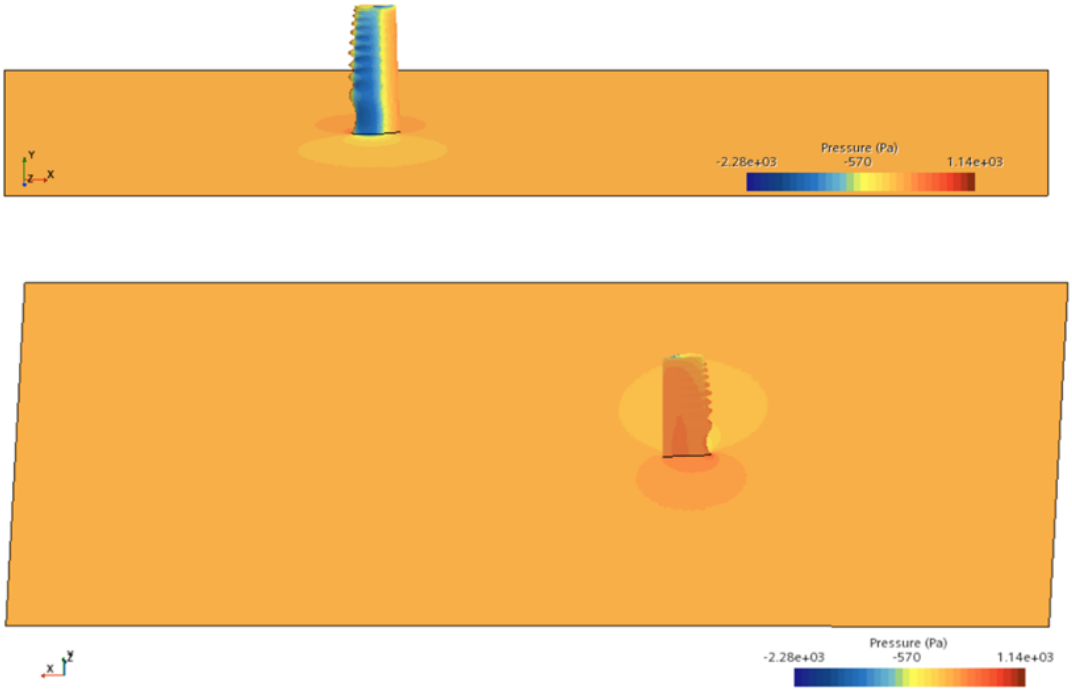

***Figure 6.39**. Pressure distribution around the 3D wing model with tubercles (side and top views).*

Once it's confirmed that the physics occurring around the profile seem to be correct, the next step is to examine the values of the aerodynamic coefficients, aerodynamic forces, and aerodynamic efficiency to choose between the previously selected profiles. For this purpose, the following tables display the results of the simulations with the mentioned physics for angles of attack ranging from 0° to 5°.

***Table 6-8**. Results of 3D analysis for Albatross airfoil wing with chord diminution.*

ALBATROSS CHORD DIMINUTION

A(°)	C_L	C_D	C_L/C_D	Lift (N)	Drag (N)	Lift/Drag
0	0,55517	0,02412	23,02	342,31	14,87	23,02
1	0,66410	0,02825	23,51	409,48	17,42	23,51
2	0,77410	0,03384	22,88	477,30	20,86	22,88
3	0,88604	0,04081	21,71	546,32	25,16	21,71
4	0,99192	0,04860	20,41	611,60	29,97	20,41
5	1,09755	0,05680	19,32	676,73	35,05	19,31

***Table 6-9**. Results of 3D analysis for Albatross airfoil wing with chord diminution and humpback whale tubercles.*

ALBATROSS CHORD DIMINUTION + WHALE

A(°)	C_L	C_D	C_L/C_D	Lift (N)	Drag (N)	Lift/Drag
0	0,56245	0,02597	21,66	346,80	16,01	21,66
1	0,67259	0,02956	22,75	414,71	18,22	22,76
2	0,78075	0,03468	22,51	481,40	21,38	22,52
3	0,8923	0,04141	21,55	550,18	25,53	21,55
4	1,00111	0,04950	20,22	617,27	30,52	20,23
5	1,11200	0,05858	18,98	685,66	36,12	18,98

***Table 6-10**. Results of 3D analysis for DAE-11 airfoil wing with chord diminution.*

DAE-11 CHORD DIMINUTION

A(°)	C_L	C_D	C_L/C_D	Lift (N)	Drag (N)	Lift/Drag
0	0,63786	0,02826	22,57	393,29	17,42	22,58
1	0,74983	0,03337	22,47	462,34	20,58	22,47
2	0,85988	0,03942	21,81	530,19	24,31	21,81
3	0,97273	0,04677	20,80	599,77	28,84	20,80
4	1,08380	0,05552	19,52	668,29	34,24	19,52
5	1,19143	0,06617	18,01	734,62	40,8	18,01

***Table 6-11**. Results of 3D analysis for DAE-11 airfoil wing with chord diminution and humpback whale tubercles.*

DAE-11 CHORD DISMINUTION + WHALE

A(°)	C_L	C_D	C_L/C_D	Lift (N)	Drag (N)	Lift/Drag
0	0,64546	0,02910	22,18	397,98	17,94	22,18
1	0,75846	0,03397	22,33	467,65	20,94	22,33
2	0,86905	0,04027	21,58	535,84	24,83	21,58
3	0,98191	0,04845	20,27	605,43	29,87	20,27
4	1,09320	0,05752	19,01	674,07	35,46	19,01
5	1,20520	0,06752	17,85	743,11	41,63	17,85

***Table 6-12**. Results of 3D analysis for DAE-11 airfoil wing with chord diminution and swept wings.*

DAE-11+CHORD DISMINUTION+ARROW

A(°)	C_L	C_D	C_L/C_D	Lift (N)	Drag (N)	Lift/Drag
0	0,63703	0,02827	22,53	392,78	17,43	22,53
1	0,74855	0,03334	22,45	461,55	20,56	22,45
2	0,85954	0,03943	21,80	529,98	24,31	21,80
3	0,97092	0,04704	20,64	598,66	29	20,64
4	1,08036	0,05619	19,23	666,14	34,65	19,22
5	1,19386	0,06608	18,07	736,12	40,74	18,07

***Table 6-13**. Results of 3D analysis for DAE-11 airfoil wing with chord diminution, humpback whale tubercles and swept wings.*

DAE-11+CHORD DISMINUTION+ARROW+WHALE

A(°)	C_L	C_D	C_L/C_D	Lift (N)	Drag (N)	Lift/Drag
0	0,64496	0,02884	22,36	397,67	17,78	22,37
1	0,75730	0,03398	22,29	466,94	20,95	22,29
2	0,86945	0,04059	21,42	536,09	25,02	21,43
3	0,98077	0,04867	20,15	604,73	30	20,16
4	1,09093	0,05792	18,83	672,66	35,71	18,84
5	1,20244	0,06813	17,65	741,41	42,01	17,65

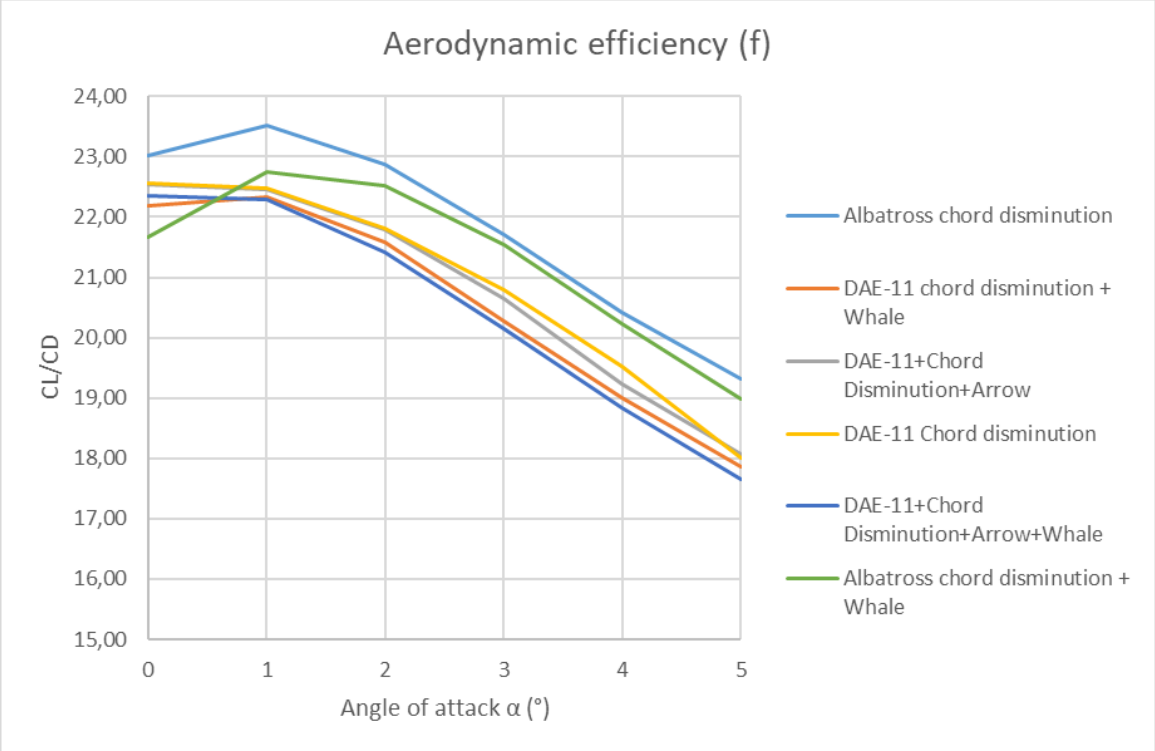

***Figure 6.40**. Aerodynamic efficiency (CL/CD) of various wing configurations of the 3D analysis at different angles of attack*

The examination of aerodynamic efficiency revealed unexpected results. Despite prior expectations based on the 2D analysis, it was the albatross profile that demonstrated superior performance in terms of maximum efficiency and overall effectiveness within the 0° to 5° angle of attack range. A comparison between the efficiency values of DAE-11 with chord reduction and

DAE-11 with chord reduction plus a 10° sweep highlighted the detrimental effect of adding sweep to the wing configuration in this Reynolds regime.

Turning attention to profiles featuring protuberances inspired by the humpback whale's pectoral fin, it became evident that these additions had a detrimental impact on aerodynamic efficiency. Nevertheless, closer examination of lift force values revealed that the protuberances were capable of increasing lift by generating depressions between them.

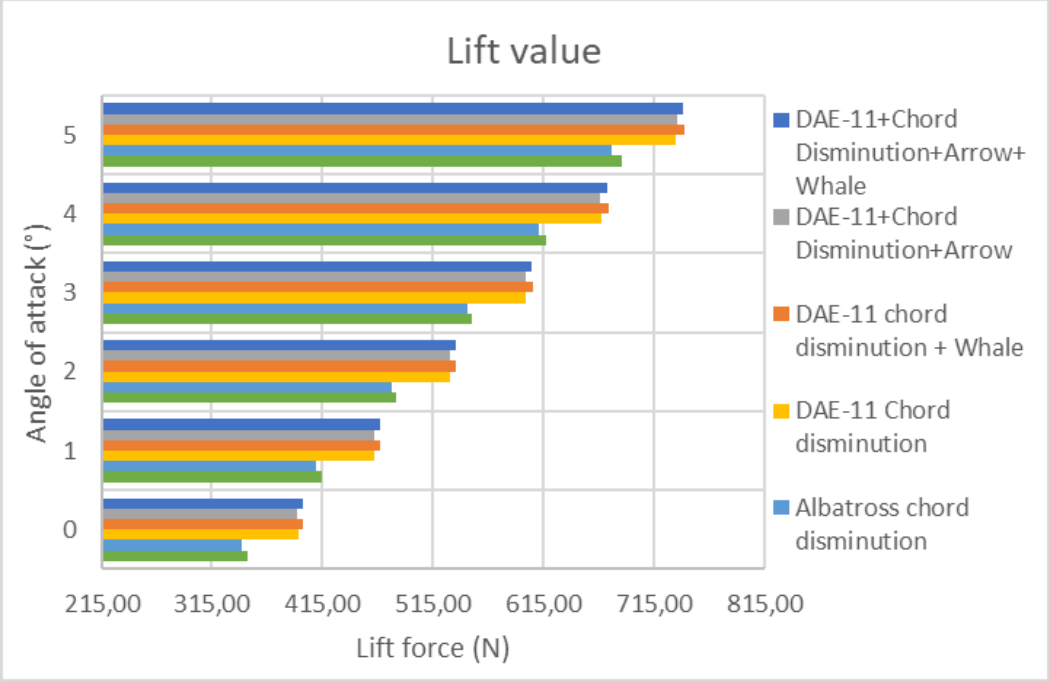

***Figure 6.41**. Lift force (N) for various wing configurations at different angles of attack (0° to 5°).*

Finally, after comparing all the configurations, it becomes evident that the best wing derived from this study is the one with only the chord change from the albatross profile.

6.6 Discussion

To draw conclusions from the entire aerodynamic study conducted throughout this chapter, it is necessary to summarize the results obtained in both the two-dimensional and three-dimensional analyses.

The 2D analysis serves to pre-select aerodynamic profiles for further study. As seen, the compared profiles in this initial phase have diverse shapes and characteristics, which can yield inconclusive results. In this case, both the reference profile DAE-11 and the bioinspired albatross profile appeared to offer the best performance in the range of 0° to 5° in the 2D analysis. However, it's important to note that these 2D analyses make certain assumptions, such as considering the wing as infinite and ignoring some turbulence phenomena that may affect the profile's performance in a more realistic setting. Nonetheless, this 2D analysis serves as a useful and computationally efficient method for pre-selecting aerodynamic profiles for a specific fluid

dynamic regime. It can be significantly faster, up to two orders of magnitude, compared to conducting a comprehensive 3D analysis.

Therefore, to obtain more realistic results, a three-dimensional study was conducted, revealing significant differences compared to the 2D analysis. Interestingly, the profile that performed exceptionally well in the 2D analysis turned out to be less efficient than the second-best profile in terms of aerodynamic efficiency in the 3D analysis. It's important to emphasize that this doesn't discredit the 2D analysis; rather, it serves as a cost-effective computational method for initial profile selection. Ideally, conducting 3D analyses for all profiles would be optimal. However, there's a trade-off between available resources and the desired results, leading to the decision to use 2D analysis as a preliminary screening method. As mentioned, the key differences between the results stem from the assumptions and simplifications inherent in 2D analyses.

Furthermore, in addition to the 3D analysis, it can be concluded that certain features like wing sweep, in the regimes expected for the studied aircraft, have an undesirable effect on wing performance. In fact, in both cases where wing sweep was applied, it was observed that aerodynamic efficiency decreased. This phenomenon has been well-documented throughout the history of aeronautics. The effect of wing sweep on the lift coefficient curve is to flatten the curve (reduce the slope), shifting the point of maximum lift to higher angles of attack. While this effect might not be desirable and is not evident in the current study, it can be observed in the provided **Figure 6.42**.

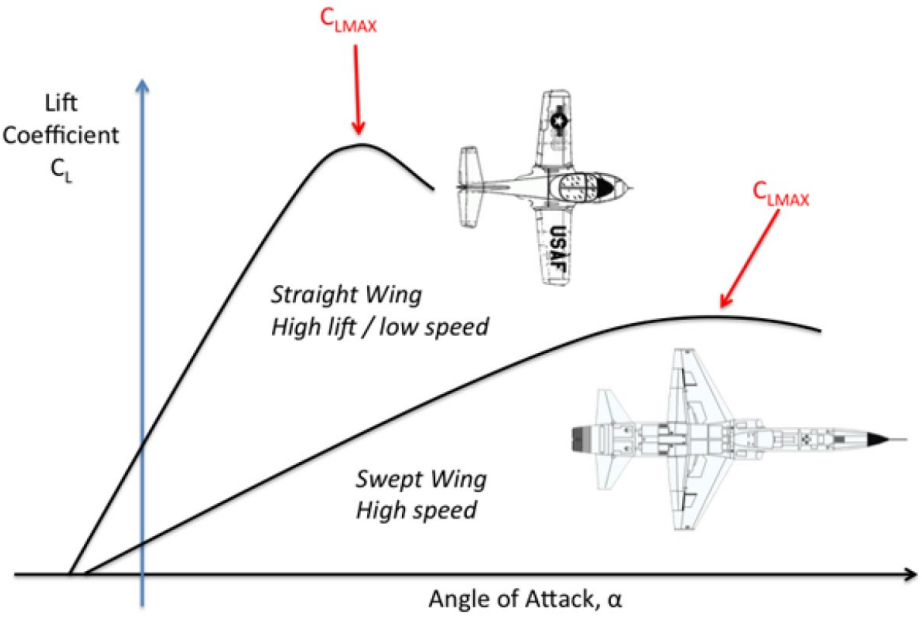

***Figure 6.42**. Comparison of lift coefficients* [39].

From the 3D study, certain conclusions can be drawn regarding the use of bioinspired humpback whale flipper-like protrusions on wing surfaces. When analyzing the two studied profiles in terms of aerodynamic efficiency, it becomes evident that these protrusions are clearly less efficient compared to smooth wings. However, when considering the lift values generated by each type of

wing, it is apparent that wings with humpback whale-inspired protrusions are capable of generating greater lift. It's important to note that, in this study, the geometry of the protrusions was not optimized to reduce aerodynamic drag and thereby improve efficiency compared to smooth wings due to time and resource constraints.

The increase in lift can be attributed to the more pronounced depressions generated on the upper surface of the wing with these protrusions as seen in **Figure 6.43**. The zero-reference value is not relevant; what matters is the magnitude of the depression or the higher pressure generated on each face of the wing, in terms of depression areas and maximum values observed in key areas. These deformations at the leading edge generate vorticity, creating depressions in areas where there are no protrusions, resulting in greater lift forces.

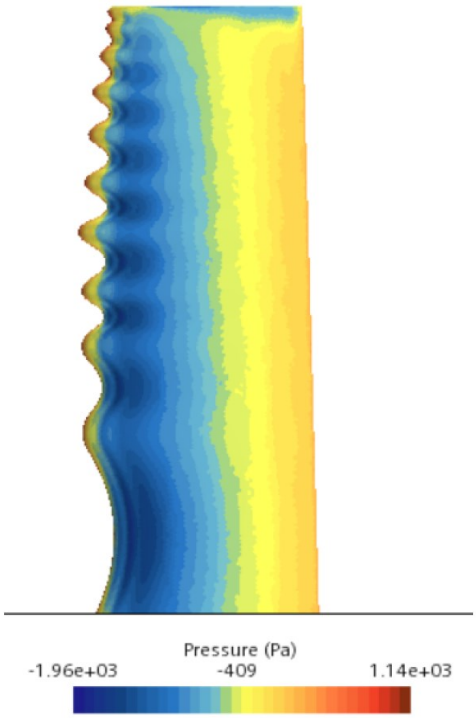

***Figure 6.43**. Pressure distribution around a 3D wing model with tubercles.*

It is important to note that, in this case, the wings are not the primary mechanism of flight but rather serve as a means to enhance lift. It would be interesting to study whether this additional lift can have a positive impact on the overall performance of the aircraft during flight.

6.7 Conclusions

The application of bioinspired design techniques has demonstrated potential beyond the specific cases discussed in this manuscript. These techniques can be effectively applied to different physical phenomena, expanding their utility and impact across various fields of study. This suggests a broad applicability of bioinspired principles, which could inspire innovative solutions in diverse engineering challenges.

However, the study has certain limitations that must be addressed in future research. Notably, the experimental validation of the most promising results using wind tunnel testing is still pending. This gap is primarily due to limited resources and the inherent complexity of such experimental setups. Addressing this will be crucial for verifying the theoretical and computational findings presented.

This study also opens avenues for further exploration, such as optimizing tubercles inspired by humpback whale fins for specific flow regimes. Additionally, exploring the performance of the proposed aerodynamic profiles across different flight regimes could yield valuable insights. These efforts could enhance the applicability and efficiency of bioinspired designs in practical scenarios.

Looking ahead, the future of bioinspired design studies should focus on translating theoretical and computational advancements into real-world applications. One promising direction is the development of reconfigurable and mobile profiles that adapt dynamically to changing flight or swimming conditions, akin to the natural adaptations seen in birds, insects, and certain marine animals. Such innovations could significantly enhance the performance and versatility of engineered systems, paving the way for more efficient and adaptable designs.

6.8 References

[1] "El-consumo-de-gas-en-la-segunda-capa-de-Ethereum-registra-nuevo-maximo-historico.webp (1147×760)." Accessed: Jul. 06, 2024. [Online]. Available: https://news.bit2me.com/wp-content/uploads/2022/11/El-consumo-de-gas-en-la-segunda-capa-de-Ethereum-registra-nuevo-maximo-historico.webp

[2] "zeppelin-NT-flying.jpg (720×360)." Accessed: Jul. 06, 2024. [Online]. Available: https://i0.wp.com/imgs.hipertextual.com/wp-content/uploads/2016/12/zeppelin-NT-flying.jpg?w=720&quality=55&strip=all&ssl=1

[3] "416890735_768650908630520_4032641815426286389_n.jpg (721×540)." Accessed: Jul. 06, 2024. [Online]. Available: https://scontent-mad1-1.xx.fbcdn.net/v/t39.30808-6/416890735_768650908630520_4032641815426286389_n.jpg?_nc_cat=107&ccb=1-7&_nc_sid=6ee11a&_nc_ohc=34hdrICeiCwQ7kNvgG84pqp&_nc_ht=scontent-mad1-1.xx&oh=00_AYAAWbI9GTqu_wUU5RsmUTk-95eExoTFkV-_GVcAF6W9aQ&oe=668F5615

[4] "20201027_134928-scaled.jpg (2560×1440)." Accessed: Jul. 06, 2024. [Online]. Available: https://aerotechnics.fr/wp-content/uploads/2021/06/20201027_134928-scaled.jpg

[5] "1610889694908Ala-delta-Mendoza2-e1646419473504.jpg (500×375)." Accessed: Jul. 06, 2024. [Online]. Available: https://www.hobbyaficion.com/wp-content/uploads/2022/03/1610889694908Ala-delta-Mendoza2-e1646419473504.jpg

[6] "flyparapente-vuelo-bautismo-05.jpg (850×755)." Accessed: Jul. 06, 2024. [Online]. Available: https://vuelaenparapente.es/wp-content/uploads/2022/02/flyparapente-vuelo-bautismo-05.jpg

[7] "eden6-paramotor-01.jpg (1920×1280)." Accessed: Jul. 06, 2024. [Online]. Available: https://www.macpara.com/media/1607/eden6-paramotor-01.jpg?center=0.4875,0.54666666666666663&mode=crop&width=1920&height=1280&rnd=131947021320000000

[8] "Matthew Field Photography." Accessed: Jul. 06, 2024. [Online]. Available: https://www.mattfield.com/

[9] "Cierva_C.6,_Madrid_2.jpg (567×425)." Accessed: Jul. 06, 2024. [Online]. Available: https://upload.wikimedia.org/wikipedia/commons/c/ca/Cierva_C.6%2C_Madrid_2.jpg

[10] "1280px-SFF_002-1055526_Fairey_Rotodyne.jpg (1280×826)." Accessed: Jul. 06, 2024. [Online]. Available: https://upload.wikimedia.org/wikipedia/commons/thumb/c/cc/SFF_002-1055526_Fairey_Rotodyne.jpg/1280px-SFF_002-1055526_Fairey_Rotodyne.jpg

[11] "An_MV-22_Osprey_prepares_to_land_USS_Iwo_Jima.jpg (2073×1327)." Accessed: Jul. 06, 2024. [Online]. Available: https://upload.wikimedia.org/wikipedia/commons/7/7c/An_MV-22_Osprey_prepares_to_land_USS_Iwo_Jima.jpg

[12] J. J. Socha, F. Jafari, Y. Munk, and G. Byrnes, "How animals glide: from trajectory to morphology1," *https://doi.org/10.1139/cjz-2014-0013*, vol. 93, no. 12, pp. 901–924, Oct. 2015, doi: 10.1139/CJZ-2014-0013.

[13] "The salamander that can parachute from atop the world's tallest trees," *Nature*, vol. 606, no. 7912, pp. 11–11, Jun. 2022, doi: 10.1038/D41586-022-01449-W.

[14] M. Penn, G. Yi, S. Watkins, M. Martinez Groves-Raines, S. P. Windsor, and A. Mohamed, "A method for continuous study of soaring and windhovering birds," *Scientific Reports 2022 12:1*, vol. 12, no. 1, pp. 1–9, Apr. 2022, doi: 10.1038/s41598-022-10359-w.

[15] "large.jpeg (1024×682)." Accessed: Jul. 06, 2024. [Online]. Available: https://inaturalist-open-data.s3.amazonaws.com/photos/221486197/large.jpeg

[16] "Vertebrate Flight: Introduction." Accessed: Jul. 06, 2024. [Online]. Available: https://ucmp.berkeley.edu/vertebrates/flight/flightintro.html

[17] P. J. Pritchard, *Fox and mcdonald's introduction to fluid mechanics.* John Wiley, 2015. Accessed: Jul. 06, 2024. [Online]. Available: https://books.google.com/books/about/Fox_and_McDonald_s_Introduction_to_Fluid.html?hl=es&id=2gFhBgAAQBAJ

[18] M. D'Ambrosio and M. Medaglia, "Vertical Axis Wind Turbines: History, Technology and Applications," 2010.

[19] "Laminar Flow and Turbulent Flow - The Constructor." Accessed: Jul. 06, 2024. [Online]. Available: https://theconstructor.org/fluid-mechanics/laminar-turbulent-flow/559432/

[20] "Boundary Layer Separation and Pressure Drag | Aerospace Engineering Blog." Accessed: Jul. 06, 2024. [Online]. Available: https://aerospaceengineeringblog.com/boundary-layer-separation-and-pressure-drag/

[21] "Turbulence Models: Which Should I Select? | SimScale." Accessed: Jul. 06, 2024. [Online]. Available: https://www.simscale.com/blog/turbulence-cfd-analysis/

[22] "(PDF) Winglet Design for a Fairchild Merlin III using CFD Analysis." Accessed: Jul. 06, 2024. [Online]. Available: https://www.researchgate.net/publication/279884127_Winglet_Design_for_a_Fairchild_Merlin_III_using_CFD_Analysis

[23] Y. Guo, C. Yang, Y. Wang, T. Lv, and S. Zhao, "Study on Inlet Flow Field Structure and End-Wall Effect of Axial Flow Pump Impeller under Design Condition," *Energies 2022, Vol. 15, Page 4969*, vol. 15, no. 14, p. 4969, Jul. 2022, doi: 10.3390/EN15144969.

[24] N. Ali, M. R. Komol, and M. T. Saki, "Study on Thin Airfoil Theory & Performance Test of Elliptical Wing as Compared to Model Mosquito Wing and NACA 64A012 Mod Airfoil," *European Journal of Engineering Research and Science*, vol. 3, no. 4, p. 48, Apr. 2018, doi: 10.24018/EJERS.2018.3.4.665.

[25] S. A. Rauscher, T. D. Ringler, W. C. Skamarock, and A. A. Mirin, "Exploring a global multiresolution modeling approach using aquaplanet simulations*," *J Clim*, vol. 26, no. 8, pp. 2432–2452, 2013, doi: 10.1175/JCLI-D-12-00154.1.

[26] M. Bennaceur, R. Delmas, and Y. Hamadi, "Passenger-centric Urban Air Mobility: Fairness trade-offs and operational efficiency," *Transp Res Part C Emerg Technol*, vol. 136, p. 103519, Mar. 2022, doi: 10.1016/J.TRC.2021.103519.

[27] "Scaling Advanced Air Mobility: Beyond Flying Cars and Drones | Cleantech Group." Accessed: Jul. 06, 2024. [Online]. Available: https://www.cleantech.com/scaling-advanced-air-mobility-beyond-flying-cars-and-drones/

[28] "Air - Density and Specific Volume vs. Altitude." Accessed: Jul. 06, 2024. [Online]. Available: https://www.engineeringtoolbox.com/air-altitude-density-volume-d_195.html

[29] "Viscosity - Absolute (Dynamic) vs. Kinematic." Accessed: Jul. 06, 2024. [Online]. Available: https://www.engineeringtoolbox.com/dynamic-absolute-kinematic-viscosity-d_412.html

[30] B. Vanderhoydonck, G. Santo, J. Vierendeels, and J. Degroote, "Optimization of a Human-Powered Aircraft Using Fluid–Structure Interaction Simulations," *Aerospace 2016, Vol. 3, Page 26*, vol. 3, no. 3, p. 26, Aug. 2016, doi: 10.3390/AEROSPACE3030026.

[31] "Airfoil Tools." Accessed: Jul. 06, 2024. [Online]. Available: http://www.airfoiltools.com/

[32] S. Klän, T. Bachmann, M. Klaas, H. Wagner, and W. Schröder, "Experimental analysis of the flow field over a novel owl based airfoil," *Exp Fluids*, vol. 46, no. 5, pp. 975–989, May 2009, doi: 10.1007/S00348-008-0600-7/METRICS.

[33] T. G. Lang, "Hydrodynamic Analysis of Dolphin Fin Profiles," *Nature 1966 209:5028*, vol. 209, no. 5028, pp. 1110–1111, 1966, doi: 10.1038/2091110a0.

[34] S. Kilimtzidis and V. Kostopoulos, "Multidisciplinary structural optimization of novel high-aspect ratio composite aircraft wings," *Structural and Multidisciplinary Optimization*, vol. 66, no. 7, pp. 1–23, Jul. 2023, doi: 10.1007/S00158-023-03600-1/FIGURES/21.

[35] E. L. Houghton, P. W. Carpenter, S. H. Collicott, and D. T. Valentine, “Wing Theory,” in *Aerodynamics for Engineering Students*, Elsevier, 2017, pp. 449–523. doi: 10.1016/b978-0-08-100194-3.00007-9.

[36] G. Sachs *et al.*, “Flying at No Mechanical Energy Cost: Disclosing the Secret of Wandering Albatrosses,” *PLoS One*, vol. 7, no. 9, Sep. 2012, doi: 10.1371/JOURNAL.PONE.0041449.

[37] “Alsomitra_macrocarpa_seed_(syn._Zanonia_macrocarpa).jpg (3940×2620).” Accessed: Jul. 06, 2024. [Online]. Available: https://upload.wikimedia.org/wikipedia/commons/c/cd/Alsomitra_macrocarpa_seed_%28syn._Zanonia_macrocarpa%29.jpg

[38] F. E. Fish, P. W. Weber, M. M. Murray, and L. E. Howle, “The Tubercles on Humpback Whales’ Flippers: Application of Bio-Inspired Technology,” *Integr Comp Biol*, vol. 51, no. 1, pp. 203–213, Jul. 2011, doi: 10.1093/ICB/ICR016.

[39] “wing_sweep_effect_on_lift_curves.jpg (2648×1834).” Accessed: Jul. 06, 2024. [Online]. Available: https://code7700.com/images/aero/wing_sweep_effect_on_lift_curves.jpg

Chapter 7: Computer aided system for casting design (eCAST)

7.1 Introduction

The casting process is one of the oldest metal fabrication techniques in human history. As knowledge about its use improved, early metal tools began to be constructed. The discovery that metals could be melted and poured into molds allowed the creation of tools in desired shapes without the need for excessive mechanical energy, as required by forging. This capability also enabled the alloying of different metals to combine their strengths in a single material.

However, the process of pouring molten metal into a mold has some limitations. Healthy cast parts could not be too massive or have very small sections, as this could result in internal bubbles or incomplete mold filling. Various defects could arise, the causes of which were not fully understood. It was not until the Industrial Revolution that the design of metal casting began to develop systematically, incorporating elements such as gating systems, vent channels, and risers, among others.

Historically, casting design has relied heavily on the expertise of experienced individuals, making it more of a craft than a science. As the scientific method advanced and casting components required stricter standards, the first rules for improving the quality of cast parts were defined. Despite this, casting design still largely depends on experts, even with the availability of software that simulates metal flow and solidification. Additionally, the rules defined are often ambiguous or inconsistent across different manuals and books.

Following the discussion throughout this manuscript, incorporating a section into the bio-inspired design algorithm that guides casting design could be highly valuable to the industry. Engineers are increasingly required to align their digital designs with manufacturing processes, yet many may not be familiar with the specificities of each process. As mentioned, casting is a science in itself. The complexity and input required from the designer to create each element necessary for the casting process pose challenges to its automation.

Nevertheless, advancements have been made in creating various models with varying degrees of efficiency for the optimal design of risers, as seen in the work of Tiryakoglu et al. [1]. There are also studies discussing the optimization of gating systems and the placement of risers [2].

This chapter aims to develop a computational tool that guides the casting design of parts in a digital environment from the conception phase, an approach similar to what He et al. [2] presented. However, in this case all would be performed inside a unique tool. Utilizing Synera's capabilities to connect various CAD-CAE-CAM engineering tools and create parameterized design algorithms, along with the ability to develop new "nodes" on the platform, the plan is to create a

tool within the software. Initially, this tool will dimension risers based on traditional casting criteria and then analyze the results by connecting to the ProCast casting simulation software by ESI Group. This approach aims to take the first steps toward developing a tool capable of designing for different types of metal alloys, casting processes, and mold materials, optimizing the necessary elements for casting and minimizing material waste due to oversized components. This will support casting knowledge for designers who may not necessarily be familiar with its intricacies.

7.2 Theoretical framework

The casting process involves transforming solid metals into liquids through the application of heat. This liquid metal is then poured into a mold shaped like the desired object. Once the metal cools and solidifies, the mold is removed to obtain the final product. The fundamental principles of the casting process include:

1. **Melting:** The initial stage of the casting process begins with loading the solid metal into a furnace suitable for the specific type of metal and the required melting method. Once loaded, the furnace is ignited, and the metal is gradually heated to ensure uniform melting.

   Understanding the metal's phase diagram at this stage is crucial, as it provides information on the solidus and liquidus temperatures. The solidus temperature is the point at which the metal begins to melt (577°C for an aluminum-silicon alloy with 1.65 wt. % silicon), while the liquidus temperature is where the metal is entirely in a liquid state (655°C for the same aluminum-silicon alloy), as illustrated in **Figure 7.1**. This knowledge allows precise control and adjustment of the furnace temperature.

   As the metal's temperature reaches and surpasses the solidus point, the solid material starts to melt. The heating process continues until the liquidus temperature is reached, and all the material has completely melted.

   During melting, gases and oxides may form in the liquid metal. These gases must be removed through degassing to prevent the formation of bubbles that could compromise the metal's integrity when poured into the mold. The removal of oxides is also essential to maintain the purity and quality of the molten metal [3].

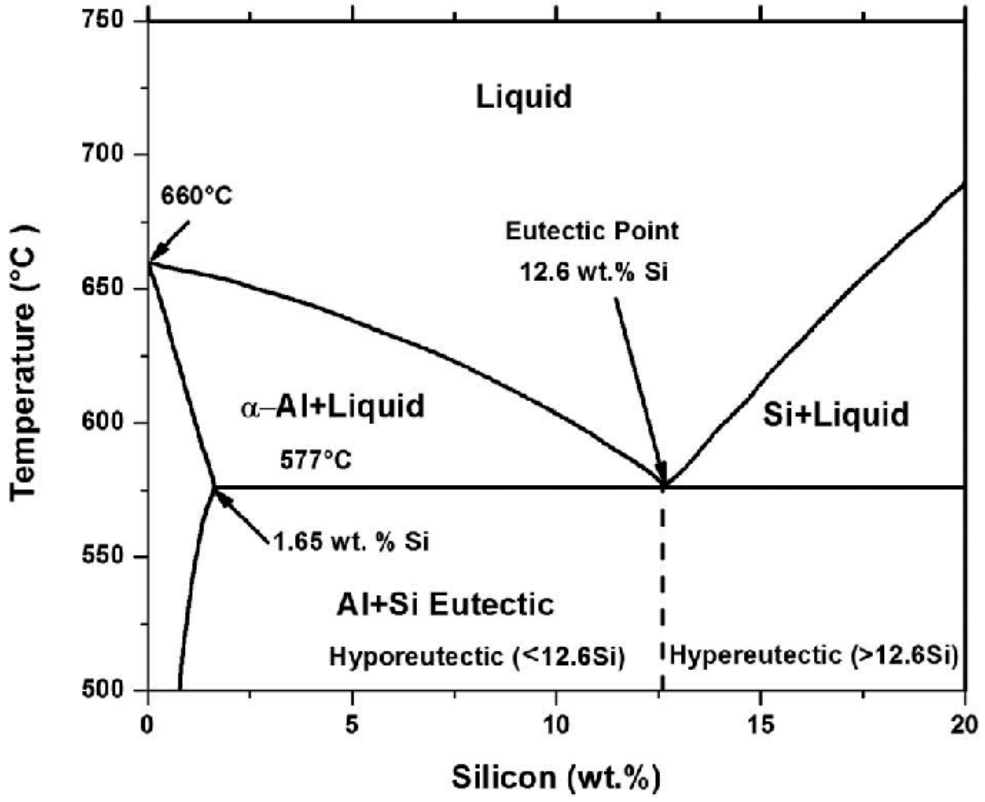

***Figure 7.1**. Phase diagram for aluminum-silicon alloys* [4]

2. **Molding**: Once the metal has been completely melted, the next stage of the casting process is molding. In this phase, the liquid metal is poured into a mold that defines the shape of the desired object. The preparation, handling, and design of the mold or its cavity are crucial to ensuring that the final product has precise dimensions and the required mechanical properties.

   Before pouring the metal, it is essential to prepare the mold adequately. Depending on the type of metal and the complexity of the piece, different types of molds are selected, such as sand molds for large and complex pieces, lost wax molds for high precision and permanent molds for mass production. The mold cavity design must consider the metal's shrinkage upon cooling and ensure proper liquid metal flow. Feeding channels and vents are designed to allow metal entry and the exit of air and gases.

   An internal coating can be applied to the mold to improve the surface finish of the piece and facilitate extraction. In some cases, the mold is preheated to prevent excessively rapid cooling of the metal. With the mold prepared, the next step is to pour the liquid metal. Maintaining the metal at the proper temperature during pouring is crucial to ensure uniform flow and avoid premature solidification. The metal can be poured by gravity, pressure, or vacuum, depending on the type of casting and the metal used. The pouring method must be controlled to avoid turbulence that could introduce inclusions and defects in the final piece [3].

The liquid metal must fill the mold cavity uniformly and completely. The feeding channels and vents allow for continuous flow and evacuation of air and gases.

3. **Solidification**: After the liquid metal has been poured into the mold, the solidification stage begins. This process is crucial for determining the microstructure and mechanical properties of the cast part as can be seen in **Figure 7.2**. Cooling must be carefully studied or controlled. The cooling rate needs to be appropriate to avoid internal stresses, cracks, and other defects. Too rapid cooling can cause fractures or incomplete filling of the mold, while too slow cooling can result in an undesirable grain structure. Ensuring the piece cools uniformly is essential to prevent distortions. This may involve using insulating materials or controlling the ambient temperature around the mold. Additionally, directing solidification through elements such as risers or chillers is important [3].

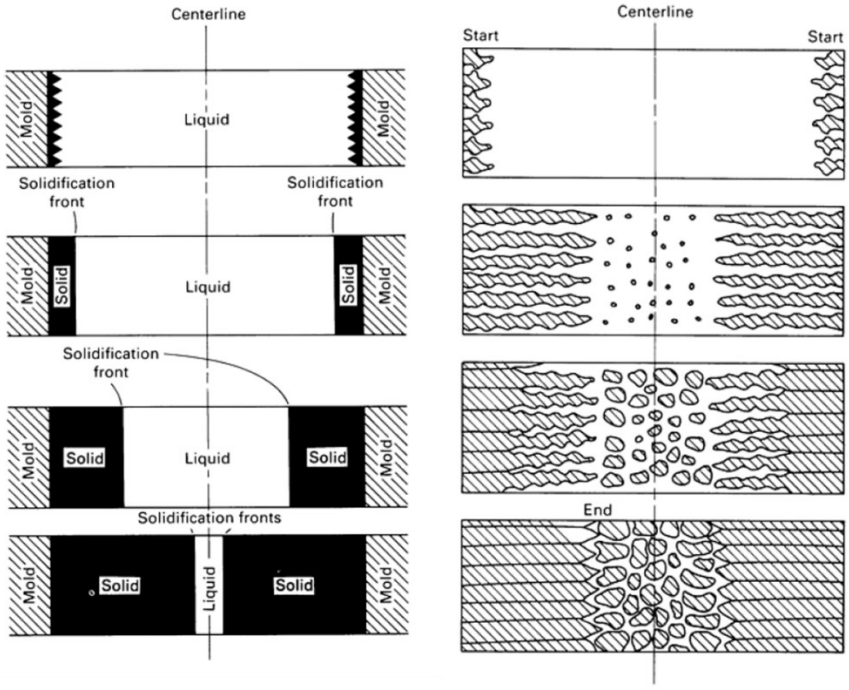

***Figure 7.2**. Schematic of mode of freezing in pure metals. Crystallization begins at the mold wall and advances into the casting interior on a plane solidification front (**left**). Schematic of intermediate mode of freezing having a moderate freezing range (**right**)* [3].

4. **Demolding**: Once the metal has completely solidified, the final stage of the casting process is demolding. This step involves extracting the cast piece from the mold and performing any necessary additional processing. Depending on the type of mold, demolding may involve breaking a sand mold or opening a permanent mold. It is crucial to perform this operation carefully to avoid damaging the piece.

   After extracting the piece from the mold, it must be cleaned to remove any residual mold material and other contaminants. This may involve using brushes, compressed air, or washing. Following demolding, additional processes are carried out to ensure the quality

of the piece. The piece undergoes visual inspection and non-destructive testing, such as radiography, ultrasonics, or dye penetrants, to detect surface and internal defects [3].

Rules for a good casting

To ensure that all phases of the casting process are successfully executed, various guidelines and manuals have been developed based on experimental data to determine the "optimal" procedures. To provide a comprehensive checklist and ensure the process runs smoothly, Campbell outlined 10 essential rules for effective casting in his book [5].

Rule 1: Start with a Good Melt

A high-quality melt is essential for producing defect-free castings. Prior to casting, the melt should be thoroughly prepared, checked, and treated to ensure it is substantially free from non-metallic inclusions and well degassed. The presence of impurities or gases can lead to inclusions and porosity, compromising the integrity of the final product [5].

Rule 2: Avoid Turbulent Entrainment of the Surface Film

During mold filling, it is crucial to avoid turbulence, which can entrap surface oxides within the metal. The metal front, or meniscus, should move smoothly and gradually, with a maximum velocity of approximately 0.5 m/s for most liquid metals. This reduces the risk of oxide films being folded into the metal, which can create weak spots [5].

Rule 3: Avoid Laminar Entrainment of the Surface Film

The advancing liquid metal front must not stop before the mold is completely filled. Stopping the metal flow can lead to the thickening of the surface film, which can then become entrapped. To maintain continuous movement, the metal should progress only in an upward direction, preventing the formation of defects associated with surface film incorporation [5].

Rule 4: Avoid Bubble Entrainment

Air bubbles introduced into the melt can cause significant defects. Properly designed pouring systems, such as offset step pouring basins and the use of ceramic filters, can help prevent bubbles from being entrained. Continuous pouring without interruptions is also crucial to avoid air entrapment [5].

Rule 5: Avoid Core Blows

Gases released from cores or molds during casting can lead to bubbles passing through the molten metal, causing defects. Cores should have low gas content and be adequately vented to prevent this issue. The use of impermeable repair pastes should be avoided to reduce the risk of core blows [5].

Rule 6: Avoid Shrinkage

Effective riser design and placement are critical to compensate for metal shrinkage during solidification. Feeding against gravity in larger sections is unreliable due to adverse pressure gradients. Following established feeding rules and using computer solidification models can ensure proper feeding design. Proper feeding design is essential to prevent shrinkage defects, which can compromise the structural integrity of the casting. Campbell's seven feeding rules are particularly crucial in this regard and will be elaborated below [5].

Rule 7: Avoid Convection

Convection currents within the molten metal can lead to defects if not properly managed. Assessing the freezing time relative to convection damage time is necessary. For intermediate sections, minimizing convective loops in the casting geometry or using rollover techniques after filling can mitigate these issues [5].

Rule 8: Reduce Segregation

Segregation, the uneven distribution of alloying elements, should be minimized to meet compositional specifications. Predicting segregation and avoiding conditions that promote channel segregation can help maintain the integrity of the casting [5].

Rule 9: Reduce Residual Stress

Residual stresses from quenching or cooling can lead to cracking or distortion. Avoiding quenching into water, especially for light alloys, and using polymer quenchants or controlled air quenching can reduce these stresses [5].

Rule 10: Provide Location Points

For dimensional accuracy and ease of machining, castings should have designated location points. These points should be agreed upon with quality auditors and machinists to ensure precise handling and further processing [5].

By following these ten rules, foundries can significantly improve the quality of their castings, reducing defects and enhancing mechanical properties. Given the objective of this manuscript chapter, particular emphasis will be placed on Rule 6, which focuses on avoiding shrinkage. Avoiding this phenomenon consists on designing a good feeding system. The most crucial component of the feeding system is the riser. The riser directs solidification by acting as a reservoir for molten metal, ensuring that porosity is concentrated within the riser itself, resulting in a sound casting.

According to Campbell, risers that are excessively small or slightly undersized can lead to significant porosity, as illustrated in **Figure 7.3**. While an oversized riser may produce slightly greater porosity than one correctly dimensioned, it does not typically result in critical porosity issues, leading to a tendency to oversize risers. However, from an ecological and economic

perspective, using excessively large risers is impractical. Therefore, proper sizing of these feeding elements is crucial for efficient and sustainable casting operations.

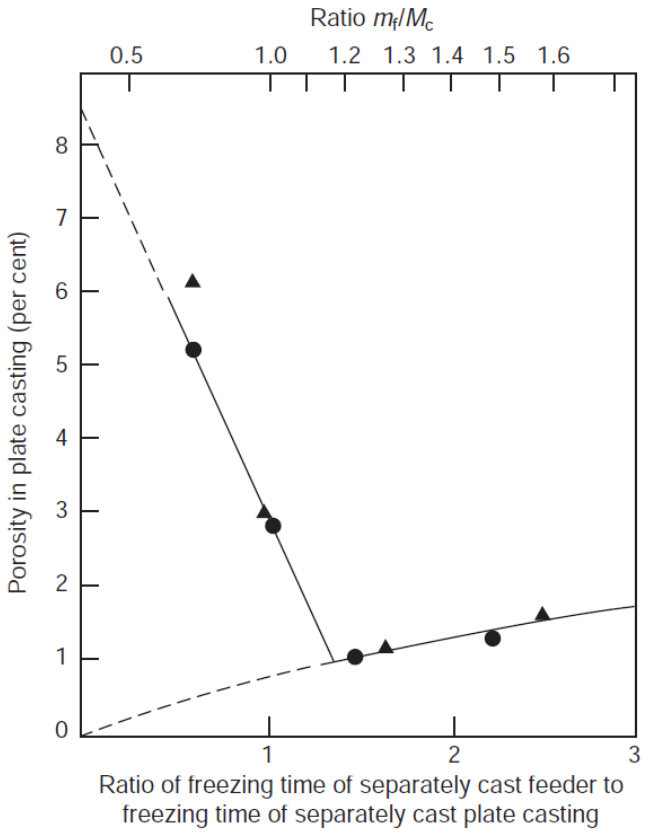

Figure 7.3. *Effect of increasing riser solidification time on the soundness of a Al-14Si alloy plate* [5].

Campbell for the Rule 6 of good casting rules, outlines seven specific feeding rules that are critical to avoid shrinkage porosity, ensuring the production of sound castings. These rules focus on the design and placement of risers to effectively feed the casting as it solidifies and contracts.

1. **Do not feed unless is necessary**. The first rule emphasizes that feeding should only be used when absolutely necessary. For example in thin-walled castings where solidification occur rapidly and even the filling system can provide extra feeding sometimes. It could also be avoided by the use of chills and cooling fins.
2. **Heat transfer requirement**. This rule involves ensuring that the riser solidifies after the casting section it feeds. Which can be defined with the Chvorinov's rule that has been studied along the manuscript. Having this in mind, the module of the riser should be defined as:

$$m_r > 1.2\, m_c \tag{1}$$

The modulus is defined as the ratio of volume to the surface area in contact with the mold, indicating the cooling rate of the section. The riser must have a higher

modulus to remain molten longer than the casting section, ensuring it can supply molten metal to compensate for shrinkage. The modulus of the riser can be artificially modified by using an insulating sleeve.

3. **Mass transfer (volume) requirement.** The riser must contain sufficient molten metal to compensate for the shrinkage of the casting. At first glance, it might seem that as long as this requirement is met, it will always be sufficient. However, this is not always the case. As shown in **Figure 7.4**, there can be instances where the solidification time is adequate, but the volume that the riser can transfer is insufficient. Therefore, it is essential to consider the efficiency of the riser and the total shrinkage of the casting, as defined by the following equation:

$$eV_r = \alpha(V_r + V_c) \tag{2}$$

Where e is the efficiency of the risers (the percentage they can effectively feed), and α is the contraction coefficient during cooling. The values of e primarily depend on the shape of the riser. The coefficient α directly depends on the metal alloy used and represents the percentage of volume lost from the superheated state at pouring temperature to the liquidus temperature (liquid shrinkage) and the volume lost from the liquidus to the solidus temperature (solidification shrinkage) [3].

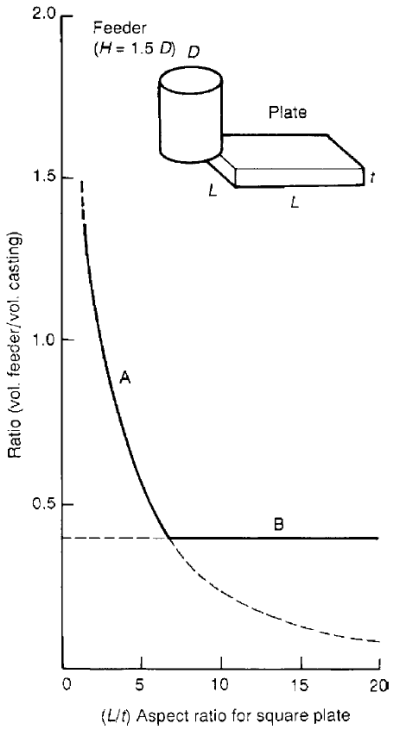

***Figure 7.4**. Riser and casting part volume ratio to part aspect ratio. Curve A is the minimum ratio to satisfy the thermal requirement and Curve B is the minimum to satisfy the volume requirement of risers* [5].

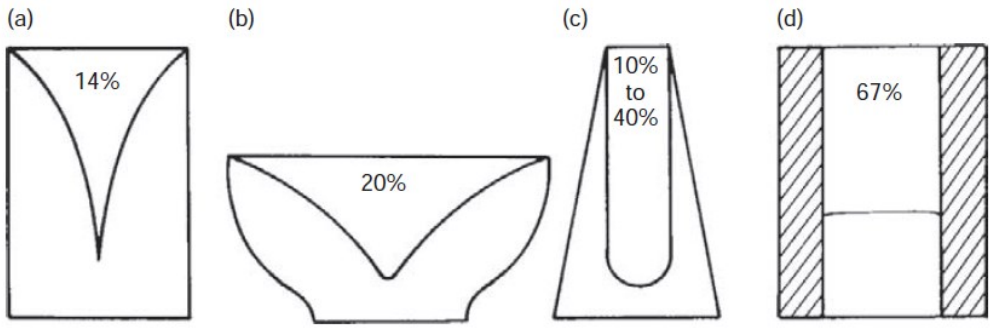

***Figure 7.5**. Volume of metal usage for different riser geometries and configurations. (a) Cylindrical, (b) hemispherical, (c) reverse tapered riser and (d) exothermic sleeve* [5].

4. **Junction requirement**. proper design of junctions where different sections of the casting meet. Sharp junctions can lead to localized hot spots and shrinkage defects. Junctions should be designed to promote smooth and progressive solidification. This can be achieved by using fillets and ensuring a gradual transition between sections.
5. **Feed path requirement (the communication requirement)**. The path through which the molten metal travels from the riser to the casting must remain open throughout the solidification process. This requires ensuring that the neck or passage connecting the riser to the casting does not freeze before the casting is fully solidified. Traditionally, the moduli of the casting, the neck and the riser are in the ratio 1:1.1:1.2 [6]. However, the riser neck dimensions can be reduced considerably based on [7] where the neck dimensions for aluminum and copper alloys can be dimensioned by:

$$\begin{cases} D_n = 0.25\ D_f \\ H_n = 0.06\ D_f \end{cases} \quad (3)$$

6. **Pressure gradient requirement**. A positive pressure gradient must be maintained from the riser to the casting to ensure that molten metal flows into the casting to compensate for shrinkage.
7. **Pressure requirement**. This rule ensures that the pressure in the riser is sufficient to overcome any resistance to flow and feed the casting effectively.

7.3 Methodology

For the development of the Computer Aided System for casTing design (eCAST), Synera has been selected as the platform of choice. This platform has been consistently used throughout this manuscript for all the bio-inspired design studies, demonstrating its versatility and robustness.

7.3.1 Introduction to Synera usage and Add-In development

Synera stands out as a low-code programming-based design tool, allowing for intuitive parameterization of geometries. This feature is essential for casting design, where flexibility and precision in component modeling are crucial. The ability to parameterize geometries facilitates the optimization and adjustment of designs efficiently, reducing time and resources in the development process.

Another significant advantage of Synera is its capability to connect with various CAD, CAE, and CAM tools. This interoperability allows for the integration and synchronization of design with advanced simulations and manufacturing processes, ensuring that the developed models are not only theoretically sound but also practical and manufacturable. The possibility to connect tools such as ProCast, used to analyze material behavior during casting, is a clear example of how Synera can enhance the design process by providing immediate and precise feedback on the performance of designs under real-world conditions.

Furthermore, Synera offers the possibility of developing new nodes specific to the platform. This capability had not been mentioned previously in the manuscript but is crucial for the development of a specialized Add-Ins. Creating custom nodes allows for adapting and extending the platform's functionalities, incorporating specific criteria and algorithms for designing feeding systems and other critical casting features.

In Synera, a node is a fundamental building block used to create and manipulate design workflows. Each node represents a specific function or operation, such as creating a geometry, performing a simulation, or executing a computation. Nodes can be connected in a sequence to form a comprehensive algorithm or design process. This modular approach allows for flexibility and scalability in design, enabling complex workflows to be constructed from simple, reusable components.

Algorithms in Synera are created by connecting nodes in a logical sequence, forming a network or graph. The connections between nodes define the data flow and the order of operations. The main structures used to organize these nodes include:

1. **Lists:** A linear sequence of nodes where each node performs an operation and passes the result to the next node in the list. This structure is simple and easy to understand, making it suitable for straightforward, linear workflows.

2. **Trees:** A hierarchical structure where a parent node branches out to multiple child nodes. This is useful for workflows that require branching logic, where different paths are taken based on certain conditions.

There exist variety of nodes categorized based on their functionality. The main categories include:

- **Geometrical nodes:** These nodes handle the creation and modification of geometrical shapes and structures. From curves to surfaces and solids, and performing Boolean

operations. As illustrated in **Figure 7.6** where a Boolean operation is performed between a sphere and a cylinder.

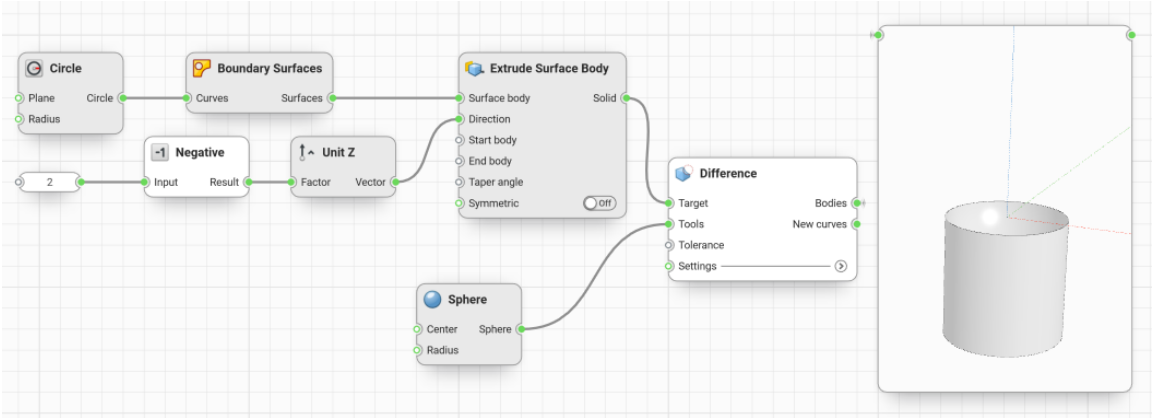

Figure 7.6. *Geometry creation and Boolean operation workflow inside Synera.*

- **Simulation nodes:** These nodes are used for setting up simulations and performing analyses on the designs. They can perform structural analysis, fluid dynamics simulations, and other engineering calculations. There is also the possibility to explore different optimization methods. As can be seen in **Figure 7.7** where a FE model of a cantilever beam is constructed.

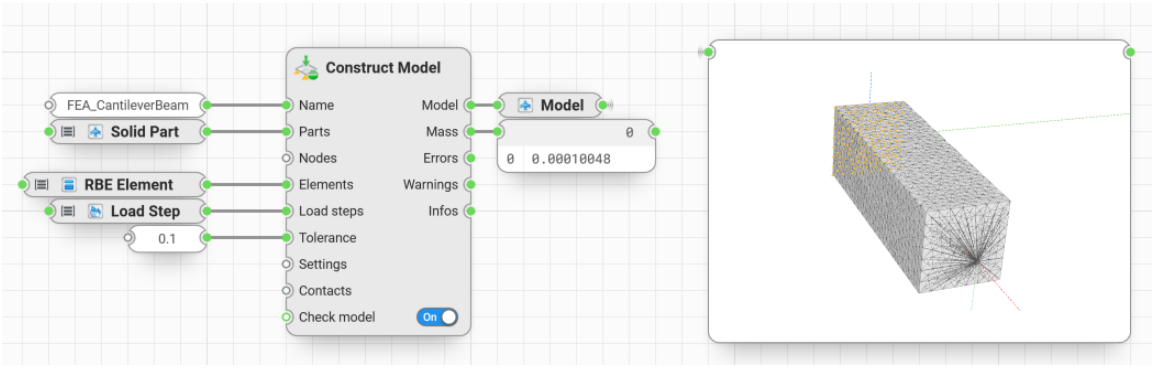

Figure 7.7*. Finite element model construction inside Synera.*

- **Data nodes:** These nodes manage data input, output, and transformation. They can handle different data types and structures, such as numerical data, strings, and complex data sets. They can perform mathematical operations and data structure transformations. These transformations can be seen in **Figure 7.8**.

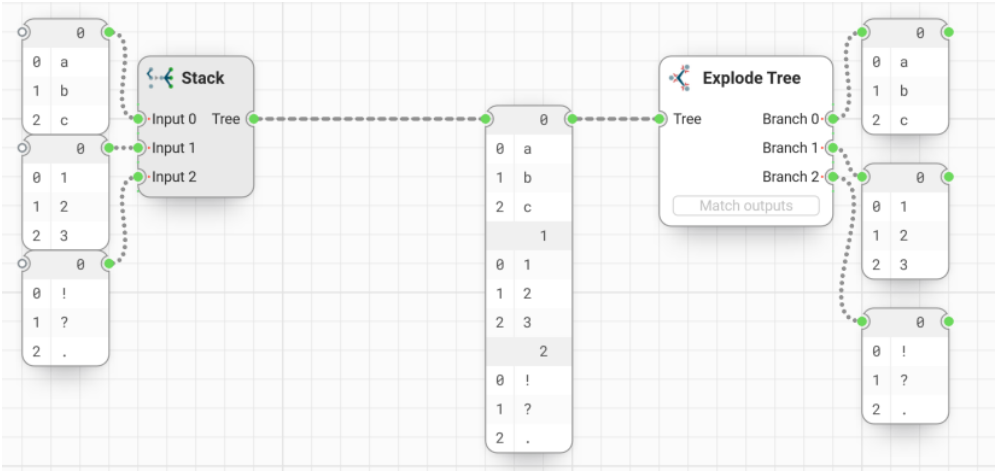

***Figure 7.8**. Data structure and data transformation workflow inside Synera.*

- **Control nodes:** These nodes control the flow of the algorithm, including conditional statements, loops, and event triggers. They enable the creation of dynamic and responsive workflows. A For loop example is shown in **Figure 7.9**.

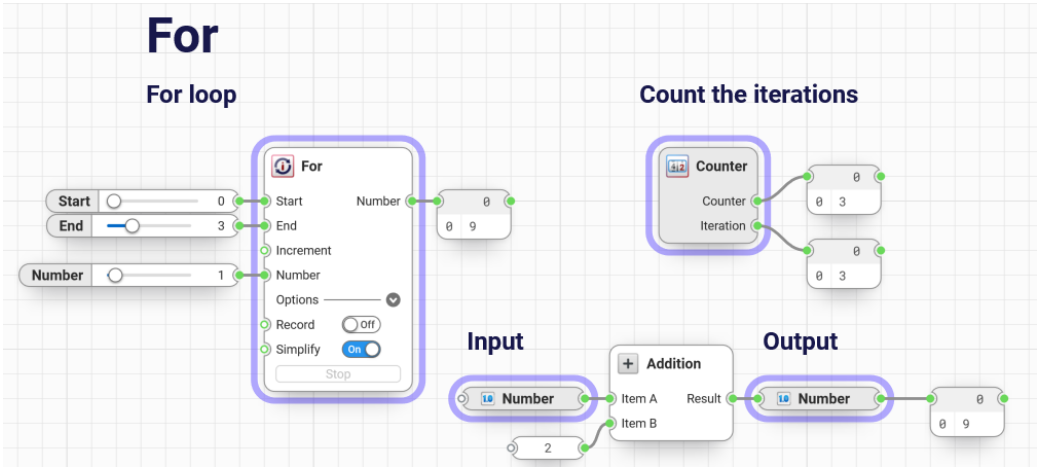

***Figure 7.9**. For loop workflow inside Synera.*

- **Custom Nodes:** These are user-defined nodes that extend the functionality of Synera. Developers can create custom nodes to perform specific tasks that are not covered by the default library. In the **Figure 7.10** some external Add-In nodes are shown.

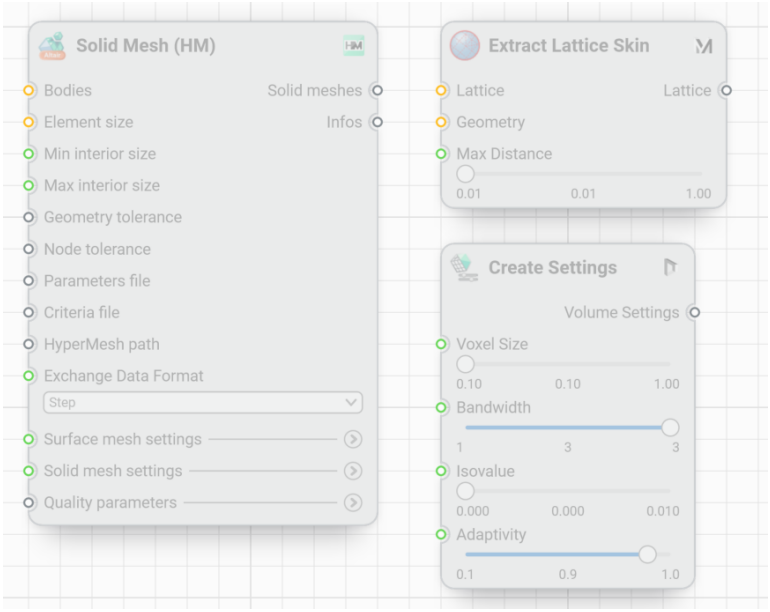

Figure 7.10. *Different private nodes inside Synera marketplace. The nodes shown are from HyperMesh, Mocha and Dendrise respectively.*

Developing a new node in Synera involves creating a custom module using C#. Synera provides a template and a dedicated development environment that includes predefined data types and utilities to assist developers. The process typically involves defining the node functionality, using the provided template, implementing the logic by writing the code for the node's functionality, testing the node through rigorous validation to ensure it performs as expected within various workflows, and finally, deploying the node so it can be integrated into the Synera environment and used in design workflows.

Synera features a marketplace where users can access and utilize nodes developed by external companies and third-party developers. This marketplace allows for the sharing and distribution of specialized nodes that extend the platform's capabilities. Users can browse the marketplace to find nodes that suit their specific needs, download them, and integrate them into their workflows seamlessly. This ecosystem fosters innovation and collaboration, enabling users to leverage a wide range of tools and solutions beyond the default library.

To use third-party nodes and the basic bundles provided by Synera, a licensing system based on tokens is employed. This token-based licensing model allows users to activate and utilize specific nodes and bundles according to their needs. Tokens can be purchased and allocated to different nodes or bundles, providing flexibility and control over the resources and functionalities available within Synera. This system ensures that users only pay for the features they need, optimizing costs while accessing advanced tools and functionalities.

7.3.2 eCAST Add-In development workflow

As previously mentioned, the aim of this study is to develop a tool within Synera capable of providing users with an optimal design of the necessary components for a successful casting

process. Given the complexity of addressing all adjacent elements, a proof of concept will focus on a tool that designs risers with optimal dimensions. To simplify development and based on the findings throughout this manuscript, aluminum has been selected as the material of study, gravity casting in sand molds as the reference casting process, cylindrical and vertical risers, and a simple geometry of the part.

Another complexity in developing such a tool is the selection of input parameters and success criteria for optimization. Numerous factors and phenomena within the casting process determine whether a cast will be successful. Initially, it must be determined if the part can be manufactured via this process, considering factors such as proper filling and the presence of overly thin or thick sections. However, these aspects are beyond the scope of this tool and are thus excluded. Nonetheless, to ascertain if the filling system is optimal, one must also consider the flow velocity in various sections, the type of flow, uniformity of filling, and the ingress of impurities. For simplification, the filling system has also been set aside in this study.

This study focuses on designing the feeding system, specifically the riser system. The location, dimensions, orientation, and shapes of risers are well-studied topics, with the success of most casting processes hinging on them. When evaluating casting process results and riser performance, whether in simulation or reality, shrinkage porosity and location are typically quantified. It is also crucial to analyze temperature distribution and the direction and timing of solidification. For simplicity and to demonstrate the tool's potential, the success criterion has been defined as the average porosity within the part, excluding porosity in the riser. While this criterion alone cannot fully determine if the feeding system is well-designed, it serves as a logical and useful parameter for showcasing initial results from the developed tool. Additionally, the tool has been designed to allow for the addition of parameters, success criteria, and functionalities with minimal structural changes.

To understand the operation of the proposed tool, it is necessary to define its constituent blocks, which will be specified throughout this section.

Riser theoretical dimensioning (1)

Inputs:

- Geometry of the part to be manufactured
- Shape ratio of the riser(s)

Outputs:

- Riser and neck dimensions (diameter/height)

Logic and internal functioning:

This block is based on the casting rules explained in the theoretical framework section. There are primarily two methods to determine riser dimensions:

1. **Thermal requirement:** The riser must solidify 20% later than the part. To achieve this, the volume of the part and its contact surface area with the mold are used to calculate the modulus of the part. Once the modulus is obtained, the equation 1 is solved for the riser height and diameter using the provided shape ratio H/D.

2. **Volumetric requirement:** The riser must be capable of feeding the volume contracted by the part, which depends on the riser's efficiency and the metal's shrinkage. In this case, the largest possible diameter is always chosen to ensure the riser's functionality. The equation 2 has to be solved.

Both equations are solved by incorporating the user-provided shape ratio H/D to derive the diameter from each method. As illustrated in **Figure 7.4**, there is a specific slenderness ratio of the part to be manufactured that determines which method will provide the most restrictive value. A series of Boolean operations are used to determine which method yields the largest diameter or the most restrictive value.

Once the height and diameter of the riser are determined, the riser neck is dimensioned. The neck must be designed to avoid hot spots and allow efficient material flow. Based on equations (3) proposed by Sciama et al. [7], both the diameter and height of the neck can be dimensioned.

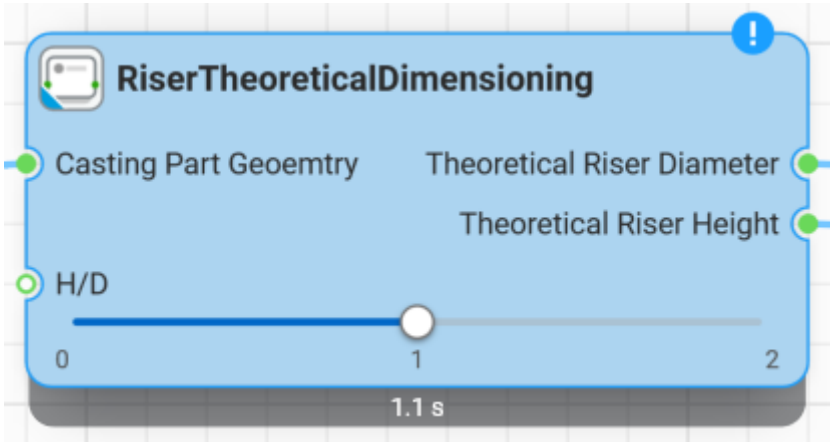

***Figure 7.11**. Overview of the node for the riser theoretical dimensioning.*

Geometry builder (2)

Inputs:

- Riser dimensions (diameter/height)
- Geometry of the part to be manufactured

Outputs:

- 3D solid geometry of the assembly

Logic and internal functioning:

This block constructs the geometry of the risers using the provided dimensions and the geometry of the part to be manufactured. The current focus is on vertical risers, strategically placed to optimize the casting process.

The process begins with receiving the riser dimensions (diameter and height) and the part geometry. The surface with the highest Z-component of the part is identified, and the central point of this surface is selected as the initial location for the riser, since the tool currently supports only vertical risers.

Using the input dimensions, a cylinder representing the riser is created. This cylinder is positioned vertically, with its base centered on the selected surface. The geometry of the cylinder is then integrated with the geometry of the part at the determined contact point, adjusting the riser neck to ensure a smooth, seamless integration.

The result is a 3D solid model that combines the part with the vertically positioned riser in the optimal location. This model can be used for subsequent simulations and detailed analyses of the casting process. In future versions of the tool, an additional input parameter will be included to specify the type of riser based on the feeding method, allowing for lateral risers or other more complex configurations.

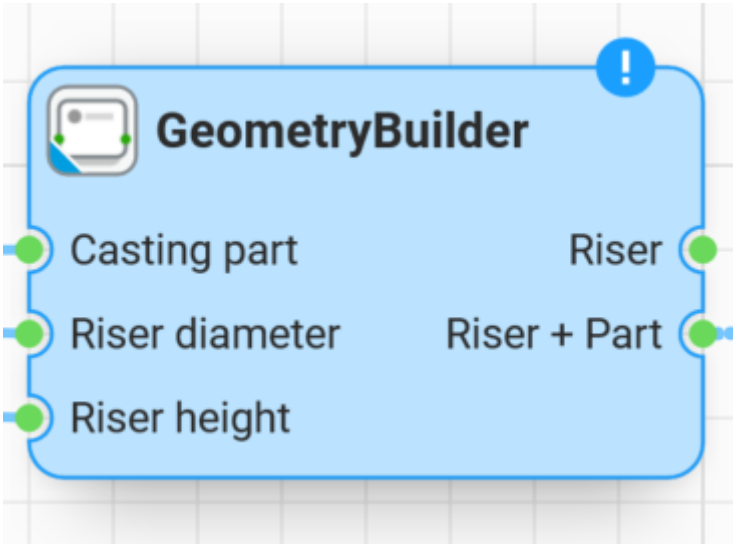

***Figure 7.12**. Overview of the Geometry Builder node.*

Geometry mesher (3)

Inputs:

- 3D solid geometry of the assembly

Output:

- Mesh understandable by ProCast

Logic and internal functioning:

This block aims to create a mesh within Synera that can be imported and understood by ProCast. Various methods were tested, given the tools available in ProCast, but only one has proven to be effective, though somewhat complex.

First, a shell mesh is created using the Altair Hypermesh connector available in Synera. It is crucial to differentiate between the meshes of the part and the risers, as ProCast requires them to be independent volumes to assign the correct properties to each geometry.

Next, different "properties" are assigned to each mesh, such as assigning a different material to each meshed volume. These materials do not have real properties; their purpose is simply to differentiate the meshed volumes in the output format. The .fem model is then constructed and translated into a format recognizable by ProCast, as HyperMesh's .fem format is incompatible.

To address this incompatibility, a Python script was developed to extract data from the .fem file (node coordinates, nodes of each element, properties of each element) and reconstruct it into a Nastran file, which is recognized by ProCast. This process ensures that the mesh created in Synera can be effectively used in ProCast, allowing for proper simulation and analysis of the casting process.

ProCast launcher (4)

Inputs:

- Mesh understandable by ProCast
- Mold temperature
- Pouring temperature of the melt
- Material type (ProCast library)

Output:

- Simulation result: average porosity in the part

Logic and internal functioning:

This block performs the simulation using the mesh obtained from the previous block, allowing the user to input critical parameters such as the pouring temperature of the melt, mold temperature, and material type, selected from the ProCast library. Currently, these are the selected input parameters, but this list is subject to modification as additional necessary parameters are defined.

The process begins with a Python script that selects the basic simulation parameters, including creating the solid mesh, mold type, mold material, and thermal parameters. This script generates a .bat file executed by Synera. The .bat file configures the simulation in ProCast, launching the

process and waiting for it to complete. The current simulation focuses on solidification, as a filling system has not yet been defined.

Once the simulation is complete, the Python script reads the results file generated by ProCast, specifically extracting the average porosity value in the part's volume. This value is written to a CSV file that Synera can read and display to the user, providing immediate feedback on the design's quality in terms of porosity.

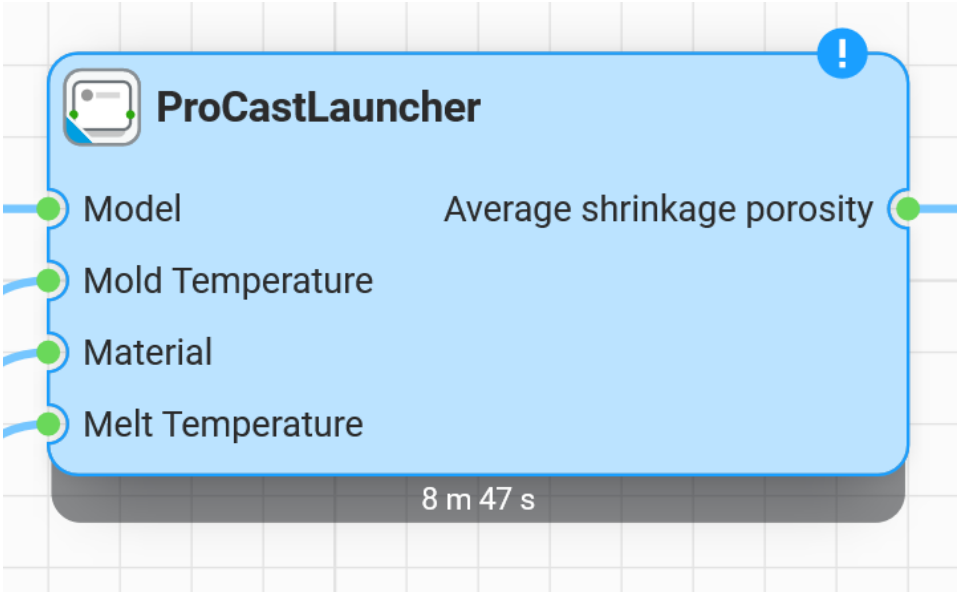

***Figure 7.13**. Overview of the ProCast Launcher node.*

Optimizer (5)

Inputs:

- Simulation result: average porosity in the part
- Initial riser dimensions
- Input parameters

Outputs:

- Optimized result of riser location and dimensions

Logic and internal functioning:

This block aims to optimize the location and dimensions of the risers based on the simulation results of average porosity and the initial input parameters. The logic behind this block focuses on defining a series of input parameters that create variations in the designs to be evaluated, such as the riser diameter and its location.

The initial parameters are values close to those obtained in the theoretical dimensioning (1), which helps avoid excessive iterations and focus the optimization more precisely. Additionally, the total number of designs to be evaluated is defined, affecting the total calculation time required for optimization.

The primary optimization criterion, for now, is to minimize the average porosity in the part. The optimizer executes a loop starting from block (2), repeating each step with the input parameters of each selected design for evaluation. During this process, multiple design variants are generated, each with adjustments in the dimensions and locations of the risers.

The optimizer evaluates each design through successive simulations, adjusting the input parameters to minimize porosity. Finally, the result is the optimized geometry of the assembly, with riser dimensions and locations that ensure superior casting quality.

The Add-In developed for Synera aims to provide an optimal design of risers in the aluminum casting process. The functioning of the block set is illustrated in **Figure 7.14**.

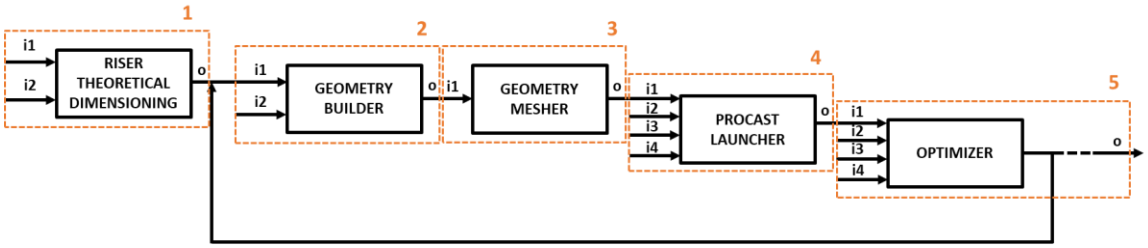

***Figure 7.14**. Diagram depicting the whole set up and workflow for the eCAST Add-In.*

The process begins with the **Riser theoretical dimensioning**. In this initial block, the geometry of the part to be manufactured and the riser's shape ratio are used to calculate its initial dimensions (diameter and height). This calculation is based on two fundamental requirements: thermal and volumetric. The thermal requirement ensures that the riser solidifies 20% later than the part, while the volumetric requirement guarantees that the riser can feed the contraction volume of the part.

Once the theoretical dimensions of the risers are determined, the next step is the **Geometry builder**. This block takes the calculated dimensions and the part geometry to create a 3D solid model. The riser is positioned vertically at the center of the surface with the highest Z-component of the part. This precise integration prepares the assembly for the meshing stage.

The next block is the **Mesh generator**, which transforms the solid geometry into a mesh understandable by ProCast. A shell mesh is created using the Altair Hypermesh connector, differentiating between the part and riser meshes so that ProCast can assign the correct properties to each volume. Subsequently, a Python script converts the .fem file to a ProCast-compatible format, such as a Nastran file, ensuring the correct import and understanding of the mesh by the simulation software.

With the mesh ready, the process moves to the **ProCast launcher**. This block runs the simulation using the generated mesh and allows the user to input critical parameters such as pouring temperature, mold temperature, and material type. A Python script selects the basic simulation parameters and generates a .bat file that Synera executes. The simulation is conducted, and upon completion, the average porosity value in the part is extracted, saved in a CSV file, and displayed by Synera.

Finally, the **Optimizer** closes the loop by using the simulation results of average porosity, along with the initial riser dimensions and other input parameters, to adjust and improve the design. This block creates design variations, evaluating different configurations of riser diameter and location to minimize the average porosity in the part. The optimizer repeats the process from the geometry construction block, executing each step with the new parameters until an optimized configuration is found.

7.3.3 Results

To illustrate the function of each block, an example must be provided that effectively represents the desired results of this tool. Given that this tool is currently a proof of concept for an aluminum sand casting piece to calculate the dimensions of its vertical and cylindrical risers, the most suitable geometry for testing its functionality is a prism with a square section but varying height, with a riser on its surface having a greater component in the Z direction, as shown in **Figure 7.15**.

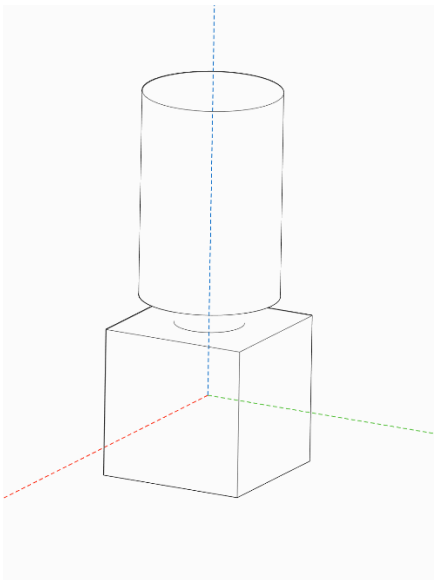

***Figure 7.15**. Geometry to be used to illustrate the application of the Add-In.*

It's important to emphasize that this Add-In was not designed solely to obtain results for the example studied here. Instead, the development was approached in a generalist manner. Although we will examine the results for the simple geometry presented earlier, we will also demonstrate how the Add-In can be utilized, with some enhancements, for more complex geometries.

To begin, the geometry of the piece to be manufactured is created or imported and input into the initial blocks of Riser Theoretical Dimensioning and Geometry Builder. Here, the geometry is theoretically dimensioned and constructed. The results obtained with different geometry inputs can be illustrated in **Figure 7.16**. As shown, it is possible to input a geometry divided into distinct parts to design an ad-hoc riser for each of the different modules.

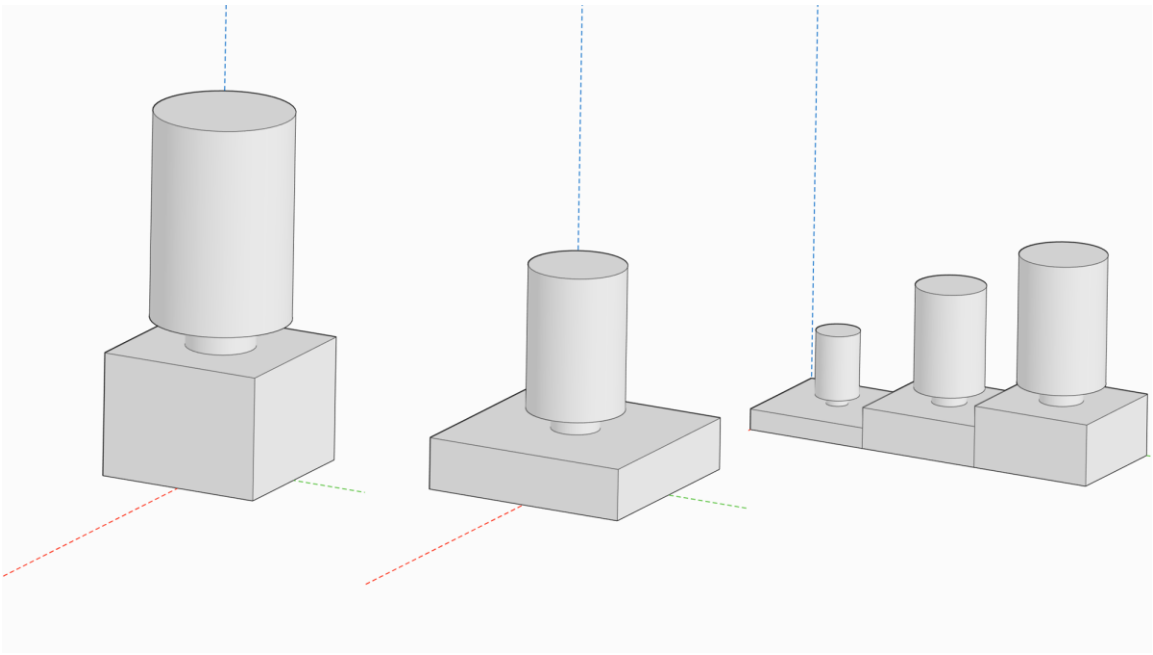

***Figure 7.16**. Geometrical output of the theoretical dimensioning for different part designs. A thick plate example of a single module (**left**), an example resembling a single-module narrow plate (**center**), and an example of a stepped part with three modules (**right**).*

The different values of the riser volume-to-piece volume ratio obtained exhibit the same trend and curve as the theoretical curve shown in **Figure 7.17**.

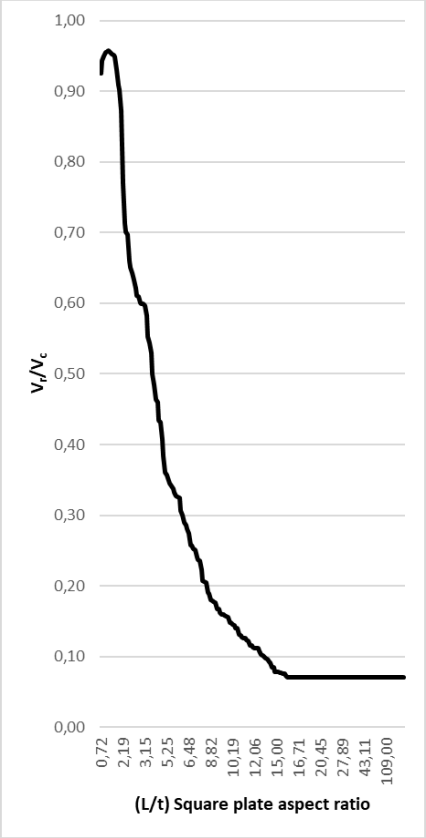

***Figure 7.17**. The actual result of the riser-to-part volume ratio based on the aspect ratio of the plate.*

For the studies conducted in this initial version of the Add-In, a mesh with triangular elements was used, with an element size of 15% of the smallest coordinate among the three dimensions defining the total contour of the part and riser geometry. The resulting mesh, shown in **Figure 7.18**, is sufficiently fine to achieve adequate precision without excessive computational time. The mesh is finalized in ProCAST. It is crucial that the different volumes are distinguishable, as illustrated in **Figure 7.18**.

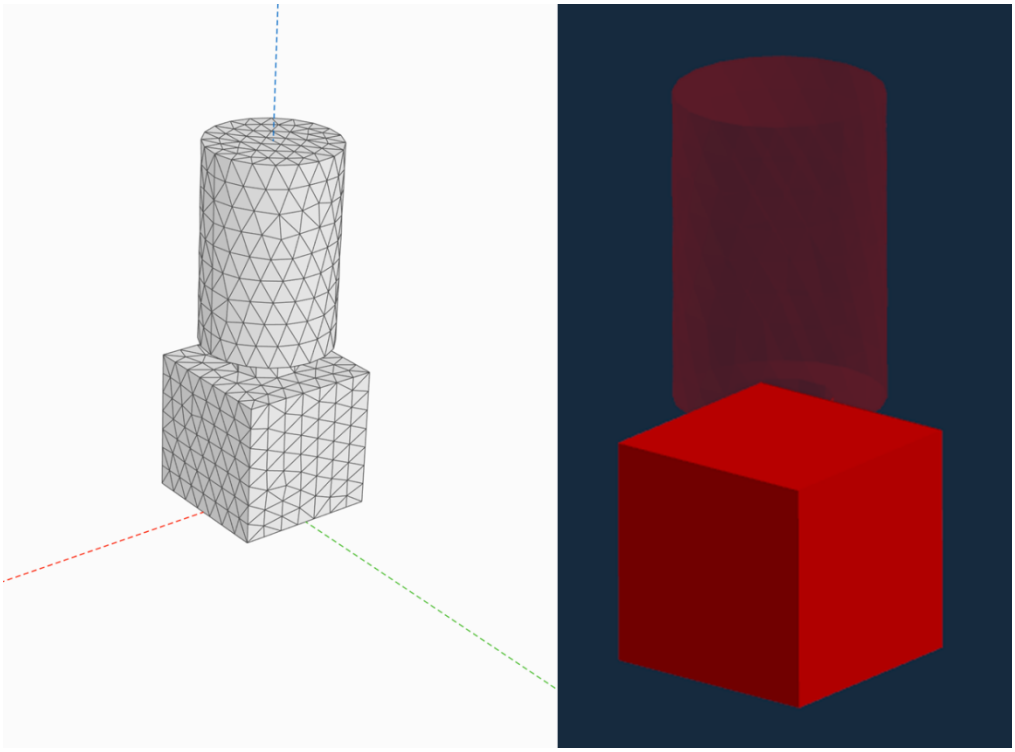

***Figure 7.18**. Result of the shell mesh after the meshing process in Synera (**left**). Result of the volume differentiation in ProCast (**right**).*

In the first loop with the theoretical dimensions of the riser, the ProCast Launcher took a total of 7 minutes and 57 seconds. In **Figure 7.19**, both the defined input parameters and the result of average shrinkage porosity can be seen. Additionally, by opening the simulation in ProCast, it can be observed that the liquid fraction remains longer in the riser than in the piece, which was desired. However, a similar porosity is observed in both the piece and the riser.

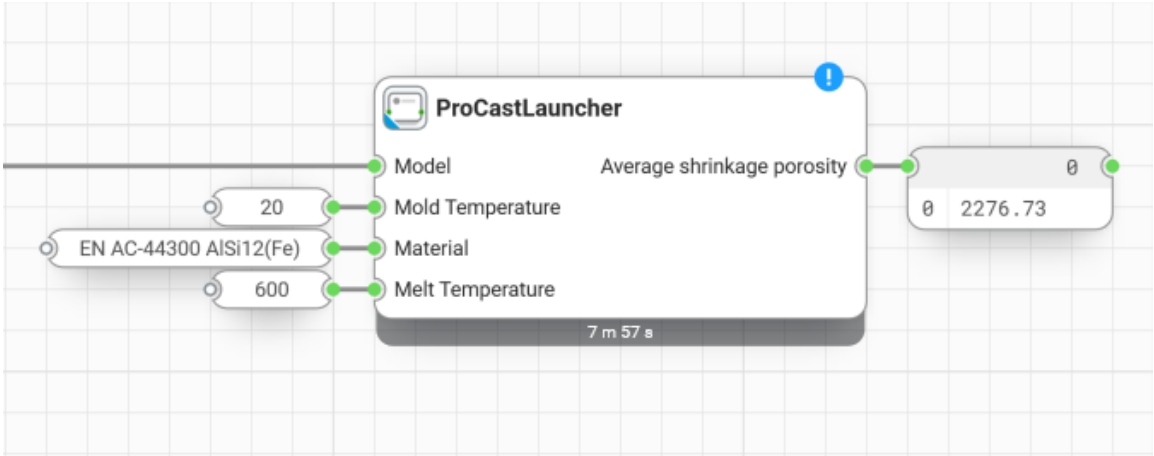

***Figure 7.19**. The ProCast Launcher node with the input parameters and the results using the theoretical dimensions of the riser.*

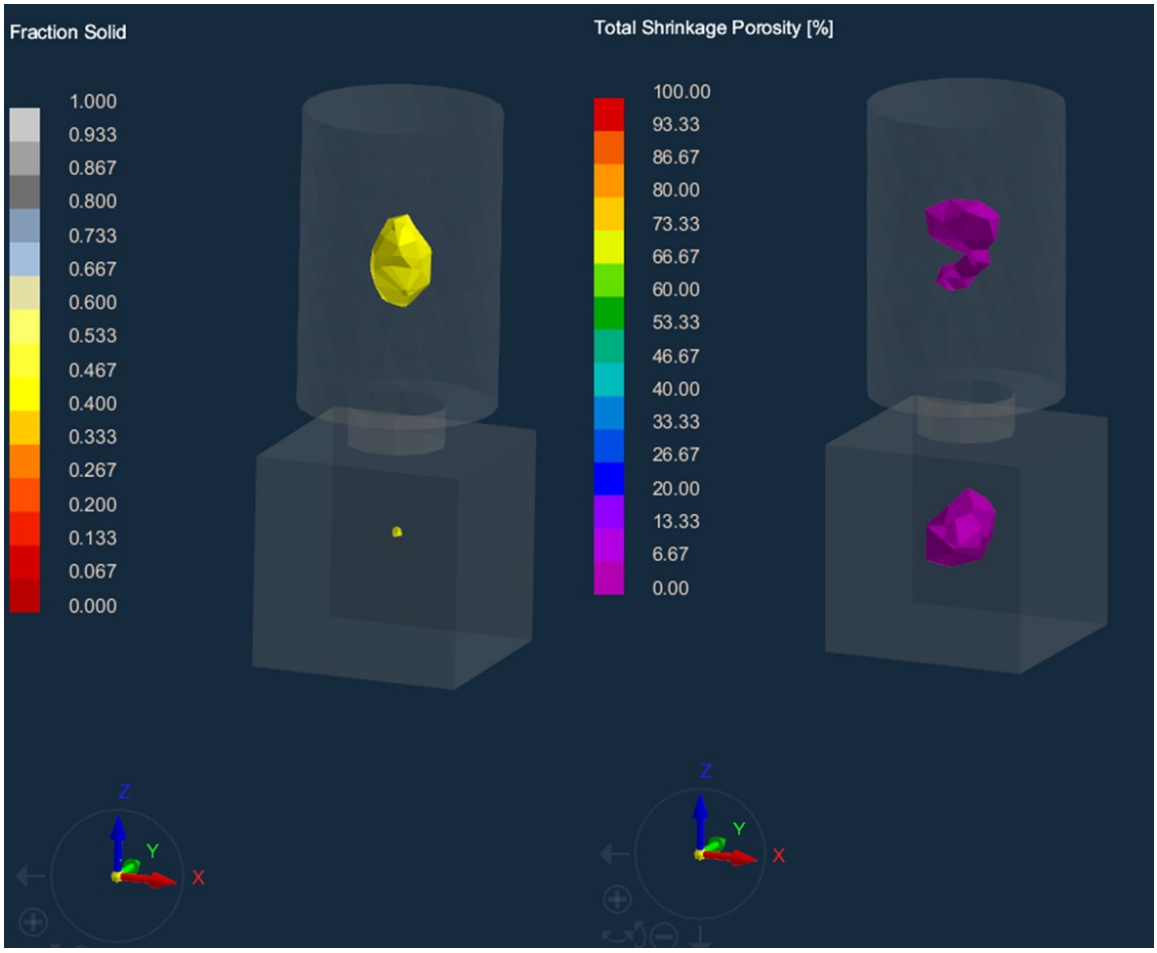

***Figure 7.20**. Result of the solid fraction of the part and riser with the theoretical dimensions of the riser (**left**). The same showing shrinkage porosity results instead (**right**).*

Next, we define the input parameters for the optimization cycle. For this test, the riser diameter is set as the optimization parameter. The initial value is based on the theoretical sizing result, which is 186 mm in this case. The optimization loop's objective is to minimize the average shrinkage porosity of the part, as illustrated in **Figure 7.21**. The optimization process is limited to 150 iterations before it is initiated.

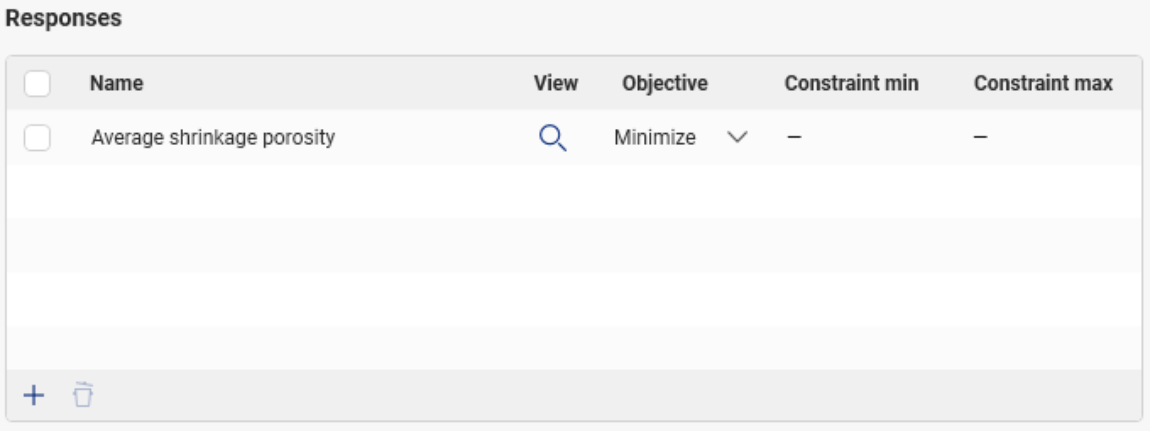

***Figure 7.21**. Optimization response definition for minimizing average shrinkage porosity in Synera.*

After defining the parameters and optimization settings, the loop is initiated. The optimization did not fully converge, although there are moments of apparent stabilization, indicating an unclear pattern in the results. The loop took approximately 7 hours to complete the 150 designs, with the best result being design #138, featuring a diameter of 205 mm and an average porosity of 2.89818%, as shown in **Figure 7.22**.

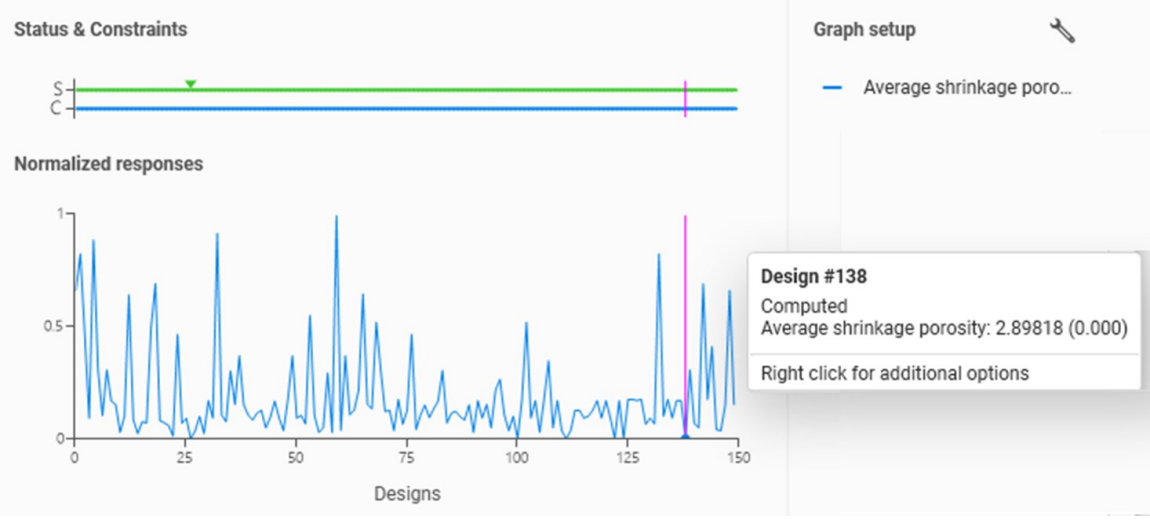

***Figure 7.22**. Optimization loop results with 150 iterations in Synera*

7.4 Discussion

The results presented in the previous section indicate that the theoretical sizing of the risers may not be entirely accurate. Notably, the theoretical diameter exhibits one of the highest porosity values at 3.07752%, suggesting that the theoretical dimensioning is suboptimal. The optimizer block plays a crucial role in accurately sizing the riser.

The optimization loop aimed to compare the graph in **Figure 7.3** with the results from ProCAST simulations. The data was analyzed and processed to generate the graph shown in **Figure 7.23**. This graph reveals that at low values (up to the minimum) of the thermal module ratio between

the riser and the part (m_r/m_c), the trend is sharply decreasing, similar to **Figure 7.3**. A minimum is observed around a ratio of 1.3, followed by a slightly negative trend, contrasting with the second section of **Figure 7.3**. However, considering the dispersion of the data points, the slope is so mild that it could be either positive or negative, thus warranting cautious interpretation.

Nonetheless, the clear minimum value occurs at a ratio of 1.32 with a porosity of 2.89818%. This contrasts with the theoretical sizing and the minimum observed in **Figure 7.3**, which occurs at a ratio of 1.2. This discrepancy could be attributed to the nature of the piece; typically, a piece as massive as the one in the example would not be manufactured by casting. If a similar case arises, this tool appears capable of detecting such a fault, providing the best possible result.

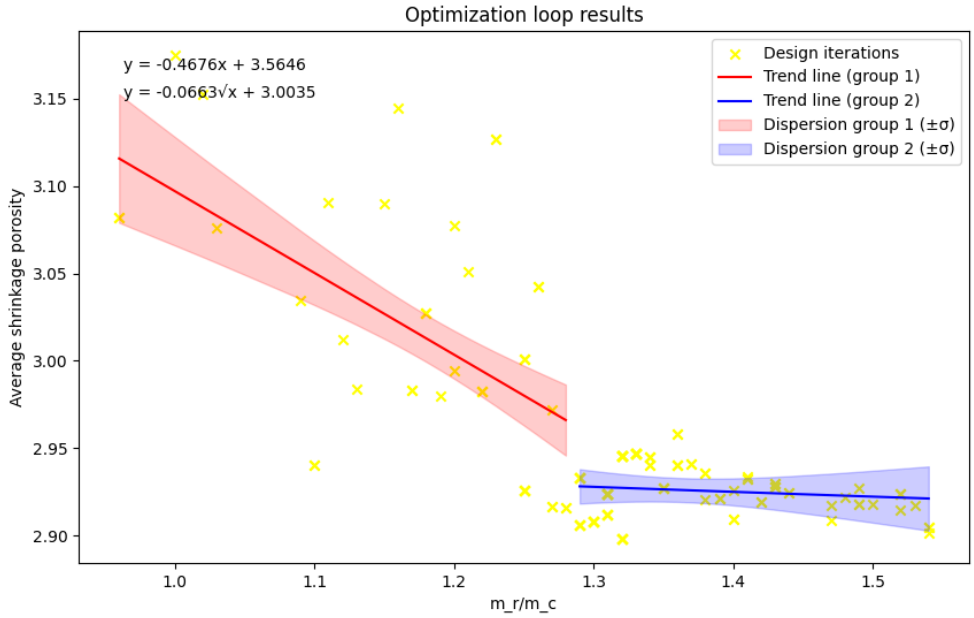

***Figure 7.23**. Average shrinkage porosity values for each optimization iteration to the ratio of riser and part thermal modules.*

In conclusion, despite being a somewhat rudimentary tool at present, it demonstrates utility in accurately sizing the riser in atypical cases. The theoretical sizing provides a useful starting point and constrains the optimization cycle, thereby reducing computational costs. The lack of full convergence in the optimization suggests that a clear minimum is not evident, as the variability in porosity values beyond an m_r/m_c ratio of 1.25 is minimal. Nevertheless, the minimum value was obtained within the expected range.

It should also be noted that the riser positioning was not included as an optimization parameter in this case. Given that the mold is a cube with equal distances from all sides, the optimal positioning is clearly at the center of the surface with the highest Z component of the cube. However, it would have been straightforward to add this positioning as an additional optimization parameter, though this would significantly increase computational costs without a clear theoretical justification.

7.5 Conclusions

The tool proposed throughout this chapter has proven effective for a specific type of casting with low complexity, which may be less significant compared to real-world manufactured parts. However, as emphasized from the beginning of the chapter, this is an initial and exploratory version of a tool that will be further developed in the future.

The results presented and discussed in the previous sections demonstrate how such a tool can dimension elements more precisely than the results proposed in various reference texts used for the theoretical framework, although data verification with real casting tests is still pending. There is a tendency to over-dimension casting elements to avoid failures, which increases material waste and energy consumption. A tool like this could optimize dimensions, reducing these issues.

Moreover, if the tool is developed further to design more casting elements and incorporate necessary modifications to ensure successful casting, it could provide comprehensive control over material quantities, manufacturable geometry, and mold design from the initial phase. This would avoid the iterative process typical of traditional engineering methods, bringing engineering design tools closer to a holistic design approach, as discussed throughout the manuscript.

However, this remains speculative as the tool is still in a rudimentary state and the science behind casting is not fully integrated. As mentioned, the selection of optimization parameters presents a significant challenge. In this example, the goal was solely the correct dimensioning and positioning of the riser, with the average porosity of the part as the only success parameter. This is not entirely realistic, as accurate determination of these magnitudes might require additional results, such as solidification patterns or thermal gradients. Due to resource limitations within this study, this is as far as the research has progressed. Nevertheless, it is believed that enough has been done to demonstrate the tool's functionality and significant potential, considering the direction of the engineering design sector.

7.6 References

[1] M. Tiryakioğlu and E. Tiryakioğlu, “A comparative study of optimum feeder models for castings,” *International Journal of Cast Metals Research*, vol. 14, no. 1. Maney Publishing, pp. 25–30, 2001. doi: 10.1080/13640461.2001.11819421.

[2] B. He, Y. Lei, M. Jiang, and F. Wang, “Optimal Design of the Gating and Riser System for Complex Casting Using an Evolutionary Algorithm,” *Materials*, vol. 15, no. 21, Nov. 2022, doi: 10.3390/ma15217490.

[3] “ASM Handbook Volume 15: Casting,” 2008, Accessed: Jun. 30, 2024. [Online]. Available: https://www.asminternational.org/asm-handbook-volume-15-casting/results/-/journal_content/56/05115G/PUBLICATION/

[4] P. Biswas, S. Patra, and M. Kumar Mondal, “Structure-property correlation of eutectic Al-12.4 Si alloys with and without Zirconium (Zr) addition,” *International Journal of Cast Metals Research*, vol. 33, no. 2–3, pp. 134–145, May 2020, doi: 10.1080/13640461.2020.1769319.

[5] J. Campbell, “Complete Casting Handbook: Metal Casting Processes, Metallurgy, Techniques and Design: Second Edition,” *Complete Casting Handbook: Metal Casting Processes, Metallurgy, Techniques and Design: Second Edition*, pp. 1–1028, Sep. 2015, doi: 10.1016/C2014-0-01548-1.

[6] P. R. Beeley, “Foundry technology,” p. 544, 1972.

[7] G. Sciama, “TAFS,” vol. 83, pp. 127–140, 1975.

Chapter 8: Conclusions and future developments

8.1 Conclusions

The traditional engineering processes have been shown to be increasingly inadequate in addressing modern global challenges such as climate change and material scarcity. These methods often rely on iterative, experience-based cycles that are slow, inefficient, and prone to overdimensioning. In contrast, this thesis explores advanced computational tools based on bio-inspired design principles to create more efficient and sustainable engineering solutions. This research aims to significantly improve the design based on functionality, manufacturability and sustainability. This conclusion chapter will revisit the problem definition and scope outlined in the introduction, assess the effectiveness of the proposed methodologies, and discuss its limitations and drawbacks.

The results obtained throughout the manuscript for the various case studies demonstrate that mimicking nature can indeed be effective. A hybrid methodology combining different bio-inspired design methods was proposed to enhance metallic components, proving to be successful in addressing the challenges outlined along the whole manuscript. This approach has shown that integrating bio-inspired principles with advanced computational tools can significantly improve the efficiency, sustainability, and performance of engineering components, validating the initial hypothesis and objectives of this research.

The analysis of the origins of natural forms conducted in the literature review of Chapter 2 provides valuable insights into why and how some of these structures can be utilized and scaled. Additionally, this analysis sheds light on the genesis of these geometries, enabling future researchers to understand how these processes can be emulated and applied across various engineering fields. As demonstrated in this study, understanding the natural formation of these structures offers a foundation for developing innovative and efficient engineering solutions.

As observed, the application of the proposed methodology or the use of natural geometric patterns applied to engineering structures, requires knowledge and the ability to locate the most relevant information. Which means that usually engineering designers lack knowledge of biological structures and therefore a major simplification may be done. This can be achieved by classifying natural patterns into categories and their functionalities independently on the being on which are based. If negative, it necessitates a level of abstraction to envision the necessary characteristics of the structure and how to apply them to the component. While the method of applying patterns in this study is primarily through topology optimization and a revision of natural palette, there is an inherent level of subjectivity, mainly in the choice of natural geometric pattern. However, by parameterizing the geometry and conducting parametric optimization, this

subjectivity is minimized. It is important to note that the process is not entirely automatic; certain decisions, such as the selection of the pattern, rely on the designer's expertise.

As discussed in Chapter 3, the methodology selected and consistently used throughout the manuscript may not be the best in all cases. However, the selection method demonstrated significant potential, which justified its use. While not universally optimal, the methodology has proven effective for the intended goals, though other options should still be considered. This flexibility and openness to alternative methods ensure that the approach remains adaptable and capable of addressing a wide range of engineering challenges.

The example of the aerodynamic element in Chapter 6 may seem somewhat outside the primary focus of the thesis. However, it is believed to offer valuable insights for researchers investigating bio-inspired designs applied to different physical domains. In fact, the study of such designs for elements like thermal management systems or electromagnetic components is currently very relevant. Therefore, these design methodologies should not be confined solely to structural design, and the results of that chapter are a testament to their broader applicability and potential.

At the beginning of the manuscript, holistic design is discussed, emphasizing the consideration of manufacturing constraints from the design phase, among other factors. However, this process remains relatively manual today. In the examples presented, manufacturing constraints are applied through geometric parameterization, limiting minimum thicknesses and selecting a favorable manufacturing direction. The inclusion of mathematical models or artificial intelligence could potentially yield components with fewer defects from the design phase. The development discussed in Chapter 7, for instance, moves in this direction. Although it does not alter the geometry of the part itself, the eCAST add-in aims to assist designers from the outset, guiding their designs to be more manufacturable through casting, thereby reducing the reliance on the experience of plant operators. It has been observed that professionals in heavy industry with knowledge of specific metallurgical processes are becoming scarce, and this tool aims to mitigate the impact of this knowledge gap.

The principles of ecodesign are guidelines that should be taken into account in the coming years, as European regulations are moving in this direction [1]. The focus is on avoiding single-use components or those with a short lifespan. There is an emphasis on using raw materials from recycled sources and ensuring that components can have a second life or be easily recyclable at the end of their life cycle. Therefore, it is always beneficial to consider these concepts from the design phase of these components. This manuscript has touched on certain aspects of this, including ecodesign studies to assess the environmental feasibility of proposed designs. Additionally, easily recyclable aluminum alloys were selected. Applying these principles in the design phase aligns with the manufacturing considerations and functionality aimed components for the holistic design approach, effectively encapsulating the lifecycle concept discussed in the introduction chapter with the analogy of a tree's lifecycle.

As discussed in the introduction, improving environmental impact are crucial goals in modern engineering and manufacturing. Lightweighting components not only leads to more efficient systems but also significantly reduces material consumption and energy use during production and operation. This manuscript has demonstrated the effectiveness of using advanced design methodologies to achieve substantial weight reduction in various components. These strategies contribute to lower fuel/power consumption and reduced greenhouse gas emissions, aligning with global efforts to combat climate change.

The methodologies explored in this manuscript, offer more efficient and precise solutions compared to traditional engineering approaches. By minimizing the repetitive cycles of design, testing, and modification, these advanced methods streamline the engineering process, saving both time and resources. Moreover, the integration of advanced manufacturing techniques, including additive manufacturing, allows for the production of complex geometries that are not feasible with conventional subtractive methods. This not only improves the performance and efficiency of the components but also reduces material waste and environmental impact. However, to fully realize the potential of these methodologies, there is a need to industrialize them for large-scale production and enhance their reliability. While this manuscript primarily focused on demonstrating the feasibility and effectiveness of the proposed methodologies, future research should aim at scaling these techniques for mass production.

All the manufacturing methods utilized throughout this manuscript rely heavily on additive manufacturing technology. Whether it is the direct fabrication of metallic components or the creation of sand molds for casting, additive manufacturing has been a key enabler for implementing designs with complex geometries. This technology has significantly expanded the possibilities for innovative and efficient design solutions, making it possible to realize intricate structures that were previously unattainable with traditional manufacturing methods.

However, there is also the potential to apply some of these advanced design methodologies to more conventional manufacturing techniques. While traditional methods may not offer the same level of flexibility and precision as additive manufacturing, they can still benefit from the principles of bio-inspired design.

One of the potential issues with these optimized components is that, when defining the load cases for the study, some aspects may be overlooked, which could eventually lead to component failure. Fatigue is a notable example; during topology optimization, cyclic loads are typically not considered as part of the study but there exist some studies already working on this [2]. This omission could result in a component failing under cyclic loads, thereby shortening its lifespan. However, with proper subsequent validation, as demonstrated in some of the cases studied here, it is possible to assess whether the component can withstand the cyclic loads it will be exposed to. Despite this, load cases involving fatigue would still follow traditional methods because, if the component were found to fail, iterations between stages would be necessary.

This manuscript has demonstrated that bio-inspired techniques can effectively overcome the limitations of traditional engineering methods, as initially discussed. By focusing on lightweight, functionality-driven, manufacturing-oriented, and eco-designed products, the case studies validated the feasibility and effectiveness of these methodologies, showcasing significant advancements in weight reduction and efficiency. Although the concept of holistic design is highly ambitious and the proposed methodology may represent only the initial steps towards a more comprehensive approach, the results indicate that combining various bio-inspired design techniques with advanced, tailored manufacturing methods can yield promising outcomes. Throughout this work, efforts have been made to adhere to the noble principles of engineering while acknowledging the limitations of the current methodology. It is now the turn of future research to build on these foundations and further advance this field.

8.2 Future developments

Given the advancements achieved in this thesis, it is essential to outline potential future developments in this area. These developments range from the most realistic and short-term to the more futuristic and somewhat speculative:

- **Extend methodology to other physical domains**: Applying the bio-inspired and optimization methodologies to other fields such as fluid dynamics, thermal management, or electromagnetism could lead to innovative solutions in these areas.
- **Enhance integration of manufacturing processes and ecodesign principles**: Further integration of advanced manufacturing processes with ecodesign principles can create a more holistic and automated design approach, ensuring sustainability and efficiency from the initial design phase. Generative design solutions are pushing towards these achievements.
- **Standardization and industrialization**: Developing standards and industrial processes for components designed and manufactured using advanced technologies can facilitate broader adoption and ensure quality and consistency across various industries. More and more optimized and additively manufactured parts are being used as main structural parts, but broader efforts need to be done.
- **AI integration for design and simulation**: Integrating design and simulation tools with advanced AI models can significantly reduce computational time and enhance the precision of results, leading to more efficient design processes. Many efforts aiming to have predictive models that allow avoiding traditional simulations by learning with a big amount of simulation data. First results seem to be promising.
- **Self-healing components**: Researching and developing materials and technologies that enable components to self-repair can extend their lifespan and reliability, reducing maintenance costs and downtime. Current advancements such as some aluminum and magnesium alloys that exhibit self-repairing mechanisms, are laying the groundwork for such innovations.

- **Large language models for design and validation**: Utilizing large language models capable of designing and validating components through natural language interaction could revolutionize the design process, making it more accessible and intuitive (akin to the concept of JARVIS). With the appearance of such models and the advancements in simulation and computation suggest significant potential for simplifying complex design tasks.
- **Self-reproducing components**: Exploring the concept of self-reproducing components, inspired by natural processes, could lead to breakthroughs in manufacturing, allowing components to be produced and maintained autonomously. While this remains speculative, foundational research in synthetic biology and autonomous systems hints at future possibilities.

These future developments aim to push the boundaries of current engineering practices, leveraging advanced technologies to create more efficient, sustainable, and innovative solutions. By pursuing these avenues, the field can continue to evolve, addressing the complex challenges of modern engineering.

8.3 References

[1] "Ecodesign for Sustainable Products Regulation - European Commission." Accessed: Jun. 16, 2024. [Online]. Available: https://commission.europa.eu/energy-climate-change-environment/standards-tools-and-labels/products-labelling-rules-and-requirements/sustainable-products/ecodesign-sustainable-products-regulation_en

[2] Y. Chen *et al.*, "Topology Optimization Design and Experimental Research of a 3D-Printed Metal Aerospace Bracket Considering Fatigue Performance," *Applied Sciences 2021, Vol. 11, Page 6671*, vol. 11, no. 15, p. 6671, Jul. 2021, doi: 10.3390/APP11156671.